Dissertation

submitted for the combined degrees of

Doktor der Naturwissenschaften in der Fakultät für Mathematik und Biowissenschaft in der Ruprecht Karl Universität von Heidelberg, Germany

Docteur de Chimie de l'Université de Bordeaux I, France

Presented by

Xavier Richard von Hatten

Heidelberg, June 2006

Toward Hydrogenase mimicry: Subjecting the problem to three different approaches

Manuscript submitted: October 15th, 2006

External referees:

Dr. S. Bellemin-Laponnaz

PD Dr. F. Breitling

Oral Examination: November 14th, 2006

Committee:

1st Referee Prof. Dr. N. Metzler-Nolte

2nd Referee: Dr. I. Huc

3rd Referee: Prof. Dr. A. Jäschke

4th Referee: Prof. Dr. J-B. Verlhac

Acknowledgements

I would like to acknowledge people who support me, encourage me and show interest for my research during my PhD Thesis.

Prof. Dr. Metzler-Nolte, for the chance he gave me to work in his group in Heidelberg, and to follow him in Bochum when it was necessary. For his open-mindness when I asked him to spend some of his research money in others working groups. I appreciate his optimism, his trust and the large degree of freedom he gave me during my research.

Dr. Ivan Huc, because he accepted me in his group, he worked hard to make the joint PhD collaboration possible and fruitful. He was always available for discussions, and capable of giving many helpful synthetic tricks.

Prof. Dr. Jeremy Smith, for the opportunity to work in his group and the access to his research resources. I particularly appreciate the time he invested in the correction of my drafts.

Dr. Srecko Kirin, for sharing his office during three years and for the all-day conversations. I would like to thank him for his permanent help in many fields at the beginning, the middle and the end of my PhD.

Dr. Ulrich Schatzschneider, for performing the DFT calculation in Chapter 3, and for helpful conversations about electrochemical measurements.

Zoe Cournia, for the time she spent to teach me the basis knowledge of molecular modelling, but also for debugging my input files when it was necessary. I particularly appreciate the controversial and motivating discussions.

Heiko Rudy, for his efficiency, his kindness, his valuability and for the 200 Elemental analyses he measured for me and surely twice as much mass spectrogram. Ohne dein Hilfe, dies alles erst gar nicht möglich gewesen wäre.

Uli Hoffmanns, Tim Kersebohm, Thomas Happ, Richard Wombacher, Mark Helm, Markus Petermeyer, Tobias Timmermann … für die „Krasses Zeit“: Fußball, Doko, Tisch Tennis, Grill-Party.

Bei allen anderen IPMB Institutsmitgliedern, es war gemütlich mit euch zu arbeiten. Alle waren nett zu mir. Ich werde euch nie vergessen.

I would like to thank people from computational chemistry in IWR, for the helpful tricks, for sharing useful input files and especially for spending time trying to find solution for my problems.

Merci aussi à Nicolas, Céline, Thomas, Loïc, et toutes les personnes que j’ai côtoyé durant mes séjours à l’IECB. Bravo pour l’ambiance que vous avez créée au sein des laboratoires, pour cette très agréable atmosphère de travail et surtout pour m’avoir intégré dans cette dynamique si rapidement et si simplement.

Mes parents, qui même après dix longues années d’études ont toujours continué d’y croire. Pour leurs soutiens, moral et financier, sans lesquels, rien n’aurait été possible.

Ma petite Anne chérie, pour tout le reste.

pour Anne,

Abstrakt

de Hatten Xavier Dipl.-Chem. 15. Juni 2006

„Drei neue Konzepte für strukturelle und funktionelle Hydrogenase-Modelle“

In dieser Arbeit wird die schwierige Aufgabe, Hydrogenase zu modellieren, drei verschiedenen Ansätzen unterworfen.

Die erste Strategie die verwendet wird ist *bioorganometallische*. Eine Reihe Ferrocen-peptid Verbindungen wurde synthetisiert und völlstandig charakterisiert. Die Thiol-Schutzgruppe wurde nachher entfernt und wurde danach durch complexierung mit Eisen carbonyl eine neue Klasse Fe-only hydrogenase Strukturmimetika mit Ferrocen-Peptid Rückgrat erlangt. Umfassende elektrochemische Untersuchung offenbart eine potentielle Elektronenübertragung zwischen den zwei Eisenenheiten des Moleküls.

Im zweiten Ansatze wird eine *theoretische* Untersuchung des Ferrocen-Peptids durchgeführt. Um eine breiteres Feld von Ferrocen-Peptiden als molekulares Gerüst zu untersuchen, wurde ein molekulares Kraft-Feld erfolgreich erzeugt und in CHARMM implementiert. Nach der notwendigen Validierung mit bekannten experimentellen Strukturen wurde das erhaltene Kraft-Feld verwendet, um mehrere Modellsysteme auf ihre Durchführbarkeit für das präsentierte Projekt zu untersuchen. Deshalb, wurden sterische Hindernisse und die Gestalt des Schwefels Ligande analysiert. Es wird gezeigt dass die erhaltenen Resultate, für viele Aspekte der Synthese nützlich sind.

Als ein drittes Ansatze wurde *organische* übergeordnete Struktur von oligoquinoline, als potentielle Ligand für Eisen-carbonyl hydrogenasemimetika studiert. Die gut definierte gefaltete Struktur erlaubte uns die Positionierung des Schwefel Monomers in der Sequenz vorauszusagen. Die vorausgesagte Struktur wurde synthetisiert und vollständig charakterisiert. Nach dem Entschützen der Thiol-Gruppe, wurde auch die complexierung mit Eisen-carbonyle durchgeführt.

In dieser Arbeit, wurde über die synthetischen, spektroskopischen und theoretischen Leistungen, die Effizienz des multidisziplinarischen Ansatzes an ein einzigartiges Ziels demonstriert.

Abstract

de Hatten Xavier Graduate Student 15. June 2006

„Toward Hydrogenase mimicry: Subjecting the problem to three different approaches“

In this work, the challenging task of modelling Hydrogenase is subjected to three different approaches. The first strategy used here is *bioorganometallic*. A wide range of sulfur containing ferrocene-peptide derivatives were synthesized and fully characterized. The thiol group was subsequently removed and after complexation with iron carbonyl, a new class of structural mimic of Fe-only hydrogenase with ferrocene-peptide backbone was obtained. A comprehensive electrochemical study led on these new derivatives reveal a potential electron transfer between the two iron sites of the molecule.

In the second approach, a *theoretical* computational study of the ferrocene-peptide derivatives is led. In order to investigate a wider range of ferrocene-peptide as a molecular scaffold, a molecular force field was successfully implemented in CHARMM. After the necessary validation step on experimental structures, thus obtained force field was used to investigate several model systems by mean of their feasibility for the presented project. Therefore, the sterical hindrance and the shape of the sulfur chelating shell were analysed during dynamic simulations. Results obtained are shown to be helpful for many aspects of the synthesis.

As a third approach, *organic* self-assembled oligoquinoline were studied as potential scaffold of hydrogenase mimics. The predictability of the well-defined folded structure allowed the positioning of sulfur modified monomer in the sequence. Thus predicted structure, were synthesized and fully characterized. After the deprotection of the thiol group, the free SH group were used as ligand for iron-carbonyl.

In this work, above the synthetic, spectroscopic and theoretic achievements we have demonstrated the efficiency of the multidisciplinary approach to serve a unique goal.

Zusammenfassung

„Drei neue Konzepte für strukturelle und funktionelle Hydrogenase-Modelle“

Bei seinen Untersuchungen zu Gärungsprozessen im Flußschlamm entdeckte der deutsche Biochemiker Ernst Felix Immanuel Hoppe-Seyler Ende des 19. Jahrhunderts erstmals, daß Bakterien molekularen, gasförmigen Wasserstoff (H_2) aufnehmen und abgeben. Im Jahre 1931 beschrieben Marjory Stephenson und Leonard Hubert Stickland ein für diese Prozesse verantwortliches Enzym und nannten es Hydrogenase. In der folgenden Zeit wurden Hydrogenasen in zahlreichen Bakterienarten gefunden. Der deutsche Biochemiker und Pflanzenphysiologe Hans Gaffron entdeckte bei seinen Untersuchungen der Stoffwechselleistungen einzelliger Grünalgen in den dreißiger Jahren, daß auch diese eukaryotischen Mikroorganismen Wasserstoff umsetzen. Außerdem erkannte er, daß der Wasserstoffmetabolismus bei Algen mit der Photosynthese im Zusammenhang steht. Lange Zeit war die biologische Wasserstofforschung nur ein Feld für Spezialisten. Erst durch die Ölpreiskrisen 1973/74 und 1979/80 und der damals gestarteten Suche nach neuen Energiequellen sowie durch die seit einigen Jahren aktuelle Umweltdiskussion mit der damit verbundenen Notwendigkeit, die Verwendung umweltgerechter Energieträger zu fördern, erlangte dieses Arbeitsgebiet auch öffentliches und politisches Interesse.

Hydrogenasen (H_2asen) sind bakterielle Enzyme, die die reversible Umwandlung von molekularem Wasserstoff in Protonen und Elektronen katalysieren. Je nach dem aktiven Zentrum unterscheidet man drei verschiedene Typen metallhaltiger H_2asen: nur Eisen enthaltende ([Fe-only]), hetero-bimetallische ([Ni-Fe]) und [Ni-Fe-Se] H_2asen, in denen ein Selenocystein an das Ni-Zentrum koordiniert ist. Die erste Röntgenstrukturanalyse einer H_2ase wurde von Volbela et al. 1995 publiziert, das Enzym wurde aus dem Sulfat-reduzierenden Bakterium *Desulfovibrio gigas* isoliert. Inzwischen sind mehrere weitere Röntgenstrukturanalysen metallhaltiger H_2asen veröffentlicht worden. Das folgende Bild 1 zeigt das aktive Zentrum einer [Ni-Fe]-H_2ase.

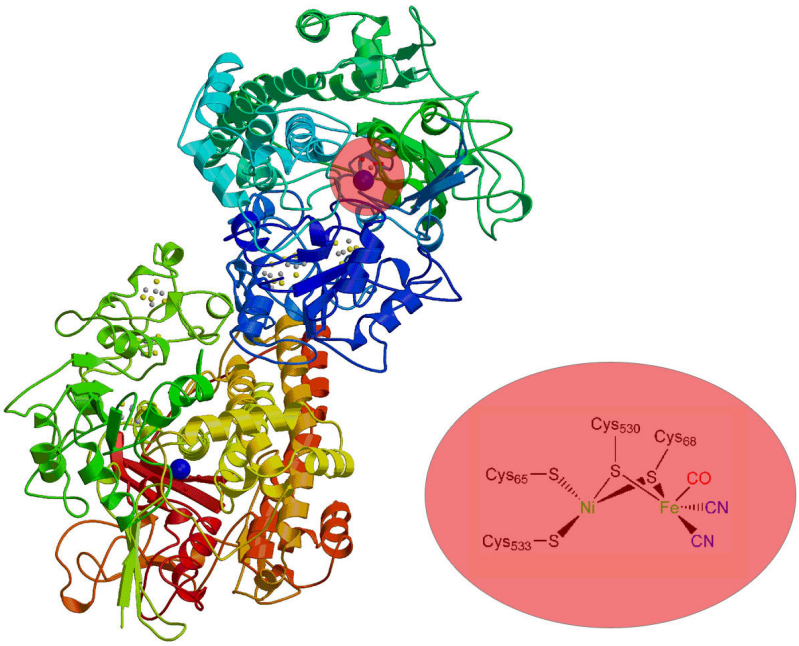

Bild 1 Tertiäre Struktur und das aktive Zentrum der [Ni-Fe]-H_2ase von *Desulfovibrio Gigas*

Alle Hydrogenasen weisen gemeinsame Eigenschaften auf, die als essentiell für die Funktion dieser außergewöhnlichen Enzymklasse angesehen werden können.

- Zweiatomige Liganden (vor allem CO und CN^-) um ein Eisenatom
- Low-spin Fe(II) Elektronenkonfiguration für dieses Eisenatom
- Eine Kette von Fe-S-Clustern verbindet das aktive Zentrum, welches im Inneren des Enzyms liegt, mit der Oberfläche.

Uns fasziniert besonders die metallorganische Koordinationsumgebung des Eisenatoms mit Cyanid- und Carbonylliganden. Beide Liganden sind zwar in der synthetischen metallorganischen Chemie ubiquitär, in der Natur ansonsten jedoch völlig unbekannt und stellen für sich genommen sogar starke Zellgifte dar. Trotz zahlreicher spektroskopischer und theoretischer Arbeiten sind der genaue Mechanismus der Hydrogenasen und die Funktion der $Fe(CN)_2(CO)$-Gruppe bisher unbekannt. Anorganische Verbindungen vermögen einzelne Schritte der Hydrogenasen wie z. B. den H/D - Austausch zu modellieren oder dienen als spektroskopische oder strukturelle Modelle. Es gibt nur sehr wenige Arbeiten zu Modellsystemen von Metalloenzymen, in denen die natürlich vorkommenden Aminosäuren oder kleine Peptide als Liganden für die Metallatome eingesetzt werden.

In diesem Projekt wollen wir drei neue Konzepte für strukturelle und funktionelle H_2ase-Modelle umsetzen. Die drei Ansätze kommen aus drei verschiedenen Bereichen der Chemie.

Erster Ansatz

Die Kernpunkte unseres Konzeptes sind a) die Verwendung von kleinen Peptiden mit Cysteinen als Liganden für die Metalle im aktiven Zentrum und b) die Verwendung eines metallorganischen Rückgrates (Ferrocen) als strukturgebendes Merkmal, zur sterischen Abschirmung und als Elektronenrelay. Eisencarbonyl wird in diesen Modellverbindungen an die Schwefelliganden eines Cysteins koordiniert

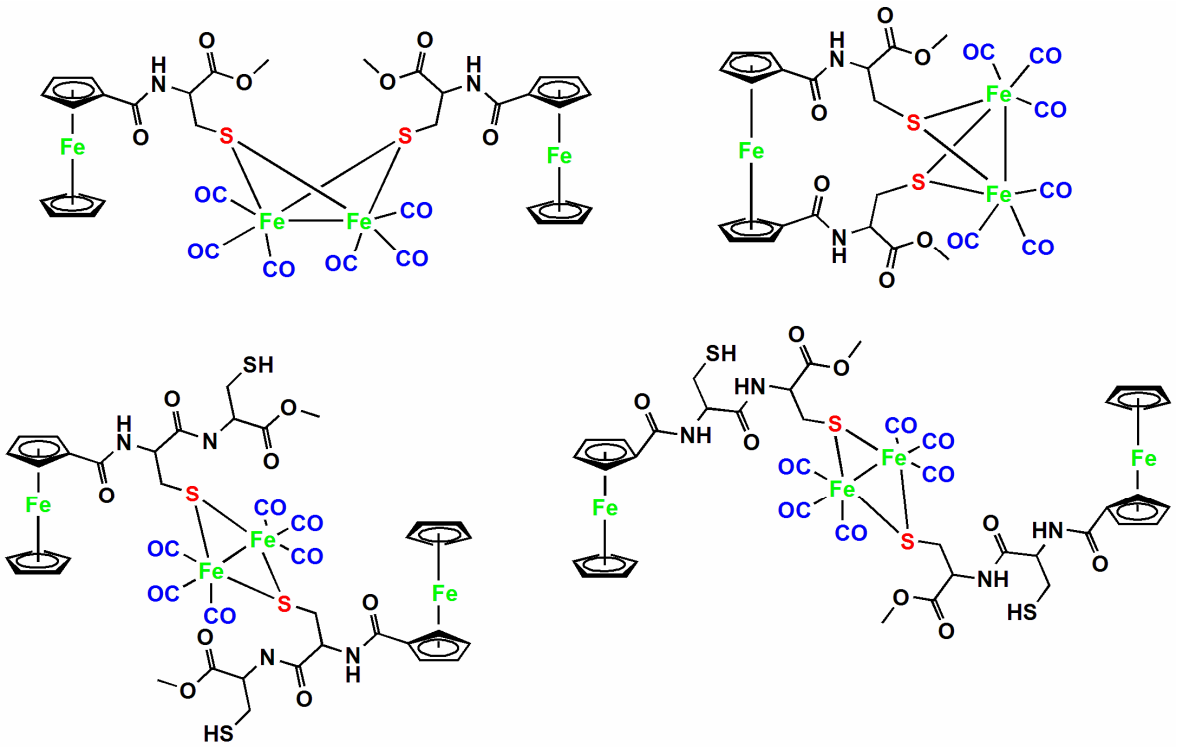

Bild 2 In dieser Arbeit dargestellte Hydrogenase-Modellkomplexe

Im Rahmen dieses Projektes konnten wir über zwei Dutzend Biokonjugate aus Peptiden mit S-haltigen Aminosäuren (Cys und Met) mit Ferrocen mono- und di-carbonsäure synthetisieren und vollständig charakterisieren. Von fünf Verbindungen konnten Einkristall-Röntgenstrukturanalysen erhalten werden. Die Eisencarbonyl-Komplexe in Bild 2 wurden auch vollständig spektroskopisch charakterisiert, insbesondere

mit Elektrochemie und Mössbauer Spektroskopie zur Untersuchung der elektronischen Eigenschaften der Eisenatome.

Zweiter Ansatz

Da die strukturellen Voraussetzungen zur Umsetzung unseres Konzeptes korrekt zu sein schienen, entschlossen wir uns, mittels Molecular Modelling die Durchführbarkeit dieses Projektes zu überprüfen. Es mussten zunächst im Programmpacket CHARMM die Parameter für substituierte Ferrocene implementiert und optimiert werden. Zunächst wurden die Partialladungen der Atome des Cp-Rings mitteln quantenmechanischen Methoden bestimmt (DFT, doppelt ξ Basissatz, B3LYP Korrelations-Austausch). Die van-der-Waals-Parameter der Cp-Sauerstoff-Atome wurden adjustiert. Die van-der-Waals-Parameter der Eisenatome wurden von dem parametrisierten Häm-Eisen übernommen. Schließlich wurden die Bindungslängen restrained und die Cp-Ringe mit dem Eisen durch eine externe Kraftkonstante zusammengehalten. Dieses Vorgehen garantiert die freie Drehbarkeit der Cp-Ringe gegeneinander, die ein zentrales Paradigma dieses Projektes darstellt. Die experimentell ermittelte Rotationsbarriere von Ferrocen (0.9 kcal mol^{-1}) wurde durch Veränderung der van-der-Waals-Parameter der Wasserstoffatome reproduziert (0.8 kcal mol^{-1}).

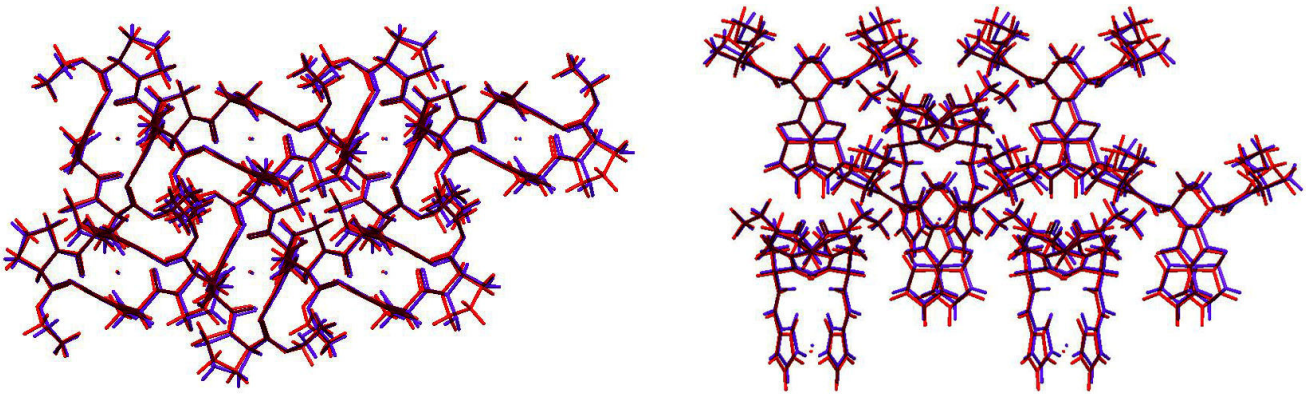

Bild 3 Überlagerung der Festkörper- (blau) bzw. berechneten (Molecular Modelling, rot) Strukturen von Ferrocenoyl-Peptiden.

Das derart erhaltene Modell für substituierte Ferrocene ist in der Lage, die strukturellen Eigenschaften verschiedener Modellverbindungen präzise zu reproduzieren. Als Beispiel zeigt Abbildung 3 eine Überlagerung der Kristallstrukturen von Fe[C_5H_4-CO-

Ala-Pro-OEt]$_2$ in Seitenansicht und Aufsicht, wie sie im Festkörper bestimmt (blau) bzw. durch Molecular Modelling (rot) erhalten wurden. Die mittlere Abweichung der wesentlichen Atome ist < 0.5 Å, was ein ausgezeichnetes Ergebnis darstellt.

Nach Etablierung eines geeignetes Modells und dessen Evaluierung wurden umfassende Berechnungen (Modelling und Molecular Dynamics Simulation) an den für diese Arbeit relevanten Ferrocenoyl-Peptiden durchgeführt. Die folgenden zwei Ergebnisse waren für die weitere Entwicklung dieses Projektes wesentlich. Auf der Grundlage eines elektrostatischen Modells ist es energetisch nicht möglich, daß vier Cysteinliganden an ein Ni(II) Zentrum koordinieren. Dabei ist es unerheblich, ob die Verbindungen Fe[C_5H_4-CO-Cys-Cys-OMe]$_2$ betrachtet wird oder das Ferrocen mit zwei verschiedenen Peptiden substituiert wird, die exakt den Aminosäure-Sequenzen in Hydrogenasen entsprechen (Strang I: Pro-Cys-Ile-Ala-Cys-Thr; Strang II: Ala-Cys-Gly-Val-Cys-Gly). Wie die folgende Abbildung (linkes Bild 4) zeigt, ist das System zu gespannt und eine der Cys-Seitenketten dissoziiert vom Metallatom ab. Das rechte Bild 4 zeigt die energieminimierte Struktur nach 1 µs Moleküldynamikrechnung.

Andererseits ist es problemlos möglich, diese beiden Peptide an einem Ni-Atom koordiniert zu halten (Startkoordinaten nach Entfernung des Ferrocens und Absättigung freier Valenzen mit H-Atomen). Die Molecular Dynamics Simulation (Bild 5) zeigt für diesen Fall jedoch, daß die *N*-Termini der Peptide auseinander driften und in der energieminimierten Form im Gegensatz dazu die *C*-Termini in räumliche Nähe kommen. Der C-C-Abstand in der minimierten Struktur beträgt nur etwa 4 Å. Dieses Ergebnis, welches durch eine Vielzahl weiterer Berechnungen abgesichert wurde, ist von zentraler Bedeutung für das Design neuer Modellsysteme in diesem Projekt.

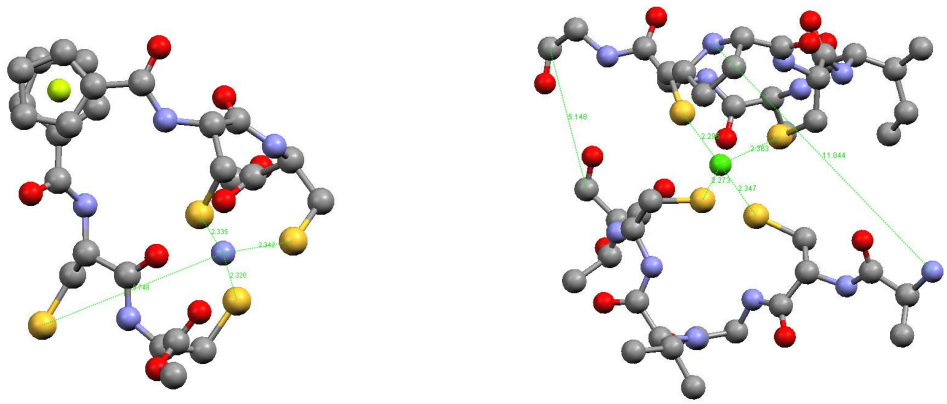

Bild 4 Energieminimierte Struktur nach 1 µs Moleküldynamikrechnung

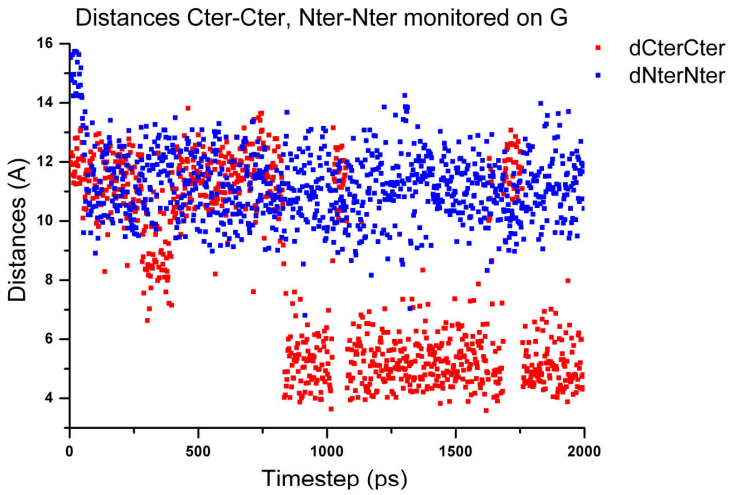

Bild 5 Die C-C und N-N Abstände der minimierten Strukturen

Dritter Ansatz

Als ein dritter Ansatz wurde die Struktur von Schwefel-substituierten Oligoquinolinen als rein organischer potentieller Ligand für Eisencarbonyl Hydrogenasemimetika studiert.

Die Strukturen wurden aus den Einheiten 2,8-Aminoquinolinecarbonyl und 1,10-Phenantrolinedicarbonyl gebildet. Wasserstoff-Brücken zwischen aufeinander folgenden Amid-Gruppen produzieren eine Selbstorganisation in der helicalen Struktur.

Diese gut definierte gefaltete Struktur erlaubte uns, Propeller zu planen, die sich vollkommen an das Bedürfnis der Synthese anpassen. In dieser Strategie wurde zuerst das "Design" der Strukturen geplant, um die Positionierung des Schwefelatoms in der Sequenz vorauszusagen.

Anhand einer molekularen Simulation mit dem Kraftfeld MM3 aus der Macromodel-Software wurden die Oligomerstrukturen berechnet und vorausgesagt. In Bild 6 sind die berechneten Strukturen des Pentamers Chinolin-Chinolin-Phenantrolin-Chinolin-Chinolin (links) bzw. des Chinolin-Hexamers (rechts) dargestellt. Die Positionen der Thiolfunktionen sind gelb hervorgehoben.

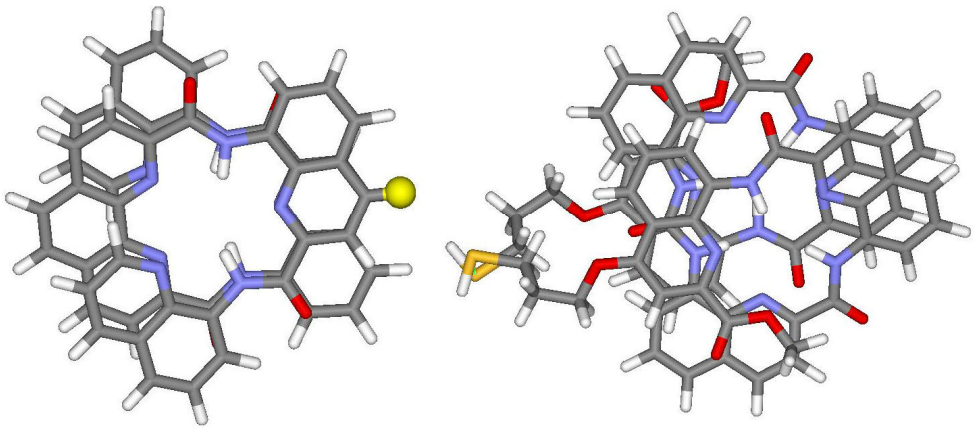

Bild 6 Vorhersage der Chinolin-Oligomere, berechnet mit Macromodel

Die vorausgesagten Strukturen wurden anschließend im Labor synthetisiert und vollständig charakterisiert. Bei der Synthese haben wir uns aus technischen Gründen auf das Pentamer **B24** und **B23** konzentriert. Die synthetisierten Verbindungen wurden vollständig durch Massenspektrometrie und NMR-Spektroskopie charakterisiert. Drei Pentameres konnten im Festkörperzustand durch Röntgenanalyse charakterisiert werden, die Struktur von **B24** ist als Beispiel in Bild 7 gezeigt.

Nach dem Entschützen der Thiol-Gruppe wurde auch die Komplexierung mit Eisen-carbonyl durchgeführt.

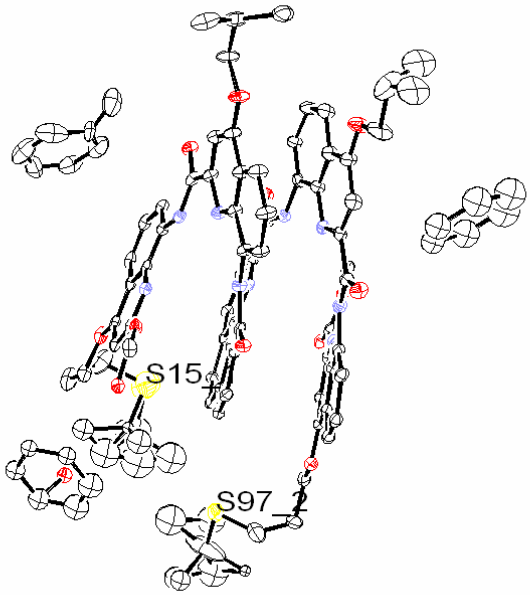

Bild 7 Kristallstruktur eines synthetisierten Oligomers (**B24**).

Résumé

„Modèle structurel et fonctionnel pour le site actif de l'Hydrogénase : Etude menée selon trois approches différentes"

Dans les années 1900, le chercheur Hoppe-Seyler découvrit une nouvelle variété de bactéries responsables de la décomposition de l'acide formique en dihydrogène et en dioxyde de carbone. Après l'isolation d'une culture de bactéries productrices de dihydrogène et d'une culture de bactéries oxydatrices de dihydrogène, l'hypothèse a été émise selon laquelle la molécule de dihydrogène pourrait avoir un rôle important dans le métabolisme des bactéries. Les enzymes responsables de l'activation du dihydrogène ont été nommées "hydrogénases" (contraction de « Hydrogen acceptor oxydo-réductase ») par le groupe de recherche dirigé par les professeurs Stephenson et Stickland en 1931. Depuis, les hydrogénases ont été détectées dans un grand nombre de micro-organismes.

Les enzymes de la catégorie des hydrogénases sont capables de catalyser l'oxydation réversible du dihydrogène en protons et en électrons. Par définition le potentiel standard à l'équilibre est de -413 mV à pH=7.0 sous 1 bar de pression en dihydrogène. Les électrons ainsi obtenus permettent à la bactérie de réduire plusieurs types de substrats, dont l'acide formique et le dioxyde de carbone, et de générer suffisamment d'énergie pour la synthèse de l'ATP.

Cette oxydation réversible produit des électrons au faible potentiel (H_2/H^+=-414 mV au pH=7.0 à la pression de 1 atm par rapport à l'électrode NHE), Mais l'activation du dihydrogène est énergétiquement non favorable au vu de la très faible acidité de la liaison H-H (pKa=35). Cependant, en liant cette dernière à un centre métallique tel qu'un noyau ferrique, la barrière énergétique serait réduite et le clivage hétérolytique de H_2 en H^+ et H^- en serait grandement facilité.

La plupart des hydrogénases connues à ce jour contiennent du fer, du nickel et du soufre. Elles sont classées selon leur composition en métaux ; on distingue trois catégories: [NiFeSe], [NiFe], [Fe]-only. L'enzyme la plus couramment rencontrée est la [NiFe], elle contient 1 atome de Nickel et 12 atomes de fer. Il s'agit aussi de la structure la plus étudiée. La structure cristalline de la [NiFe]-hydrogénase issue de la bactérie *Desulfovibrio Gigas* (*D. Gigas*) a été publié par Volbeda *et coll*. en 1995. Une de ses formes inactives a été caractérisée par rayon X (Schéma 1). Cette enzyme est une protéine hétérodimérique

périplasmique comportant deux sous unités, une petite (28 kDa) et un grande (60 kDa). Le centre actif (Schéma 1) de l'enzyme contient un centre bimétallique dans lequel l'atome de Nickel et lié à 4 atomes de soufre, deux d'entre eux forment un pont entre le Nickel et un atome de fer. L'atome de Fer est lui-même lié à trois ligands bimoléculaires non protéiques: un ligand carbonyl et deux ligands nitrile. Le nickel et les ligands bi-atomiques sont très rarement observés dans les systèmes biologiques naturels

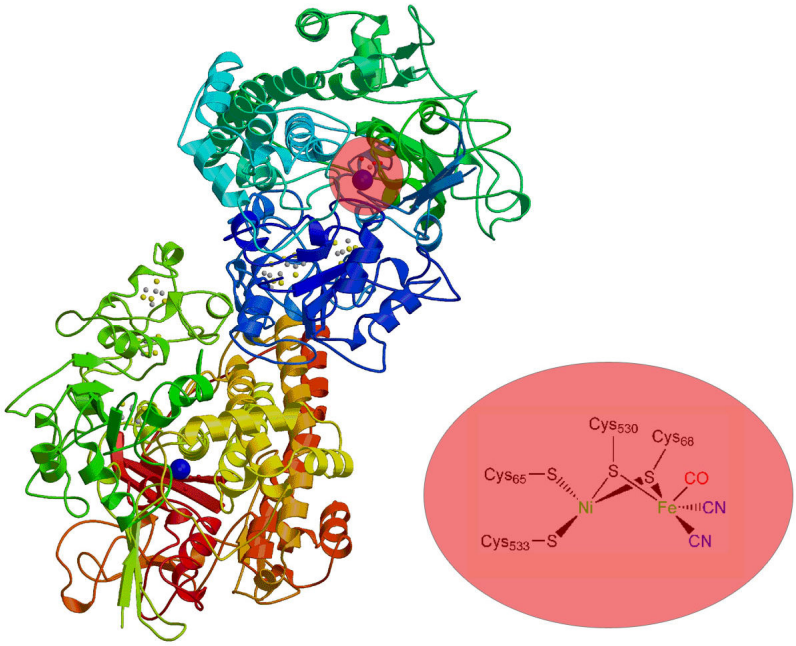

Schéma 1 Site actif de l'enzyme [NiFe]-Hydrogénase du *Desulfovibrio Gigas* and the active form of its active center in red

Jusqu'à présent le mécanisme et le mode de fonctionnement de cette enzyme restent inconnus. De plus, de nombreux groupes de recherche ont essayé en vain de dévellopper des modèles de cette enzyme, aussi bien sur le plan structurel, que sur le plan fonctionnel. Pourtant il existe de gros intérêts politico-commerciaux au développement d'un modèle de ce genre. Après la crise pétrolière de 1973, l'intérêt porté aux hydrogénases s'est accru. Ceci étant du aux multiples applications possibles de cette enzyme. Une des idées alors émises est, que les hydrogénases, en combinaison avec la capacité du système de photoactivation des chloroplastes ou des cyano-bactéries d'oxyder l'eau en oxygène, et en dihydrogène pourraient être employée à la fabrication d'un réacteur de biophotolyse de l'eau fonctionnant à l'énergie solaire. Les produits ainsi formés pourraient être utilisés pour retrouver l'énergie stockée simplement en brûlant le dihydrogène en eau. Plusieurs tests préalables attestent de la faisabilité de cette approche.

Ces réactions chimiques, qui sont très difficiles à reproduire de façon synthétique (cf. catalyseur à base de poudre de platine stabilisée sur une couche de carbone), sont réalisées naturellement dans des conditions «normales» de température et de pression par des systèmes enzymatiques. La mise au point de petits modèles mimétiques, aisément synthétisables en laboratoire, et reproduisants parfaitement les caractéristiques structurelles, mais aussi fonctionnelles de cette enzyme, pourrait permettre de comprendre le mécanisme d'action, jusqu'alors indéterminé, de cette classe d'enzyme. De plus, de tels modèles fonctionnels, synthétisables à grande échelle en industrie, pourraient avoir un énorme impact sur l'économie mondiale de l'hydrogène, et donner une réponse efficace aux problèmes de production de gaz carbonique, dus à la combustion de dérivés du pétrole, et à l'épuisement des gisements de fuels fossiles.

Depuis la résolution de la structure cristallographique du site actif de cette enzyme, de nombreux modèles structuraux ont été élaborés mais aucun ne présente d'activité satisfaisante. Le travail présenté traite du design et de la synthèse de modèles synthétiques des sites actifs des hydrogénases. Pour ce faire trois techniques d'approches ont été développées dans trois domaines différents de la chimie.

Première approche

La première approche développée est une approche bioorganometallique. En effet, nous avons pensé utiliser des complexes métalliques de type métallocène afin de servir d'échelle moléculaire pour la fabrication de modèles synthétiques de sites actifs d'enzyme.

Plusieurs groupes à travers le monde, ont observé la pré-organisation en feuillet bêta de petits peptides fixés sur les deux cyclopentadiènes formant le ferrocène. Cette faculté de pré-organisation du ferrocène, combinée à son activité électrochimique, fait de ce composé un candidat idéal pour l'élaboration de modèles électro-actifs.

La première partie du travail effectué est le développement de la synthèse de complexes bio conjugués de ferrocène et de peptide contenant des résidus soufrés (présence de cystéine dans la séquence). De petits peptides ou des acides aminés ont été greffés sur les noyaux aromatiques de type cyclopentadiène composant le ferrocène. Les méthodes de couplages classiques ont été utilisées pour faire réagir de petits peptides avec le ferrocene acide carboxylique; activation de l'acide carboxylique puis couplage avec une amine primaire. Après une étape de déprotection qui permet de recouvrer le thiol présent dans la

séquence, une étape de complexation avec un complexe fer-carbonyle a été effectuée afin de reproduire le centre bimétallique constituant le centre actif de l'enzyme à l'état naturel. Les complexes obtenus lors de l'application de cette méthode sont schématisés ci-dessous (Schéma 2).

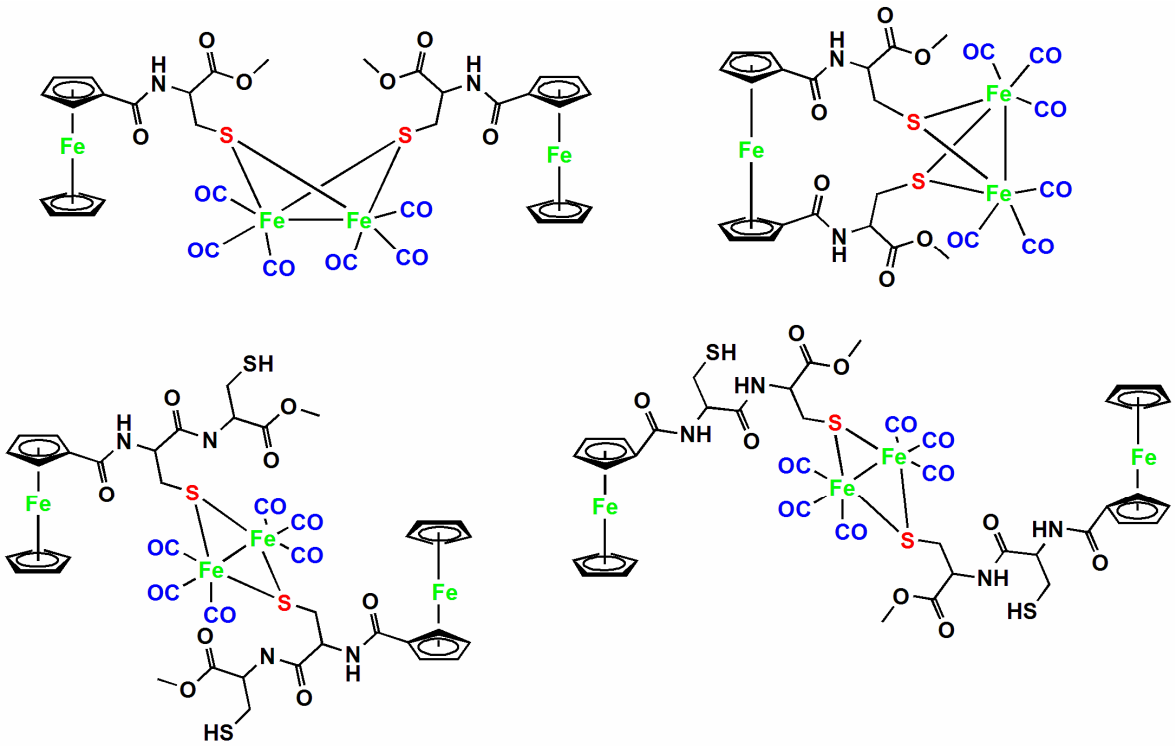

Schéma 2 Complexes fer carbonyles mimique du site actif de l'enzyme hydrogénase

Les complexes obtenus ont été caractérisés par spectroscopie RMN (^{1}H et ^{13}C), spectrométrie de masse (FAB, EI), spectroscopie infrarouge, électrochimie (Cyclique (CV) et linéaire (SW)), spectroscopie UV, analyse élémentaire et spectroscopie EPR. Les complexes obtenus sont de très bons modèles structuraux du site actif de l'enzyme hydrogénase. La synthèse d'un complexe de fer-carbonyle coordonné à une séquence peptidique est rapportée ici pour la première fois. De plus la présence du ferrocène dans la structure comme centre électro-actif et comme agent d'organisation structurale ajoute une composante supplémentaire au mimétisme étant donné que dans les structures naturelles ces deux facteurs sont existants; d'une part par la présence des clusters {FeS} pour le relais d'électrons et d'autre part par l'organisation tertiaire des protéines pour la dimension structurale. Néanmoins, la fonctionnalité de ces complexes n'a pas encore été validée à ce jour.

Deuxième approche

Lors de la deuxième approche développée dans ce travail, l'aspect théorique est traité. Dans un premier lieu, un champ de force de mécanique moléculaire pour les dérivés ferrocène-peptide est crée et implémenté dans le logiciel CHARMM. Parmis les méthodes utilisées, l'« Automated Frequency Matching Method » (AFMM) qui consiste à ajuster un set de paramètre de dynamique moléculaire sur les données obtenu par calcul quantique par projection des eigenvectors dans le même espace, s'est révélée particulièrement efficace. Le champ de force ainsi crée est, d'abord testé sur des structures expérimentales connues. La spectaculaire précision des résultats obtenus lors des calculs dynamiques effectués sur le réseau cristallin du dérivé Fc-$(Ala\text{-}Pro)_2$, nous permette de valider le champ de force (voir Schéma 3).

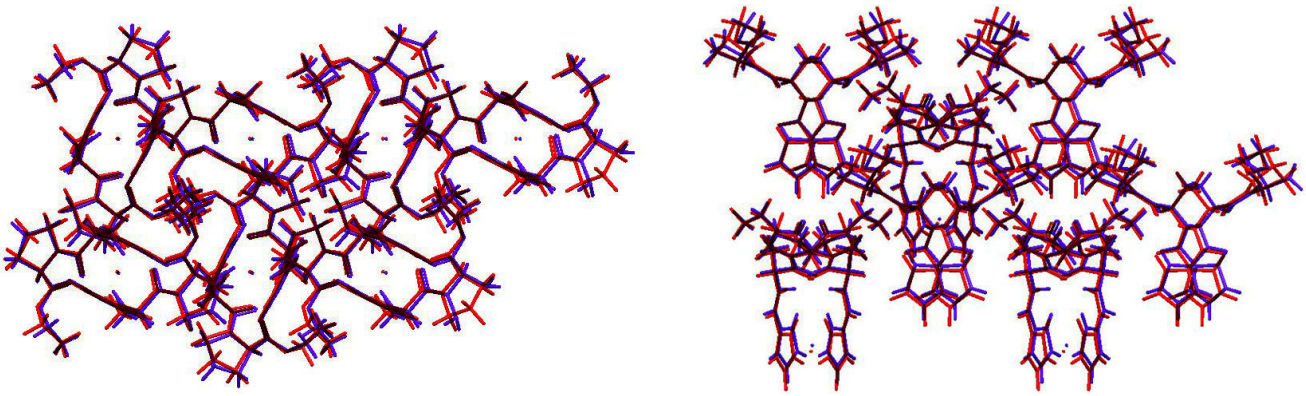

Schéma 3 Superposition des réseaux cristallins de Fc-$(C_5H_5\text{-}COO\text{-}Ala\text{-}Pro)_2$. En rouge le réseau obtenu expérimentalement par diffraction des rayons X et en bleu le réseau obtenu après 0.5 ms de dynamique moléculaire.

Le champ de force validé est utilisé pour l'étude de dérivé de type ferrocène-peptide, avec des séquences peptidiques fonctionnalisées par des groupements thiols. Les modèles crées sont analysés comme potentielle échelle moléculaire pour le site actif de l'enzyme hydrogenase. A ce propos, la taille et la forme du ligand chelate formé par les soufres présents dans la structure, sont analysés et comparés aux résultats expérimentaux obtenus sur des molécules similaires ou alors mesurés directement sur la structure cristalline du site actif de l'enzyme.

La coordination d'un métal par ces ligands a aussi été testée de manière théorique par l'introduction d'un modèle pour l'atome de nickel dans la poche chélate lors des simulations. Les résultats obtenus démontrent en principe la faisabilité du model proposé,

mais d'un point de vu stérique et géométrique uniquement. Ainsi, sur la figure de gauche du Schéma 4 un atome de nickel est virtuellement connecté aux atomes de soufres du dérivé Fc-(C_5H_5-COO-Cys-Cys-OMe)$_2$. Les caractéristiques géométriques du ferrocène sont suivies durant 1 ms de calcul dynamique à température ambiante. La structure reste stable durant cette période, aucun changement dramatique n'intervient dans la structure du ferrocène durant la période de simulation.

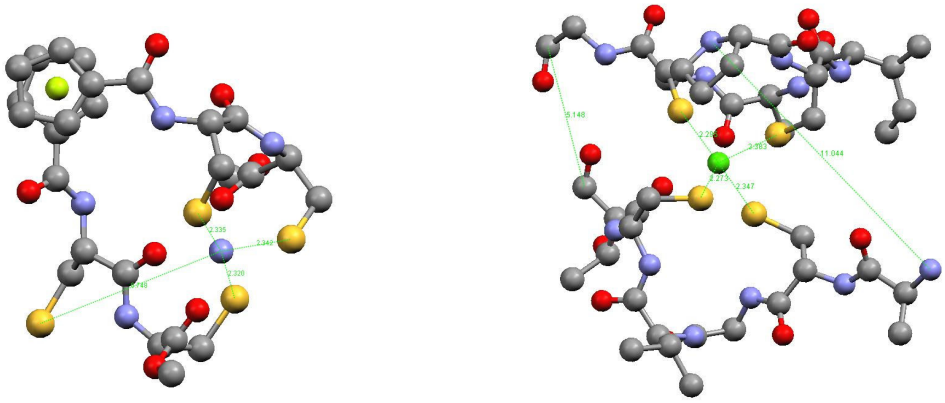

Schéma 4 Structure minimisée de Fe[C_5H_4-CO-Cys-Cys-OMe]$_2$ (à gauche) avec un nickel coordonné aux atomes de soufre. A droite une minimisation de la séquence du site actif de l'enzyme [NiFe] coordonnée avec un atome de soufre

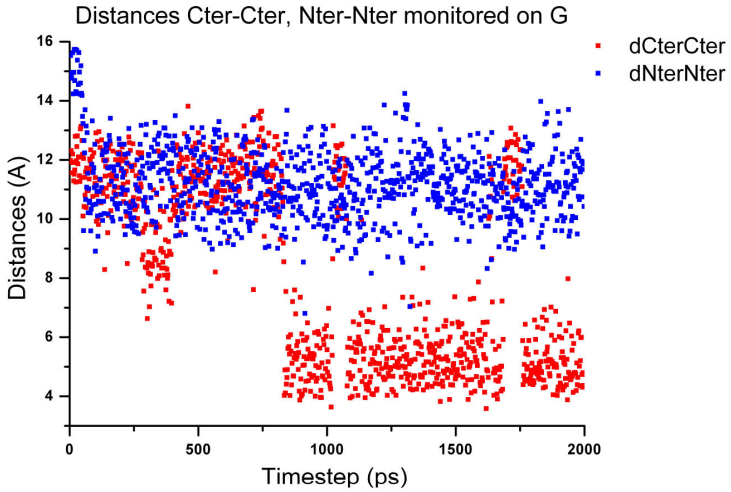

Graph 1 Distance N-N entre les deux N-terminations et C-C entre les deux C-terminations mesurées sur 2 ns de simulation dynamique

La figure de droite du Schéma 4 et le Graph 1 montre une autre expérimentation menée sur les modèles dynamique: les séquences peptidiques environnantes du site actif de l'enzyme à l'état naturelle ont été modélisées. Un atome de nickel a été inclus dans la

« poche » créée les atomes de soufres. Les distances entre les extrémités N-ter et C-ter de ces deux peptides ont été mesurées pendant 2 ns de dynamique moléculaire et il en résulte que les extrémités C-ter des brins peptidiques ont une distance moyenne plus courte que les deux extrémités N (voir Graph 1). Nous en déduisons que la fixation d'un ferrocene sera plus facile du cotés C de la séquence peptidique que du coté N. Ce résultat nous as aidé a réorienté notre stratégie de synthèse.

Troisième approche

La deuxième approche présentée dans cette thèse, est l'étude et l'application d'oligoamides aromatiques, portant des chaînes soufrées comme échelle moléculaire pour la synthèse de mimiques du site actif de l'enzyme hydrogénase. Des brins moléculaires constitués d'unités 2,8-aminoquinolinecarbonyle et 1,10-phenantrolinedicarbonyle alternées ont été conçus dans le but d'induire une auto-organisation en structure hélicoïdale par formation de liaisons hydrogènes intramoléculaires entre les groupements amides successifs et de recouvrements intramoléculaires entre les groupements aromatiques périphériques. Il a été démontré par le passé la grande prédictibilité de ces systèmes, ce qui a permis de concevoir des hélices s'adaptant parfaitement au besoin de la synthèse.

La stratégie est d'abord le « design » des structures afin de déterminer les positions des fonctions thiols en vue d'obtenir une géométrie favorable à l'incorporation d'un métal ou d'un noyau métallique. Des prévisions de molécules faites à partir d'une simulation moléculaire avec le champ de force MM3 implémenté dans le logiciel Macromodel, sont schématisées ci-dessous (Schéma 5), à gauche un pentamère quinoline-quinoline-phenantroline-quinoline-quinoline, à droite un hexamère quinoline uniquement. Les positions marquées par la couleur jaune ont été choisies pour le placement des thiols.

La deuxième étape est la synthèse des oligomères en commençant par la fonctionnalisation des monomères par des chaînes contenant des fonctions thiols, protégées par le groupement tertio-butyl. Suivi de l'oligomérisation par étape, selon une stratégie convergente afin d'arriver à la pré-organisation des noyaux soufrés dans la configuration souhaitée. Lors de la synthèse nous nous sommes orientés vers le brin pentamérique, pour des raisons techniques, de synthèse et de rendement. Dans cette configuration, les monomères modifiés devront occuper les positions 2 et 4 de la séquence, c'est-à-dire accolés de part et d'autre du motif phénantroline central.

Les conformations en hélices ont été caractérisées par spectrométrie de masse et par spectroscopie NMR. Quatre de ces composés pentamériques ont été caractérisés à l'état solide par diffraction des rayons X. la structure cristalline de l'un des brin moléculaire synthétisé est montrée sur le Schéma 6.

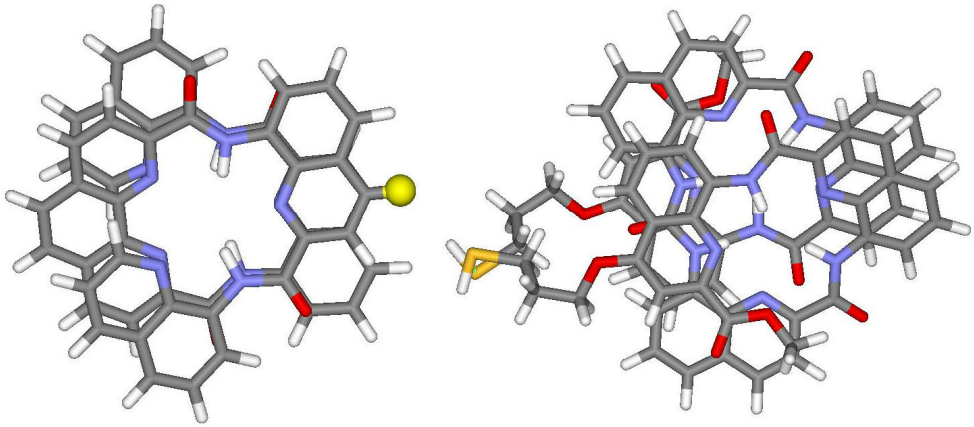

Schéma 5 Prévisions moléculaire de suprachelate à base d'oligoamides contenant des chaînes soufrées

La troisième étape est une étape de déprotection pour recouvrer les thiols libres afin d'obtenir un ligand S-S de type suprachelate en vue de l'introduction d'un noyau fer-carbonyle, mimique du site active de l'enzyme hydrogénase.

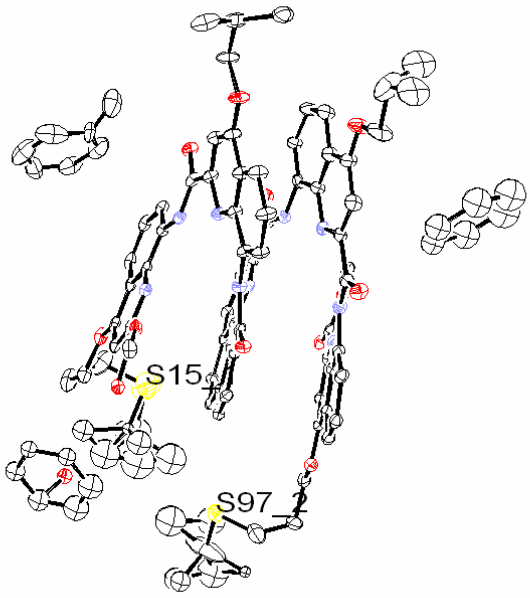

Schéma 6 Structure cristallographique d'un brin moléculaire pentamérique et des molécules de solvants co-cristallisés, créee avec Ortep (avec 20 % de probabilité)

Table of contents

1. Introduction **1**

1.1 Biomimetism of enzymes *1*

1.2 Hydrogenases *2*

1.3 Designing and modelling Hydrogenase's active site *5*
1.3.1 Specifications sheet for molecular model for Hydrogenases 5
1.3.2 State of the art 6
1.3.3 Emerging ideas 9

1.4 Ferrocene as a molecular scaffold for hydrogenase mimics *10*
1.4.1 Bio-organometallic chemistry of ferrocene 10
1.4.2 Ferrocene-bearing peptide derivatives 11

1.5 Aromatic helical oligoamides *13*
1.5.1 Peptidomimetic Foldamers 13
1.5.2 Designing a foldamer 13
1.5.3 Aromatic oligoamides 14

1.6 Objectives of this thesis *15*
1.6.1 Supramolecular chelates for hydrogenase mimics 15
1.6.2 Objectives 15
1.6.3 Techniques 16

2. Sulfur Protecting Groups and Peptide Syntheses **17**

2.1 Protective groups tested *17*

2.2 Synthesis *19*
2.2.1 Preparation of the amino acids 19
2.2.2 Peptide synthesis 21
2.2.3 Removal of side-chain protective groups 23

2.3 Concluding remarks *24*

3. Ferrocene-Peptides Derivatives **25**

3.1 Synthesis of ferrocene bearing sulfur containing peptide *26*
3.1.1 Helical chirality 27

3.2 Characterization *28*
3.2.1 Infra Red Spectroscopy 28
3.2.2 NMR 30
3.2.3 Circular Dichroism 33
3.2.4 X-ray 35
3.2.5 Electrochemistry 38

3.3 DFT study of H-bonds patterns *41*

3.4 Discussion *43*

4. Molecular Dynamic Simulations 45

4.1 Methods 46
4.1.1 Model Systems 46
4.1.2 Computational details 47
4.1.3 Ferrocene Topology 49
4.1.4 Parameters refinement 51

4.2 Parameterization 54
4.2.1 Parameterization of ferrocene-1(*L*)proline-1'(*L*)alanine 54

4.3 Testing of the parameters 55
4.3.1 Fc-(D-Ala-D-Pro)$_2$ crystal simulations 55
4.3.2 Fc-(D-Ala-D-Pro)$_2$ and Fc-(L-Ala-L-Pro)$_2$ single molecules in vacuum 60
4.3.3 Fc-[(D)Met-(L)Met]$_2$ in the crystal lattice 62
4.3.4 Fc-[(D)Met-(L)Met]$_2$ single molecule in vacuum 64
4.3.5 Ferrocene crystal simulation 65

4.4 Prediction 68
4.4.1 Model systems δ, ε, ϕ and γ 68
4.4.2 Simulation of the Hydrogenase active center (models η and ι) 73
4.4.3 New direction for the synthetic work 75

4.5 Conclusion 77

5. Functionalized Aromatic Oligoamides 79

5.1 Design of the structures 79

5.2 Synthesis 82
5.2.1 Monomers and dimers 82
5.2.2 Oligomerization 85
5.2.3 Deprotection step 87

5.3 Characterization 89
5.3.1 Solution phase structural analysis by NMR 89
5.3.2 Solid state structural studies by X-Ray analysis 91

5.4 Concluding remarks 95

6. Iron-Carbonyls Complexes 97

6.1 Ferrocene-cysteine/iron-carbonyls derivatives 97
6.1.1 Deprotection of side chain protective groups 97
6.1.2 Complexation with Iron-carbonyls 99
6.1.3 Characterization 101

6.2 Electrochemical properties 104
6.2.1 Electrochemistry 104
6.2.2 Moessbauer Spectroscopy 107

6.3 Complexation with Quinoline derived oligomer 110

6.4 Concluding remarks 111

7. Summary & Conclusion **113**

7.1 Summary *113*

7.2 Concluding remarks and Outlook *117*

8 Experimental Section **119**

8.1 Materials and Methods *119*
8.1.1 Materials 119
8.1.2 Standard procedures 122

8.2 Syntheses and Characterization of ferrocenoyl compounds *123*
8.2.1 Synthesis of literature compounds 123
8.2.2 Solution phase peptide synthesis 127
8.2.3 Removal of Boc and Fmoc 129
8.2.4 Peptide coupling with ferrocene 130
8.2.5 Preparation of methionine derivatives 138
8.2.6 Preparation of ethylendiamine derivatives 140
8.2.7 Deprotection of sulfur protective groups 141
8.2.8 Preparation of disulfide bridged derivatives 146
8.2.9 Complexation with Iron carbonyl 147

8.3 Syntheses and Characterization of Oligoamides *148*
8.3.1 Synthesis of the monomers 149
8.3.2 Dimers 153
8.3.3 Trimers 157
8.3.4 Pentamers 158
8.3.5 Deprotection of tertio butyl group 160
8.3.6 Iron carbonyls complexation 163

8.4 Crystallographic Tables *164*

9. Literature **167**

10. Appendix **183**

10.1 Appendix of Chapter 4 *183*

10.2 Appendix of Chapter 5 *185*

10.3 Appendix of Chapter 6 *186*

Abbreviations

Å	angström
Aaa	any amino acid
Ac	acetyl
Acm	acetamidomethyl
ADT	azadithiolate
AFMM	automated frequency-matching method
Ala	alanine
Alk	alkyl
app	apparent
ar	aromatic
b, br	broad
B	magnetic field
bb	backbone
Boc	*tert*-butyloxycarbonyl
bt	benzotriazole
Bu	butyl
Bzl	benzyl
cb	chloro benzoyl
CD	circular dichroism
CHARMM	chemistry at Harvard molecular mechanics
cm	centimeter
COSY	correlated spectroscopy
Cp	η^5-cyclopentadienyl
CT	charge transfer
CV	cyclic voltammetry
Cys	cysteine
d	doublet
DCC	dicyclocarbodiimide
DCM	dichloromethane
DFT	density functional theory
DIEA	diisopropylethylamine

DMAP	4-dimethylaminopyridine
DMF	dimethylformamide
DMSO	dimethylsulfoxide
δ	chemical shift
E	potential
EA	elemental analysis
E_a	anodic potential
E_c	cathodic potential
ECPs	effective core potentials
EDA	ethylendiamine
EDC	*N*-(-3-dimethylaminopropyl)-*N*'-ethylcarbodiimide
EI	electron impact
EPR	electron paramagnetic resonance
ESI	electro-spray interface
ESR	electron spin resonance
Et	ethyl
EtOAc	ethylacetate
EtOH	ethanol
ε	molar extinction coefficient
FAB	fast atom bombardment
Fc	ferrocenyl
FF	force field
Fmoc	fluorenyl-9-methoxycarbonyl
Gly	glycine
H_2ase	hydrogenase
h	hours
HBTU	2-(1H-benzotriazole-1-yl)-1,1,3,3-tetramethyluronium
HFS	Hartree-Fock-Slater
HOBt	1-hydroxy-1H-benzotriazole
HOMO	highest occupied molecular orbital
HPLC	high performance liquid chromatography
Hz	hertz
IBCF	isobutyl chloroformate
Ile	isoleucine

Q.S.	quaternary splitting
IR	infrared
I.S.	isomer shift
J	joule
J	coupling constant
k	kilo
K	kelvin
λ	wavelength
L	ligand
LJ	Lennard-Jones
LUMO	lowest unoccupied molecular orbital
m	multiplet, milli
m	meta
M	molare, mega
μ	micro
Me	methyl
MeOH	methanol
Met	methionine
min	minute
MM	molecular mechanics
m/z	mass per charge
n	nano
ν	frequency
NbS	2-Nitrobenzenesulfenyl
NMN	N-methylmorpholine
NMR	nuclear magnetic resonance
NOE	nuclear Overhauser effect
NpyS	3-Nitro-2-pyridinesulfenyl
NR	Newton-Raphson
o	ortho
O	oxidised state
p	pico, pseudo
p	para
PDT	propyldithiolate

PEF	potential energy function
PG	protective group
pOMeBzl	paramethoxybenzyl
PPA	polyphosphoric acid
ppm	part per million
Pro	proline
q	quartet, quaternary
QM	quantum mechanics
qu	quintuplet
R	reduced state
rt	room temperature
s	singulet, sharp
SD, σ	standard deviation
sep	septuplet
sub	substituted
sx	sexuplet
TBTU	2-(1H-benzotriazol-1-yl)-1,1,3,3-tetramethyluronium tetrafluoroborate
tBu	tertiobutyl
TEA	triethylamine
tert	tertiary, tertio
TES	triethylsilane
TFA	trifluoroacetic acid
THF	tetrahydrofuran
Thr	threonine
TIS	triisopropylsilane
TMS	tetramethylsilane
Trt	trityl
unsub	unsubstituted
UV	ultraviolet
VdW	Van der Waals
Vis	visible
vs	versus
w	weak

1. Introduction

1.1 Biomimetism of enzymes

Chemists dream of catalyzing reactions the way enzymes do: working at room temperature and low pressure, using simple starting materials like nitrogen to make only useful products and benign by-products like ammonia and water. The only ways that researchers can currently duplicate many enzyme-catalyzed reactions are by applying high temperatures and pressures, or by using exotic (and often toxic) metals.

Besides, scientists have been extending Nature's achievements for centuries. For chemistry, this has taken the form of producing new compounds that did not exist in nature, new remedies, new colorants, new polymers, and more generally new materials. At this point less than 1/10 of all known chemical substances are natural products. Nevertheless, new chemicals were often developed by imitating the general style of natural substances. Many reasons could motivate this approach, as curiosity for instance, but the major one is that a useful new property might emerge. "Biomimetic chemistry" describes chemistry that is inspired by that done in living systems. Artificial enzymes are an important part of this field, in which one tries to imitate the catalytic process that occurs in the wild type of an enzyme, and not just the substances of biology.

Materials found in nature combine many inspiring properties such as sophistication, selectivity, efficiency, resistance, and adaptability. We hope to achieve these properties, which are typical of enzymatic conversions by imitating the general principles; in particular the well-defined geometry of enzymes, but not every detail as, e.g. the exact peptide sequence.

Increasing our understanding of natural processes is another important goal of biomimetic chemistry. One of the obstacles to understand enzymes is their large size. Each enzyme comprises thousands of atoms, with various sections of an enzyme performing

different functions. At a specific location within the enzyme, called the "active site," reacting molecules come together, break apart, and recombine as they interact with the enzyme, and then leave as different molecules. Other sections of the enzyme can block the active site, allowing only certain molecules access, or permitting approaches to the active site from only one direction. The studies of artificial enzymes help us to understand and to evaluate the properties of natural enzymes. One great challenge to be achieved using artificial enzymes is the outstanding catalytic activity that the best natural enzymes can achieve on reactions that are not available to chemists.

One example is the reversible reduction of proton to dihydrogen. This is deceptively the simplest reaction but also one that requires multistep catalysis to proceed at practical rates. However, in the wild type, the members of an enzyme class called Hydrogenases easily perform this reaction. The biological processing of hydrogen performed by Hydrogenases is exceptionally efficient, with rates for proton production in the range of 6000 - 9000 turnovers per second and dihydrogen production of 10000 turnovers per second [1, 2]. Fancy extrapolation suggest that 1 mole of Hydrogenase could produce enough hydrogen to fill the airship *Graf Zeppelin* in ten minutes, or the main liquid-hydrogen tank of the *Space Shuttle* in two hours. Although this calculation disregards the time required to transfer hydrogen from solution to the gas phase, it illustrates quite well the economical interest, notably to storage of solar energy. The feasibility of such an approach as already been extensively reviewed in the early seventies [3]. This economic aspect but also the fact that the active site of Hydrogenases resembles well-known species currently observed and synthesized by inorganic chemists around the world has attracted specific attention of the modelling community [4-6].

1.2 Hydrogenases

Hydrogenases were first discovered in 1931 [7] in colon bacteria. They are found in diverse microorganisms as methanogenic, acetogenic, nitrate and sulphate reducing bacteria and numerous archaebacteria. Hydrogenases have the ability to control H_2 concentration and reduction activity by facilitating the uptake and the oxidation of H_2 to protons with release of electrons; or its production, according to the reverse reaction [8, 9]. They provide a reversible sink for multi-electron transfer. Reducing equivalents thus

obtained enable bacteria to reduce a variety of substrates, and to generate sufficient energy for ATP synthesis. The reversible oxidation of H_2 provides electrons at a low potential (H_2 / $2H^+$: E_0 = -414 mV at pH 7 and 1 atm of H_2 versus NHE) [10], but H_2 activation is energetically unfavourable due to the low acidity of the H-H bond (pK_a = 35).

All of the 80 known Hydrogenases are rich in sulfurs and in iron. They are divided in three classes according to their metal content; [Fe] -only, [NiFe], [NiFeSe] -H_2ases (depicted in Figure 1.1). In addition, existence of a metal-free Hydrogenase has been reported [11] but its existence is still a matter of controversy and discussion.

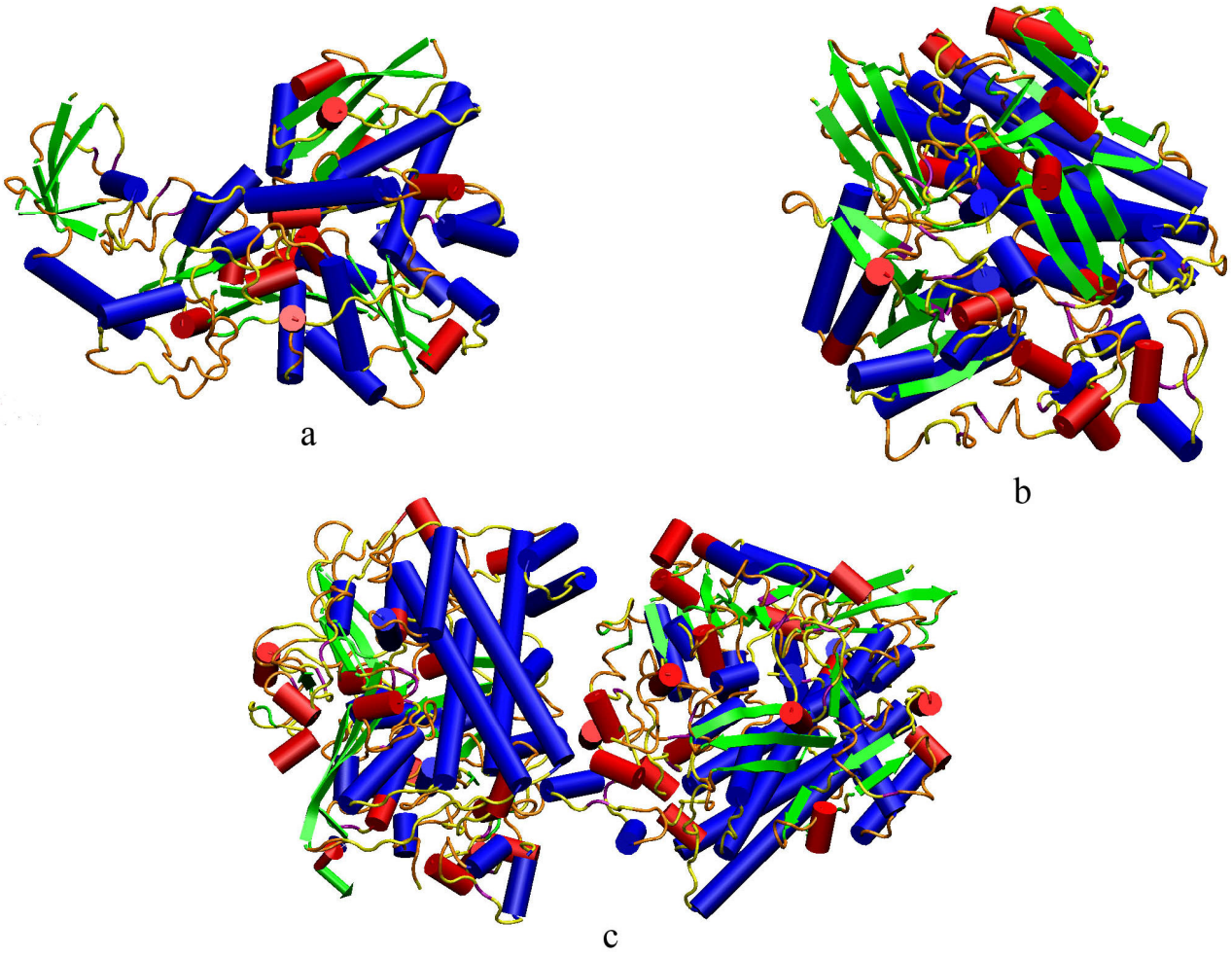

Figure 1.1 Tertiary structures of the three different types of hydrogenases (a) Fe-only (b) NiFeSe (c) NiFe. α-helices are depicted in blue, 3,10-helices in red, π-helices in pink, extended β-sheets in green, bridged β-sheets in purple, turns in orange and coils in yellow

The most common Hydrogenase, [NiFe], has focused the interest of biologists, biochemists, and chemists for 25 years. In 1995, impressive protein crystal structures of the

[NiFe]-H_2ase enzyme, isolated from the sulfate reducing bacterium *Desulfovibrio Gigas*, have been determined by X-ray crystallography at resolutions 2.85 Å and 2.54 Å [12]. As isolated, in an oxidised and inactive form, the enzyme is a heterodimeric periplasmic protein consisting of two subunits: one large (60 kDa) and one small (20 kDa) as it is depicted in Figure 1.2. The protein contains a total of 12 iron atoms, 12 acid labile sulfides and one atom of nickel. Eleven of the twelve Fe atom are incorporated within the three Fe-S cluster, one $[3Fe\text{-}4S]^{+1/0}$ and two $[4Fe\text{-}4S]^{2+/+}$ moieties [13]. The active site comprises a truly organometallic, heterobimetallic centre, in which the Ni centre is ligated by four cysteinates, two of which are terminal, and two of them bridge to Fe. The Fe centre is ligated further by three non-protein diatomic ligand (cyanide and carbon monoxide), with a third bridging ligand that has been assigned to oxo-oxygen. This is rarely observed in biological systems since the cyanide and the monoxide are normally associated with inhibition and poisoning.

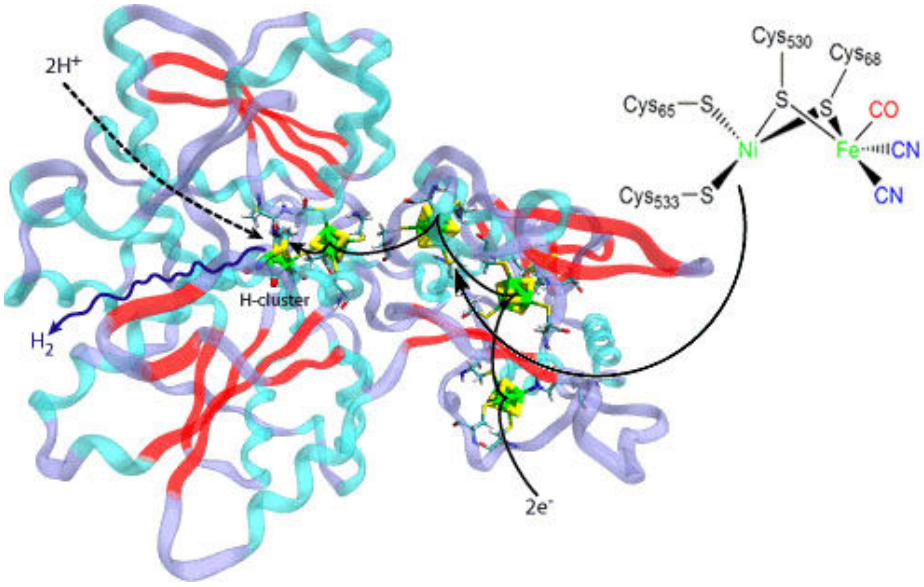

Figure 1.2 [NiFe] - H_2ase and the hydrogen evolution within its active site. Enlargement of the heterobimetallic center in its active form

X-ray crystallographic data of Fe-only hydrogenases from *Desulfovibrio desulfuricans* and *Clostridium pasteurianum* together with the spectroscopic data on Fe-only hydrogenase from *Desulfovibrio vulgaris* show that the active site at which protons are reduced to dihydrogen (or dihydrogen oxidised to protons), can be viewed as a conventional {4Fe4S}-cluster linked by a protein backbone bridging cysteinyl sulfur ligand to a {2Fe3S}-subsite [14-16]. The Fe-atom distal to the {4Fe-4S}-cluster has a

coordinated water molecule (or vacancy) in the paramagnetic oxidised state of the molecule, $\{H_{ox}\}$. This site is occupied by carbon monoxide in the CO inhibited form of the enzyme $\{H_{ox}\}$ and this is where hydride / dihydrogen are likely to be bound during turnover [17].

Finally, both classes of hydrogenases are able to catalyse either proton reduction, or hydrogen oxidation, but it is commonly claimed, according to their different affinities for molecular hydrogen that Fe-only hydrogenases have greater activity for H_2 production, while [NiFe]-Hydrogenase are more efficient for hydrogen uptake.

1.3 Designing and modelling Hydrogenase's active site

1.3.1 Specifications sheet for molecular model for Hydrogenases

One of the main directions of study, among many others, of a bioinorganic chemist, is to prepare synthetic, low molecular weight metal analogues of the active site of metal-containing enzymes, in order to reproduce its catalytic activity. The advantage of such models is that they are smaller and therefore easier to handle in terms of isolation and spectroscopic data collection, than the enzyme itself.

The success of a synthetic catalyst is based on three characteristics: cost, efficiency and robustness:

• A good catalyst is a cheap catalyst; hydrogenase are fascinating because they catalyse the fundamental $[2H^+ + 2e^- / H_2]$ interconversion at high rate and small overpotentials from equilibrium, using cheap first row transition metals at the active sites. Mimicking the functions of the active site of an enzyme could lead to the replacement of unsustainable platinum electrocatalyst in electrolyser/fuel cell applications. The replacement of platinum with inexpensive materials is critical to the large-scale use of hydrogen as a clean energy vector.

• A good catalyst is an economically viable catalyst; application of an electrocatalyst in large-scale electrolyser or fuel cell obviously requires high turnover frequencies to achieve high currents and low overpotential. From the viewpoint of solar energy conversion the development of photocatalysis, for overall water splitting, is an attractive goal.

• A good catalyst is a robust catalyst; the crucial point for any technological application is the robustness of the catalyst, which means both thermodynamic and kinetic stability under normal atmospheric conditions and high turnover numbers. Up to now, all promising molecular chemical systems for proton reduction or hydrogen uptake, have been abandoned because they were not reliable enough. The following points should be considered: (1) involvement of two electron transfers in the catalytic cycle implies that the selected catalysts, at the deprotonated or hydridic state (depending on the mechanism), should display electrochemically and chemically reversible redox features occurring at a relatively mild potentials, to avoid any irreversible ligand decomposition. (2) The chelate effect has been widely used as a general strategy for the design of robust complexes. By preventing ligand exchange in the active intermediate states, this indeed ensures the conservation of the entire set of ligands governing the reactivity of the metallic centre over the catalytic cycle. Note that the biomimetic approach could be in contradiction with this strategy, since the carbonyl ligand could be likely subjected to irreversible displacement during catalysis.

1.3.2 State of the art

In the mid 1980's, the first biomimetic studies concerning iron-only [18] and nickel-containing [19] hydrogenases were reported. Great efforts have been directed towards the preparation of model complexes mimicking the structure as well as the activity of the natural system (for an comprehensive review see ref. [20]). For example, the simplest structural model: the propyldithiolate (PDT)-bridged $[(\mu\text{-PDT})Fe_2(CO)_6]$ has been synthesized and elaborated. Similar complexes have been prepared where carbonyl ligands were replaced by isonitriles [21], cyanides [22], thioethers [23], and phosphines [24]. Darensbourg and co-workers have reported that $[(\mu\text{-H})(\mu\text{-PDT})Fe_2(CO)_4(PMe_3)_2]^+$ is a catalyst for H_2/D_2 scrambling [25], whereas Rauchfuss *et al.* demonstrated that $[(\mu\text{-PDT})Fe_2(CO)_4PMe3(CN)]^-$ serves as a catalyst for electrochemical hydrogen evolution [26]. In addition, Sun and co-workers have reported about $[\mu\text{-}SCH_2\text{-}NHR\text{-}CH_2\text{-}S)Fe_2(CO)_6]^+$ which catalyzes the electrochemical reduction of protons at a moderately negative potential [27]. Recently, a model of the [Fe]-Hydrogenase active site has been reported, which concomitantly carries a proton and a hydride [28]. The electron-donating ligands at the di-iron core carry the hydride, and an azadithiolate linker carries the proton. This double protonated structure is reduced at a mild potential that is

considerably more positive than that of any other iron hydrogenase mimic ever reported. Finally yet importantly, Pickett *et al.* have reported the assembly of the iron-sulfur framework of the active site of iron-only hydrogenase [29], and that it functions as an electrocatalyst for proton reduction. Through linking a di-iron subsite to a {4Fe4S} cluster, the first synthesis of a metallosulfur cluster core involved in small-molecule catalysis was achieved.

A purely biomimetic approach of [Fe]-only hydrogenases [30] has been exquisitely and successfully developed where the two iron nuclei are coordinated by cysteinyl ligands the complex was obtained by an oxidative addition of cysteine to $[Fe_3(CO)_{12}]$ and is accessible as a mixture of e,e and e,a isomers. However, no catalytic activity is presented for this model compound.

Nickel complexes are also possible candidates for the construction of small functional models of the active site of hydrogenases. Soon after it became apparent that some of the hydrogenases contained nickel in their active site, the first corroborative models were reported. The synthesis, X-ray structure, reactivity and electrochemistry of the homoleptic nickel thiolate complex $[Ni(SR)_4]^{2-}$ was reported, and the Ni^{2+} -> Ni^{3+} oxidation potential was compared with those of the hydrogenases [19]. A series of substituted arene thiolates have been used, among which are *p*-MeC_6H_4S-, *m*-MeC_6H_4S-, *p*-ClC_6H_4S- and *p*-$NO_2C_6H_4S-$ [31]. Nearly at the same time, Rosenfield *et al.* have reported the synthesis and properties of the mononuclear $(R_4N)_2[Ni(SAr)_4]$ complex with Ar =C_6H_5, *p*-C_6H_4Cl, *p*-$C_6H_4CH_3$ and *m*-C_6H_4Cl [32]. After the first reports of homoleptic complexes of nickel with monodentate thiolate ligands, the focus shifted to the use of chelating bidentate thiolate ligands such as ethane-1,2-dithiol or butane-2,3-dithiol and benzene-1,2-dithiol [33].

Nickel complexes have been synthesised with a variety of thiolatothioether ligands, some of them including heteroleptic ligand containing nitrogen and oxygen donors in S6, S5, OS4, NS4, S4, and S3 donor sets [34, 35].

Despite the fact that phosphanes are not naturally occurring ligands, phosphane groups have been successfully used as chelating ligands to stabilise various oxidation states of nickel. Some of those complexes show interesting catalytic activities. For example, the reaction of $Et_2PCH_2NMeCH_2PEt_2$ (PNP) with $[Ni(CH_3CN)_6](BF_4)_2$ results in the formation of $[Ni(PNP)_2](BF_4)_2$, which possesses both hydride- and proton-acceptor sites. This complex has been found to be an electrocatalyst for the oxidation of hydrogen to protons,

and stoichiometric reaction with hydrogen occurs. Another example is the $[HNi(PNP)(PNHP)](BF_4)_2$ in which a hydride ligand is bound to Ni and a proton is bound to a pendant N-atom of one PNP ligand. The hydride ligand and the NH proton undergo rapid intramolecular exchange with each other and intermolecular exchange with protons in solution. $[[HNi(PNP)(PNHP)](BF_4)_2$ undergoes reversible deprotonation to form $[HNi(PNP)_2](BF_4)$ [36].

Another topic of interest is the possibility to link covalently a photosensitizer to a small mimic of the hydrogenase active site to produce a single macromolecule with two active sites [27, 37, 38]. This homogeneous systems for hydrogen photoproduction consist in a photosensitizer S, held in an excited state S^* upon irradiation. Then, S^* transfers electrons to a relay R capable to effect proton reduction. For example, a binuclear iron complex, related to the active site of Fe-hydrogenases, has been covalently linked to a redox active ruthenium tris-bipyridine type photosensitizer as it is depicted in Figure 1.3. This approach is the first attempt to link iron hydrogenase mimics in supramolecular systems.

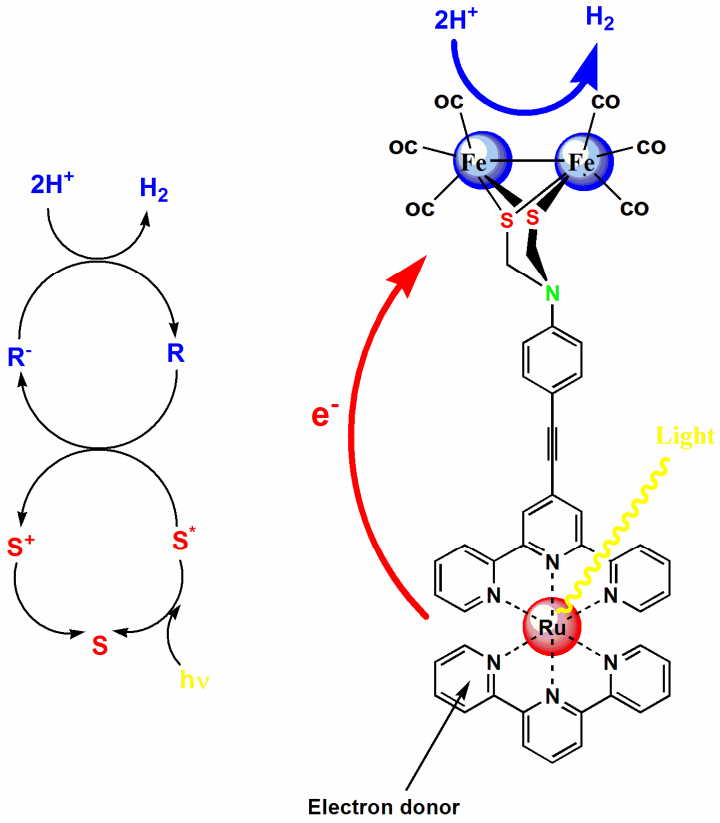

Figure 1.3 Principle of photoinduced electrocatalytic production of protons and the photosentizer that undergoes this conversion

However, despite these significant achievements in the structural modelling of the hydrogenases active site, the new biomimetics show a relatively small activity associated with high overvoltages so that immediate optimization perspectives appear quite limited for this kind of approach.

1.3.3 Emerging ideas

Enlightened by this literature review, it appears that the actual biomimetic models for hydrogenase lack in a major resemblance with the wild type complex; in nature, the chelate effect of the sulfur ligand pocket is at a supramolecular level. One of the new ideas developed in this thesis is to design and to synthesize supramolecular sulfur containing chelate ligands that could be used as new scaffolds for the next generation of hydrogenase mimics. The new orientations chosen for this purpose are first a ferrocenoyl-peptide scaffold thought to act as an electroactive scaffold, and the second is a folded aromatic oligoamide ligand system, which will act as self-organized proteomorphic structure as proteins. Two potential scaffolds are depicted in Figure 1.4.

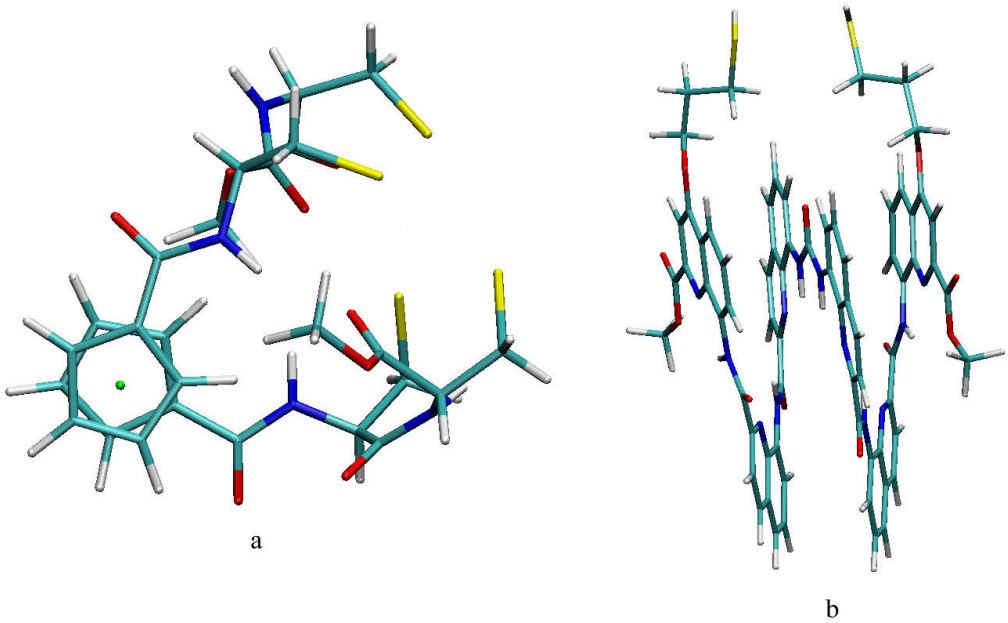

Figure 1.4 Theoretical rationalizations of the two molecular scaffolds that were studied as S-ligand for iron carbonyl core; (a) the ferrocenoyl-peptide approach (b) the aromatic oligoamides approach

1.4 Ferrocene as a molecular scaffold for hydrogenase mimics

In 1951, Kealy and Paulson [39] tried to obtained fulvalene by the oxidation of cyclopentadienyl magnesium bromide with anhydrous Iron(III) in ether. But the reduction of the Iron(III) to Iron(II) by the Grignard species led to the formation of orange crystals that were analysed to be of the general formula $C_{10}H_{10}Fe$. The ferrocene was thus discovered by serendipity. Only few months after, the particular "sandwich"-like structure was predicted from its NMR and IR [40] and then confirmed by X-ray crystallography in 1954 by E. O. Fisher. The term *ferrocene* was coined by Woodward [41] owing to its physical and structural resemblance with benzene. The discovery of ferrocene led to an explosion of interest in *d*-block metal carbon bonds and brought about development and the now flourishing study of organometallic chemistry. The rapid growth in the study of organometallic compounds by research groups around the world led to the Nobel Prize awarded in 1974 to Ernst Otto Fisher and Geoffrey Wilkinson for their contribution to the field.

1.4.1 Bio-organometallic chemistry of ferrocene

In recent years, bio-organometallic chemistry has developed as a rapidly growing area which links classical organometallic chemistry to biology, medicine and molecular biotechnology [42, 43]. The stability of the ferrocenoyl group in aqueous and aerobic media, the accessibility of a large variety of derivatives through ring substitution, along with its particular electrochemical properties, have made ferrocene and its derivatives a very popular molecule for biological applications and for conjugation with biomolecules such as peptides. Ferrocene exhibits interesting properties as an anti-anaemic agent [44, 45], as biomolecular markers [46], but also, for the vectorisation of small peptides through the blood brain barrier [46] or through the nuclear membrane of cells [47]. Conjugates of ferrocene with well-known drugs were reported e. g. with antibiotics such as penicillin and cephalosporin [48-50]. In addition, structural variations of established drugs with the ferrocenoyl moiety were also reported such as ferrocenoyl aspirin [51], the anti-malarial drugs chloroquine [52], quinine, mefloquine [53], and finally the anti-cancer drug tamixofen to give ferrocifen [54].

Lastly ferrocene has been shown to have good catalytic properties notably Ferrocenophane shows high activity in photoelectrochemical production of hydrogen. The coating of a platinum electrode with conducting polypyrrole containing ferrocene sulfonate as counter-ion or with polypyrrole covalently bound to 1,1-ferrocenophane indeed induces a 0.27 V anodic shift for proton reduction in molar sulfuric acid and a sevenfold amplification of current density when poised at −0.44 V / SHE [55].

1.4.2 Ferrocene-bearing peptide derivatives

The first ferrocenoyl amino acid derivative has been reported in 1957, by Schlögl [56]. From the many existing possibilities to couple the ferrocene to amino acids, the most extensively reported is the amide formation between ferrocene carboxylic acid and the terminal amino group. Up to now about 70 different amino acids and peptides were successfully coupled to ferrocene carboxylic acid and comprehensively characterized (for a comprehensive review see ref. [57]). In the solid state, hydrogen bond interactions are a dominant feature [58]: zigzag [58, 59], sheet-like and helical packing have been observed [60]. In solution, most of these derivatives do not appear to have an ordered structure.

In addition to mono-substituted ferrocenoyl amino acids, a large amount of 1,1'-disubstituted peptide derivatives have been prepared. In 1996 [61], Herrick *et al.* found that compounds of general formula $Fe(C_5H_4\text{-}CO\text{-}Aaa\text{-}OMe)_2$, have an ordered structure in solution. This order is comprised of two symmetrically equivalent hydrogen bonds between the amide NH and the carbonyl of the methyl ester moiety of the other strand.

Structural studies in the solid state have shown that two kinds of hydrogen-bonding patterns have been experimentally observed in parent molecules as it is depicted in Scheme 1.1; the "Herrick's" [61] conformation, with two H-bonds connecting both strands and the "van Staveren's" [62] conformation with one H-bond connecting the peptide strands. When both substituents are trans, no intramolecular H-bonds are observed and this conformation is called "open" conformation [63-65].

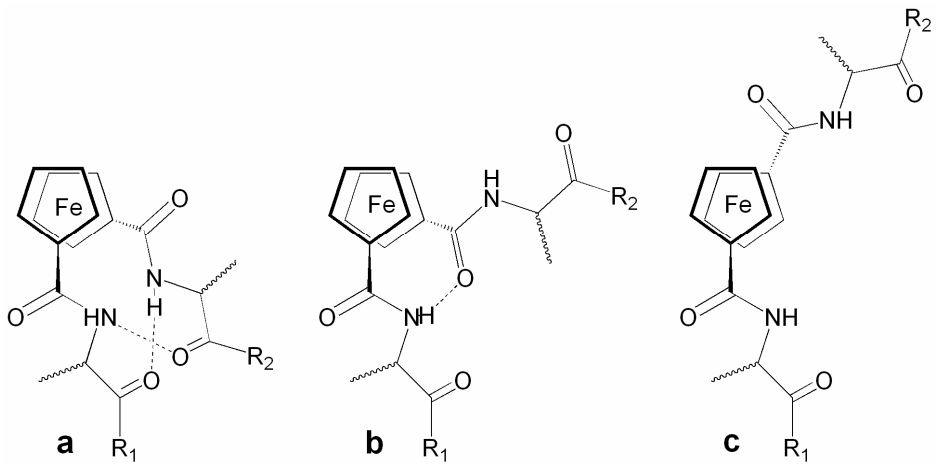

Scheme 1.1 The three different conformation of Fc-peptide derivatives (**a**) Herrick, (**b**) van Staveren and (**c**) open conformation

Seeing ferrocene's capacity of pre-organisation of peptide strands combined with its electrochemical activity and motivated by the multiple successful use of ferrocene in biological systems, we became intrigued by the possibility of linking covalently a biomimetic model of the hydrogenase active site to a ferrocene moiety. The design and the synthesis of these supramolecular organometallic derivatives are discussed along this work. Three majors parts are developed here: (1) the synthesis and the characterization of a wide range of ferrocene-bearing sulfur containing peptides derivatives. (2) The computational simulation of these new derivatives and theoretical investigation of those as chelate for hydrogenase mimics. (3) The synthesis through coordination of iron carbonyl core in S-ligand pocket and the characterization of these novels hydrogenase mimics are also presented.

This successful design and synthesis of supramolecular scaffold based on ferrocene peptide derivative led us to investigate other supramolecular assembly to the same purpose. Therefore, as a second major part of the presented PhD thesis, and based on the same strategy, self-assembled aromatic oligoamides were studied as a second potential scaffold for hydrogenase active site.

1.5 Aromatic helical oligoamides

1.5.1 Peptidomimetic Foldamers

The definition of a foldamer is any oligomer that folds into a conformationally ordered state in solution, the structures of which are stabilized by a collection of non-covalent interactions between nonadjacent monomer units. There are two major classes of foldamers: single-stranded foldamers that only fold (peptidomimetics and their abiotic analogues) and multiple-stranded foldamers that both, associate and fold (nucleotidomimetics and their abiotic analogues).

The field of peptidomimetics aims at mimicking peptide structure through substances having controlled spatial disposition of functional groups. A peptidomimetic is a protease resistant unnatural substance mimicking the structural and potentially the functional behaviour of a peptide. Peptidomimetics have general features analogous to their parent structure, polypeptides, such as amphiphilicity. They have been largely developed for replacing peptide substrates of enzymes or peptide ligands of protein receptors. Peptidomimetic strategies include the modification of amino acid side chains, the introduction of constraints to fix the location of different parts of the molecule, the development of templates that induce or stabilize secondary structures of short chains, the creation of scaffolds that direct side-chain elements to specific locations, and the modification of the peptide backbone.

1.5.2 Designing a foldamer

Synthetic oligomers that fold into well-defined helical secondary structures are of considerable interest in supramolecular chemistry but also for mimicking the secondary structures of biopolymers. Consequently, great efforts have been made in the development of helical oligomers during the past decade [66]. Series of aliphatic β-, γ-, and δ-homologues of α-peptides have been reported, comprising various linkages such as amides, sulfonamides, sulfoximines, N-oxo-amides, ureas or hydrazides [67-70]. Several families of aromatic oligoamides have been shown to adopt stable linear, bent, and helical

conformations stabilized by hydrogen bonds between amide groups and donor / acceptor in the aromatic rings [66].

Although a wide range of different supramolecular structures have been reported, few applications such as biological, catalytic or polymeric properties were studied. Research in this field is still largely devoted to structural studies. Most of the work led on these oligoamides deals with conformational and structural properties of the three dimensional arrangement as double helix formation [71] and molecular cages [72].

1.5.3 Aromatic oligoamides

The path to creating useful foldamers involves several daunting steps. (i) One must identify new polymeric backbones with suitable folding propensities. This goal includes developing a predictively useful understanding of the relationship between the repetitive features of monomer structure and conformational properties at the polymer level. (ii) One must endow the resulting foldamers with interesting chemical functions, to complete a specific goal. (iii) For technological utility, one must be able to produce a foldamer efficiently, which will generally include preparation of the constituent monomers in stereochemically pure form and optimization of heteropolymer synthesis. Each of these steps involves fascinating chemical challenges.

Two kinds of monomers are used along this work to design aromatic oligoamide foldamer; the 2-amino-8-quinoline carboxylic acid with a side chain in position 4 and disubstituted 1,10-phenantroline-dicarboxylic acid, as depicted in Scheme 1.2. Once assembled in a sequence, these monomers form a H-bonds network and induce folding into helical structures as depicted in Figure 1.4 (b).

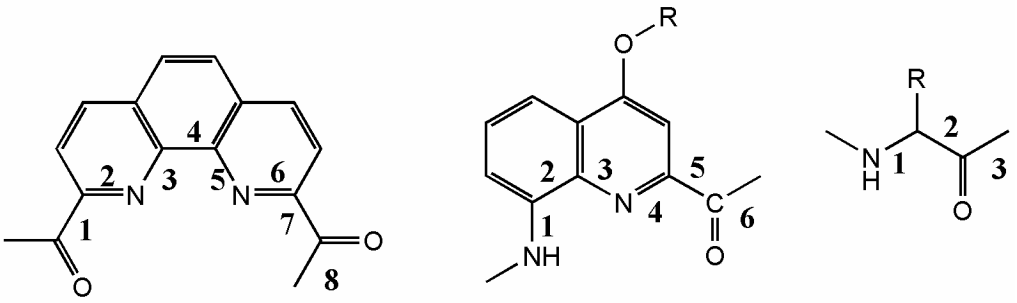

R = side chain

Scheme 1.2 Building blocks of aromatic oligoamide backbones versus a building block of a peptide backbone. The numbering correspond to the number of carbon constituting the backbone

1.6 Objectives of this thesis

1.6.1 Supramolecular chelates for hydrogenase mimics

Hydrogenases active site is electrochemically active; its role is to produce electrons, which are further used as reducing equivalents. These electrons have first to be transferred through the peptide to the location where the reduction has to occur. It has been suggested that ferrocene could replace the Fe-S clusters by performing electron relay using reversible conversion of iron II to iron III [73]. The idea is to synthesize small peptide sequences containing cysteine residues as mimics of this active site and to connect them to ferrocene. The complexes thus obtained serve as a chelate for a nickel and/or for an iron-carbonyl core, thus mimicking the Hydrogenase active site. Ferrocene will hopefully act ambivalently as an electron pathway but also as a scaffold using its original geometrical properties as a β-turn inducer.

We propose that helical oligoquinolines could be used as a molecular scaffold for mimicking hydrogenase active sites using their predefined arrangement to design new supramolecular sulfur-containing ligand for organometallic complexes. To step from peptidomimetic to enzymomimetic, the aromatic oligoamides require the introduction of an orthogonal functionalization that mimics peptide side chains. The quinoline monomer depicted on Scheme 1.2 was functionalized with sulfur containing side chains as a mimic of natural cysteine. The synthesis of this modified monomer was followed by the oligomerisation to obtain a folded helical arrangement. The modified side chain placed at key positions, previously determined by theoretical prediction, affords a new kind of suprachelate that is further used for coordination with a bimetallic iron core mimicking the active site of Fe-only hydrogenase.

1.6.2 Objectives

The goals of this PhD thesis are numerous.

First the synthesis and the characterization of ferrocene-peptide derivatives with sulfur containing amino-acid was performed. Therefore, a protecting group strategy for cysteine has to be found and optimized. This strategy will subsequently be adapted to the

organometallic solution phase synthesis. The free thiols thus obtained will serve as a chelate for iron carbonyl core.

Second, this issue will be theoretically studied by molecular mechanics calculations. Since no available force field is parameterized for ferrocene-peptide derivatives, we will have to create this force field and to test it on independent structures before we start simulating potential scaffolds for hydrogenase mimics.

Third, experience gained in sulfur chemistry will serve for a third approach, as two sulfurs will have to be placed at key position of an oligomer sequence and subsequently deprotected in order to afford free thiol. Complexation on this free thiol will also be tested.

1.6.3 Techniques

Elucidating the basic components and building principles of hydrogenases selected by evolution to propose reliable, efficient and environment respecting materials requires a multidisciplinary approach [74]. In this work the design, the synthesis, and the properties of structural models for hydrogenase are studied from two different synthetic approaches. The *bioorganometallic approach* consists of using the particular geometry and properties of ferrocene-bearing peptide derivatives to create a scaffold and an electron relay to mimic small model of hydrogenases by using the different techniques of inorganic chemistry. In the *bioorganic approach*, quinoline-derived foldamers will serve as pre-organised organic scaffolds. Their preparation involves multistep organic syntheses. These two different projects were both tightly connected to theoretical rationalization, this third approach is coined as *theoretical*; both bioorganometallic and bioorganic structures were predicted and studied in term of feasibility for the challenging project presented in this work.

2. Sulfur Protecting Groups and Peptide Syntheses

One of the most challenging tasks for the modern synthetic chemist is to find a suitable protective group strategy. It is essential to find a group, which is stable under the reactions conditions, but easy to remove during the last step of the synthesis, which is only feasible by using specific reagent.

Protection for the thiol group is very important for many areas of chemistry; for example for the protection of the thiol group in β-lactam chemistry [75], for the synthesis of coenzyme A, in which a carboxylic group is converted into a thioester [76], and last but not least in peptide synthesis, which often involve cysteine [77]. This field has been, therefore extensively studied and can be traced back to the beginning of the century. Up to now, about 80 different groups are referenced in literature for the protection of thiol [78, 79], and about two dozens for the protection of cysteine have hitherto been described. Nevertheless, the problem of cysteine protection remains unsolved. The preferred protecting group is obviously dependent on the nature of the synthesis and in fact more dictated by preparative aspects such as compatibility of the cleavage conditions, ease of purification, and technical and/or commercial availability.

2.1 Protective groups tested

A free –SH group can be protected as a thioether, a thioester or oxidized to a symmetrical or unsymmetrical disulfide [79]. Thioethers are, in general, formed by reaction of the thiol with a halide in a basic media. They are cleaved by reduction, by acid-catalyzed hydrolysis, or by a reaction with a heavy metal such as Ag(I) or Hg(II), followed by hydrogen sulfide treatment to recover the free thiol. Thioesters are formed and cleaved as oxygen esters. However, they are more reactive to nucleophilic reduction, as

indicated by their use as "activated ester." The disulfide protecting groups are usually prepared by substitution from a thioether. Besides, several miscellaneous protective groups, including thiazolidine, dithio acetal, and phosphine-sulfur derivatives are reviewed in literature [80]. A summary of the most commonly used protecting group for cysteine in peptide synthesis is shown in Table 2.1 along with their conditions of formation and cleavage.

Table 2.1 The most commonly used thiol protecting group in peptide chemistry along with their formation and cleavage conditions

Groups	Name Type Reference	Formation	Cleavage
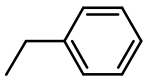	benzyl Thioether **[81, 82]**	1) $PhCH_2Cl$, Cs_2CO_3, DMF 2) $PhCH_2Br$, n-BuLi, THF	1) Na, NH_3 2) HF, anisole 3) Electrolysis
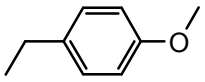	p-methoxybenzyl Thioether **[82, 83]**	1) 4-$MeOC_6H_4CH_2Cl$, Na/NH_3 2) 4-$MeOC_6H_4CH_2OH$, TFA/DCM	1) $Hg(OAc)_2$, TFA 2) TFA, reflux 3) NpySCl, AcCOOH
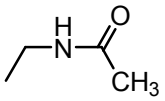	acetamidomethyl Thioether **[84]**	1) $AcNHCH_2OH$, HCl conc 2) $AcNHCH_2OH$, TFA	1) $Hg(OAc)_2$, H_2S 2) NpSCl, AcCOOH, $NaBH_4$ 3) TFA, TIS
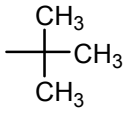	tertiobutyl Thioether **[85]**	1) Isobutylene, H_2SO_4, DCM 2) *t*-BuOH, HCl conc	1) $Hg(OAc)_2$, TFA, anisole 2) HF, anisole 3) NpSCl, AcCOOH, $NaBH_4$
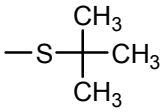	S-*tert*-butyl Disulfide **[86]**	1) $CH_3OC(O)SCl$, t-BuSh, MeOH 2) t-BuO_2CNHN(S-t-Bu), H_2O	1) $NaBH_4$ 2) Bu_3P, trifluoroethanol/water
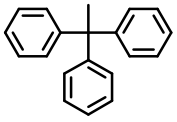	trityl Thioether **[87]**	1) $OHC(C_6H_5)_3$, TFA 2) $ClC(C_6H_5)_3$, TFA	1) HCl, AcCOOH, TIS 2) TFA, TIS
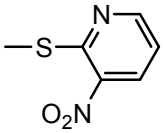	3-nitro-2-pyridine sulfenyl Disulfide **[88-90]**	1) Thioether, NpySCl, AcCOOH	1) CH_2H_5SH 2) Bu_3P, H_2O
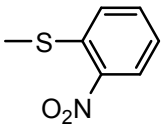	2-nitro-phenyl sulfenyl Disulfide **[91]**	1) Thioether, NpSCl, AcCOOH	1) CH_2H_5SH 2) Bu_3P, H_2O
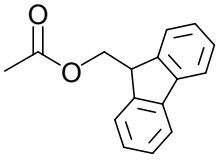	fluorenomethyl Thioester **[92]**	1) FmocCl, TEA, CH_2Cl_2	1) 20 % piperidine in CH_2Cl_2

Several protecting group, chosen among the mostly used for peptide chemistry, were tested by means of their suitability for our synthetic project. Except the H-Cys(Bzl)-OMe, which has been purchased from Novabiochem, the methyl ester protection was performed by using standard procedure described in ref. [85].

2.2 Synthesis

2.2.1 Preparation of the amino acids

Most of the cysteine derivatives presented herein were bought from commercial sources in their S-protected form, excepted for the nitro-phenyl derivatives and the fluorenomethyl derivatives, which were synthesized according to literature protocols [93-95].

The 9-fluorenylmethoxycarbonyl group, introduced first introduced in 1970, has become one of the most widely used protecting group in peptide chemistry. Fmoc is often used to protect nitrogens and alcohols, but Fmoc protecting group has been recently reported for the protection of thiol [92]. This protective group is labile under mild basic conditions, which is interesting for peptide chemistry, since its cleavage is orthogonal to the one of Boc for example. This is also of a great interest for the S-protection of cysteine since no basic labile protective group is available from commercial sources. The H-Cys(Fmoc)-OH was synthesized according to the protocol described in ref. [92]. The Fmoc-Cl reacts with both; the amino group and the sulfhydryl group to give the Fmoc-Cys(Fmoc)-OH. The Fmoc that protect is the amino group is subsequently cleaved by using 20 % Piperidine in CH_2Cl_2 at 0°C to control the reaction, the Fmoc S-protection remains untouched through this selective cleavage step. The carboxyl group was then esterified with a methyl ester to afford **6b** (see Scheme 2.1) in relatively good yield. The synthesis of Fluorenylmethyl (Fm) as another basic labile S-protective group has also been described in literature, but we were not able to obtain the product by following the protocols described in ref. [95, 96]. The *tert*-butyl protective group [97] is commercially available, but expensive. It has been found that within one day work and spending less then 20 € we were able to obtain about 20 g of the H-Cys(tBu)-OH for a commercial value of 200 €, by a simple addition tert-butyl alcohol on cysteine in acidic media as described in ref. [85]. A summary of the synthesis performed on cysteine is depicted in Scheme 2.1.

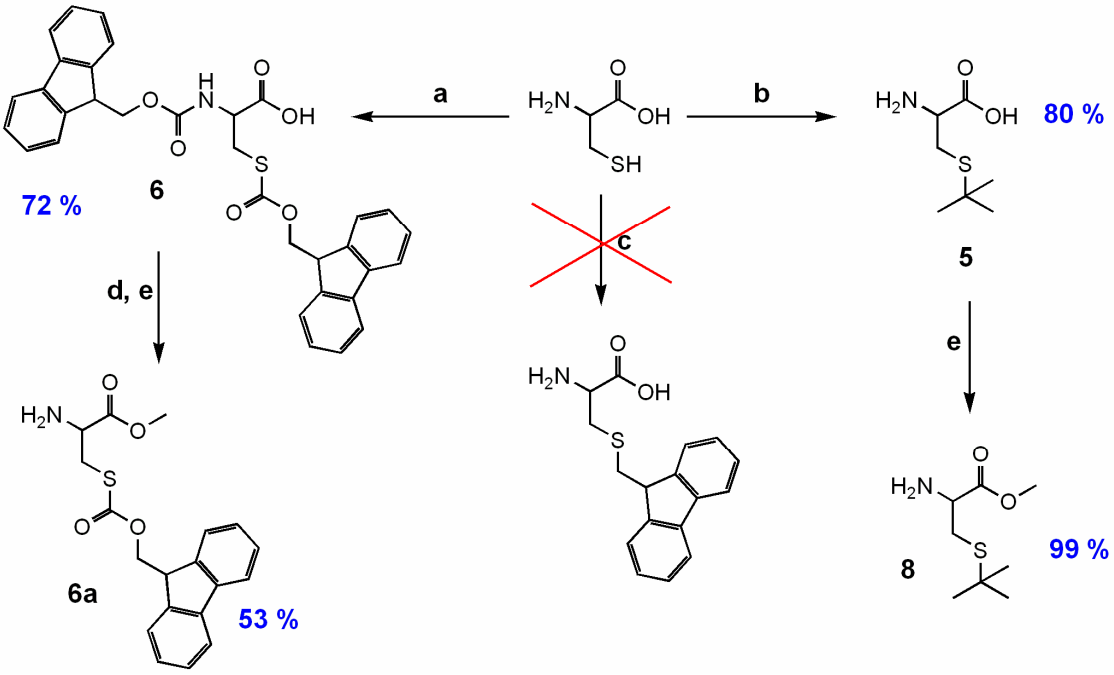

Scheme 2.1 Synthetic pathway for synthesis of protected cysteine; (a) Fmoc-Cl; CH_2Cl_2, 4 h; (b) tBuOH, 2 N HCl, 12 h, reflux; (d) 20 % piperidine in CH_2Cl_2, 1 h, rt; (e) $SOCl_2$, MeOH, 90°C reflux

The cysteine synthetically or commercially obtained was subsequently transformed into a methyl ester, using a standard procedure involving thionyl chloride and methanol, either refluxed overnight or at room temperature over 48 h [85] (see Scheme 2.1). For all amino acids, the yield was quantitative, except for the disulfide derivatives for which the yield varies between 70 % and 80 %. It is interesting to note that this procedure also provides good results for acid labile protecting group such as Trityl, even though the reaction of esterification releases HCl gas in the medium.

However, other protecting groups are available. It has been reported in literature that most of the conventional S-protecting group of cysteine could be selectively converted to the 3-nitro 2-pyridine-sulfenyl [85] group after treatment with the corresponding halide. The *tert*-butyl derivative of cysteine is placed in glacial acetic acid in presence of either 3-nitro 2-pyridine-sulfenyl or 3-nitro benzene-sulfenyl for a complete conversion of Bu in either NpyS or NbS. This part is discussed in details in Chapter 5.

2.2.2 Peptide synthesis

All of the peptides have been synthesized via solution phase synthesis. A peptide bond is generally formed by nucleophilic attack of the amine nitrogen of on amino acid on the carbon of the activated carboxylate group of the other amino acid. The reagent that transforms the carboxylate group to a better leaving group are called coupling reagent. Solution peptide coupling agents include several classes of reagents, N,N'-dicyclocarbodiimid, isobutyl chloroformate, phosphonium reagent, or benzotriazole derivatives. The most attractive coupling method for the synthesis of dipeptides in solution appeared to be the mixed-anhydride method [98] depicted in Scheme 2.2.

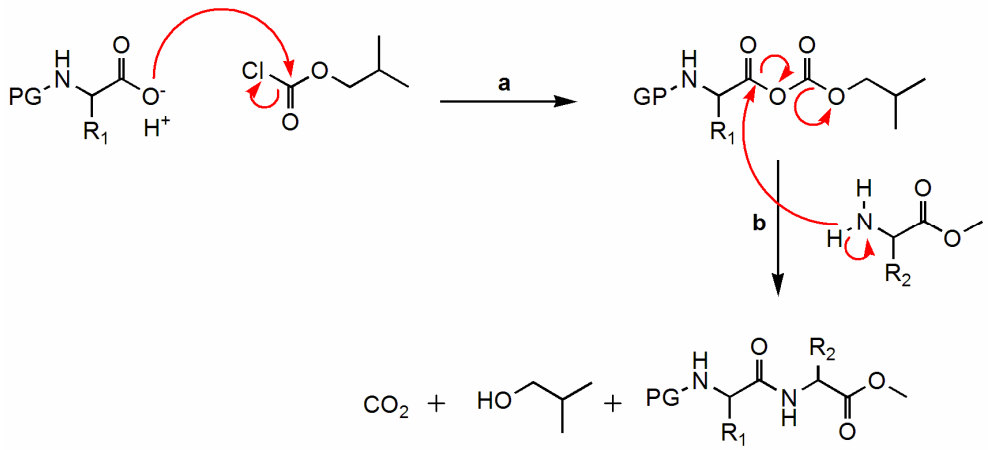

Scheme 2.2 Mixed anhydride coupling strategy used for dipeptide synthesis; (a) NMN, IBCF, THF, 1 h; rt; (b) H-Cys(PG)-OMe, THF, 4 h, rt.

First, the carboxylic acid is deprotonated by N-methylmorpholine; the carboxylate is subsequently transformed into a mixed anhydride derivative through a reaction with IBCF, yielding a reactive intermediate. Upon nucleophilic attack, of the amine nitrogen atom, the dipeptide is formed under elimination of isobutanol and CO_2. To prevent the polymerization of homopeptides, and unwanted reaction with the side chain the amino group of one of the amino acid is protected with either a Boc or an Fmoc protecting group and the carboxylate function of the other amino acid is was protected with a methyl ester. The side chain is protected with the protecting groups depicted before. These three kind of protecting groups could be, in the ideal case, selectively cleaved while leaving the other unaffected.

The dipeptides presented in Table 2.2 were synthesized using the mixed anhydride strategy. Boc group has been removed, with quantitative yield, by the reaction in pure TFA yielding the trifluoroacetate ammonium salt, the volatile isobutylene and CO_2 [99]. The N-Fmoc group can be easily cleaved with the mixture Piperidine / DCM (1:1) [100]. Methyl esters can be efficiently hydrolysed under basic condition in MeOH / THF mixture or 1,4-dioxane in presence of KOH as it is described in ref. [101] for example.

Table 2.2 Synthesized dipeptides in their N-protected and deprotected forms, along with the yield of the coupling and their numbering.

Dipeptides	Yield[a] Number[b]	N-deprotected form	Yield[c] Number[b]
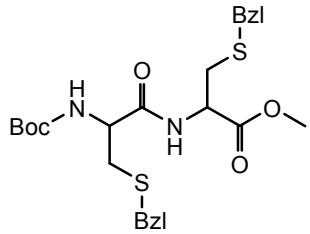	**93 %** **13**	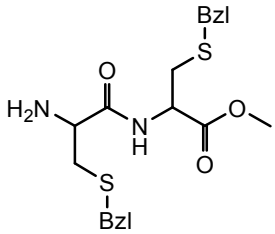	**Quant** **19**
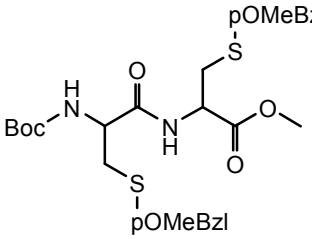	**90 %** **14**	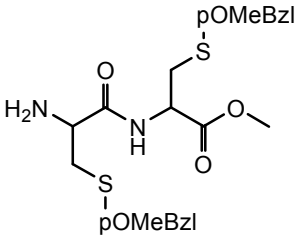	**89 %** **20**
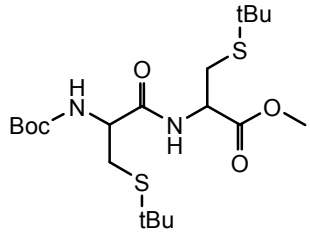	**87 %** **17**	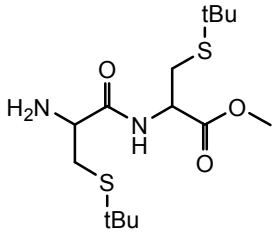	**Quant** **21**
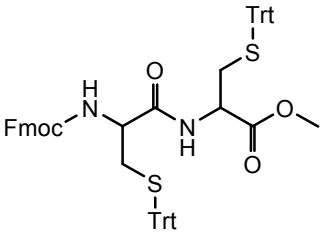	**72 %** **16**	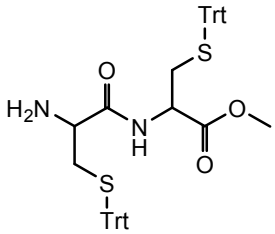	**61 %** **22**

[a] Yields obtained either for the coupling step
[b] Numbers are consistent with the experimental part
[c] Yields for the Boc / Fmoc deprotection step

2.2.3 Removal of side-chain protective groups

Removal of the side chain protective groups was tested on these dipeptides in their N-protected form. The different reaction conditions are summarized in Scheme 2.3. Isolation of the free thiol from the reaction mixture was performed by liquid chromatography on silica gel using most of the time a mixture of ethyl acetate and n-hexane as eluting system. In several cases product was difficult to purify due to the polarity of thiol combined with its instability in basic media.

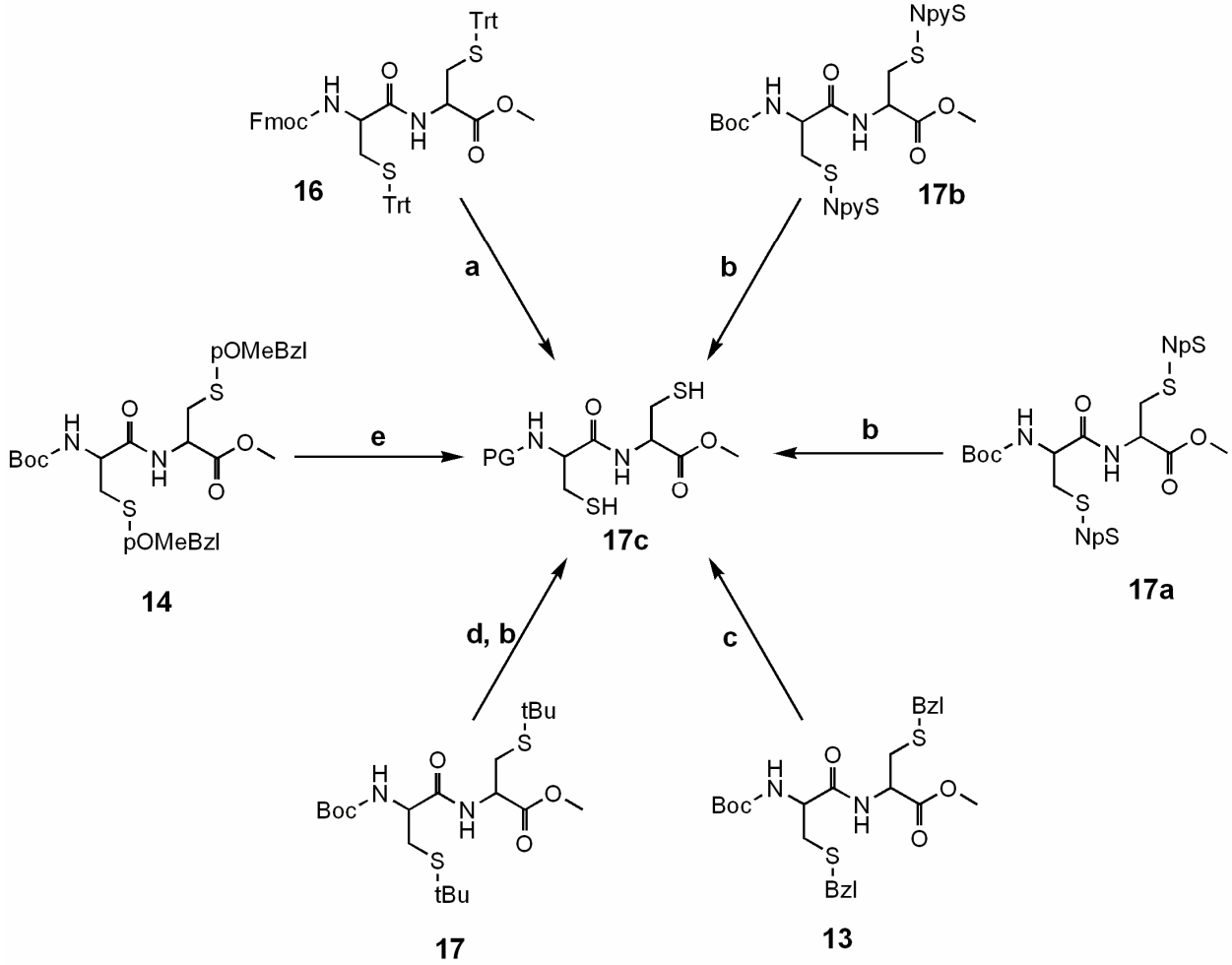

Scheme 2.3 Cysteine side chain protecting group removal procedure; (a) TFA 1 % in CH_2Cl_2, 1 h, rt; (b) n-tributylphosphin, acetone/water, 4 h, rt; (c) liquid NH_3, Na, 1 h, -73°C; (d) NpyS, acetic acid, 2 h, rt; (e) liquid NH_3, Na, 1 h, -73°C

From this first experiment about cleavage of cysteine side chain we were able to classified the protecting group in terms of the ease of cleavage, the criteria were yield, ease of purification and stability of the obtained thiol. Resulting in a stability classification: Trt > NpyS > NbS > tBu > pOMeBzl > Bzl. Unfortunately, the easier is the cleavage step, the

more sensitive is the protecting group. Further tests are necessary to determine the stability of these groups during ferrocene derivatization.

2.3 Concluding remarks

In the selection of a protective group, it is of a paramount importance to know the reactivity of the resulting protected functionality toward various reagent and reactions conditions of the synthesis. The numbers of protective groups available is large and their availability either commercial or technical is broad. In this first Chapter we have pursued to browse the most well known protective group for thiol that are used for peptide synthesis. These protecting groups were subsequently tested in term of stability, ease of cleavage, as well as commercial availability and price. From this technical review, we have found two potential candidates for the following work: (1) The trityl group, which is quite stable and easily removable, but certainly bulky (2) the *tert*-butyl, which is extremely stable but cleavable in two steps. Others tested protective groups had some drawbacks; S-S*t*Buthio is too sensitive and Acm too expensive. Benzyl and paramethoxy benzyl, which are, extremely stabile and therefore their cleavage conditions may be too harsh that is why their compatibility with the reactions conditions used along this work has to be further tested in the next Chapter.

3. Ferrocene-Peptides Derivatives

Conjugates of ferrocene and amino acids or peptides have been intensively studied in recent years [102]. The resulting conjugates were mostly investigated as electrochemical sensors for organic substrates [60, 103] or for anions [104]. In addition, such systems may serve as organometallic mimics of turn structures in peptides as first suggested by Herrick and co-workers [105]. Real organometallic turn mimics with anti-parallel peptide strands can be realized by use of the organometallic amino acid 1'-aminoferrocene-1-carboxylic acid [106-108] as demonstrated in a recent communication [109]. However in most cases studied so far, ferrocene carboxylic acid or ferrocene 1,1'-dicarboxylic acid **2** were coupled to the N-termination of the biomolecules. In those compounds, the question of structural organization through hydrogen bonds has been investigated in detail in the solid state by X-ray crystallography and IR spectroscopy as well as in solution by IR, NMR and CD spectroscopy, notably through the work of Moriuchi *et al.* [110-113].

A literature survey reveals that most compounds studied so far were composed of lipophilic amino acids without functional groups in the side chain [57]. These compounds are straightforward to prepare because no protecting groups are required. However, it is certainly desirable to provide additional functionality for further derivatization. In this work, we present results on the synthesis and characterization of ferrocenoyl derivatives with sulfur-containing amino acids and dipeptides, such as methionine and cysteine.

The amino acids and peptides described in Chapter 2 were coupled to ferrocene moiety, either to ferrocene mono carboxylic acid or to ferrocene 1,1'-dicarboxylic acid. A large range of novel ferrocene-peptide derivatives containing protected sulfhydryl residue were synthesized and fully characterized. They were subsequently investigated as potential scaffold for Hydrogenase active site.

3.1 Synthesis of ferrocene bearing sulfur containing peptide

Most of the differently protected amino acids or dipeptides were coupled to ferrocene moiety via a standard peptide coupling procedure. Ferrocene carboxylic acid or ferrocene 1,1'-dicarboxylic acid **2** were activated either with EDC and HOBt or with DIPEA, TBTU. Subsequent addition of either Met or Cys amino acid ester yields the amino acid conjugates. Enantiomerically pure *L* amino acids were used in all cases. The thiol of the cysteine derivatives were protected by either benzyl (Bzl), *p*-methoxy-benzyl (*p*-OMe-Bzl), trityl (Trt) or tertiobutyl (tBu) groups. Ferrocene-dipeptide conjugates were obtained the same way, after addition of the dipeptides H-Cys(PG)-Cys(PG)-OMe. However, this synthesis scheme did not work satisfactorily for the methionine and the Trityl dipeptides. Instead, the methyl ester in ferrocene-methionine conjugates **25a** and **25b** were hydrolyzed to yield the free acids Fe[C_5H_4-CO-Met-OH]$_2$ **25a'** and Fc-CO-Met-OH **25b'**. Activation of the acid and coupling to H-Met-OMe yielded the desired methionine dipeptides **25c** and **25d** in good yield. This iterative strategy also failed in the case of Trityl dipeptide, we assumed that Trityl is too bulky and therefore induce a steric hindrance that prevents dipeptide to be coupled to ferrocene moiety. However, coupling of the protected amino-acid cysteine-trityl has worked without any problems. A summary of the synthesized compounds with the numbering is presented in Scheme 3.1 along with the reactions conditions and synthetic strategy.

Derivatives **33a**, **33b**, **33c** and **33d**, were prepared from the deprotection of corresponding derivatives **27a**, **27b**, **28c**, and **28d** (these syntheses are detailed in Chapter 6). All compounds were purified by column chromatography on silica. Crystallisation yielded orange crystals, which were suitable for X-ray crystal determination in the case of **23b**, **23c**, **25a** and **25d**.

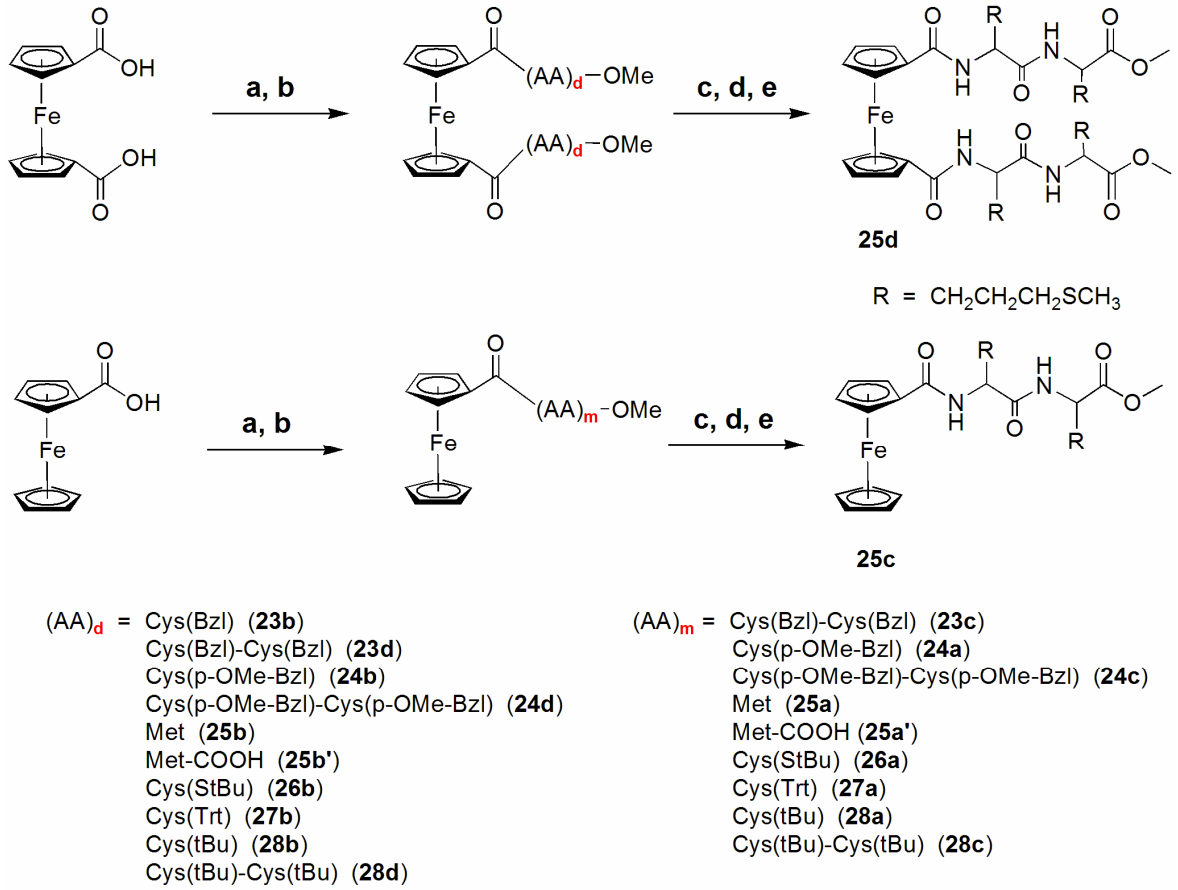

$(AA)_d$ = Cys(Bzl) (**23b**)
Cys(Bzl)-Cys(Bzl) (**23d**)
Cys(p-OMe-Bzl) (**24b**)
Cys(p-OMe-Bzl)-Cys(p-OMe-Bzl) (**24d**)
Met (**25b**)
Met-COOH (**25b'**)
Cys(StBu) (**26b**)
Cys(Trt) (**27b**)
Cys(tBu) (**28b**)
Cys(tBu)-Cys(tBu) (**28d**)

$(AA)_m$ = Cys(Bzl)-Cys(Bzl) (**23c**)
Cys(p-OMe-Bzl) (**24a**)
Cys(p-OMe-Bzl)-Cys(p-OMe-Bzl) (**24c**)
Met (**25a**)
Met-COOH (**25a'**)
Cys(StBu) (**26a**)
Cys(Trt) (**27a**)
Cys(tBu) (**28a**)
Cys(tBu)-Cys(tBu) (**28c**)

Scheme 3.1 Reaction conditions and synthetic pathway for the synthesis of ferrocene peptide derivatives (a) HOBt, EDCl, Ipr_2NEt, CH_2Cl_2; (b) H-$(AA)_n$-OMe, CH_2Cl_2; (c) NaOH, dioxane/water (1:1); (d) IBCF, NMN, NEt_3, CH_2Cl_2; (e) H-Met-OMe, CH_2Cl_2.

3.1.1 Helical chirality

Dipeptides derivatives of ferrocene were found to have a helical chirality du to the H-bonds that interconnect both peptide strands. This helicity can be detected by CD-spectroscopy (results are presented later). It's interesting to point out that the for the Herrick and van Staveren conformation, L-amino acids were so far always found to induce *P*-helical chirality of the ferrocene moiety, while D-amino acids induce M-chirality. *M* and *P* refer respectively to the helicity of the ferrocene, for this type of ferrocene peptide; P helicity will lead to a positive cotton effect in CD spectroscopy as it is shown in Scheme 3.2. In unsymmetrical D,L-amino acids substituted ferrocene derivatives mixture of *P* and *M* helical conformer is formed. In this work, the absolute configuration used for all amino acids used is the L-configuration unless otherwise noted. The helical chirality of ferrocene is usually not taken in account unless specified.

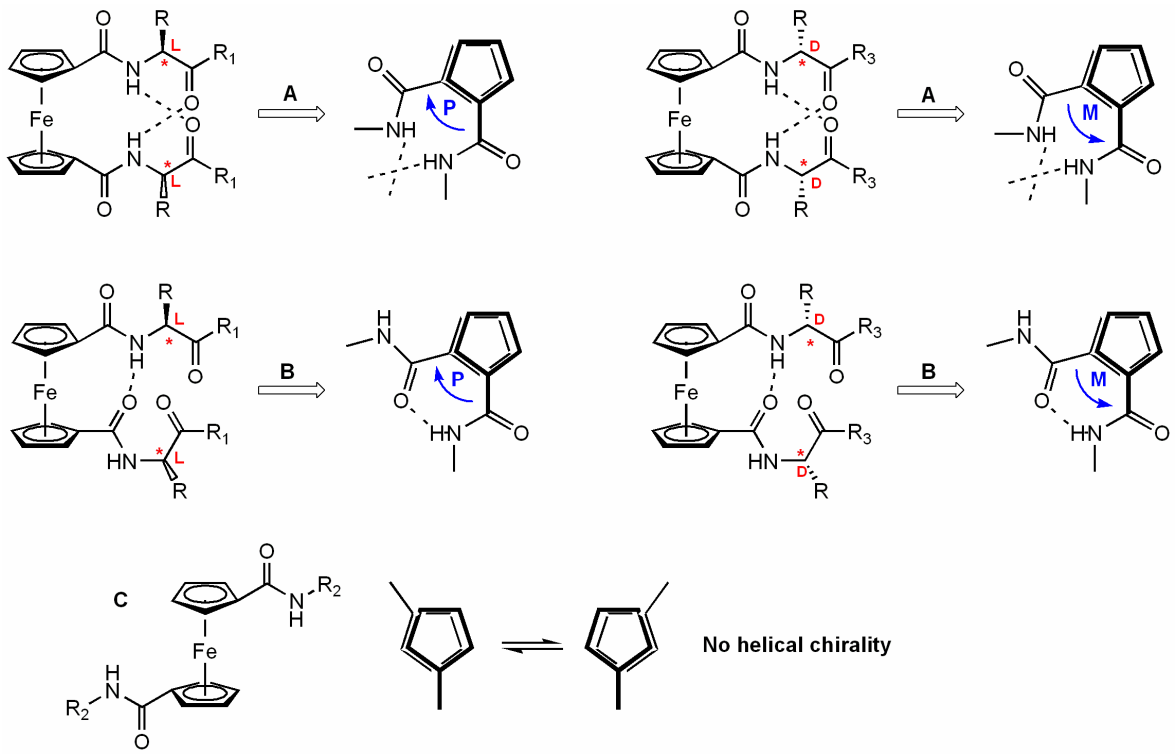

Scheme 3.2 Helical chirality of ferrocene bearing peptides derivatives in (**A**) Herrick (**B**), van Staveren and (**C**) Xu conformations

3.2 Characterization

All new compounds were extensively characterized using the standard spectroscopic method. Electron ionization (EI) mass spectrometry clearly confirms the composition of all new compounds. Indeed, the M^+ peak is one of the strongest signals in many compounds. Naturally, the dipeptide conjugates with higher mass were less volatile and therefore, the M^+ peak is lower in intensity, although still clearly detectable. The orange colour is attributed to an absorption in the visible region around 445 nm. The UV properties were not extensively studied at this stage of the work.

3.2.1 Infra Red Spectroscopy

The question of hydrogen bonding can be elucidated by a variety of techniques as IR spectroscopy. IR studies appears to be interesting in this case since the both, solid state and solution phase structure can be studied by the same method. We thus measured IR spectra

as KBr disks but also in chlorinated solvents, either $CHCl_3$ or CH_2Cl_2, which are known to enhance H-bond character. From these too sets of measurement, we have extracted the NH stretching vibration and deformation, the ester carbonyl stretching vibration and the amide carbonyl stretching vibration. The amide carbonyl stretching vibration and the amide-bending mode are also frequently referred as "amide I" and "amide II". These bands are among the strongest absorptions in the spectra, along with the ester carbonyl stretching vibration. It is well established that NH stretching vibrations below 3400 cm^{-1} indicate hydrogen bonding of the amide proton [114, 115]. In solution, this is the case for all disubstituted compounds as it has been reported previously [64]. For monosubstituted derivatives, the intermolecular hydrogen bonds, which exist in the solid state, are broken up in solution and NH-stretch values above 3400 cm^{-1} are observed for this class of compounds. For the bis-(dipeptide) derivatives two bands should be observed which are assigned to the two amide bonds, one, which is engaged in hydrogen bonding, and the other, which is not. It is surprising; however, that most of the compounds show only one NH band. This seems to suggest that also the other amide proton is engaged in a hydrogen bond most probably intermolecular. For a comprehensive study, Kraatz and co-workers have also discussed the significance of other IR bands in relation to amide hydrogen bonding [116].

In this study, eighteen different derivatives are listed in Table 3.1. It have been hitherto reported that only the NH deformation ("amide II") in solution is of any diagnostic value, in that a shift of 30 cm^{-1} to higher wavenumbers indicates hydrogen bonding. Values around 1540 cm^{-1} do indeed correlate with hydrogen bonding, whereas in non-hydrogen bonded derivatives values of 1500 – 1510 cm^{-1} are observed. However in this case, it seems that in solid state all measured derivatives a NH bending band between 1530 cm^{-1} and 1550 cm^{-1}, which account for hydrogen bonding.

Nevertheless, some trends can be deducted from data collected for the amide carbonyl stretching vibration. Values around 1650 – 1670 cm^{-1} do indeed correlate with hydrogen bonding, whereas in non-hydrogen bonded derivatives values of 1620 – 1630 cm^{-1}. For the bis-(dipeptide) derivatives two bands are observed as for compounds **28b**, **28d**, **33b**, **33d**, and **34b**, which are assigned to the two amide bonds, one which is engaged in hydrogen bonding, and the other which is not. They are the first clues of intramolecular H-bonding for these derivatives in the solid state. On the contrary, for compounds **25b**, **25d**, and **23b**, **23d** just a single band is observed in the NH bending region (see Table 3.1). Similar results are obtained in solution.

Table 3.1 Infra red data collection on synthesized ferrocene derivatives in solid phase

Compounds	ν (NH valence) [a]	ν (C=O$_{ester}$ valence) [a]	ν (C=O$_{amide}$ valence) [a]	ν (NH deformation) [a]
23a[*]	3278	1734	1628	1541
23b	3273	1745	1627	1540
23c	3272	1747	1629	1550
23d	3275	1745	1627	1541
25a	3269	1747	1625	1530
25b	3306	1739	1634	1539
25c	3267	1744	1647	1545
25d	3279	1744	1628	1545
28a	3274	1754 / 1735	1631	1542
28b	3304	1744	1654 / 1628	1535
28c	3294	1752	1635	1542
28d	3288	1750	1664 / 1635	1539
33a[b]	3299	1745	1635	1531
33b[b]	3294	1752	1654 / 1628	1542
33c[b]	3284	1747	1654 / 1624	1539
33d[b]	3293	1745	1671 / 1626	1542
34a	3298	1744 / 1730	1629	1532
34b	3265	1749	1663 / 1644	1543

[*] reported by Kraatz *et al.* in ref.[117], [a] in cm^{-1}, [a] syntheses of these derivatives are discussed in Chapter 6

3.2.2 NMR

NMR spectroscopy also confirms the composition of the compounds even at first glance. All signals for the amino acid side chains are readily assigned by 2D spectroscopy or comparison to literature values. Ester hydrolysis (in **25a'** and **25b'**) is evident from the disappearance of the singlet for the methyl ester at about 3.8 ppm. The amide protons appear between 7.0 – 8.5 ppm in $CDCl_3$ solution as a doublet due to coupling with the CH_α proton. Their position is indicative for the presence or absence of hydrogen bonding, as will be discussed below. The ferrocene groups show characteristic patterns between 4.0 - 4.5 ppm in all compounds (see Figure 3.1). Signals with respective intensity 5:2:1:1 are observed for the mono-substituted ferrocene derivatives. In contrast, the disubstituted

derivatives show four signals, with the same intensity, for the Cp rings between 4.2 – 4.4 ppm.

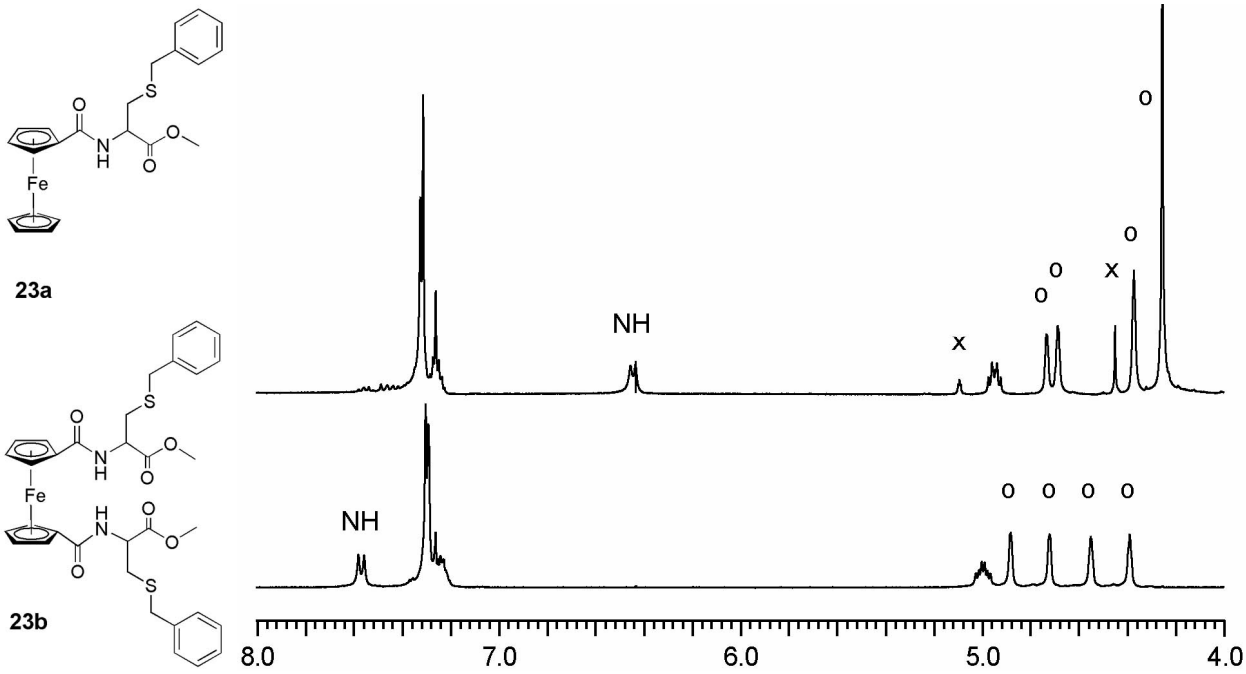

Figure 3.1 NMR spectra of **23a** (top) and **23b** (bottom), Cp and aromatic/amide region only. Cp signals are marked with "o", "x" denotes an impurity.

Depending on solvent and sample concentration, broad signals in the ^{1}H NMR spectra are observed for some compounds in $CDCl_3$ even still after addition of small amount of MeOD to cleave intermolecular H-bonds. This may be due to intermolecular interactions in solution through hydrogen bonding, especially in higher concentrations for the dipeptide derivatives. On the other hand, some of the disubstituted derivatives do indeed show extremely well-resolved ^{1}H NMR spectra as it is the case for **23b** for example. By manual iterative simulation, we were able to extract all coupling constants for one derivative as shown in Figure 3.2 (see legend of Figure 3.2 for values). The numbering of the protons of the Cp-ring is given in Scheme 3.3.

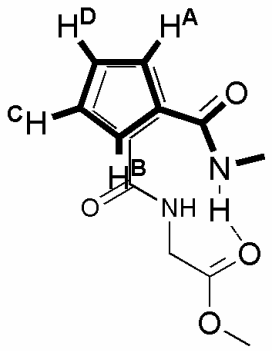

Scheme 3.3 Numbering of the different type of proton of the Cp-ring in disubstituted ferrocene

In combination with 2D-NOESY spectra, we were able to assign signals A – D (Scheme 3.3), assuming a 1,2' conformation of the substituents in solution (see below for discussion of this point). The two signals A and B at lower field are both *ortho* to the amide substituents, as deduced from their chemical shift and coupling constant pattern. A strong NOE is observed between the Cp amide proton and proton B, which is therefore assigned. From there, coupling constants suggest the order of protons given in Scheme 3.3, which is also supported by the 2D NMR data.

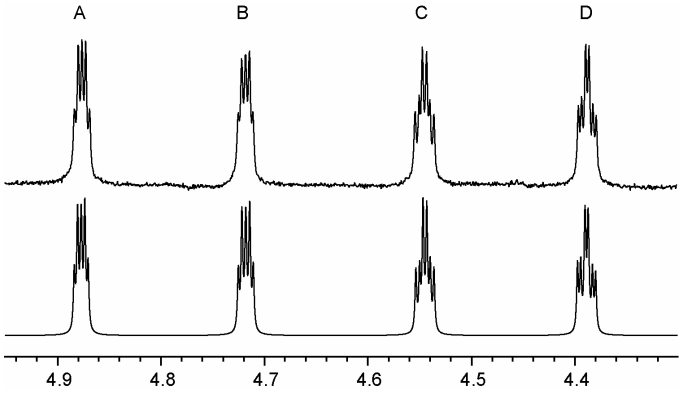

Figure 3.2 Cp region of the NMR spectrum of **23b** (top) and simulation with MestreC (bottom). The following parameters were used in the simulation: $\delta_A = 4.88$; $\delta_B = 4.72$; $\delta_C = 4.54$; $\delta_D = 4.39$; $J_{AB} = 1.2$ Hz; $J_{AC} = 2.5$ Hz; $J_{AD} = 1.1$ Hz; $J_{BC} = 1.3$ Hz; $J_{BD} = 2.7$ Hz; $J_{CD} = 2.5$ Hz. see discussion for assignment of signals.

A second criterion for hydrogen bonding is a significant downfield shift of the amide proton in the ^{1}H NMR spectrum of about 1 ppm [118]. This is confirmed for all compounds in this study as it is shown in Table 3.2. Indeed, two amide resonances are observed for dipeptide derivatives, suggesting two different amide protons with and without hydrogen bonding. The resonances observed around 6.4 ppm observed in the case

of **23a** and around 8.5 ppm in the case of **25d**. This acknowledges the difference in H-bonding pattern with respect to the size of the podand peptide.

A value of $^3J_{H\alpha\text{-}NH}$ coupling constant > 8 Hz is also indicative for hydrogen bonding, although this is not a stringent criterion. In the case of compound **28c** the down field shift of the amide proton (7.35 ppm) that suggests a low H-bond character and the $^3J_{H\alpha\text{-}NH}$ coupling constant (9.9 Hz) are not consistent.

Table 3.2 NMR data collection for some ferrocene-peptide derivatives

Compounds	δ_{NH}[a]	$^3J_{HH}$[b]	Compounds	δ_{NH}[a]	$^3J_{HH}$[b]
23a	6.43	7.2	**28b**	7.48	8.4
23b	7.54	8.3	**28c**	7.35 / 6.67	9.9 / 6.0
23c	7.12 / 6.55	7.4 / 7.0	**28d**	8.19 / 7.45	8.5 / 7.9
23d	8.21 / 7.23	8.0 / 7.7	**33a**	6.58	7.2
25a	6.57	7.8	**33b**	7.55	8.5
25b	7.8	8.7	**33c**	7.20 / 6.64	-[c] / 7.3
25c	7.2 / 6.32	-[c] / -[d]	**33d**	8.10 / 7.2	8.0 / -[c]
25d	8.55 / 7.81	8.7 / 6.0	**34a**	6.63	6.7
28a	6.48	7.6	**34b**	7.34	6.9

[a] in ppm; [b] in Hz; [c] could not be determined because the signal overlapped the residual solvent signal [d] could not be determined because the signal was too broad

3.2.3 Circular Dichroism

We have also recorded CD spectra of compounds from the families **23**, **25**, **38**, **33** and **34**. Representative examples are depicted in Graph 3.1. Spectra were recorded in CH_2Cl_2 at concentrations of about 1.0 mM and 0.1 mM. Ellipticity maxima, λ_{max} and Ellipticity minima, λ_{min} are given in nm. Molar ellipticity coefficients, M_θ, were calculated as described in Equation 1.

$$M_\theta = \frac{100 \times \theta}{c \times l} \qquad 1$$

Where the ellipticity θ is given in is in deg, concentration c in mol.L^{-1} and path length l in cm, thus giving deg L mol^{-1} cm^{-1} for M_θ [119, 120].

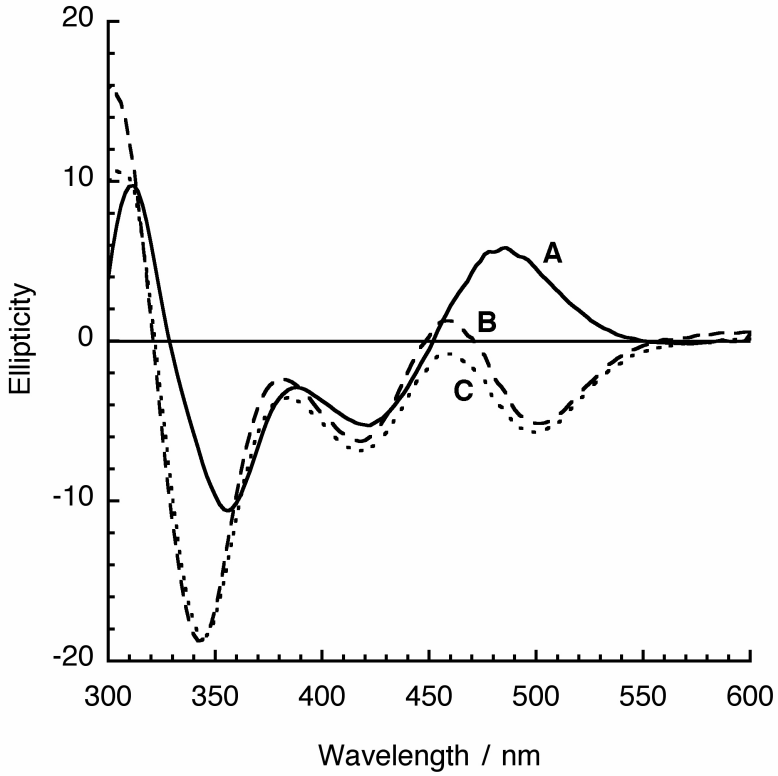

Graph 3.1 CD spectra of **25b** (**A**, conc. is 0.15 mM in $CHCl_3$), **25a** (**B** conc. is 3.2 mM in $CHCl_3$) and **25a** (**C** conc. is 3.2 mM in $CHCl_3$:MeOH (9:1)). Please note the different concentration for **25b** and **25a**, see discussion for explanations.

In this experiment, the concentration for **25b** was chosen ten times lower than for **25a** in order to display both spectra on the same absolute ellipticity scale in Graph 3.1. Naturally, molar ellipticity coefficients are much higher for **25b** than for **25a** [121]. Metal-centred transitions are expected in the region above 400 nm. For the disubstituted derivatives a strong positive Cotton effect is observed around 480 nm (**25b**: M_θ = 38950 L.mol^{-1}.cm^{-1} at 485 nm). A 100 fold weaker positive band is seen for the mono-substituted derivatives around 460 nm (**25a**: M_θ = 402 L mol^{-1} cm^{-1} at 460 nm), followed by a weak negative band around 500 nm (**25a**: M_θ = -1610 L mol^{-1} cm^{-1} at 500 nm). A spectrum of **25a** was also recorded in $CHCl_3$ / MeOH (9:1) in order to clarify

whether the ferrocene-based bands above 400 nm in monosubstituted compounds originate from inter- or intramolecular hydrogen bonding interactions (spectrum C, 3.2 mM). In the region below 400 nm, which is attributed mainly to transitions of the amino acids, all spectra are rather comparable.

The CD spectroscopic measurements correlate nicely with results from Hirao and co-workers [59, 111]. A positive Cotton effect at 480 nm is indicative for a *P*-helical arrangement of the substituents on the Cp rings in disubstituted derivatives as compound **23b** (Graph 3.1, spectrum A). A similar conclusion was also drawn for a tetrapeptide containing the unnatural amino acid 1-aminoferrocene-1'-carboxylic acid [109]. It is interesting to note that also the monosubstituted derivatives as compound **25a** show an appreciable CD signal above 400 nm. It is, however, much weaker than in derivatives **25b**, and has a different appearance. One might argue that this signal is due to the proximity of the chiral centre (C_α) on one Cp ring, which induces a polarization in the metal-centred d-d or metal-to-ligand transitions and thus a CD signal at low wavelength. Alternatively, it might be due to intermolecular hydrogen bonding interactions. To test this hypothesis, we have added 10 % MeOH to the solution of **25a** in $CHCl_3$ (spectrum C) and the resulting results is that spectra B and C look very similar. Therefore, we conclude that the observed CD bands above 400 nm are an intrinsic property of a single molecule and not due to intermolecular hydrogen bonding interactions.

In a second experiment, the effect of the protecting group is studied. Therefore, the family **33** and the **28** were measured and their Molar Ellipticity were plotted. The results are discussed in Chapter 6.

3.2.4 X-ray

Single crystals suitable for X-ray analysis were obtained by slow diffusion of pentane in a solution of ethyl acetate for **23b**. Single crystal for both **23c** and **25a** were obtained by slow evaporation of CH_2Cl_2 from a CH_2Cl_2 / heptane mixture. Single crystals for **25d** were obtained by slow evaporation of $CHCl_3$ from a $CHCl_3$ / heptane mixture. In order to determine the conformation and possible hydrogen bonding interactions, the X-ray single crystal structures of those derivatives were determined (see Experimental section for experimental details). All compounds crystallize in chiral space groups, as expected and frequently observed before for metallocene amino acid derivatives [105, 122]. Ortep plots are depicted with 50 % probability in Figure 3.3.

All structures confirm the proposed composition of the compounds. Excepted for **25d**, none of the compounds shows any intramolecular hydrogen bonding. However, all amide protons are engaged in intermolecular hydrogen bonding. In compound **25a**, only one amide bond per molecule is present, and this leads to extended chains in the solid state through hydrogen bonding between the amide proton and the carbonyl oxygen atom of the amide group of the neighbouring molecule (N(7)H-O(26) and N(27)H-O(6A)). For both other compounds, several amide bonds are present and a more complicated three-dimensional intermolecular hydrogen-bonding pattern is observed. It is noteworthy that the disubstituted derivative **23b** shows a 1,3'-substitution pattern of the ferrocene moiety. Consequently, the distance between the two Cys residues is too large for intramolecular hydrogen bonding.

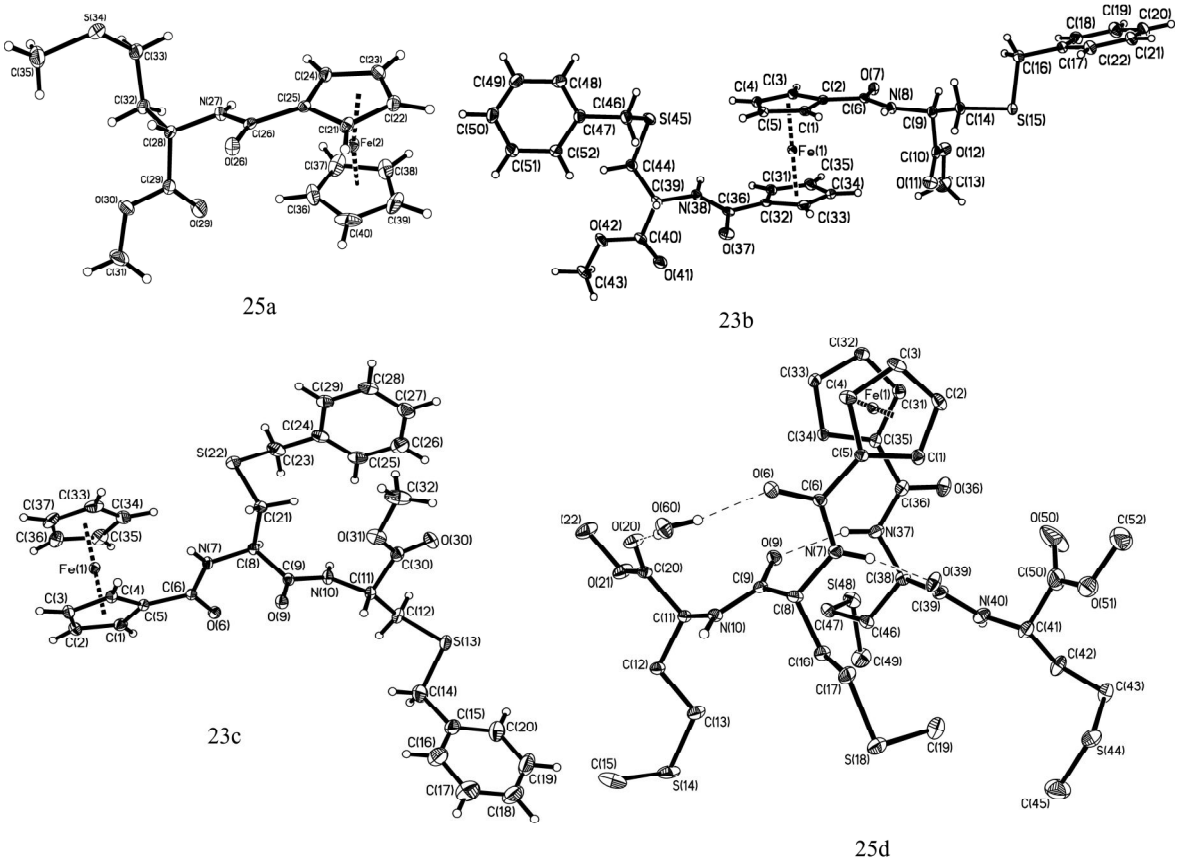

Figure 3.3 Ortep plot of the asymmetric units of **25d**, **25a**, **23c**, **23b**. Thermal ellipsoids are depicted at 50 % of probability. In the case of **25d** only the major isomer is depicted.

In the case of **25d**; the compound crystallizes in orthorhombic space group $P2_12_12_1$. An ORTEP plot of one molecule is shown in Figure 3.3. Metrical parameters of the

ferrocene moiety are comparable to those of other ferrocenoyl dipeptides reported previously and will therefore be discussed only briefly [62, 64].

The Cp(centroid)-Cp(centroid) distance is 3.302 Å and the dihedral angle θ between the two Cp rings is 0.7°. With a torsion angle C(5)-Cp(centroid)-Cp(centroid)-C(35) of $\omega = 67.5°$, the two Cp rings are in a nearly eclipsed conformation. The carbonyl groups are slightly tilted from the mean plane of the Cp rings with dihedral angles β of 1.7° and 9.0° (see Figure 3.4 for a definition of these parameters).

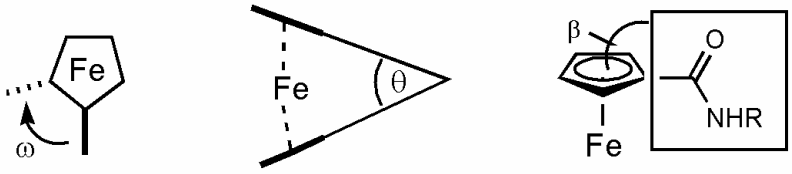

Figure 3.4 Some important structural parameters in 1,n'-disubstituted ferrocene peptides derivatives

The molecule **25d** adopts the "Herrick conformation" with two symmetrically equivalent hydrogen bonds between the amide NH on one and the proximal (relative to the Fc moiety) methionine carbonyl group on the other peptide chain [61]. In addition, the carbonyl group O(6) adjacent to one Cp ring is bridged to the methyl-ester carbonyl atom O(20) on the same peptide chain by a water molecule O(60) forming a 12-membered ring. The distal amide NH on this peptide chain is involved in an additional intermolecular hydrogen bond with a bridging water molecule of an adjacent molecule with a distance of N(40) ··· O(60) of 2.782 Å, thus forming a zig-zag chain along the crystallographic *b* axis.

Even more remarkable is the stereochemistry of the helical chiral ferrocene moiety. As mentioned above, all ferrocenoyl dipeptides studied so far with the "Herrick conformation" in the solid state were found to have *P* helicity at the ferrocene moiety for L amino acid side chains and *M* helicity when using D amino acids instead, thus leading preferentially to L,*P*,L or D,*M*,D isomers, respectively [123-125]. In contrast to all other ferrocenoyl dipeptides characterized so far, **25d** is a mixture of two isomers in the solid state: L,D,*M*,D,L (major isomer, > 80 %) and L,D,*M*,L,L (minor isomer). Both isomers are depicted in Scheme 3.4. This finding can be explained if a partial racemisation of the two Met residues directly bound to the ferrocene during the deprotection of the ester groups in basic media is assumed. The two bands observed in IR and the weak CD signals (see Graph 3.1) are consistent with a mixture of diastereomers.

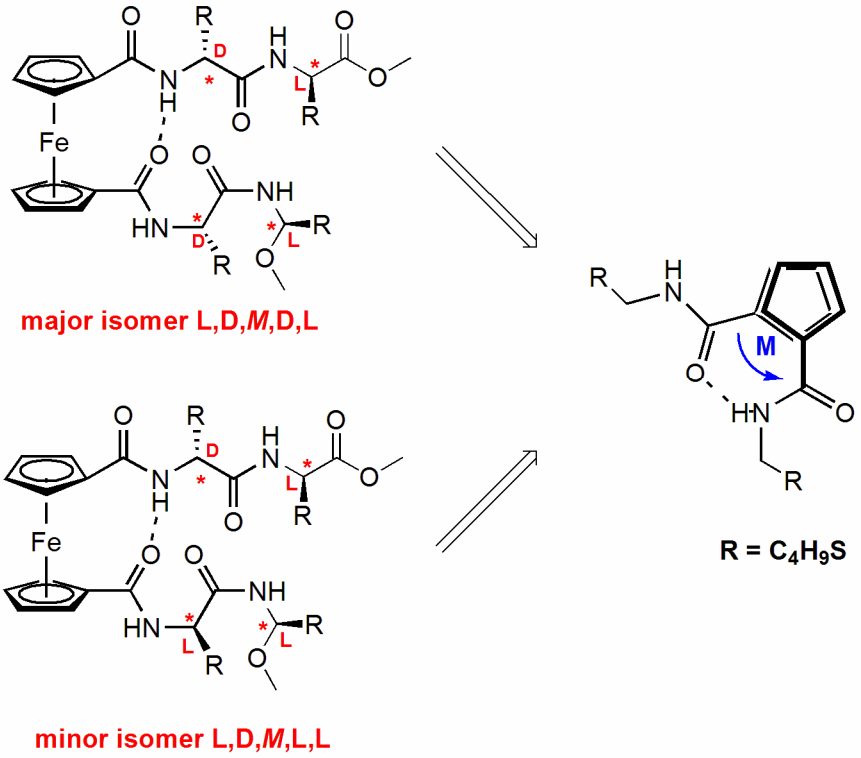

Scheme 3.4 Schematic representation of both isomers of **25d** observed in the crystal lattice

3.2.5 Electrochemistry

In order to elucidate another interesting feature from this kind of compound, several experiments of square wave and cyclic voltammetry were performed on some of these compounds. All measured compounds containing ferrocene show a reversible one-electron oxidation for the ferrocene moiety in solution. Ferrocene moiety undergoes a simple outer sphere one-electron redox process. Influence of the substituents was also estimated, a maximum difference of 50 mV between the various amino acids is observed.

At the start of the experiment, the bulk solution contains only the reduced form of the redox couple namely, in this case (Figure 3.5) Fc, **25a**, **25b** so that at potentials lower than the redox potential, i.e. the initial potential, there is no net conversion of reduced state R into oxidised state O. As the redox potential is approached, there is a net anodic current, which increases exponentially with potential. As R is converted into O, concentration gradients are set up for both R and O, and diffusion occurs down these concentration gradients. At the anodic peak, the redox potential is sufficiently positive that any R that reaches the electrode surface is instantaneously oxidised to O. Therefore, the current now

depends upon the rate of mass transfer to the electrode surface and so the time dependence is "qt" resulting in an asymmetric peak shape. Upon reversal of the scan, the current continues to decay with "qt" until the potential nears the redox potential. At this point, a net reduction of O to R occurs producing a cathodic current, which eventually causes a peak-shaped response.

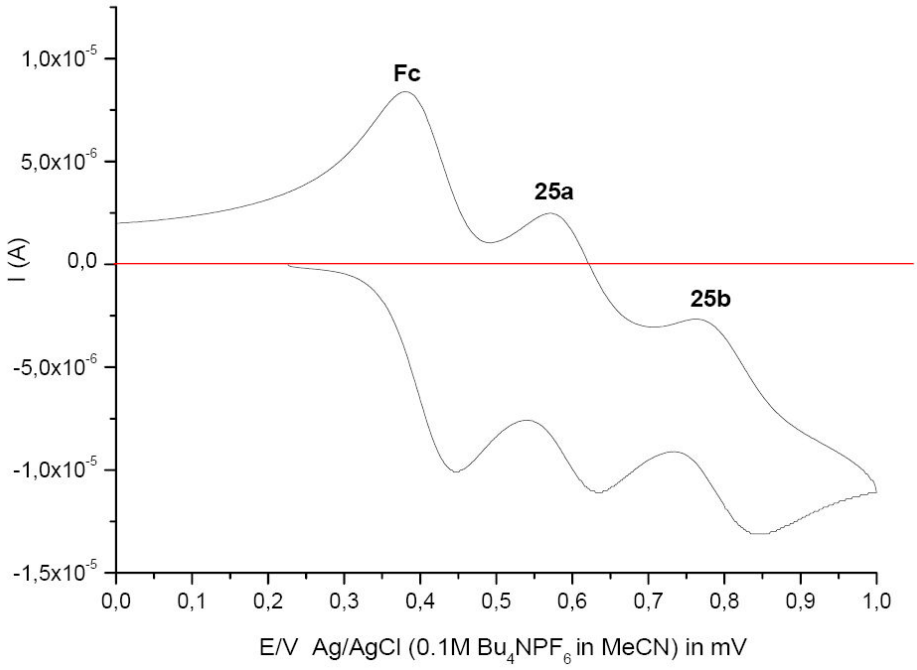

Figure 3.5 Cyclic voltammogram of a mixture of Fc, **25a** and **25b** measured in pure acetonitrile using Bu_4NPF_6 (0.1 M) as a supporting electrolyte; comparison of the one electron process of the non-substituted, the monosubstituted and the disubstituted ferrocene. This spectra is not calibrated to Fc/Fc^+

The redox potential for some ferrocene derivatives are shown in Table 3.3. The substituted derivatives display higher oxidation potential than ferrocene (set to 0.00 V by definition); the oxidation potentials for mono-substituted derivatives are observed around 200 mV vs. Fc / Fc^+, whereas they are observed around 400 mV (see Table 3.3) for the disubstituted derivatives. It appears that the substituents effect are additive, because the redox potential difference between ferrocene and the monosubstituted derivatives is approximately equal to the difference between the later and the disubstituted derivative. The increase of the oxidation potential upon substitution of the Cp ring by amide groups can be explained by the withdrawal of electron density from the ferrocene moiety by these substituents, resulting in a derivative that is more difficult to oxidise. A molecular orbital treatment of the interaction between the orbitals of the ferrocene and the orbitals of

ferrocene with several electron-withdrawing substituents has already been reported [117]. The authors of that publication stated that one of the components of the e_{2g} set (the HOMO) has a higher interaction with the orbitals of the substituents. This results in the stabilization of one of the components of the e_{2g} set, with the other component remaining about identical in energy and thus, this component becomes the HOMO of the compound. Although the authors could correlate trends in bond-lengths observed for various substituted ferrocene derivatives, this molecular orbital treatment does not provide an explanation for the shift of oxidation potential, because the new HOMO of the system is at nearly the same energy as the previous e_{2g} set. Nevertheless, photoelectron spectroscopic investigations clearly demonstrate that the HOMO shifts to lower energy upon addition of electron withdrawing substituents on the Cp-rings.

Table 3.3 Half-wave potential determined from cyclo-voltammogramm for compounds and calculated versus Fc/Fc^+ potential.

Compounds	$^{Fc/Fc^+}E_{1/2}$ (mV)	Compounds	$^{Fc/Fc^+}E_{1/2}$ (mV)
Fc(COOH)	238	**2**	456
23a	187	**23b**	448
23c	182	**23d**	387
28a	193	**28b**	395
28c	202	**28d**	448
33a	199	**33b**	417
33c	196	**33d**	396

From the data summarized in Table 3.3 it is difficult to extract a relationship between the size or the nature of the substituents and a shift in the oxidation potential. However, it is interesting to note that the oxidation potential is shifted from about 40 - 50 mV from the simple ferrocene carboxylic acid (238 mV) or 1,1'-dicarboxylic acid (456 mV) to the peptide derivatives (monosubstituted around 200 mV, disubstituted around 400 mV). This can be attributed to the fact that a carboxylic acid group is more electron withdrawing than an amide group.

3.3 DFT study of H-bonds patterns

Density functional theory is the method of choice to study the electronic and geometrical structure of transition metal-based systems [126]. It has already been successfully applied to investigate the conformational preference of substituted ferrocene derivatives [108, 127]. All calculations of this part of the work were performed using the Gaussian98 commercial package [128]. The coordinate files were prepared and worked-up with Molden 4.3 software facilities [129]. The B3LYP [130, 131] exchange correlation-functional and the level of theory Lanl2DZ were used [132, 133]. Effective core potentials theory was used for the heavy atoms during the geometry optimizations. All converged geometries were characterized as stationary points by analytical calculation of vibrational frequencies due to the absences of imaginary frequencies.

Three different conformation were considered for ferrocene-1-glycine-1'-glycine, the "Herrick conformation", with two symmetrically equivalent hydrogen bond, the "van Staveren conformation", with only one hydrogen bond and the "Xu conformation" without intramolecular H-bonds. The glycine was chosen because of its achirality, to simplify the calculation and the subsequent output. Models of all three structures with truncated side chains to reduce the calculation time were built from available crystal structure obtained from CCDC. The geometries of the models were fully optimized without symmetry constraints. The results are compared to the experimental data from the X-ray structure. The main geometry is obviously conserved, distances and angles are accurately reproduced even though the well-known overestimation of metal-ligand bond lengths in DFT calculations [134]. It is assumed that the model chemistry used is able to reproduce the important geometrical feature of ferrocene-glycine derivative.

The relative energy of the three different conformation of a same node was compared. The Herrick's conformation **A** (see Figure 3.6) appear to be the most stable conformation, followed by the van Staveren's conformation **B** (see Figure 3.6) with an energy difference of about 33.9 kJ mol^{-1} and finally the Xu's conformation **C** (see Figure 3.6) with an energy difference of 29.7 kJ mol^{-1}. These results are in good agreement with the hydrogen bonding enthalpy of water, which has been estimated to be 23 kJ mol^{-1}. This is also in the line with the fact that the Herrick's conformer is the only detectable species in

solution, in most of the case. We thus confirm that intramolecular H-bonding is a stabilizing factor in this family of compounds.

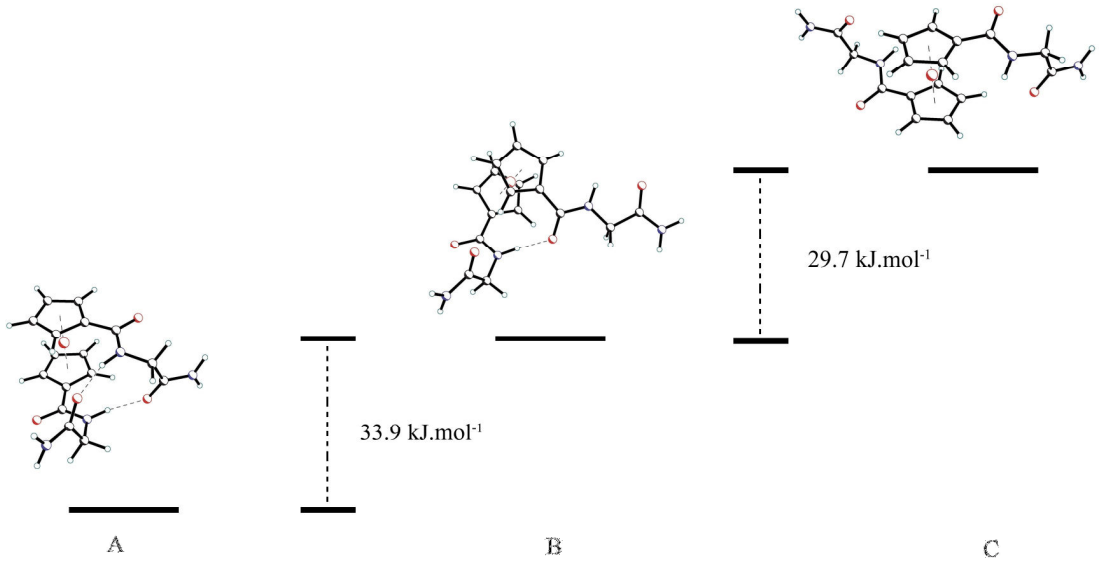

Figure 3.6 Relative stability of conformers **A**, **B**, **C** of $Fe[C_5H_4\text{-}CO\text{-}Gly\text{-}NH_2]_2$, calculated by DFT B3LYP/LanIDZ.

However, in the solid state, the most stable conformation seems to be determined by a delicate balance of the relative strength of the various intra- and intermolecular possible H-bonds.

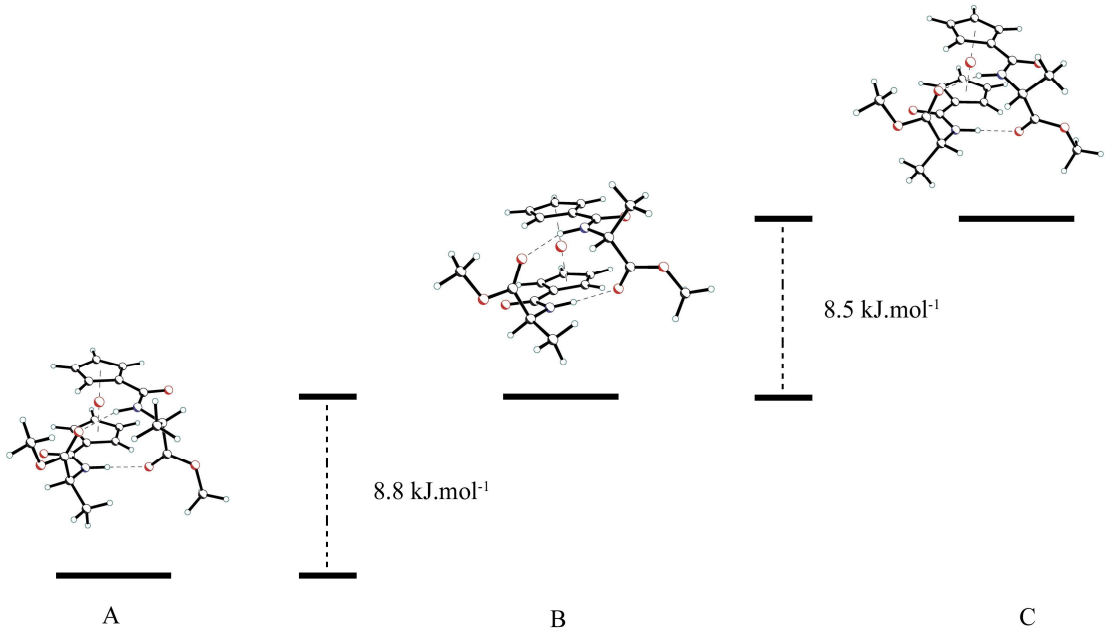

Figure 3.7 Relative stability of conformers **D** L,*P*,L; **E** L,*P*,D; **F** D,*P*,D of $Fe[C_5H_4\text{-}CO\text{-}Ala\text{-}NH_2]_2$, calculated by DFT B3LYP/LanIDZ.

A second calculation was performed on ferrocene-1-(*L*)alanine-1'-(*L*)alanine, Using a chiral amino acid, an additional three diastereoisomeric conformations are possible for the Herrick conformer depending on the helical chirality of the ferrocene moiety and the chirality of the amino acids. Their conformational preference was investigated using $Fe[C_5H_4\text{-}CO\text{-}Ala\text{-}OCH_3]_2$ as model compound, as it is depicted in

Figure 3.7). The energy differences between the three conformations are in the range of 8.5 to 8.8 kJ mol^{-1}. It is not possible to predict any general trend from such small energy differences.

3.4 Discussion

The synthesis of mono- and disubstituted amino acid and peptide derivatives of ferrocene carboxylic acid and ferrocene 1,1'-dicarboxylic acid proceeds without problems. Coupling of the dipeptide is possible as well as two sequential couplings. The preferred sequence is obviously dependent on the nature of the amino acids and in fact mostly dictated by preparative aspects such as ease of purification. In our hands, the Met-Met dipeptide derivatives **25c** and **25d** were best prepared in the latter fashion, whereas the Cys-containing peptides were most easily obtained by direct coupling of the dipeptide. The Cys derivatives only differ slightly in the protecting group (benzyl vs. *p*-methoxy-benzyl) and are indeed almost identical in their chemical and spectroscopic properties. Most compounds in this study are crystalline solids and as such easily obtained in high purity. Full characterization is possible, and all analytical data corroborate the proposed composition of the compounds. Compound **23a** has been previously prepared by Kraatz and co-workers [116]. This group has also reported sulfur-containing ferrocene derivatives, although not with amino acid but cystamine substituents [135]. Finally, a Chinese group has recently reported the synthesis of the S-ethyl protected derivative $Fe[C_5H_4\text{-}CO\text{-}Cys(SEt)\text{-}OMe]_2$ [136]. Unlike in this derivative, the Cys protecting groups that were chosen in this work may be removed under reductive conditions.

In most disubstituted compounds studied so far, a 1,2' substitution pattern of the Cp rings was observed. This conformation is stabilized by hydrogen bonds between the two amino acid esters involving the Cp amide hydrogen atom and the carbonyl oxygen atom of the ester group ("Herrick conformation") [61]. In all those cases, cysteine was the first amino acid on the Cp-ring. We have recently observed a different hydrogen bonding

pattern in the bulkier phenylalanine derivative $Fe[C_5H_4\text{-}CO\text{-}Phe\text{-}OMe]_2$ [119], involving the amide hydrogen of one Cp ring and the amide carbonyl oxygen atom of the other Cp ring in the same molecule ("van Staveren conformation") [62]. For compound **23b** in this study, the situation is again different. This compound has a 1,3' conformation in the solid state, and therefore does not show any intramolecular hydrogen bonding in the solid state. All spectroscopic data measured in solution, however, are similar to previously reported data and thus a 1,2' conformation with "Herrick-like" intramolecular hydrogen bonding is likely. This hydrogen bonding interaction is very strong indeed. CD spectra of **23a** look the same in $CHCl_3$ and in pure MeOH, which may compete for hydrogen bonds. In particular, the strong positive Cotton effect at 480 nm is observed in both solvents. One might argue that the 1,3' conformation in the solid state is due to steric interactions of the bulky Cys(Bzl) side chains. However, a 1,3' conformation in the solid state has also been observed for the glycine ethyl ester derivative $Fe[C_5H_4\text{-}CO\text{-}Gly\text{-}OEt]_2$ by Kraatz and co-workers. In fact, the related free acid $Fe[C_5H_4\text{-}CO\text{-}Gly\text{-}OH]_2$ shows the well-known 1,2' "Herrick conformation" in the solid state [137]. It seems therefore reasonable to summarize that the factors governing the solid-state structures are not yet fully understood and further studies are needed.

Nevertheless, we have demonstrated that a supramolecular self-assembly occurs in ferrocene-peptide derivatives containing cysteine. The question we would like to answer next is: What assembly is the more adapted to connect a late transition metal to the sulfur atom present in the sequence?

4. Molecular Dynamic Simulations

A wide range of compounds containing ferrocene and cysteine with different protecting groups have been synthesized and fully characterized in Chapter 3 [64]. These compounds are seen as potential chelate for nickel and iron. Therefore, some questions arise concerning sterical and mechanical interactions that occur in this family of compounds. It is assumed that one of the major limiting factors in the synthesis of these compounds is the steric hindrance upon incorporation of the metal in the tetra-dentate sulfur ligand pocket, where all cysteine residues are connected to the same ferrocene moiety. We have pursued the answers to these questions using Molecular Dynamics (MD) simulations, in order to determine from a geometrical point of view the feasibility of such a synthesis.

The application of computational methods to inorganic chemistry has developed at a slower pace than other branches, due to the complexity that arises from modeling d-block elements [138]. Ligand-metal bonds can adopt multiple conformations, determined by the ligand-ligand and ligand-metal interactions that are difficult to accurately model. Nevertheless, the application of computational methods to inorganic chemistry remains attractive as a means of investigating the formation and the stability of new complexes. Molecular Mechanics (MM) has been widely used in organic and bioorganic chemistry. Most common MM simulation packages, such as CHARMM [139], are equipped with parameter sets for biomolecules but not for transition metal complexes. Only few attempts using CHARMM for modeling of metallocenes have been reported [140-142].

In this work, the development and the implementation of a new MM force field for ferrocene-bearing peptides in CHARMM are presented. The resulting force field was first tested on independent experimental crystal structures. Secondly, potential synthetic models of the hydrogenase active site are studied with molecular dynamics (MD) simulation. The structural and dynamic features of different model systems are thus explored.

4.1 Methods

To complete this study several model systems (depicted in Figure 4.1) were designed and implemented in CHARMM.

4.1.1 Model Systems

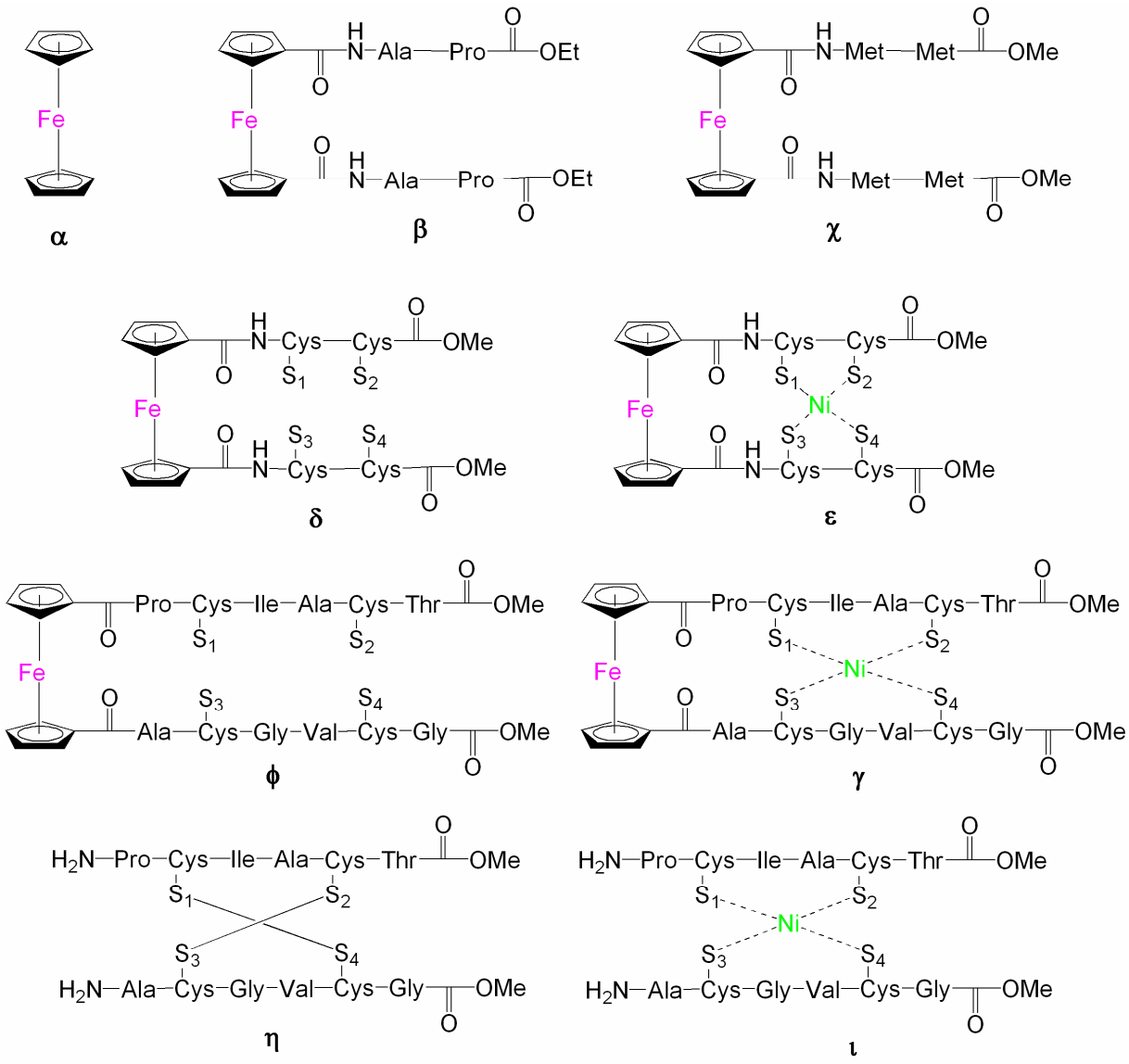

Figure 4.1 Schematic representation of the molecules studied

The structures of model systems **α** and **β** (see Figure 4.1) have been solved by X-ray diffraction, and thus these were chosen in order to test the parameter set. The initial coordinates were taken from the experimental X-ray structures obtained from the CCDC database [40, 62]. System **χ** was crystallized as a diastereomer mixture as described in Chapter 3. As the crystal structure obtained was a weighted average between two enantiomers, attempts of MD simulation were ambiguous. System **δ** was synthesized and fully characterized in our laboratory, but has not been crystallized yet. However, very strong spectroscopic evidence of its formation has been obtained (results not published). Model system **ε** represents the next step of the synthesis after system **δ**, in which the nickel atom is incorporated in the sulfur ligand pocket. The synthesis of this compound has not yet been successful. Model systems **ε**, **ϕ**, **γ**, **η**, **ι** were chosen as hydrogenase so as to examine any present unfavourable steric interactions that might hinder the synthesis of these compounds. In model systems **ϕ** and **γ**, the ferrocene is bonded to two 6-mer peptides with identical peptide sequences that surround the metal core in the natural active site of the [Ni-Fe]-Hydrogenase of *Desulfovibrio Gigas*. Systems **η** and **ι** were constructed with the same double 6-mer strands as models **ϕ** and **γ**, but without including ferrocene. Two disulfide bridges hold both strands together in the model **η** and a nickel atom has the same role in model **ι**. The model systems **δ**, **ε**, **ϕ**, **γ**, **η** were constructed starting from the crystal structures obtained from CCDC or PDB databases and corrected with the graphical interface software Insight II [143]. Model **ι** was constructed from the crystal structure of Hydrogenase from *Desulfovibrio Gigas* [12] by isolating the active site with the program Insight II.

4.1.2 Computational details

All molecular mechanics calculations were performed using the CHARMM package [139]. Except for the new parameters derived here, the existing CHARMM parameters were used [144]. The molecular mechanics minimizations were carried out using the Steepest Descent (SD) algorithm for initial minimization and then followed by the Adopted Basis Newton-Raphson (ABNR) minimization with a convergence criterion for the energy gradient of 10^{-6} kcal $mol^{-1}Å^{-1}$. A 13 Å cut-off distance was applied to non-bonded interactions using the CHARMM shifted potential [139].

In CHARMM, the potential energy of a molecule is considered to be the sum of contributions from the energy terms associated with bond stretching, angle bending,

dihedral rotation, out-of-plane bending, non-bonded, van der Waals and electrostatic interactions. Equation 2 gives the empirical potential energy function:

$$V\left(r^N\right) = \sum_{bonds} k_b\left(l-l_0\right)^2 + \sum_{ub} k_{ub}\left(s-s_0\right)^2 + \sum_{angles} k_\theta\left(\theta-\theta_0\right)^2 + \sum_{dihedrals} k_\chi\left(1+\cos(n\chi-\chi_0)\right) + \sum_{impropers} k\psi\left(\psi-\psi_0\right)^2 + \sum_{non-bonded} \varepsilon ij\left[\left(\frac{R_{ij}^{\min}}{r_{ij}}\right)^{12} - \left(\frac{R_{ij}^{\min}}{r_{ij}}\right)^{6}\right] + \left(\frac{q_i q_j}{D r_{ij}}\right) \qquad 2$$

where k_b, k_{ub}, k_θ, k_χ, k_ψ, are: the bond, Urey-Bradley, angle, dihedral and improper dihedral force constants, and l, s, θ, χ, ψ the bond lengths, Urey-Bradley 1-3 distances, dihedral angles and improper torsion angles, respectively. Non-bonded interactions between pairs of atoms are described by the Lennard-Jones (LJ) 6-12 term for the van der Waals and by the Coulomb interaction. $r_{i,j}$ and $\varepsilon_{i,j}$ are the distance between atom i and j at which the Lennard-Jones potential minimum and the depth of the potential well for the same pair of atoms, respectively. D is the effective dielectric constant which was set to 1 and q_i is the partial charge on atom i. Where missing, hydrogens were constructed using idealized geometric parameters from the HBUILD module in CHARMM.

All quantum mechanical (QM) calculations were performed with the NWChem 4.5 package [145]. The Hartree-Fock and the MP2 levels of theory provide poor results for the description of metallocenes [146]. On the other hand DFT calculations have been shown to give accurate results in the optimization of metallocene geometry [147]. Therefore, the structure optimizations and normal mode analyses of ferrocene and of ferrocene-1-(*L*)alanine-1'-(*L*)proline in vacuum were performed using the DFT/B3LYP level of theory with a triple zeta valence basis plus double polarization (DZVP2) [148]. The geometry optimizations were performed to a maximum gradient of 0.00045 a.u. and a root mean square (rms) gradient of 0.0003 a.u. in Cartesian coordinates. The frequencies were calculated numerically. A frequency scaling of 0.97 was used to compensate for the use of the harmonic approximation to the potential energy surface [149].

The partial atomic charges were calculated for the ferrocene structure with the CHELPG method [150] on the DZVP2-optimized structure. CHELPG employs a least squares fitting procedure to determine the set of atomic partial charges that best reproduces the quantum mechanical electrostatic potential at selected grid points. The grid was

extended to 3 Å from any of the atomic centers and the grid spacing was set to 0.1 Å. The grid points for which the QM electrostatic potential was evaluated and used in the fitting procedure of the partial atomic charges, all lie outside the van der Waals radii of the atoms and within a cut-off distance from the atomic centers. In this study, all grid points lying within a distance of less than 2 Å from any of the atomic centers were discarded. The fitting was subjected to the constraint that the sum of the charges should be equal to the net charge on the molecule. To ensure that the charges on symmetrically equivalent atoms are equal, additional constraints on the partial atomic charges were imposed during the fitting procedure: the iron was constrained to have a charge of +2 and each of the cyclopentadienyl groups were constrained to have a total charge of –1.

Following energy minimizations, the MD simulations were performed using the Verlet algorithm [151] and an integration time step of 0.001 ps. For the isolated molecule calculations, MD simulations were performed on the model systems (Figure 4.1) in the microcanonical (NVE) ensemble. Initially, the systems were heated to room temperature (298 K) in 5 K temperature increments. Then, equilibration for 10 ps using velocity rescaling followed, with a second phase of equilibration without velocity rescaling for another 10 ps at the same temperature. Finally, production dynamics followed for 1 μs at 298 K.

For calculations including the crystal environment, the MD simulations were performed at constant pressure and temperature with periodic boundary conditions in all directions. Starting from experimental coordinates and after minimization, the system was heated to the desired temperature in 5 K steps. Subsequently, the structures were equilibrated for 50 ps at this temperature using velocity rescaling followed by a second phase of equilibration without velocity rescaling for another 10 ps. Finally, production dynamics followed for 100 ns for the ferrocene-1-(D)alanine-(D)proline-1'-(D)alanine-(D)proline crystal and 10 ns for the ferrocene crystal. The unit cell dimensions were allowed to vary during both the energy minimization and the MD calculation.

4.1.3 Ferrocene Topology

The topology of bis-cyclopentadienyl complexes of the type $[M(Cp)_2]^{n+}$ requires the description of the metal-ligand π-bond. Four different approaches have been used in the literature to model ferrocene with MM (Figure 4.2).

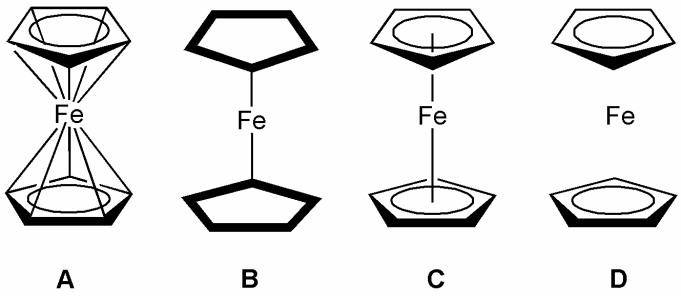

Figure 4.2 Representative scheme of the four different approaches to reproduce ferrocene molecular topology: (**A**) "Fe–C bonds" (**B**) "Rigid-Body" (**C**) "dummy atom" (**D**) "electrostatic"

The first method, uses 10 harmonic springs connecting each carbon of the Cp-ring to the iron centre (Figure 4.2 (**A**)) [152]. The second, called the 'Rigid-Body' approach treats the Cp ligand as a single pentagon rigid unit. The third method introduces a massless 'dummy' atom placed at the centre of geometry of each of the Cp rings. The metal is connected with a spring to the dummy atom, which is in turn connected with springs to the five carbon atoms around it (Figure 4.2 (**C**)). This dummy atom approach has been shown to give fairly accurate results for ferrocene simulation in CHARMM [153]. However, for this approach unrealistic force constants are needed to maintain the dummy atom at the centroid during minimization and spurious vibrational modes are generated when the force field is used to calculate the vibrational spectra [140]. The last method (Figure 4.2 (**D**)) is a non-bonded approach in which, the ferrocene aromatic moieties are held together by electrostatic and van der Waals interactions [141].

In the present work, a modified electrostatic model was implemented. It is known that due to the partly-covalent nature of the d-block metal-carbon bonds [154] the forces that maintain ferrocene cannot be solely described with MM Coulombic electrostatic interactions. Since current force fields are unable to describe fully the metal-ligand bond, an additional constraint is required. Therefore, in the present model the substituted Cp-rings and the iron atom interact with each other not only *via* non-bonded terms but also via harmonic springs hold together the Cp and iron moieties. All atoms on the Cp-rings were constrained to be equidistant from the central iron (0.64 Å) with a harmonic constraint force constant of 100 kcal $mol^{-1}Å^{-2}$.

For the models containing nickel, the special nature of Ni-S carbon bond cannot be only described by electrostatic interactions in MD simulations. Therefore, harmonic springs were introduced between each of the four sulfur atoms and the nickel atom. The

four sulfur atoms were constrained to be equidistant from the nickel core (2.25 Å) using 100 kcal $mol^{-1}Å^{-2}$ harmonic constraints. It was found that for model system **1**, the active site of hydrogenase, no additional spring was needed to hold the nickel atom in the chelating pocket.

4.1.4 Parameters refinement

The reliability of an MM calculation is dependent on the functional form of the potential energy function and on the numerical values of the parameters incorporated in it. Therefore, the values of the various parameters in Eq.1 have to be determined. For the derivation of the missing intramolecular parameters we used the AFMM method [155]. AFMM optimizes the parameters by adjusting the eigenvalues and eigenvectors of normal modes calculated with CHARMM to fit the normal modes calculated with high-level quantum chemistry methods. This method has been successfully used to derive parameters for a range of biologically-important compounds [156-159].

An efficient way to check simultaneously for both eigenvector orthonormality and frequency matching is to project each of the CHARMM eigenvectors onto the reference set of QM eigenvectors, to find the frequency, $\nu_j^{\max}$, that corresponds to the highest overlap, and to compare this frequency with the corresponding QM frequency, ν_i. In the ideal case $\nu_i = \nu_j^{\max}$ and $\overline{\chi_i^M} \cdot \overline{\chi_i^Q} = \delta_{ij}$ (where δ_{ij} is the Kroenecker delta, $\{\overline{\chi_i^M}\}$ is the set of the MM eigenvectors and $\{\overline{\chi_i^Q}\}$ is the reference set of eigenvectors). AFMM is based on iteratively minimizing the sum-of-squares, Y^2, of the deviations from the ideal situation as follows:

$$Y^2 = \sum_{3N-6} (\nu_i - \nu_j^{\max})^2 \qquad 3$$

where N is the number of atoms in the molecule and there are 3N-6 independent vibrational frequencies.

The LJ parameters $\varepsilon_{i,j}$ and $R_{i,j}$ depend mostly on the atomic properties and are relatively insensitive to changes in the molecular environment. Here, these were directly transferred from original CHARMM values and were not modified during refinement. Iron is parameterized in CHARMM and has been implemented in numerous heme calculations

[160, 161]. However, in CHARMM, the ε value of the LJ potential that governs the depth of the potential well was set to zero to avoid unwanted repulsive interactions between the iron and the heme group. This approximation, although valid within the heme group, cannot be used in the present study, where the repulsive and attractive van der Waals interactions within ferrocene are of crucial importance. Sets of non-bonded parameters for the iron and nickel were supplied by Bredenberg (personal communication – unpublished results) [162]. The nickel-coordination equilibrium bonds, angles and dihedrals were derived from the available crystal structure [163]. Nickel can adopt numerous geometries [164-170], but for the current study, only the hydrogenase active site conformation was taken into account. Equilibrium values for bonds (l_0), angles (θ_o) and dihedrals (χ_0) that were not existing in the original CHARMM force field parameter file [171, 172] were determined from the crystal structure and were not further optimized. Before refinement of the unknown parameters, an initial set of parameters was determined, based on similar, already-existing CHARMM parameters and on chemical intuition, carefully considering the equilibrium values and hybridization of the atoms.

A desirable property of an MM force field is the transferability of the parameter set. Therefore, when designing a new parameter set, the addition of new atom types to the force field should be limited to those specific cases in which existing type cannot be used. Because of the particular geometry of present ferrocene compounds and the characteristic distribution of the partial charges of the atoms along the Cp-rings, it was found necessary to introduce a new CHARMM atom type (CA2) for the carbons in ferrocene belonging to five-membered aromatic rings. The van der Waals parameters for the new atom type CA2 were taken to be the same as those for aromatic carbons (type CA). The nickel atom type (Ni) also did not exist in CHARMM and was therefore added with a partial charge of +2 (see Appendix). For the nickel coordination centre, the existing cysteine residue (CYS) was used as a starting point to develop a new cysteine residue (CYN) (see Appendix), which was adapted to a cysteine that can accommodate a coordinating bond with nickel. This residue was used only for the model systems containing nickel. In the CYN residue, the proton of the thiol group was removed and thus the total charge for this residue was set to -0.50. The rest of the negative charge was transferred to the sulfur atom, which was set to -0.57.

For the hydrogen atoms of the Cp-ring, the existing atom type HP was used with a modified partial charge (see Appendix) as calculated from QM. The charge of the oxygen atoms on the carbonyl group of the first amide bond connected to ferrocene was changed

from -0.51 to -0.61 to maintain the total charge at -1 for the Cp-ring residue (FEC residue, see Appendix). It was therefore necessary to determine new parameters also for the energy terms involving the newly-created atom types.

The initial parameter set was used for minimization and calculation of normal modes (eigenvalues and eigenvectors) with CHARMM. The parameters were optimized by comparing the normal modes thus obtained with reference normal modes calculated with the quantum chemistry methods, by employing the AFMM method [157]. AFMM uses an iterative procedure to refine the parameters to reproduce the quantum-chemical reference normal modes (both eigenvalues and eigenvectors). An efficient way to check simultaneously for both orthonormality and frequency matching is to project each of the CHARMM eigenvectors onto the reference set of eigenvectors and to find the frequency $v_j^{\max}$ corresponding to the highest projection. Plotting this frequency against the corresponding frequency v_i, would in the ideal case, give a one-to-one relationship: $v_i/v_j^{\max}$. Points that deviate from the ideal plot may indicate exchanged or mismatched frequencies. AFMM is based on iteratively minimizing the sum-of-squares, Y^2 of the deviations from the ideal situation as follows:

$$\sigma = \sqrt{\frac{\sum_{3N-6}\left(\nu_i - \nu_j^{\max}\right)^2}{3N-6}} \qquad 4$$

During the automated parameter refinement, the range over which force constants were allowed to vary was $10 - 500$ kcal mol^{-1}Å^{-2} for bonds, $1 - 200$ kcal mol^{-1}rad^{-2} for angles, $0.1 - 100$ kcal mol^{-1} for dihedrals and $0.1 - 100$ kcal mol^{-1}rad^{-2} for improper torsions. It was observed that by restarting the calculation by using the optimized force constants that were obtained from the previous optimization and by limiting the range each time around the new optimized parameter value, the normal-mode matching was significantly improved. In this manner the optimizations for all force constants were ran four times. For the first run, the convergence of the function Y^2 was set to 10000 steps for which the value of Y^2 remained unchanged. The last three optimizations were allowed to run until the value of Y^2 remained constant for at least 1000 steps. The root-mean-square deviation, σ, from the reference case was also calculated.

4.2 Parameterization

4.2.1 Parameterization of ferrocene-1(*L*)proline-1'(*L*)alanine

For the synthesis of a ferrocene-bearing peptide, a ferrocene carboxylic acid is connected to the N-termini of two amino acids *via* a peptide bond. This special peptide bond has the same topology for all amino acids except for proline. Thus, to derive a complete parameter set for the present purposes, ferrocene-1-(*L*)proline-1'-(*L*)alanine (Figure 4.3 (A)) was chosen for the parameterization of ferrocene-bearing peptides as this compound contains both proline and non-proline connections to ferrocene.

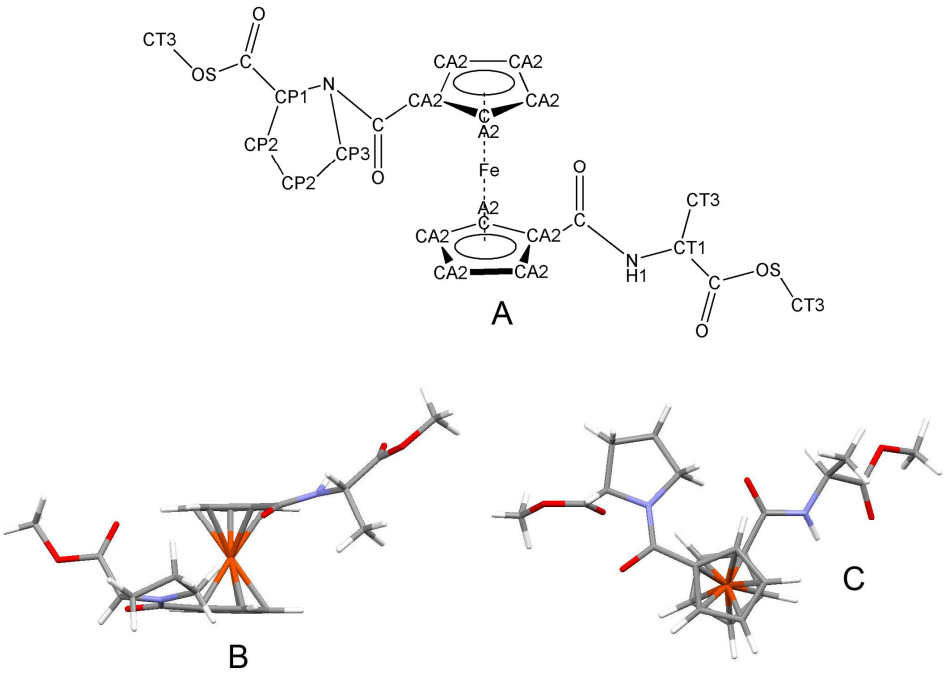

Figure 4.3 (**A**) Topology of ferrocene-1-proline-1'-alanine showing the CHARMM atom types, (**B**), (**C**) its DFT/B3LYP energy-minimized structure viewed along the *b* and the *c* axes, respectively

Parameters for ferrocene-1-(*L*)proline-1'-(*L*)alanine were developed using a two-step procedure. Firstly, the charges on ferrocene were calculated on the QM optimized structure as described in "Methods". The AFMM method was then used to obtain a complete set of parameters. The resulting ν^{max} versus ν_i plot is shown in Figure 4.4. The corresponding value of $\boldsymbol{\sigma = 77.2\ cm^{-1}}$ is within the range of previous benchmark studies [155, 159].

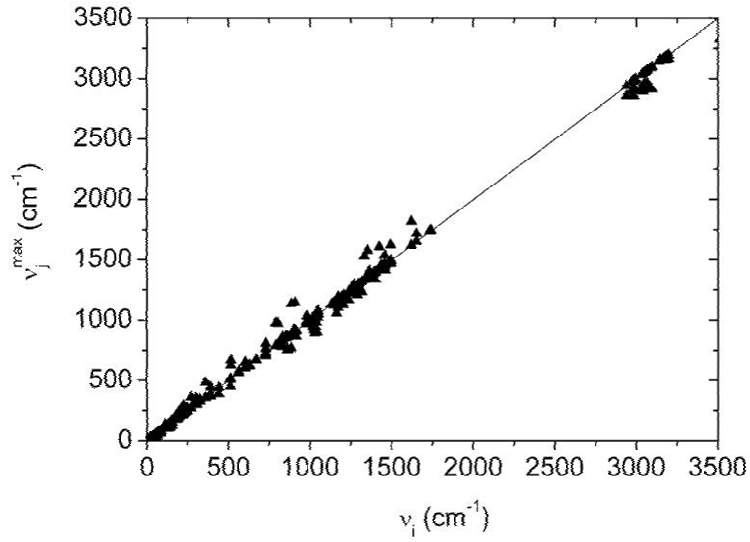

Figure 4.4 Frequency-matching plot (ν^{max} *vs.* ν_i) for ferrocene-1-alanine-1'-proline. The line is the ideal case where $\nu^{max} = \nu_i$, *i.e.* of perfectly matched frequencies and eigenvector projections. Symbols refer to optimized parameters. (σ = 77.2 cm^{-1})

Atom type assignments and atomic partial charges, as well as the parameters obtained from AFMM are listed in the Appendix. Only the newly-derived CHARMM parameters are reported.

4.3 Testing of the parameters

4.3.1 Fc-(D-Ala-D-Pro)$_2$ crystal simulations

Final testing of a parameter set should be performed against independent experimental and/or theoretical data. The present force field was tested on the available crystal structure of Fc-(*D*-Ala-*D*-Pro-OEt)$_2$, a ferrocene-peptide derivative [111-113]. MD simulations of the isolated molecule and its enantiomer, Fc-(*L*-Ala-*L*-Pro-OEt)$_2$, were performed.

Fc-(D-Ala-D-Pro-OEt)$_2$ crystallizes in a tetragonal crystal, I-centered lattice with group symmetry $I4_1$ and with four molecules into the unit cell. The crystal structure was determined at 296 K. The MD calculations were performed for the whole crystal using periodic boundary conditions. The crystal was defined as tetragonal and the unit cell dimensions were allowed to vary during both the energy minimization and the MD

calculation. The energy minimized and the experimental cell vectors are reported in Table 4.1 as well as their average values after 0.1 μs MD. The crystal lattice parameters are conserved over the simulation. After minimization, the cell volume was computed to be **3175.9 Å^3**, within 0.001 % of the experimental volume of **3175.6 Å^3**.

Table 4.1 Unit cell dimensions of Fc-(*D*-Ala-*D*-Pro-OEt)$_2$ crystal structure

Terms	Experimental [a]	Minimized [b]	Dynamics [c]
a	14.573(2) Å	14.466 Å	14.8(1) Å
b	14.573(2) Å	14.466 Å	14.8(1) Å
c	14.953(2) Å	15.176 Å	15.2(2) Å
α	90°	90°	90°
β	90°	90°	90°
γ	90°	90°	90°

[(a)] Measured on the crystal structure geometry [(b)] Measured on the minimized crystal unit cell after 10000 steepest descent steps followed by 10000 Newton-Raphson minimization steps [(c)] Mean values calculated over 0.1 μs dynamics at 298 K using the new CHARMM force field. Standard deviation in parentheses

Ferrocene-bearing dipeptide chains are known to adopt a chiral organization in the solid state *via* a novel H-bond pattern, which interconnects both peptide strands. As already explained, two kinds of intramolecular H-bond patterns have been experimentally observed: the "Herrick" [61] conformation, where two H-bonds connecting both strands and the "van Staveren" [62] conformation where only one H-bond connects the peptide strands. When both substituents are trans, no intramolecular H-bonds are observed and this was coined as the "open" conformation [64]. The experimentally-observed H-bond pattern in the Fc-(*D*-Ala-*D*-Pro-OEt)$_2$ crystal is of Herrick's type. This H-bond pattern introduces two C_2-symmetric intramolecular hydrogen bonds between the CO of alanine and the NH of the other alanine of each dipeptide chain thus introduces a chiral structure. Although, due to the free rotation of the Cp-rings a wide range of relative orientations is possible. The two dipeptide chains are always arrayed in the same direction during the MD, as two intramolecular hydrogen bonds induce an ordered structure.

To examine the stability of the intramolecular H-bond patterns, the distances between the hydrogen-bonded heavy atoms (O…N distance) were calculated. The MD H-bonds are slightly longer (0.2 Å on average) than those reported experimentally. However, the H-bonding pattern remains stable throughout the 100 ns simulation. The time series of the hydrogen-bond, namely N - O distances, is plotted in Figure 4.5.

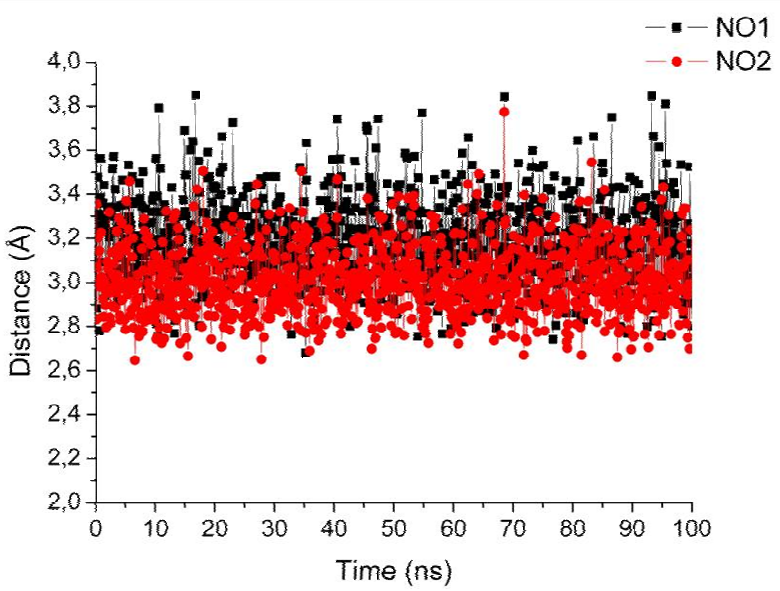

Figure 4.5 Time series of d_1(N-O) (here NO1), where N is the nitrogen of the first amide bond of the first peptide strand and O the carbonyl oxygen of the second amide bond of the second peptide strand. For d_2(N-O) (here NO2) distances N is the corresponding nitrogen of the second peptide and O the carbonyl oxygen of the first peptide strand

Another interesting feature of this crystal is that the ferrocene moieties are packed in a helically-ordered arrangement with one turn of 14.95 Å pitch height (see Figure 4.6 (**c**)), within which the distance between the closest ferrocene unit is 4.46 Å. The helical pitch was monitored during the MD simulations and is plotted as a time series in Figure 4.6 (**d**). The mean value of the pitch height was 14.24 ± 0.15 Å, a value within 5% of the experimentally-measured helical pitch.

A further feature is that the ferrocene adopts a herringbone motif arrangement, in which the proline and the ethyl ester moieties individually form the columns (Figure 4.6 (**a**) and (**b**)). The dipeptide chains (-Ala-Pro-OEt) induce this molecular aggregation through the stacking of the intramolecular H-bond sites formed between the two alanines and also through the stacking of the hydrophobic proline rings. In this way, both the hydrophilic and the hydrophobic parts of molecule stack to form the columns of the herringbone motif. The herringbone motif was preserved throughout the MD simulation. Both the proline and ethyl ester moieties remain stacked during the dynamics (see Figure 4.6 (b)). The supramolecular assembly remained stable throughout the 100 ns simulation.

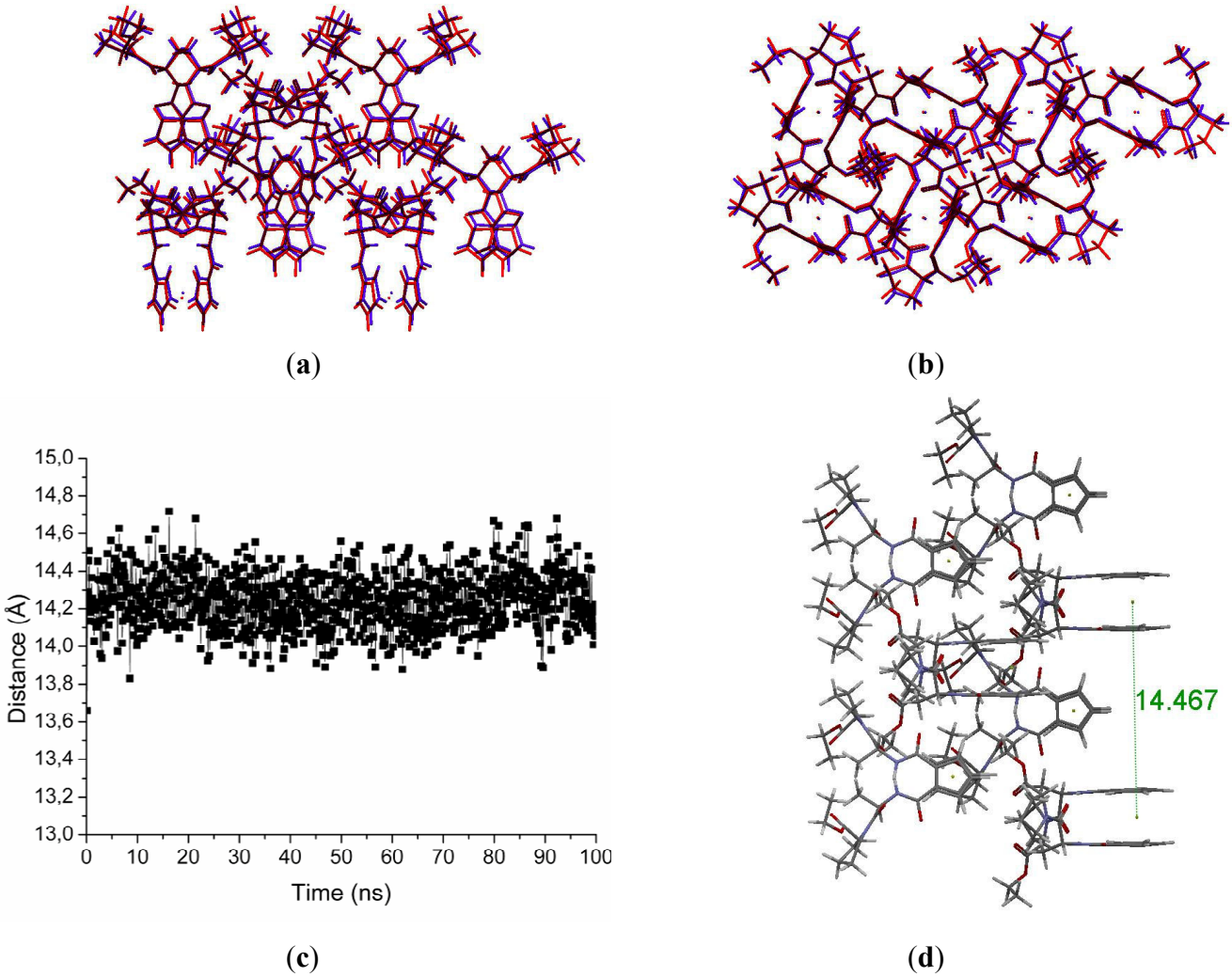

Figure 4.6 (**a**) and (**b**) superimposition one and a half unit cell of the minimized and experimental structures [113] seen along the *b* and the *c* axes, respectively. (**c**) Time series of the helical pitch during 100 ns MD (**d**) Crystal seen along the a axis showing the helical pitch.

As shown on Figure 4.6, the minimized and experimental structures are very similar. The RMS deviation calculated on the four molecules of the primary cell was found to be **1.35 Å** (for this calculation, all non-hydrogen atoms were taken into account). The atoms of the side chains of the dipeptide and the C-termini of both strands are flexible and exhibit more freedom of movement than the backbone atoms, as evidenced by the crystallographic temperature factors (B-factors),which are larger (10 to 15 $Å^2$) in the side chain than in the backbone atoms (2 to 9 $Å^2$). The RMSD between the calculated and experimental backbone atoms structures of a single molecule in the crystal lattice was **0.32 Å**.

The atoms of the C-termination of the molecule are more flexible than the atoms that are directly attached to Cp-ring atoms of ferrocene. Therefore, they are expected to exhibit more freedom of movement, corresponding to spreading of the probability distribution of each atom over a small region of space. Diffraction is affected by this spreading out of the

atomic positions, as manifested by temperature factors (B-factors), assigned to each atom. Assuming isotropic, harmonic dynamics, the B-factors is given by the Equation 5:

$$B_{eq} = \frac{8}{3}\pi^2 \langle u^2 \rangle \qquad 5$$

where $<u^2>$ is the mean-square fluctuation of the positif an atom.

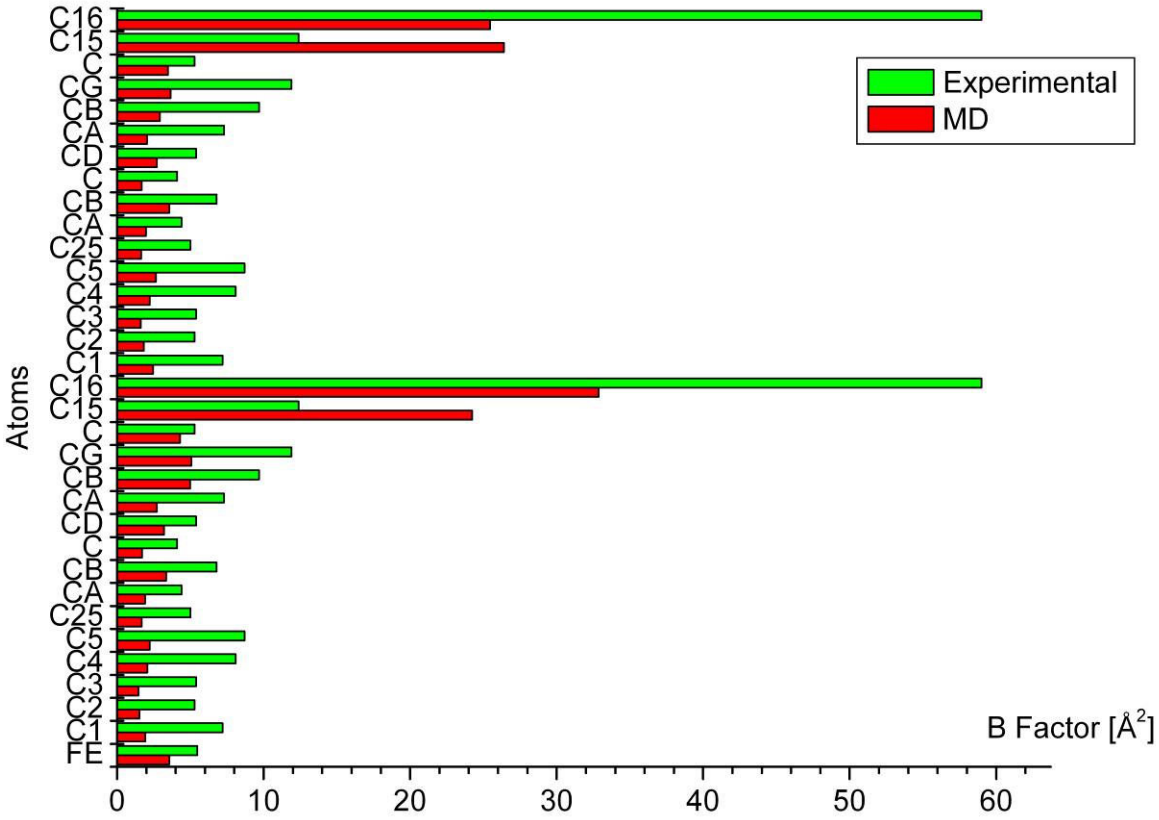

Figure 4.7 Experimental vs. the calculated B-factors for the carbon and iron atoms.

In Figure 4.7, the average experimental and calculated isotropic B-factors for the carbon and the iron atoms of Fc-(D-Ala-D-Pro-OEt)$_2$. This representation indicates parts of the molecule that are particularly flexible and parts that are particularly rigid. The C-terminal B-factors are larger and more varied than those of the Cp-ring atoms. The B-factors obtained from MD are smaller than those experimentally derived. These differences might arise from the use of isotropic, harmonic approximation in the experimental refinement. Nevertheless, general trends are respected.

4.3.2 Fc-(D-Ala-D-Pro)$_2$ and Fc-(L-Ala-L-Pro)$_2$ single molecules in vacuum

To assess the stability of Fc-(*D*-Ala-*D*-Pro-OEt)$_2$ and Fc-(*L*-Ala-*L*-Pro-OEt)$_2$ in vacuum and to estimate the role of the crystal environment in conferring the stable intramolecular H-bond pattern in these molecules, a 1 μs MD simulation of the isolated molecules was performed. As these two structures are enantiomers all the results have been found to be equivalent for the two structures. For simplicity, only the results for the *D* conformation are shown.

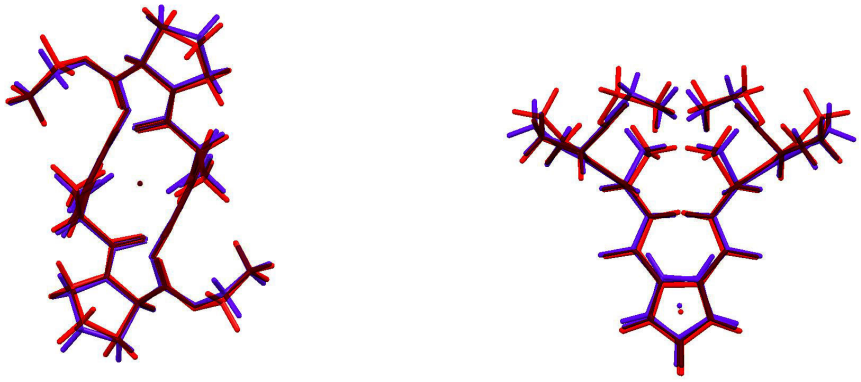

Figure 4.8 Superimposed minimized single molecule and crystal structure of ferrocene-1,[(D)alanine-(D)proline]-1',[(D)-alanine-(D)proline] [113], along the *a* and *c* axis respectively. The vacuum MD calculations were performed for both the *L* and *D* isomers.

As shown in Figure 4.8, the superimposition of minimized and experimental structures is very close. The RMSD of the peptide backbone atoms with respect to the crystal structure was found to be 0.58 ± 0.14Å.

Table 4.2 Geometrical features of hydrogen bond pattern for Fc-Ala-Pro

H-bonds	d_1(H-O) [Å]	d_2(H-O) [Å]	d_1(N-O) [Å]	d_2(N-O) [Å]	a_1(N-H-O) [deg]	a_2(N-H-O) [deg]
Experimental [a]	2.053	2.053	2.98(1)	2.98(1)	146(5)	146(5)
Crystal MD [b]	2.2(2)	2.0(2)	3.2(2)	3.0(2)	158(10)	162(9)
Vacuum MD [c]	2.1(2)	2.1(2)	3.0(2)	3.0(2)	153(11)	153(11)

[(a)] Average distances measured on the crystal structure [113], [(b),(c)] distances calculated over the simulations, in parentheses the standard deviation.

The geometrical properties of the two intramolecular H-bonds were monitored during the MD and the results are shown in Table 4.2. In , the H-bond, distances are shown

as a time series over 1 μs. The MD reproduces the *C2*-symmetric intramolecular H-bonding network to within **2 %** of the experimentally-observed distances. The H-bond pattern remains stable over the simulation and is not significantly affected by the absence of the crystal environment. Again, although a wide range of relative conformations and orientations of the dipeptide chains are in principle possible, due to the free rotation of the Cp rings, the hydrogen bonds are not broken at any time of the simulation. This implies that these interactions confer additional stability to the complex and that the thermal motions at room temperature are not strong enough to break these bonds.

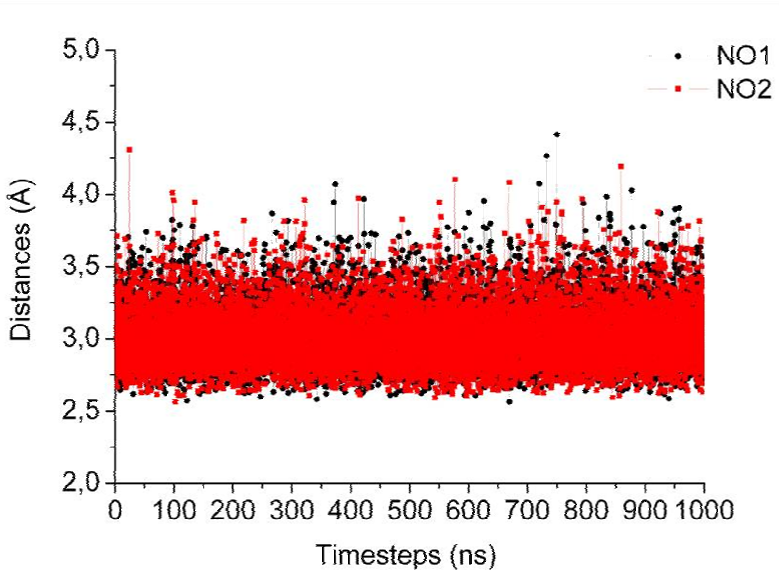

Figure 4.9 Time series of d_1(N-O) (here NO1), where N is the nitrogen of the first amide bond of the first peptide strand and O the oxygen of the second amide bond of the second peptide strand. For d_2(N-O) (here NO2) distances N is the corresponding nitrogen of the second peptide and O the oxygen of the first peptide strand

This result is in good agreement with the experimental solid-state structure observed in the crystal, and with liquid-phase experiments such as NMR studies. It has been reported that in the ^{1}H NMR spectra of Fc-(Ala-Pro)$_2$ only one kind of N-H resonance was detected at a lower field (8.96 ppm) (the two H-bonds are equivalent because of the plane of symmetry) [110]. Moreover, this N-H resonance was not perturbed by the addition of aliquots of DMSO-d_6 to $CDCl_3$. This indicates that the two identical intramolecular hydrogen bonds between the dipeptide chains, observed during the simulation, are present also in the solution phase.

4.3.3 Fc-[(D)Met-(L)Met]$_2$ in the crystal lattice

Fc-[(*D*)Met-(*L*)Met]$_2$ crystallizes in orthorhombic lattice symmetry with the space group $P2_12_12_1$. The unit cell contains four molecules. The crystal data was collected at T = 100 K. For this study, the newly-developed parameter set was tested on an enantiomerically pure compound, built with only L-methionine and based on the data of the experimental crystal lattice. The crystal was obtained by applying the symmetry operations using the experimental unit cell vectors and starting from an enantiomerically pure molecule. Cell vectors calculated after minimization are reported in Figure 4.10 and Table 6, along with the experimental and MD results. The size and the shape of the crystal unit cell are mainly respected. However an expansion of about **2 Å** was observed along the b axis and a slight reduction of **1 Å** along the a axis. The volume of the unit cell was also monitored as a time series and was shown to decrease along the MD run. The energy of the system was calculated after each minimization. The energy of the crystal lattice shows a convergence over the different minimization steps (Figure 4.10). The newly-developed parameter set allowed the disordered system to escape from the local minimum.

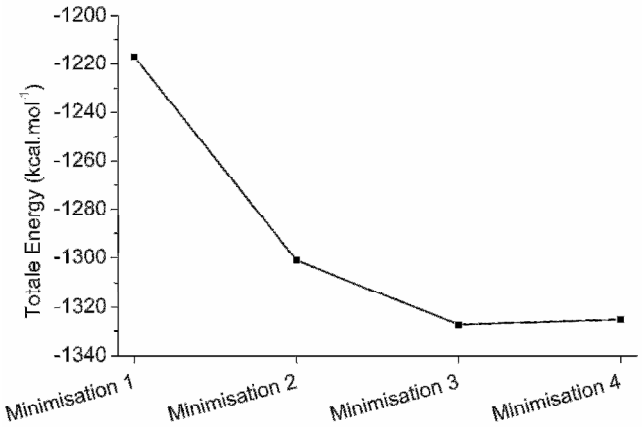

Figure 4.10 Total energy calculated after the four sequential minimizations of the crystal lattice

The infrared (IR) spectrum of **25d** measured in dichloromethane [119, 173], shows 3 amide bands for N-H stretching over 3500 cm^{-1} which provide evidence for three different kinds of hydrogen atom and therefore, three different conformations (Figure 4.11 (**b**)). Circular Dichroism (CD) spectra also show a mixture of H-bond interactions, (Figure 4.11 (**c**)) [173]. In the solid state, an enantiomeric mixture of Fc-(*L*-Met-*L*-Met)$_2$, Fc-(*D*-Met-*L*-Met)$_2$ and (Met-*D*-Met-*L*)-Fc-(*D*-Met-*L*-Met) is observed. Two of these conformers

co-crystallized in the same crystal lattice (ca. 20% (Met-*L*-Met-*L*)-Fc-(*D*-Met-*L*-Met) and 80% Fc-(*D*-Met-*L*-Met)$_2$) [173]. The X-ray structure we obtained is a weighted average between these enantiomers. The presence of these two structures during the measurement leads to uncertainty in the position of the peptide atoms, and therefore the crystal lattice obtained was disordered.

The above experimental observations are clear evidence of different conformations, as is the simulation. However, no clear trends can be deducted from the calculation. Further investigation may involve a mixture of racemate in order to increase the quality of the model.

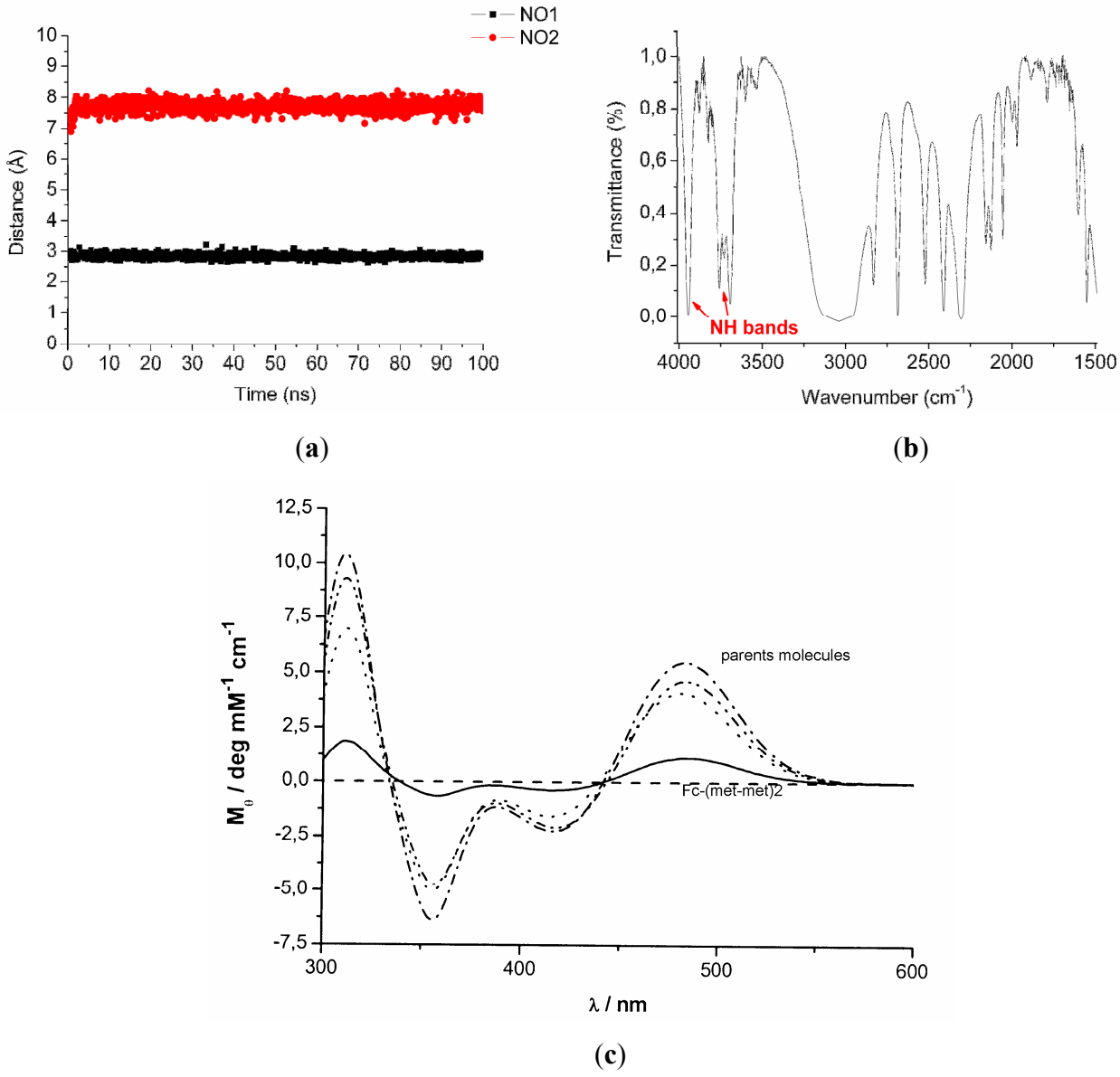

Figure 4.11 (**a**) Time series of intermolecular H-bonds over 1 µs dynamics (**b**) Experimental IR spectra (**c**) Experimental CD spectra

Table 4.3 Unit cell dimension of Fc-(*D*-Met-*L*-Met)$_2$ crystal structure

Terms	Experimental [a]	Minimized [b]	Heated [b]	Rescaled [b]	Dynamics [c]
a	19.88 Å	18.70 Å	18.69 Å	18.9(7) Å	18.5(3) Å
b	11.33 Å	12.82 Å	13.15 Å	13.3(2) Å	13.2(1) Å
c	17.60 Å	17.70 Å	17.31 Å	18.2(7) Å	17.9(4) Å
α	90°	90°	90°	90°	90°
β	90°	90°	90°	90°	90°
γ	90°	90°	90°	90°	90°

([a]) Measured on the crystal structure geometry ([b]) Measured on the fourth minimized, heated, rescaled crystal unit cell ([c]) Measured after 0.1 μs dynamics at 100 K. Standard deviation in parentheses

4.3.4 Fc-[(D)Met-(L)Met]$_2$ single molecule in vacuum

As the crystal, simulation cannot be correlated to the experimental results because they are too ambiguous. The single molecule simulation was tried on Fc-[(D)Met-(L)Met]$_2$. The simulation was performed at the temperature of 100 K. A time series of the H-bond pattern is shown in Figure 4.12. The backbone RMSD between calculated isolated molecule and experimental structures was **1.2 Å** (for this calculation, side chain atoms were removed). This confirms a poor structural similarity between the simulation and experimental results.

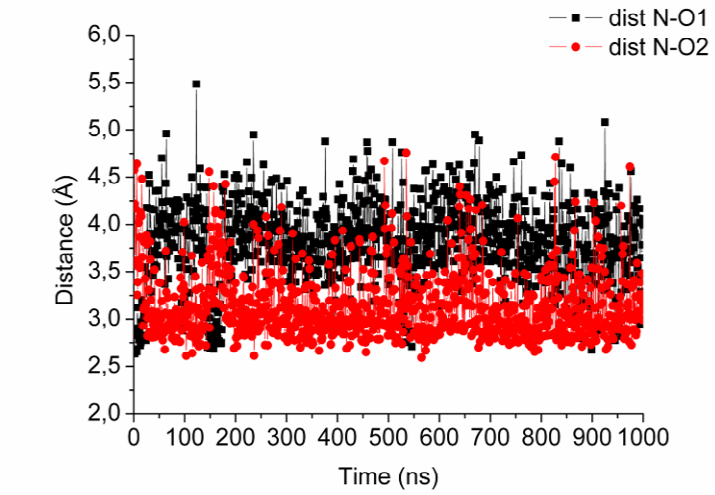

(a)

(**b**) (**c**)

Figure 4.12 (**a**) time series of intermolecular H-bonds over 1 μs dynamics on the single molecule simulation (**b**) and (**c**) top and side views of the minimized structure of the derivative ferrocene-1-[(*D*)methionine-(*L*)methionine]-1'-[(*D*)-methionine-(*L*)methionine]

Table 4.4 H-bond geometrical properties; experiment versus calculation, d_1(N-O) represents NO1 d_2(N-O) represents NO2

H-bonds	d_1(H-O) [Å]	d_2(H-O) [Å]	d_1(N-O) [Å]	d_2(N-O) [Å]	a_1(N-H-O) [deg]	a_2(N-H-O) [deg]
Experimental [a]	2.152	2.017	2.992	2.913	137.8	159.6
Minimized	2.029	1.896	2.862	2.889	138.8	172.2
Calculated [b]	3.3(5)	2.3(4)	3.8(4)	3.1(4)	128(3)	144(13)

([a]) average distances measured on the crystal structure, ([b]) distances calculated from mean structures on a 1 μs dynamics scale. Standard deviation in parentheses

An interesting feature is observed; during the heating, an H-bond, d_1(N-O), is unstable and shows a deviation that can reach up to 1 Å from its starting position (Figure 4.12). Here again, accuracy of the simulation cannot be properly evaluated because of the ambiguous nature of the experimental results.

4.3.5 Ferrocene crystal simulation

The new force field was further tested by performing an energy minimization and MD simulation of ferrocene in its crystalline state. This crystal was obtained by crystallization at room temperature and determined at 173 K. It has a monoclinic symmetry and belongs to the P21/a space group with two molecules of ferrocene in the unit cell. The cohesion of the crystal is maintained by π-stacking of the Cp unit along the *a* and *b* axes. The MD calculations were performed for the whole crystal using periodic boundary conditions at T = 173 K for 10 ns dynamic. The unit cell dimensions were allowed to vary during both the energy minimization and the MD calculation. The energy minimized, and

the average dynamics cell vectors are reported in Table 4.5 along with the experimental values. The Root Mean Square Deviation (RMSD) was not calculated as the Cp rings are very mobile due to their free rotation along the Cp-Fe axis. To the best of our knowledge this is the first time that the ferrocene crystal packing has been modeled. However, the dynamics of the ferrocene lattice at 173 K, as well as the parameters measured as the volume and crystal cell vectors (shown in Table 4.5) show that the crystal changes (expands) along the run. This variation could be explained by the fact that ferrocene is known to adopt different geometries depending on the experimental conditions of the crystal grown and the temperature; a transition state occurs around 164 K. Seiler and Dunitz report an orthorhombic geometry at 98 K [174], an F-centered triclinic cell at 101 K [175], and a monoclinic symmetry at 173 K.

Table 4.5 Unit cell dimensions of the ferrocene crystal structure

Terms	Experimental [a]	Minimized [b]	Dynamics [c]
a	10.45 Å	12.95 Å	11.2(4) Å
b	7.58 Å	6.94 Å	7.1(3) Å
c	5.81 Å	5.82 Å	6.2(3) Å
α	90°	90°	90°
β	120.9°	117.5°	124(2)°
γ	90°	90°	90°

([a]) measured on the experimental crystal [174] ([b]) measured on the minimized crystal unit cell after 10000 Steepest Descent followed by 10000 Newton-Raphson minimization steps, ([c]) mean value calculated over 10ns dynamics at 173 K. Standard deviation in parentheses.

It is known that, even at low temperatures, at which Cp rotation is hindered, ferrocene adopts an eclipsed conformation rather than a staggered one. This is because of the C_{5h} symmetry, which corresponds to the eclipsed conformation, confers an additional stability compared to the D_5 symmetry of the staggered conformation. According to solid state studies, the barrier for the internal rotation along the axis connecting the centers of the two Cp rings was estimated to be 3.8 ± 1.3 kJ.mol^{-1} (ca. 0.9 ± 0.3 kcal.mol^{-1}) [176]. To date activation energies for rotation have only been determined in the solid state or from relaxation measurements and these energies appear to be dominated by intermolecular interactions rather than internal electronic constraints [176]. The energy difference between the staggered and the eclipsed form of a single molecule of ferrocene calculated in vacuum was found to be 0.05 kcal.mol^{-1}. This value is, by a factor of 20, smaller than the

experimentally-observed barrier. Precision of energy calculation in CHARMM are around 0.1 kcal.mol^{-1}, this value measured for the rotational barrier is below the accuracy of the calculator and can therefore not be trust. However, the same rotational energy barrier calculation for a molecule of ferrocene in the crystal environment yielded an energy difference of 0.7 kcal.mol^{-1} between the staggered and eclipsed conformations. Table 4 contains the calculated energies associated with the two forms. This result demonstrates the importance of the environment on this rotational barrier. Decomposition of the rotational energy barrier in the ferrocene crystal (see Table 4.6) shows that the van der Waals interactions, rather than electrostatics, govern the rotational barrier of the Cp-ring.

Table 4.6 Comparison of the different energy terms for the eclipsed and staggered conformation of ferrocene

	Bond [kcal.mol^{-1}]	**Angle [kcal.mol^{-1}]**	**Torsion [kcal.mol^{-1}]**	**VDW [kcal.mol^{-1}]**	**Elect. [kcal.mol^{-1}]**	**Total [kcal.mol^{-1}]**
Eclipsed [a]	0.245	0.003	1.893	160.391	-315.973	-153.441
Staggered [a]	0.245	0.003	1.893	160.423	-315.955	-153.391
Eclipsed [b]	0.297	0.021	1.121	157.839	-246.119	-86.841
Staggered [b]	0.297	0.021	1.121	158.471	-246.118	-86.208

([a]) Energy term of a single molecule of ferrocene in vacuum ([b]) Energy terms of a single molecule of ferrocene in the crystal lattice

Results obtained for the validation of the parameter set are very encouraging especially for Fc-(*D*-Ala-*D*-Pro-OEt)$_2$. In the case For the Fc-(*D*-Met-*L*-Met-OMe)$_2$ and ferrocene alone, the nature of the experimental results prevent us to compare the simulation and the experiment. Nevertheless, the quality of the parameter set is assumed to be good enough to use it for prediction about new unsynthesized model systems.

4.4 Prediction

4.4.1 Model systems δ, ε, ϕ and γ

General structural and geometrical features of the models β, χ, δ, ε, ϕ and γ characteristics for the shape of ferrocene, such as the distance between the Cp-ring carbons and the iron and dihedrals in the Cp-ring, and for the shape of H-bond pattern between both peptide stands (bond length, angle dihedrals of the H-bonds) are shown in Table 4.7.

Table 4.7 Summary of geometrical data monitored over 1 μs vacuum MD

Models	C_{Cp}-Fe [Å]	H-O [Å]	H-O [Å]	N-H-O [deg]	N-H-O [deg]	O-C-N [deg]	C_{Cp}-C_{Cp}-C_{Cp}-C_{Cp} [deg]	C_{Cp}-C_{Cp}-C-N [deg]
β	2.06(3)	2.1(2)	2.1(2)	153°(11)	153°(11)	119°(3)	0°(3)	3°(5)
β'[(a)]	2.06	2.053	2.053	145.5°	145.5°	119°	0.3°	5.2°
χ	2.07(2)	2.2(5)	-[(b)]	114°(11)	-[(b)]	118°(3)	0°(2)	7°(5)
χ'[(a)]	2.06	2.02	-[(b)]	138.2°	-[(b)]	121.9°	0.2°	0.6°
δ	2.07(2)	2.1(3)	2.1(3)	149°(12)	149°(12)	119°(3)	0°(2)	1°(3)
ε	2.08(2)	2.2(2)	-[(b)]	150°(11)	-[(b)]	119°(4)	0°(2)	6°(6)
ϕ	2.05(2)	2.4(3)	-[b]	134°(14)	-[b]	122°(3)	0°(2)	7°(6)
γ	2.10(2)	-[(b)]	-[(b)]	-[(b)]	-[(b)]	119°(3)	1°(3)	7°(5)

[(a)] experimental data [62] [(b)] no H-bond observed. Standard deviations in parentheses

From comparison of models β with β' and χ with χ' one can conclude that the calculated geometries are in overall good agreement with the experimental geometries observed in ferrocene-peptides. In all instances both Cp-rings remained parallel and the first amide bond attached to the ferrocene remained coplanar with the Cp-ring. It is interesting to note that model δ (2-mer peptide) has one intramolecular H-bond, while the longer peptide in model ϕ (6-mer peptide) has none. This is probably due to the steric hindrance resulting in the proximity of two 6-mer peptides strands. The size of the peptide might have an effect in the H-bond formation and potentially on the degree of freedom of the strands.

Model δ forms two intramolecular H-bonds, while model ε forms just one, the only difference between these two structures being the nickel atom chelated by the sulfur atoms.

A similar difference is observed in comparing models **ϕ** and **γ** (model **ϕ** form one intramolecular H-bond and model **γ** none), as no H-bond forms between the two peptide strands when nickel is incorporated. The formation of a chelating pocket for nickel hinders the formation of H-bond between the two strands (see Table 4.7). Nevertheless, it is encouraging to see that in model system **δ**, which is synthetically the ligand for nickel complexation, the two strands remain H-bonded, since the open conformation would have meant the unfeasibility of the chelation of metal between these both strands. The size and the shape of this chelating pocket are studied below.

Model system **δ** was subsequently synthesized and corresponds to the derivative **33d** (numbering of this thesis). Unfortunately, it has not yet been crystallized. The calculation on compound **33d** (Figure 4.13 (**b**)) shows that two Herrick-type H-bonds are formed. We therefore performed an NMR experiment and a CD measurement (Circular Dichroism) on compound **δ** to validate this result. From the downfield shift of the amide protons (Figure 4.14 (**c**)) observed in NMR, we were able to deduct that two types of proton amide displacement are observed in this spectrum (δ = 8.22 ppm and δ = 7.46 ppm). This means that there are only two different kinds of amide bonds present, probably the one connected to ferrocene and the one connecting two cysteines in a dipeptide. Therefore, only one type of H-bonding is present in the compound. This NMR proton downfield shift is typical for the Herrick-type H-bond. On the CD spectra shown in Figure 4.14 (**d**), a positive Cotton effect around 485 nm is observed. This is known to be characteristics from a Herrick type H-bond pattern between both peptide strands in this type of derivatives. These two experimental measurements clearly show that compound **33d** adopts a Herrick conformation in solution. This is consistent with the calculations, since the simulation predicts a Herrick conformation for this model in vacuum.

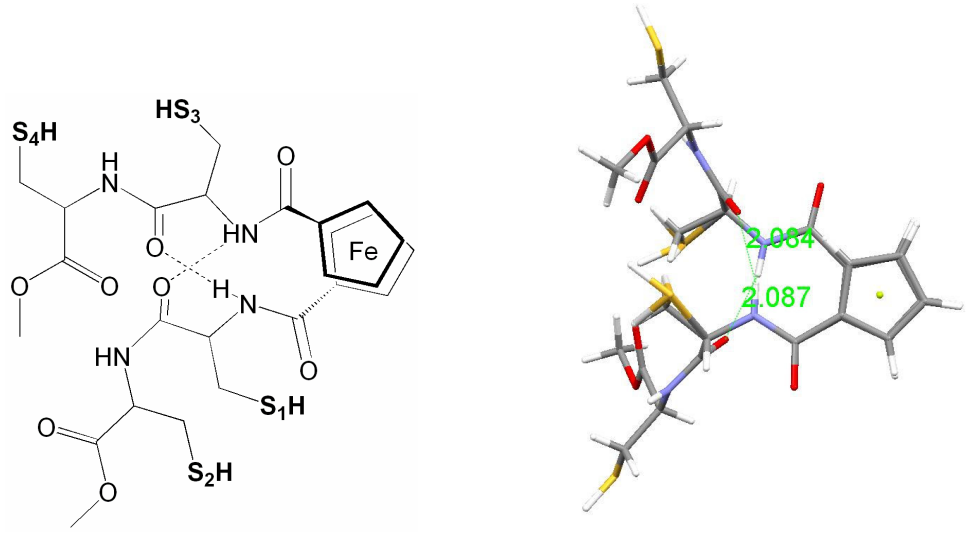

(a) (b)

Figure 4.13 Representative scheme of (a)"Herrick" H-bond pattern (b) model **δ** after minimization

To examine the influence of the length of the peptide strands on the shape and the flexibility of the sulfur chelating shell the distances between the sulfur atoms, in the simulations of models **δ** and **ϕ**, are plotted as time series (Figure 4.15).

The results are also shown in Table 4.8, revealed an unexpected feature: the distances between the sulfur atoms are in the same range for both models. The standard deviations of these distances indicate that the degree of flexibility is even larger for the shorter sequence.

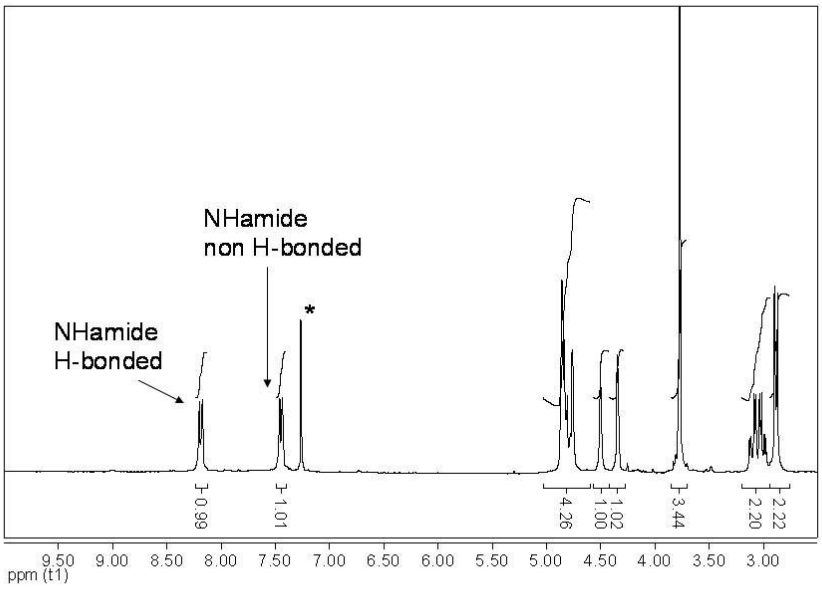

(a)

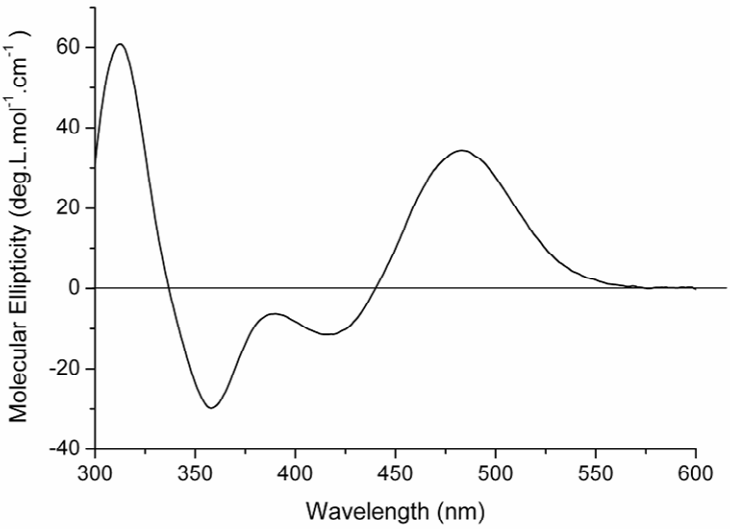

(**b**)

Figure 4.14 (a) NMR spectra of compound **33d** (model **δ**)(*) chloroform residual peak (b) Experimental CD spectra of compound **33d** measured in CH_2Cl_2

Table 4.8 Averages Sulfur-sulfur atomic distances for models **δ** and **ϕ**.

Models	S^1-S^2 [Å]	S^1-S^3 [Å]	S^1-S^4 [Å]	S^2-S^3 [Å]	S^2-S^4 [Å]	S^3-S^4 [Å]
4	6.7(9)	7.0(9)	8.0(9)	8.2(10)	12.1(9)	6.1(11)
6	12.7(6)	8.0(5)	12.7(9)	7.9(6)	6.1(10)	6.7(7)

Standard deviation in parentheses

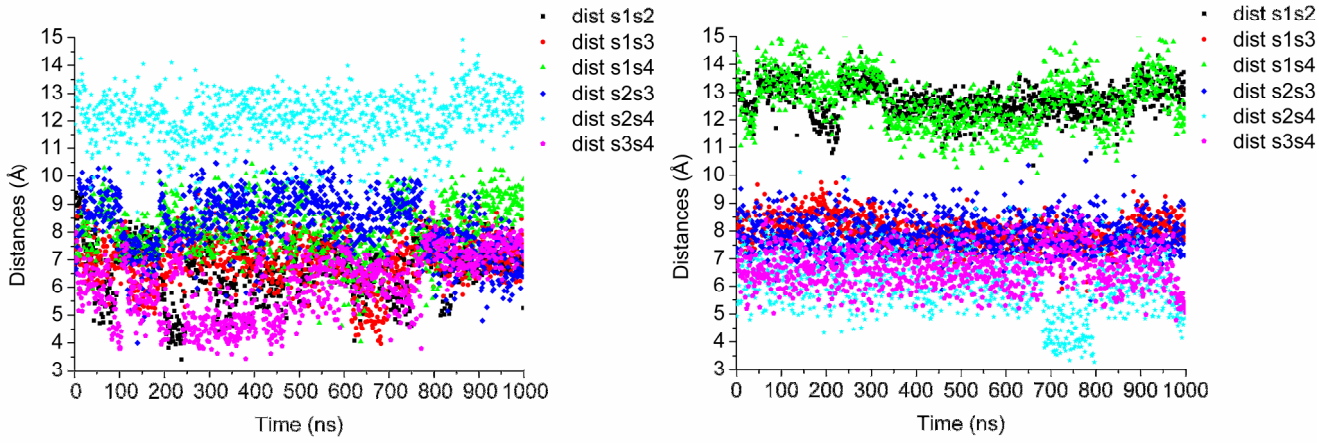

(**a**) (**b**)

Figure 4.15 Time series of the distances between sulfurs, in molecules (**a**) **δ** and (**b**) **ϕ** monitored over 1 μs

The distances between any two sulfur atoms, in the active site of the experimental crystal structure of the enzyme are in the range of 4.5 - 6 Å [177]. The time series plotted in Figure 4.15 indicates that for model **δ** thermal energy alone is high enough to bring two sulfurs as close as 4 Å at some instances during the MD and therefore to bond to a nickel atom, or at least to create favorable conditions for coordination. Therefore, there is no steric hindrance and the coordination of nickel seems feasible from the steric view point.

The next step was to include a nickel core in the ligand pocket of models **δ** and **ϕ**, so as to obtain models **ε** and **γ**. The nickel atom was implemented in CHARMM using a harmonic energy term between the sulfur atoms and nickel. We do not intend to reproduce neither the d-orbitals of the nickel nor the ligand field stabilization of the sulfur atoms. The model presented here is hold by an electrostatic harmonic force and is therefore a purely steric and geometric approximation.

Simulation in vacuum was performed on each molecule with the same protocol as described in the "Methods". Resulting structures are shown in Figure 4.16. Mean values for Ni-S atomic distances and S-Ni-S angles are reported over 1 μs MD in Table 4.9.

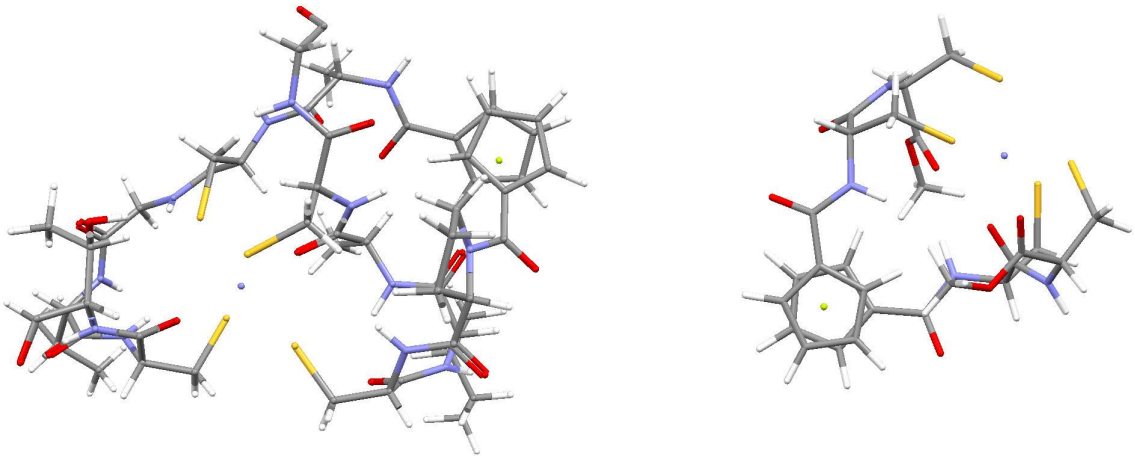

(**a**) (**b**)

Figure 4.16 Simulation of (**a**) model **ε** and (**b**) model **γ** after 1 μs MD in vacuum at 298 K

Table 4.9 Parameters of Nickel-sulfur center

Models	S^1-Ni [Å]	S^2-Ni [Å]	S^3-Ni [Å]	S^4-Ni [Å]	S^1-Ni-S^2 [deg]	S^1-Ni-S^3 [deg]	S^1-Ni-S^4 [deg]
Exp[(a)]	2.51	2.37	2.49	2.48	93.3°	181.8°	74.6°
ε	2.31(5)	2.25(4)	2.30(5)	2.27(6)	96°(4)°	160°(5)	94°(4)
γ	2.33(6)	2.29(5)	2.28(5)	2.28(5)	90°(3)	173°(3)	89°(3)
ι	2.33(7)	2.32(7)	2.34(7)	2.37(0.8)	96°(4)	95°(4)	95°(8)

[(a)] Experimental values are measured on the hydrogenase active site from experimental crystal structure [163]. Standard deviation in parentheses

For model systems **ε** and **γ**, there was no apparent distortion of the peptides during the simulation. No steric hindrance due to the connection of the nickel in the sulfur ligand pocket is observed. Nickel-sulfur complexes connected to an aliphatic carbon chain are rare in the literature; only about 30 crystal structures have been published. In the present simulation, the S-Ni bonds, are in the range of **2.25 Å** to **3.0 Å** (see Table 4.9), similar to the size of data measured in the crystal structures [163] which are in the range of **2.37 Å** to **2.51 Å**. These results are also in good agreement with DFT/B3LYP optimizations performed on different nickel complexes [178].

4.4.2 Simulation of the Hydrogenase active center (models η and ι)

For this study, only the two peptides strands without ferrocene were simulated in CHARMM, using the commercial CHARMM parameter and topology files, except for the nickel, which was implemented as described in the section "Methods". The sequence that surrounds the metal core in the natural enzyme active site are: -NH-Ala-Cys^1-Ile-Ala-Cys^2-Thr-CO- and –NH-Pro-Cys^3-Gly-Val-Cys^4-Gly-CO- (see Figure 4.17). In Model **η**, Cys^1 is connected to Cys^4 and Cys^2 to Cys^3 via two disulfide bridges. In Model **ι**, a nickel atom is incorporated between the sulfurs and bridges the cysteine residues on opposite peptide chains. In the latter case, it was found that no additional harmonic constraint was needed for holding the nickel atom in the sulfur ligand pocket; non-bonded interactions were sufficient to hold the structure together over the time of the MD run. An MD simulation of these two systems in vacuum was performed for 500 ns.

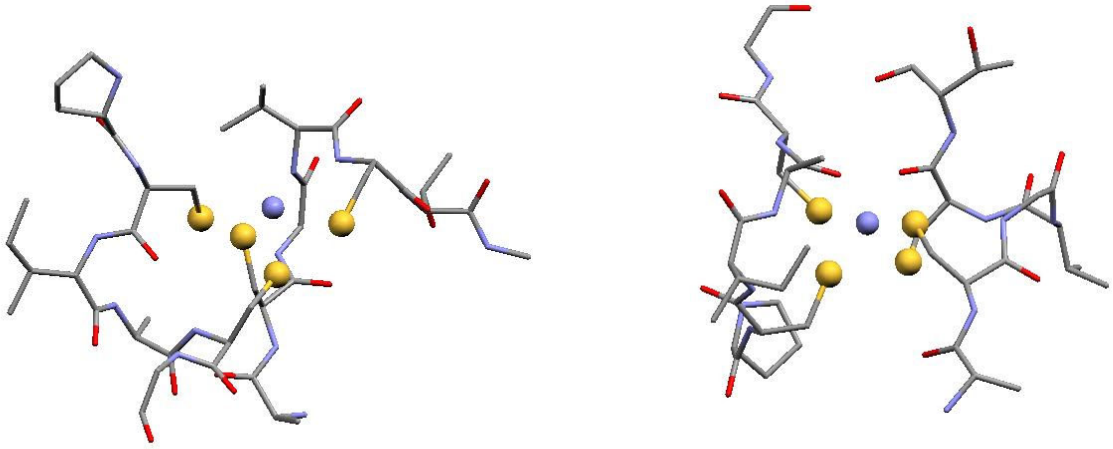

(**a**) (**b**)

Figure 4.17 Hydrogenase active site; (**a**) calculated versus (**b**) experimental structure (active site obtained from PDB database and worked-out with Insight II)

Table 4.10 Cter-Nter distances in models **η** and **ι**.

Models	**Cter^1-Cter^2 [Å]**	**Nter^1-Cter^1 [Å]**	**Nter^1-Cter^2 [Å]**	**Nter^1-Nter^2 [Å]**	**Nter^2-Cter^1 [Å]**	**Nter^2-Cter^2 [Å]**
η	5.3(2)	5.3(7)	6.6(3)	9.6(8)	8.1(11)	5.1(7)
ι	10.0(0.58)	10.4(1.48)	6.5(2.61)	12.19(1.80)	6.25(1.31)	14.2(1.45)

Cter^1 belongs to the threonine on the first strand; Cter^2 belongs to the glycine of the second sequence. Nter^1 is attached to the alanine of the first strand and Nter^2 to the proline of the second one. Standard deviation in parentheses

The distances between the C and N termini of the two strands were monitored for systems **η** and **ι** as time series over 500 ns dynamics at room temperature (results are shown in Table 4.10). As it is shown in Figure 4.18, in both cases, the mean distance between both N-termini (about **9 - 12 Å**) is longer than mean distance between C-termini (**5 - 10 Å**). Since the Cp-Cp distance in ferrocene is about 3.3 Å, this indicates that ferrocene could be attached more easily to the C-termini than the N-termini. The Nter-Cter distances are also in the range of 3 - 5 Å. Therefore, anti-parallel incorporation of the peptides on ferrocene with the C-terminus of one strand and the N-terminus of the other strand attached to ferrocene is also a possible synthetic route. We assume that the connection of ferrocene to either the C-termini or anti-parallel to the C- and N-termini is geometrically more favourable and induces less strain in the molecule. The asymmetric

synthetic path has already been published by us [109, 179]. Its synthesis is technically challenging and tricky.

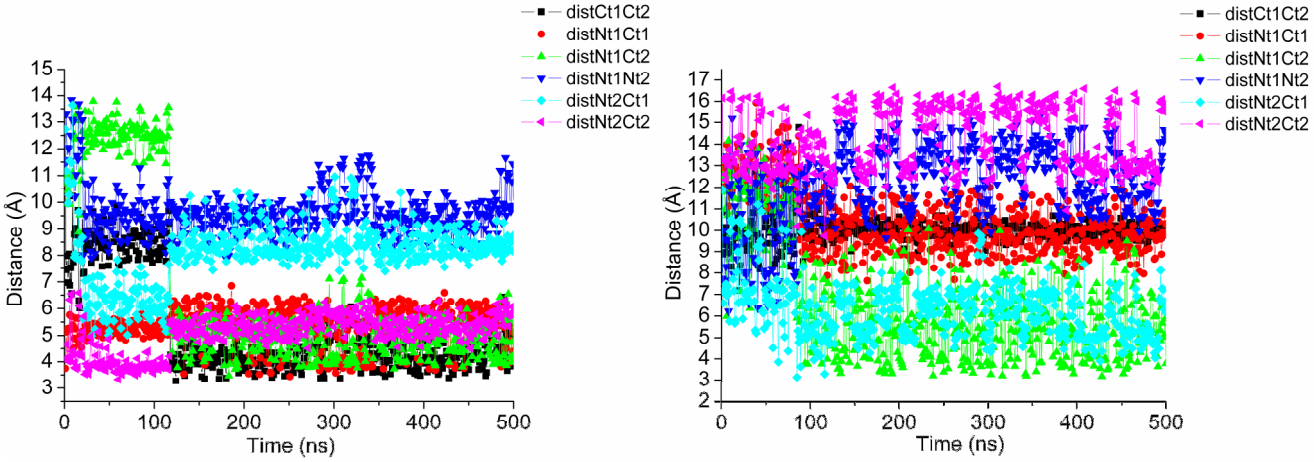

Figure 4.18 Time series of the distances between C and N termini in model system (**a**) **η** and (**b**) **ι** monitored over 0.5 μs

4.4.3 New direction for the synthetic work

Based on the simulation results, the synthetic pathway for the connection of ferrocene to C-termini instead of the N-termini has been investigated. Therefore, it is required to attach two amines to the ferrocene moiety, so as to enable the carboxylic acid termination of the peptides to react. The synthesis and the application of 1,1'-diaminoferrocene in peptide synthesis have already been reported [180]. One of the steps for the synthesis of 1,1'-diaminoferrocene is the formation of 1,1'-diazidoferrocene [109], which is extremely temperature sensitive, and prohibits the reaction from being scaled up, which is certainly desirable since this derivatives will be further used as building blocks. Another possible synthetic pathway has therefore been pursued and consists of the intercalation of an ethylendiamine linker. The ethylene diamine could be coupled with ferrocene carboxylic acid to afford the desired product. In this manner, the diazido intermediate is avoided and the addition of the linker enhances the flexibility of the molecule. Three different synthetic approaches were tested; the Boc-protected, the Fmoc-protected or the unprotected ethylendiamine (EDA) were attached to ferrocene with standards coupling conditions. The protecting groups were subsequently cleaved as it is depicted in Figure 4.19.

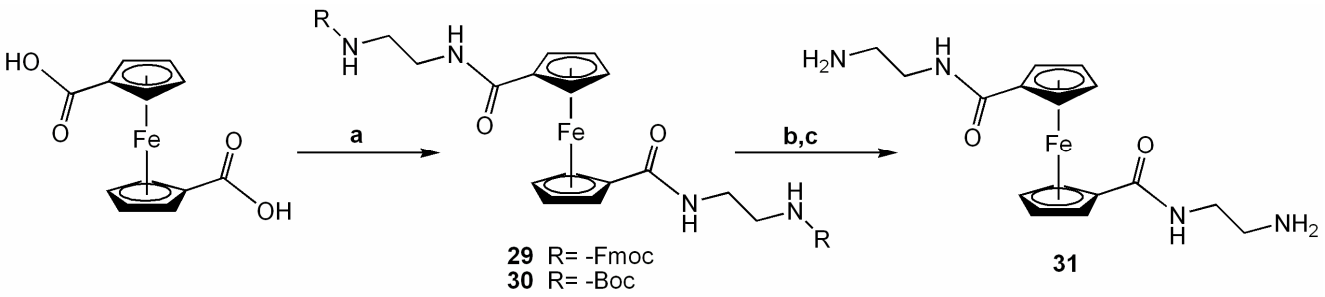

Figure 4.19 Synthetic pathway for the new orientation of experimental work (a) HOBt, DCC, DIPEA, CH_2Cl_2, 1 h, 20°C NH_2-$(CH_2)_2$-NH-R, 4 h, 20°C (b) Piperidine/CH_2Cl_2, 30 min, 20°C c TFA/Phenol 1 h, 20°C

Each of these different pathways includes some drawbacks; the Fmoc cleavage in solution produces pyridine salts and Fluorenomethyl polymers [100]. Cleavage of the Boc protecting group takes place in TFA with a large excess of phenol to avoid the side reactions observed when ferrocene is in prolonged contact of a strong acidic media. For the third synthetic path, activation of the ferrocene carboxylic acid and its isolation from the activation reagent is needed. Subsequently, in a second, independent step, coupling with ethylene diamine (EDA) follows. The reaction mixture has to be largely diluted to avoid chain polymerization. Even so, about 20 % of the ferrocene-EDA macrocycle and/or polymers were isolated, when both extremities of EDA connect both Cp-rings that belong either to the same ferrocene moiety or to two different molecules. The large excess of phenol, that has to be used for the Boc strategy in order to avoid side reactions as well as the large dilution necessary for the unprotected strategy, increases preference for the use of the Fmoc strategy. The synthesis is described in the experimental section. The ferrocene ethylene diamine **31** thus obtained was fully characterized and its synthesis was optimized. This compound will be further used as starting material for coupling with amino acids and peptide derivatives. This part of the work is not discussed here.

4.5 Conclusion

A parameter set for ferrocene-bearing peptides has been developed for the all-atom CHARMM molecular mechanics force field. Fitting of the molecular mechanics potential to that derived by quantum chemical calculation produced a good matching of normal modes for ferrocene-1-proline-1'-alanine. This molecule was used to derive the parameters for ferrocene and for the connection between ferrocene and the first amide bond of the peptide sequence.

The new parameters were subsequently tested on independent, experimental structures and the results obtained are overall in good agreement with experimental data. Energy minimization and molecular dynamics of the Fc-(D-Ala-D-Pro)$_2$ crystal structure led to unit cell dimensions and volume being reproduced within less than 0.1 % of the experimental values. Intrinsic structural features of the crystal, such as the intramolecular H-bond pattern and the helical ferrocene arrangement are also accurately reproduced.

The structures and dynamics of possible hydrogenase mimics were subsequently studied. MD simulations of the model systems exhibited the formation of intramolecular hydrogen bonds between the two peptide strands on models **β**, **χ**, **δ**, **ε** and **ϕ** that are consistent with the available experimental data. Our MD studies show that longer peptide sequences such as -NH-Ala-Cys^1-Ile-Ala-Cys^2-Thr-CO- and –NH-Pro-Cys^3-Gly-Val-Cys^4-Gly-CO- attached to a ferrocene moiety result in multiple steric and stability hindrances. In contrast, small peptide sequences attached to a ferrocene moiety (such as model systems **δ**, **ε**, **ϕ**, **γ**) have a much more promising behavior. This led us to the conclusion that, from a steric view point, the metal coordination seems to be feasible for this type of compound. Finally, two non-ferrocene hydrogenase mimics (model systems **η** and **ι)** were studied, and the time series of the distances between the termini of both strands were monitored. The mean distance between the C-termini of the peptides during the MD was smaller than that of the N-termini; suggest that ferrocene attachment might be easier on the C-termini of the peptides rather than on the N-termini, as is the synthetic strategy hitherto followed. A novel synthetic strategy using diamino-ferrocene instead of ferrocene dicarboxylic acid was thus developed. Preliminary synthetic results, i.e. the synthesis of the first building block of this new synthesis, demonstrate the technical feasibility of this new approach.

5. Functionalized Aromatic Oligoamides

In the following, we present the theorical prediction, the synthesis, the functionalization and the structural study of a family of quinoline derived amide oligomers with appended thiols. The following results illustrate the efficiency of computational rationalization, and the relative ease of synthetic production of oligoamides that mimic the folding of peptides. The potential suitability of these molecules as ligands for an iron-carbonyl metal core and therefore as scaffolds for mimicking hydrogenase active site is also demonstrated.

5.1 Design of the structures

The predictability of the folding of oligomeric molecules is largely increased when multiple stabilizing intramolecular interactions, such as hydrogen bonds and aromatic π-stacking, take place between the different units constituting the structures. When conformational preferences arise locally at every rotatable bond, as in the oligomers discussed hereafter, computational and / or experimental studies provide accurate data on the relative positioning of consecutive units that, in many cases, may be extrapolated to longer oligomers.

Oligoamides of some *meta*-substituted pyridine- and benzene-derived amines and acids have been shown to fold into crescent and helical structures [181, 182]. In principle, a *meta* substitution defines an orientation of 120° between substituents and should lead to 6 units per turn in these bent conformations. In practice, intramolecular hydrogen bonding has an effect on the bending of the strands, and helices of *meta*-substituted aromatic oligoamides comprise from 4.5 to 8 units per turn, to compare with the 2 - 4 units per turn encountered in helices of aliphatic α, β, and γ peptides. Our group has recently reported

that aromatic oligoamides with substituents oriented at 60° (for example, *ortho* substituents) are more bent, and give rise to helices with 2.5 units per turn [183]. Quinoline monomers were designed for this purpose; 8-amino-4-isobutoxy-2-quinolinecarboxylic acid and 8-amino-4-tertbutylthiopropoxy-2-quinolinecarboxylic acid were used as building blocks for the preparation of oligoamides. The alkoxy substituents in position 4 diverge from the helices and determine their solubility and potential functions. Moreover, we became intrigued with the use of 1,10-phenantroline-2,9-diacid as monomeric unit. Indeed, the two acids groups also define an angle of 60°, which leads to the same bending of the strand as observed for quinoline oligomers. Thus, the units depicted in Figure 5.1 were incorporated in oligomers.

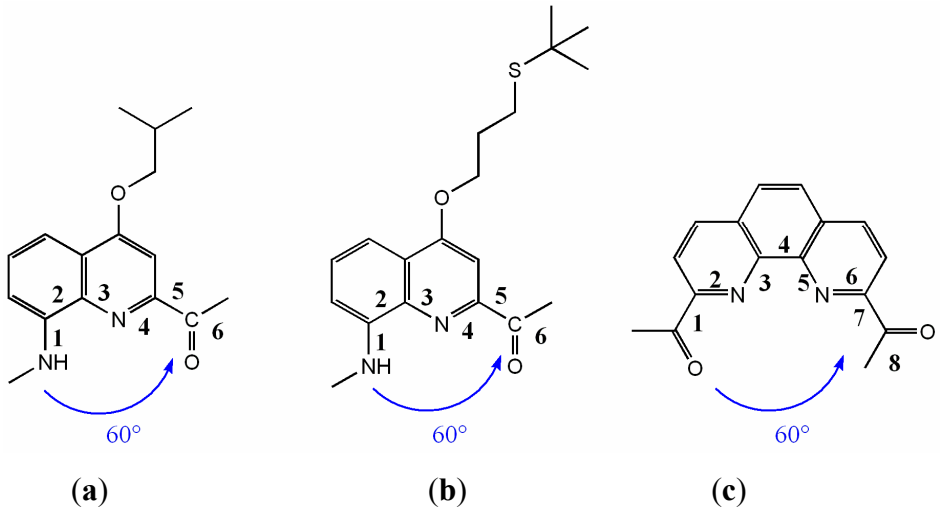

Figure 5.1 Single units incorporated in oligomers exhibit structural similarity. (**a**) Isobutoxy quinoline, named **B4** in its nitro-ester form; (**b**) tert-butylthio-isobutoxy quinoline named **B5** in its nitro-ester form; (**c**) 1,10-phenantroline named **B22** in its bis-(acid chloride) form.

In oligomers of **B4**, **B5** and **B22,** intramolecular hydrogen bonding between the amide hydrogen and both adjacent quinoline nitrogens stabilize a bent shape, and give rise to a helix for strands as short as a trimer. This well-defined three-dimensional geometry can be accurately predicted by molecular modelling by using commercial force fields, as demonstrated for quinoline oligomers [183]. A simple energy minimization using the standard MM3 force field in Macromodel [184], was performed on sequences of quinolines, and quinolines and phenantroline (see Figure 5.2 and Figure 5.3). The aim of these simulations was to find the most suitable position of the S-functionalized quinoline units in the sequence so as to create a sulfur chelate pocket capable of complexation with a

diiron carbonyl core. Therefore, the ligand should have similar size and shape than those observed in the wild-type or already reported in literature [31, 185].

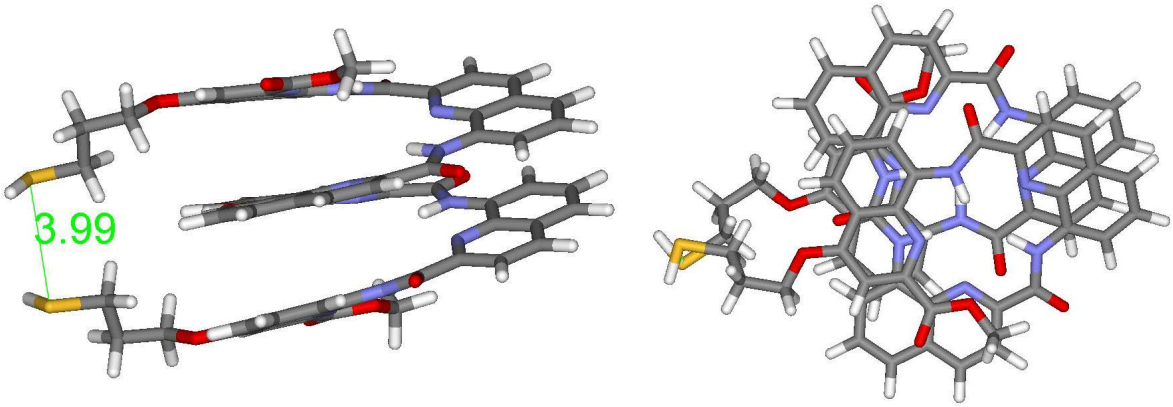

(**a**) (**b**)

Figure 5.2 Side view (a) and top view (b) of a hexameric quinoline-oligomer structure bearing thiol side-chains in position 1 and 6, obtained from a simple energy minimization (MM3 force field in Macromodel)

In the simulation of the hexameric quinoline oligomer depicted in Figure 5.2, the distance between both sulfurs placed on residues 1 and 6 of the sequence is of about 4.0 Å this is of good agreement with the distance measured between two different sulfur atoms in the crystal structure of the wild-type complex of the hydrogenase active site. The calculated hexamer is centro-symmetric; two identical trimers are connected via a urea cross-link.

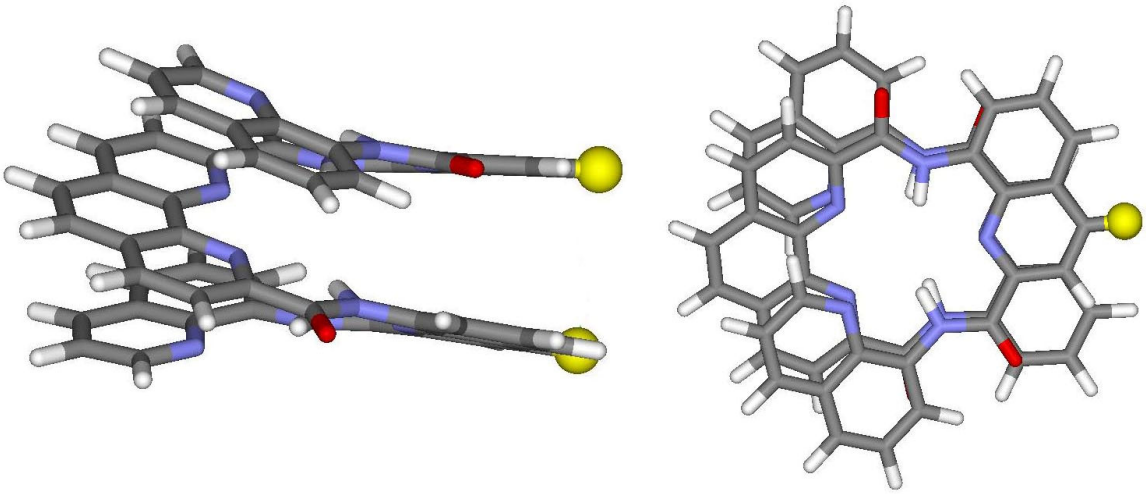

(**a**) (**b**)

Figure 5.3 Side view (**a**) and top view (**b**) of a pentameric structure, with a phenantroline as central unit, obtained from a simple energy minimization (MM3 force field in Macromodel)

In a second step, theorical predictions performed on the same basis on a mixed phenantroline-quinoline sequences, led us to investigate oligomers with a 1,10-substituted phenantroline as central unit connecting to two identical quinoline dimers.

As shown in Figure 5.3, we focused on a pentameric oligomer having two thiol-functionalized quinoline units placed at the key positions “2” and “4” of the sequence (starting from one end), right besides the central phenantroline, so as to produce a convenient chelating pocket. In this case, the thiol side-chains are expected to lye right above each other and diverge from the helix. As comparison the synthesis of a second pentamer, in which the modified monomers are in places 1 and 6, was also performed and discussed later. The phenantroline carboxamide building block has already been successfully used in the design of supramolecular assemblies [186] and presents some advantages. The features that allow it consistent incorporation in quinoline oligomers are the following: (i) The 1,10 diacid units define angle of 60°, which leads to the high bending of the strands and therefore strong π-π stacking interactions between the phenantroline and adjacent aromatic units. (ii) Two nitrogen atoms in the phenantroline unit are hydrogen-bond acceptors that can form intramolecular hydrogen bonds with adjacent amide hydrogens to restrict the conformation of the strands. (iii) When the strands fold into helical structures, aromatic stacking interactions between different units can further stabilize the conformation. (iv) The symmetry of the phenantroline introduces a C2-symmetry axis perpendicular to the helix. Symmetry allows a convergent synthetic scheme and simplifies the (NMR) spectroscopic signature.

At this point, we would like to emphasize the fact that prediction was here a powerful tool, which allow us to screen, virtually, a wide range of possible structures and sequences.

5.2 Synthesis

5.2.1 Monomers and dimers

The preparation of monomer **B4** was easily carried out in three steps (Scheme 5.1), as described in literature [187]. The addition of 2-nitro-aniline to dimethyl acetylene dicarboxylate affords **B2**, which can be isolated by crystallisation from cold MeOH with yields above 85 %. The subsequent conversion of enamine **B2** to quinolinone **B3** was carried out by ring closure in polyphosphoric acid (yield: < 70 %) [188, 189]. The

isobutoxy monomer **B4** was subsequently obtained by the alkylation of the oxygen in position 4 of **B3**, which was achieved under Mitsunobu conditions with isobutanol. The tertiobuthiolpropoxy monomer **B5** was obtained by the O-alkylation of **B3** with 3-(tert-butylthio)propan-1-ol **B1** which was prepared by nucleophilic substitution of 3-chloropropan-1-ol with sodium 2-methylpropane-2-thiolate as described in ref. [190]. Both **B4** and **B5** can be isolated by crystallisation from chloroform / methanol mixtures in 90 % yield and were used without further purification. No trace of N-alkylation of the quinolinone nitrogens was detected in these reactions, contrary to other compounds studied in the laboratory (e.g. hydroxy-naphthyridines).

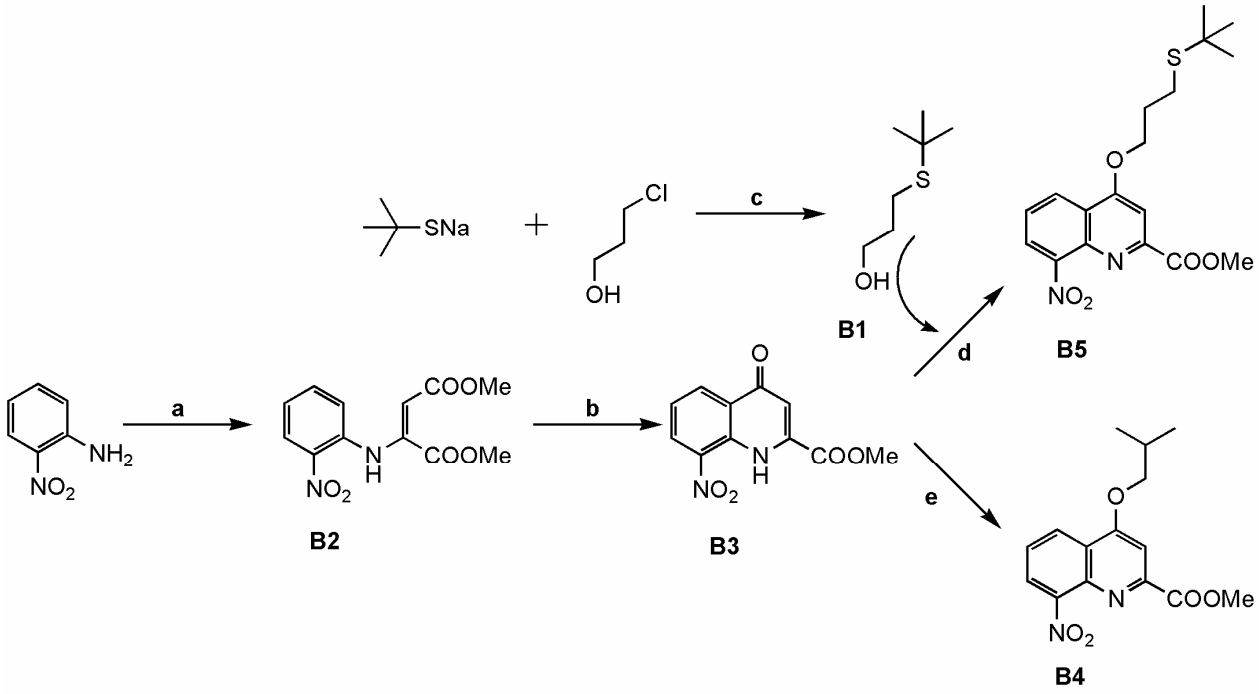

Scheme 5.1 Synthetic pathway leading to the monomers isobutoxy and tertbutyl-thiopropoxy. (a) dimethyl acetylenedicarboxylate, MeOH, rt; (b) polyphosphoric acid, 130°C; (c) CH_2Cl_2, rt; (d) DEAD, PPh_3, THF, rt; (e) iBuOH, DEAD, PPh_3, THF, rt.

As it is depicted in Scheme 5.2, the saponification with potassium hydroxide and reduction of the nitro groups by hydrogenation on Palladium catalyst of **B4** and **B5** under standard conditions gave quantitative yields of nitro-acid **B6**, **B7**, and amino-esters **B10**, and **B11**, respectively. Nevertheless, it has been noted that the reduction of the sulfur containing monomer can be problematic. The thiol group, with its strong affinity for late transition metals, may pose some problems. Because of the poisoning of the catalyst, the amount of catalyst and the reaction time was increased. Only few publications address this problem and no better solution was found in the literature since, in general, thioethers

(sulfides) groups are known to be among the most compatible with the use of palladium catalysts [191]. The activation of **B6** proceeded smoothly in refluxing $SOCl_2$ over 15 min to yield quantitative amount of acid chloride **B8**. Activation of acid **B7** in $SOCl_2$ gave raise to multiple side reactions, which were avoided using activation with a chlorenamine (Ghosez's reagent) in dichloromethane to give **B9** in good yield.

The subsequent condensations of either **B8** on **B10, B8** on **B11,** or of **B9** on **B10** in dry dichloromethane in presence of diisopropyl ethylamine yielded the dimers nitro-ester **B12**, **B13** and **B14,** respectively, in excellent yield. With drastic reaction control, the dimers can be obtained in good purity by crystallisation from methanol / chloroform mixtures. When the reactions are carried out on larger scales, the yields tend to be higher.

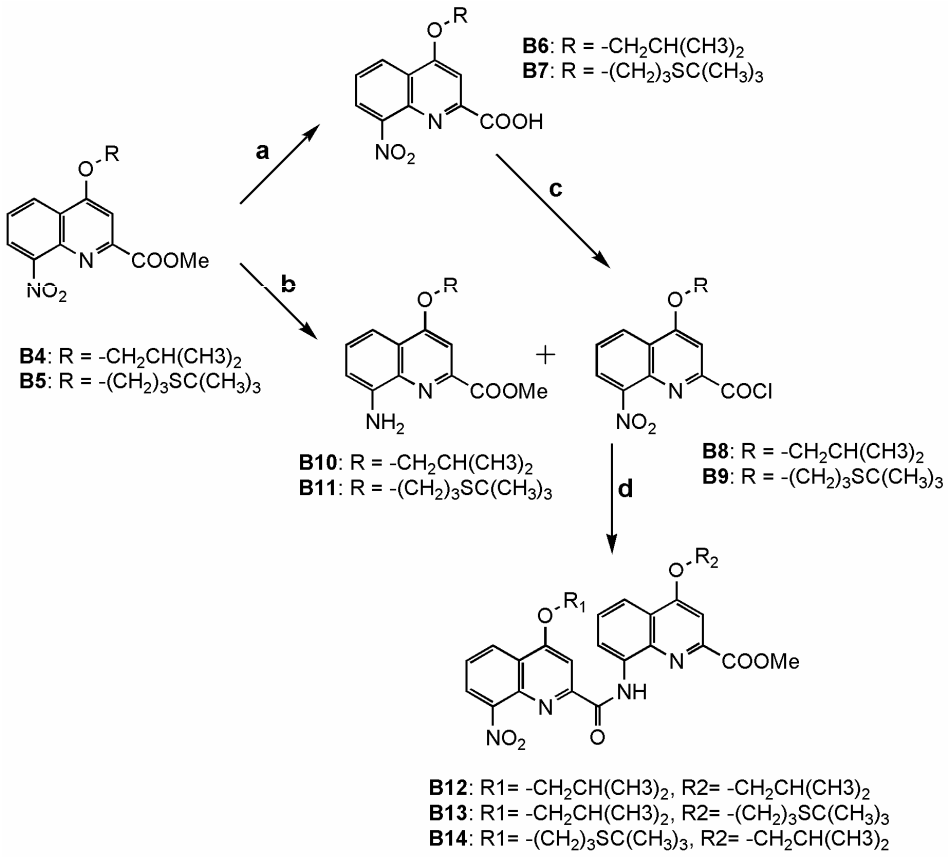

Scheme 5.2 Synthetic pathway leading to the dimers. (**a**) KOH, MeOH/THF, overnight, rt; (**b**) H_2, Pd/C, EtOAc, 4 h, rt; (**c**) either $SOCl_2$, reflux, or chlorenamine, CH_2Cl_2, 2 h, rt; (**d**) DIEA, CH_2Cl_2, overnight, rt.

The hydrogenation, saponification, activation, and coupling were applied successfully to the different dimers with slightly different reaction time and concentration. Indeed, we observed that hydrogenation and the saponification step require increasing reaction time and / or higher temperature as the length of the oligomers increases. The

oligomer with an S-quinoline unit should be treated with the special care described above to prevent the side reactions of the thioether group during the synthesis.

5.2.2 Oligomerization

The mostly used synthetic approach to longer oligomers in our laboratory is a semi-iterative approach. Coupling reactions are known to work better when one of the reagents has a folded structure and the other is short and unhindered than when both reagents are large and folded. Though less efficient then a convergent strategy, an iterative approach, where small (monomeric or dimeric) units only are coupled at time, should be effective to incorporate a series of different monomers in a sequence as it is the case for peptide solid phase synthesis. To prepare sequences including protected thiol side-chains such those shown in Scheme 5.1 and Scheme 5.2, syntheses may proceed first with the coupling of two monomers to give a dimer. An additional monomer is then coupled to this dimer, the resulting trimer may be condensed to itself to afford a hexamer. Alternatively, a divergent strategy may be envisaged where two dimers are coupled to a phenantroline central unit. The synthetic pathways that led to the relevant oligomers are described in Scheme 5.3.

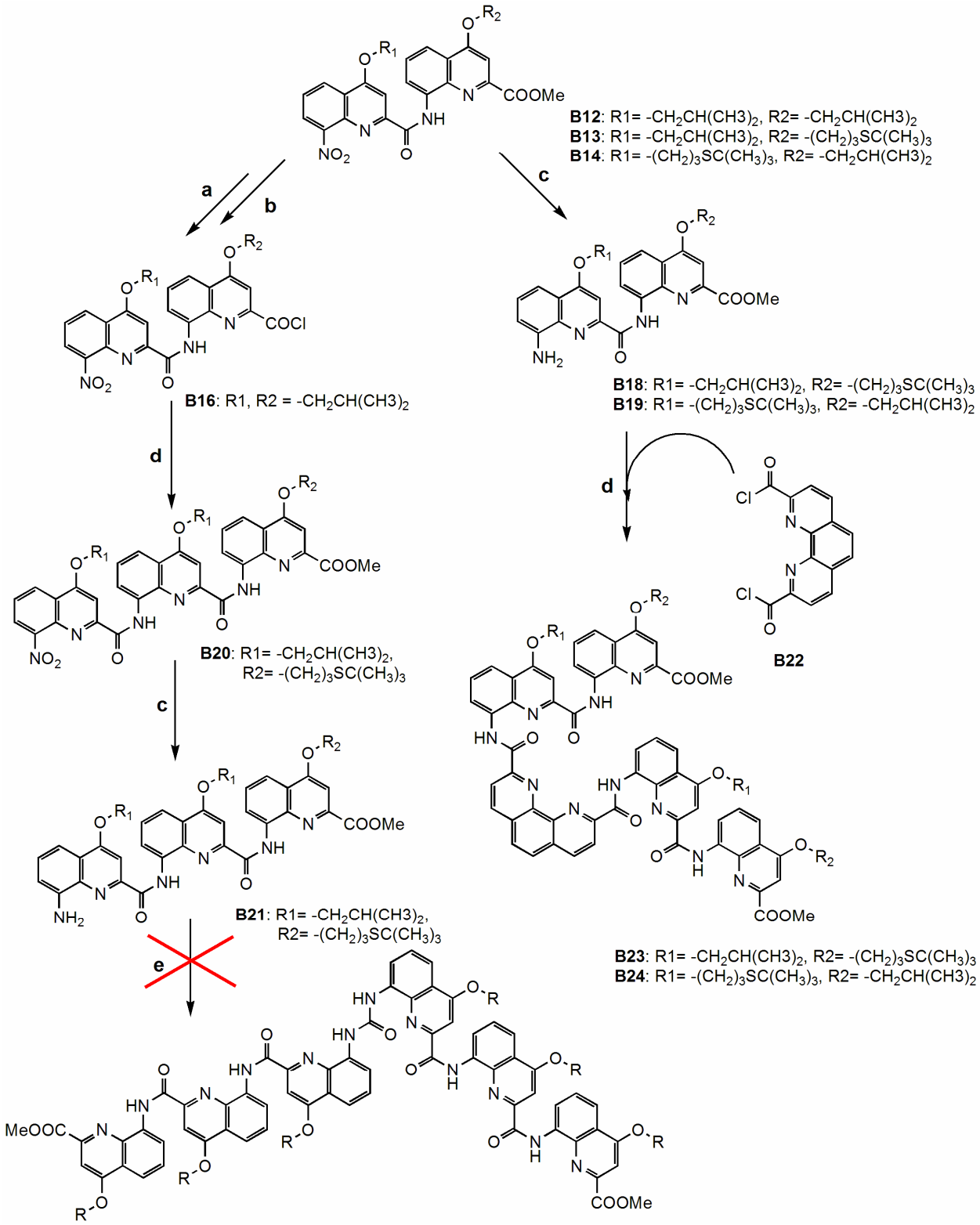

Scheme 5.3 Synthetic pathway leading to pentameric structures; (**a**) KOH, MeOH/THF, overnight, rt; (**b**) either $SOCl_2$, reflux, or chlorenamine, CH_2Cl_2, 2 h, rt; (**c**) Pd/C, EtOAc, 12 h, rt (**d**) DIEA, CH_2Cl_2, overnight, rt. (e) trisphosgene, CH_2Cl_2, 24h rt.

The first synthesis that was investigated was the synthesis of the hexamer. This synthesis involve; first the formation of the nitro-ester heterotrimer **B20** by reaction of the

monomer amino-ester **B11** on the activated nitro-acid dimer **B16**. The resulting **B20** was subsequently reduced by catalytic hydrogenation to form the amino-ester **B21**. Unfortunately, the reaction of urea cross-linking between both N-terminations of the trimer in presence of trisphosgene described in ref. [192], failed in our hands. **B21** could be recovered from the reaction mixture after purification of the reaction mixture.

The synthetic pathway including the phenantroline as a central unit was then investigated. The synthesis of pentamers **B23** and **B24** were performed by condensation of the carbonyl chloride **B22** with two equivalents of the dimers **B18** or **B17**, respectively, with yields in the range of 70 %. The activation of the phenantroline dicarboxylic acid can be performed in refluxing thionyl chloride during 3 h. Reaction times has to be multiplied by 10 in comparison with the isobutoxy-quinoline monomer because of the poor solubility of the diacid in the $SOCl_2$.

5.2.3 Deprotection step

The tert-butyl group was selected to protect the thiol functions during synthesis because it was thought to be the most adapted to the various reactions conditions. Tert-butyl thioethers are resistant to strong acids, strong bases, nucleophilic reagents, as well as electrophilic reagents. This group is convenient for the investigated synthetic pathways, because of the harsh reaction conditions that are used here, such as activation in refluxing thionyl chloride or saponification with potassium hydroxide. The tertio-butyl groups present in compound **B5**, **B23**, **B24**, were cleaved in a two-steps procedure depicted in Scheme 5.4 and Scheme 5.5.

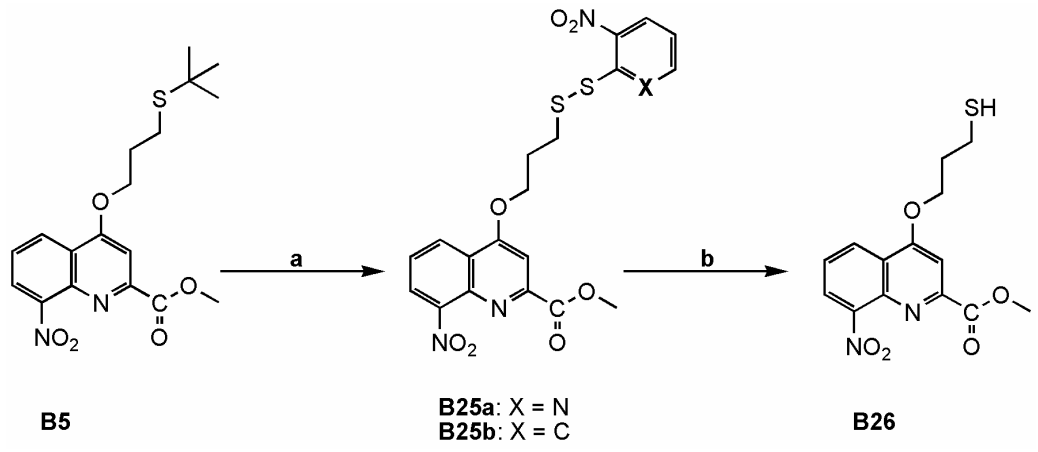

Scheme 5.4 Deprotection steps on the monomers: (**a**) either NpySCl (X = N) or NbSCl (X = C), acetic acid, 2 h rt; (**b**) tri-n-butylphosphine, acetone/water, 12 h, rt.

The derivatives **B25a**, **B27**, **B28**, were synthesized by substitution of sulfenyl halides on compounds **B5**, **B23**, **B24**, in acidic medium with yields within the range of 70 %. It has been found that both para-nitropyridine sulfenyl chloride and para-nitrobenzene sulfenyl chloride work properly for this substitution. However, reaction with para-nitropyridine is faster. For the second step of the synthesis, the para-nitrosulfenyl group was reduced to thiol in presence of tri-n-butylphosphine and water to yield final compounds **B26**, **B29**, **B30**. Free thiols derivatives are, in general, air sensitive and they rapidly form intra or intermolecular disulfide bridge. They should be handled carefully and used within couples of days.

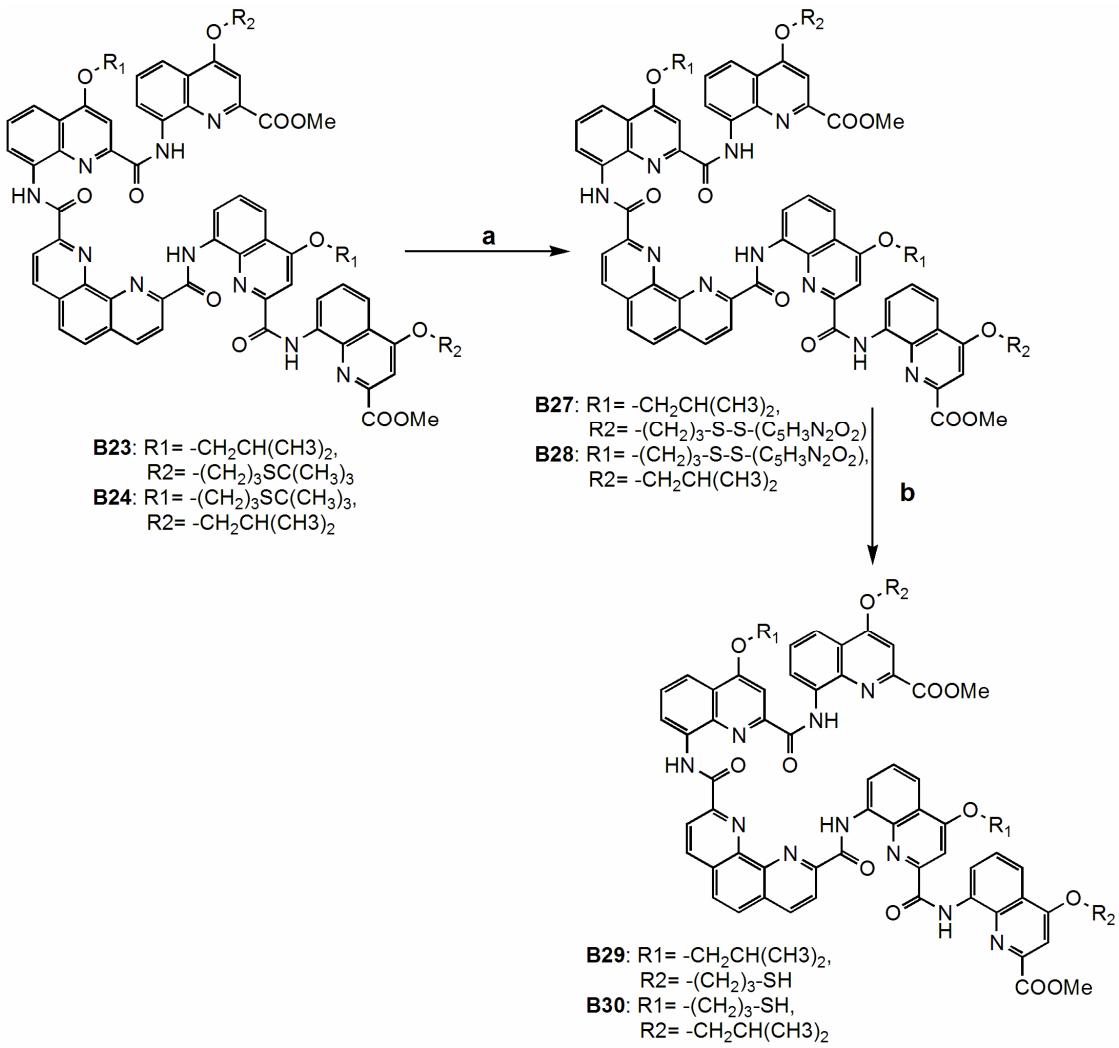

Scheme 5.5 Deprotection steps on the pentamer: (**a**) NpySCl, acetic acid, 6 h rt; (**b**) tri-n-butylphopshine, acetone/water, 12 h, rt.

5.3 Characterization

All synthesized product were comprehensively characterized using standard analytical method such as elemental analysis, mass spectrometry, high resolution mass spectrometry for longer derivatives, and NMR (^{1}H and ^{13}C). In the case of compounds **B23**, **B24** and **B29** crystal diffraction data were also collected. The crystallographic data are listed in the experimental part along with the rest of the analysis.

5.3.1 Solution phase structural analysis by NMR

The conformation of pentamers **B23**, **B24**, **B27**, **B28**, **B29** and **B30** were investigated in solution by NMR spectral methods. All of the intermediates and target compounds have good solubility in non-polar solvents such as chlorinated solvents, but they are almost insoluble in protic solvent such as methanol. NMR spectra were recorded in $CDCl_3$ at ambient temperature. As expected from the C2-symmetry of the pentamers, the two quinoline dimers placed beside the phenantroline core are magnetically equivalent. Therefore, only one set of signals observed in NMR for the two quinolines dimers. However, the NMR spectra are too complicated to be unambiguously assigned without additional correlation experiments. Protons signals can be tentatively attributed based on literature data and comparison with assigned spectra of related molecule [193]. In Figure 5.4, partial NMR spectra of a monomer, dimer, trimer, tetramer, and pentamer, are stacked so as to compare the difference in chemical shifts.

The ^{1}H NMR spectra of the synthesized pentamer are sharp and show no indication of hybridization into double helices or other types of aggregates, as was observed for pyridine derived oligoamides [71, 194]. The signals are spread over a large range of chemical shift despite the repetitive nature of the sequences suggesting different environments of each unit. Amide protons are deshielded to 11.7 - 12.8 ppm, as is expected for a hydrogen-bonded structure. NMR analyses also show a strong shielding of aromatic, amide and ester protons that can be attributed to tight contacts between aromatic rings. For example, the signal of the ester shifts from 4.23 ppm in the dimer **B13** to 3.20 ppm for the pentamer **B23**, and the singlet assigned to the protons in position 3 of the quinoline are found at 7.99 and 7.67 ppm in **B13** and at 6.87 and 6.40 ppm in **B23**. Another interesting feature is that signals assigned to the OCH_2 groups of the alkoxy side chains (either

isobutoxy or *tert*-buthiopropoxy) at 3.7 – 4.1 ppm in the pentamers, show diastereotopic patterns, which are consistent with the intrinsic chirality of a helical conformation. The right and left-handed helical conformers are in slow exchange on the NMR time scale.

Moreover, swapping the isobutoxy and the *tert*-butylthiopropoxy residues (from pentamer **B29** to pentamer **B30**) does not significantly affect the folding of the oligomer.

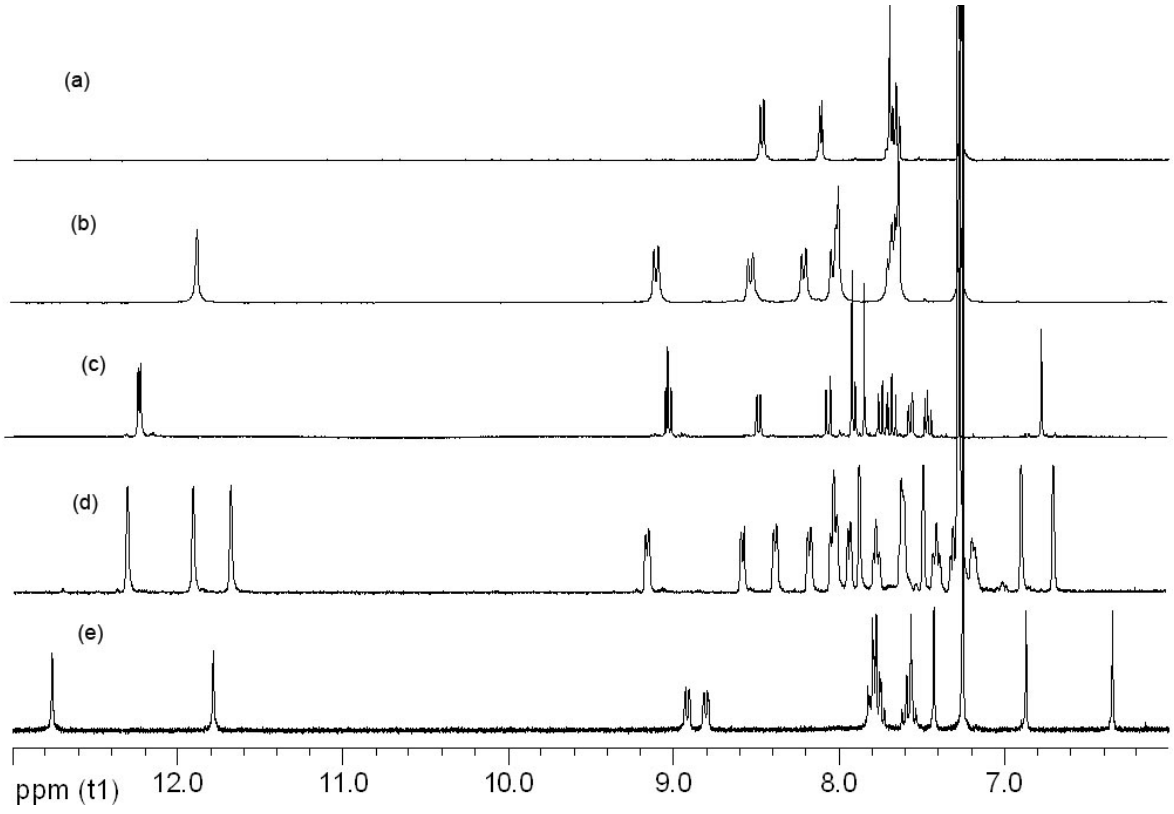

Figure 5.4 Comparison of partial ^{1}H NMR spectra for (**a**) monomer **B5**, (**b**) dimer **B18**, (**c**) trimer **B20**, (**d**) tetramer isobutoxy, (**e**) pentamer **B23**; in $CDCl_3$

The formation of the aromatic oligoamide-based helical foldamers reported so far is driven by intramolecular hydrogen bonds, which are strong in solvents of low polarity such as $CHCl_3$. However, we have found that the pentamers **B23**, **B24**, **B27**, **B28**, **B29** and **B30** could fold into the same helical structure in the presence of methanol, which is known to disrupt H-bonds assembly. As it is shown in Figure 5.5, no obvious spectral changes of **B23** in methanol-d_4 and in chloroform-*d* occurred. These observations imply that strong aromatic stacking interactions that exist between the units of the pentamer are able to hold the structure in its helical conformation without the help of the H-bonds. Hu *et al.* have reported a structure based on 1,10-phenantroline diacid and *o*-phenyldiamine which were found to have a more stable helical conformation in methanol than in chloroform. They

attributed this enhanced stability of the helical structures in methanol to the intermolecular hydrogen bonds between the methanol molecule and the helices [186].

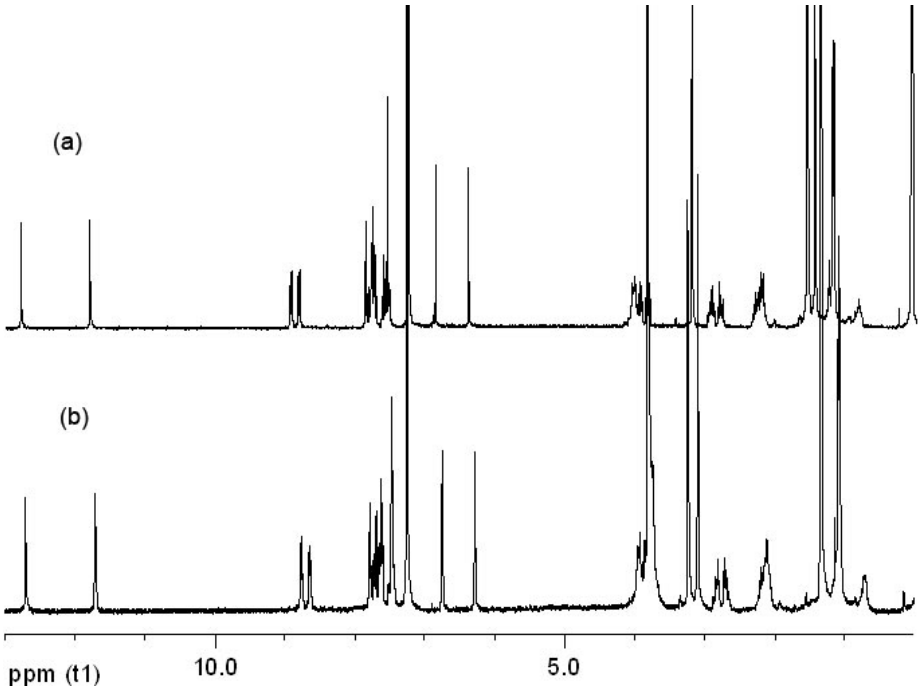

Figure 5.5 Comparison of ^{1}H NMR spectra for (**a**) **B23** in $CDCl_3$, (**b**) **B23** in $CDCl_3$/MeOD (1:3)

5.3.2 Solid state structural studies by X-Ray analysis

Single crystals of **B23**, **B24**, and **B29** suitable for X-ray analysis, were respectively obtained by crystallisation from the liquid / gas system Toluene / Methanol, the liquid / liquid system Dichloromethane / n-Heptane and the liquid / gas system Chlorobenzene / n-Hexane at room temperature.

The structures of **B23**, **B24** and **B29**, are helical. The five units of the pentamers are needed to complete two helical turns (see Appendix for detailed pictures). This is among the highest curvature reached by helical aromatic oligoamides. The terminal quinoline units of each pentamer indeed overlap with the central phenantroline unit. The pitch of the helix is consistent with the pitch of other helical aromatic oligoamides and corresponds approximately to the thickness of one aromatic ring (3.5 Å). The inner rim of the helix accomplishes exactly one turn every 15 main chain atoms and adopt a conformation similar to that of a pentaaza-15-crown-5 macrocycle, with alternating amido and pyrido nitrogens, as it has already been shown for quinoline only oligomers. The amido protons

fill the helix hollow, and completely prevent penetration of solvent molecules. They are all involved in two hydrogen bonds with the adjacent quinoline nitrogens that set the orientation of the amido and quinoline moieties. The relative inclination of consecutive units can be estimated from the torsion angles between the N(1)–C(2) bond of a quinoline and the C(8)–C(9) of the next quinoline or between the C(9)-C(10) bond of a phenantroline. With a range of 147.7° to 167.38° for two adjacent quinoline and 159° to 168.4° for the torsion between the phenantroline and the quinoline unit. The sulfur containing side chain adopt various conformations according to the free rotation along the CH_2-CH_2-CH_2 moieties, but the position of the first –O–CH_2 carbon always point away from the hydrogen in position 5 of the quinoline as it is the case for isobutoxy side chains. The anisotropic displacements calculated during the parameter refinement of pentameric structures were too large to assign properly the position of the *tert*butyl group. This uncertainty probably results from the free rotation of this group leading to disorders in the crystal lattice.

The core of the helix (see Figure 5.6) has a very regular structure. This is illustrated by almost constant distances between the same atom in symmetrical units and constant distance of the H-bond pattern within the rim, with hydrogens bonds measured on the crystal, in the range of 2.15 Å to 2.25 Å for the length, and 138.25° to 138.9° for the angle. Bending is even along the strand and does not depend upon the central or terminal position of the units, or the conformation of the side chain or interactions associated with crystal packing.

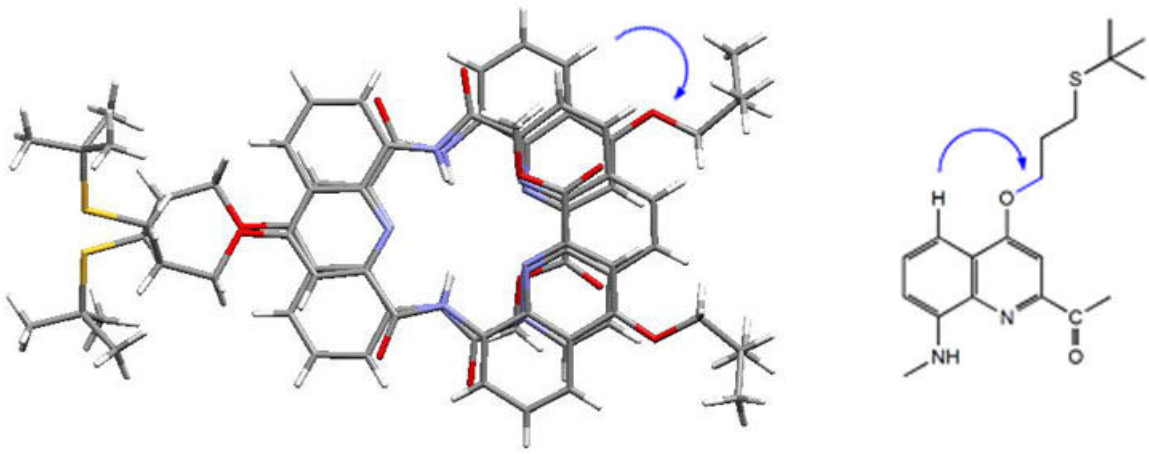

Figure 5.6 Top view of the crystal structure of **B24**; Included solvent molecules have been omitted for clarity. The blue arrow shows that –O–CH_2 carbon always point away from the hydrogen in position 5 of the quinoline

The principles used to design the folded conformation of these oligomers essentially are the hydrogens bonds between consecutive units within the sequence. However, the solid state structure shows extensive aromatic overlap which plays an important role in the stabilization of the helix. This is consistent with the results obtained in the solution phase NMR studies in polar and protic solvent. Computational studies may provide an estimation of the strength of interaction between these stacked aromatic, but have not yet been undertaken. Nevertheless, a simple observation of the structure reveals that intramolecular π-stacking is extensive in **B23**, **B24** and **B29**. As depicted in Figure 5.7, the aromatic ring 1 of the first quinoline matches perfectly above the ring 3 of the phenantroline. So as the ring 2 of the quinoline in position 5 match perfectly with the ring 1 of the central phenantroline (in position 3) and finally, the ring 1 of quinoline in position 2 is exactly above the ring 2 of the quinoline in position 4. This suggests that the curvature of the strand is also governed by the π-π interactions. However, it is interesting to note that in the case of **B23**, the match is not perfect, probably due to steric hindrance due to the presence of the S-tertio butyl protective group.

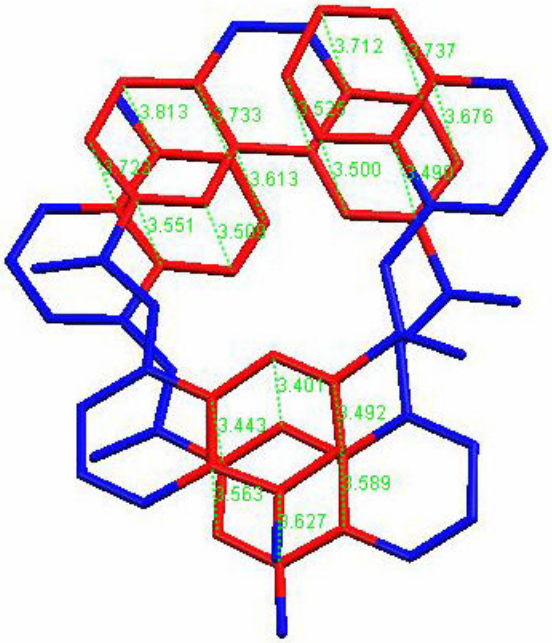

Figure 5.7 Crystal structure of **B24;** solvent molecules, hydrogens, side chains and methyl ester termination have been omitted for clarity. In red the aromatic rings that match perfectly one upon the other.

Derivative **B24**, crystallize in the space group P-1 with a simple inversion center as unique symmetry operation. It was found to pack in stacks of helices of the same

handedness at regular 10.78 Å intervals (see Figure 5.8). This arrangement seems to be held by intermolecular π-stacking interactions since no hydrogen bonds connect two consecutive pentameric units, thus creating parallel supramolecular nano-tube in the solid state. This demonstrates again the important role of aromatic interaction in this phenantroline containing oligomers. Furthermore, the pentameric units arrange in a herringbone motif, where the quinoline side chains, isobutoxy and *tert*-thiobutoxy, individually form the columns. Indeed, as it is shown in the top view of Figure 5.8, in the crystal lattice the side chains stack one upon the other.

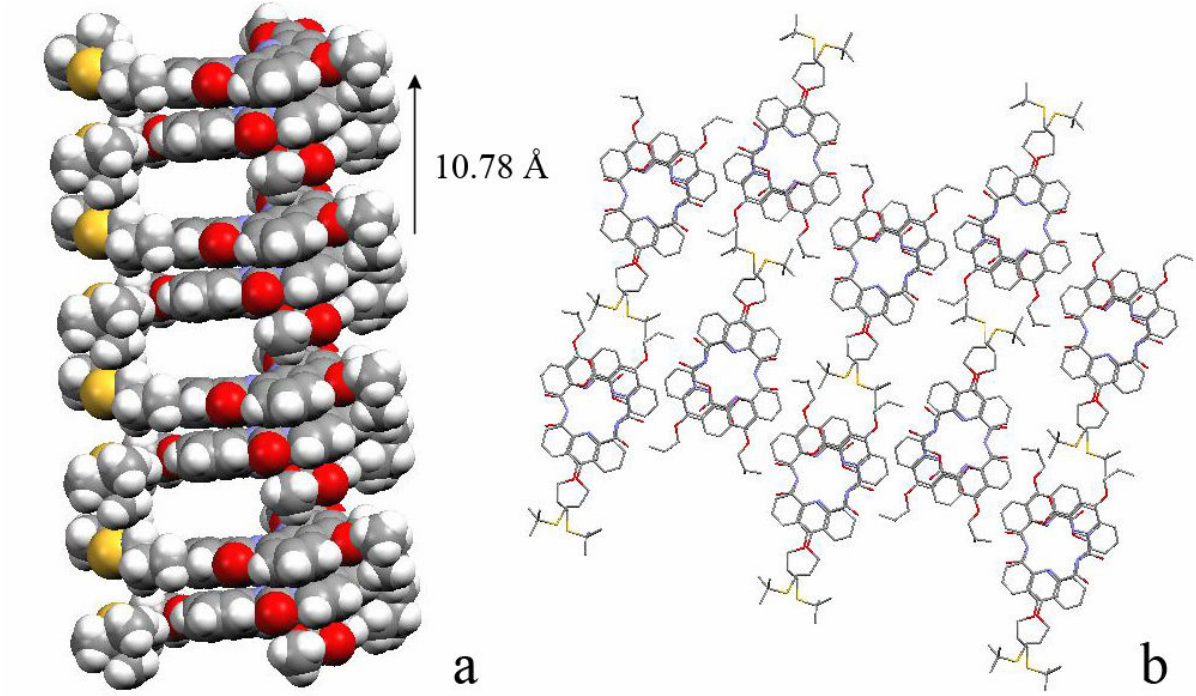

Figure 5.8 (**a**) Side view (**b**) Top view of a portion of a layer containing the helical arrangement of crystal packing of **B24** (**a**) pitch height (**b**) herringbone motif

The structure obtained for **B24**, also allows us to rate the quality of the prediction made by very simple molecular modelling methods as explained before. Figure 5.9 shows the superimposition of the helix of **B24** in the solid state, and the helix predicted for **B24** by an energy minimization using the MM3 force field in Macromodel. A side view of the helix shows an almost perfect prediction of its diameter and of the pitch, within a root mean square deviation of less than 5 %. The top view shows something even more remarkable; the aromatic π-stacking has been predicted, even thought it has not been explicitly implemented during the simulation. However, the experimental structure looks

more bent than the calculated one, the aromatic effect is certainly underestimated in this case.

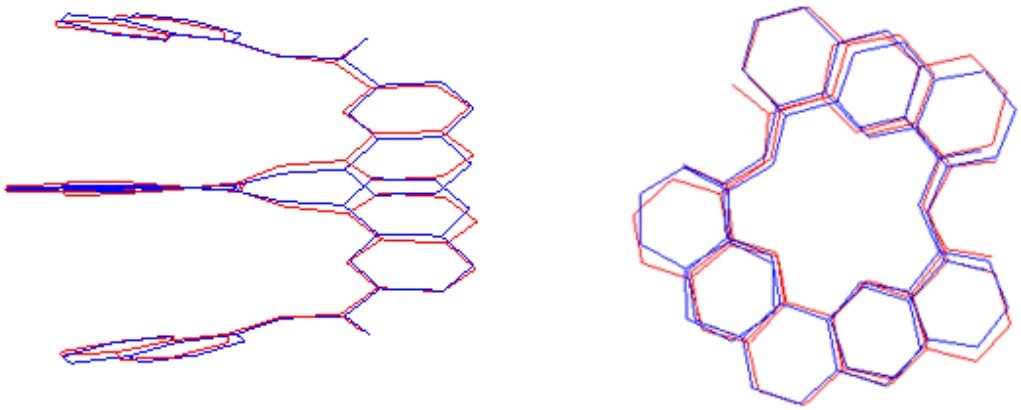

Figure 5.9 Superimposition of experimental (blue) and simulated (red) structures

5.4 Concluding remarks

In light of the remarkably consistent reliance of biological systems on polymeric agents to perform complex chemical tasks, it is very tempting to conclude that unnatural polymeric agents will also prove to be capable of performing useful functions, such as mimicking the structure and the functionality of enzymes active site. In this chapter, we have demonstrated that the great ability to design foldamers open the way to structures with well-defined and predictable shapes, notably through computational simulation based on simple molecular mechanics force field. We were able to determine a sequence of monomeric building block to design the shape of a sulfur suprachelate in order to obtain a complexation shell capable of reaction with d-block metal.

In this Chapter, the synthesis and the characterization of the pre-designed foldamer are presented and the solid-state conformation of the experimental structure confirms the theorical prediction. Conformations of the helices were studied in solution and in the solid state and they show a strong helical character. We also demonstrated that, the helices are held merely by π-stacking interactions in the solid state as well as in solution. This is of a major importance since most of the helical arrangements reported in literature are held by hydrogen bond interactions. The thiol functions deprotection step was successfully performed and reported. Free SH groups are readily prepared for further functionalization.

Preliminary results obtained about complexation of iron-carbonyl core on the free thiol chelate thus, obtained are presented in the next chapter.

6. Iron-Carbonyls Complexes

Although known for more than 75 years [195], the sulfur-containing binuclear complexes of iron have recently experienced a renaissance as interesting synthetic targets as they closely resemble the active site of iron hydrogenase. Model complexes that exhibit catalytic features related to those of the iron hydrogenases have so far relied solely on propyldithiolate (PDT) or azadithiolate (ADT) bridges. For example, Rauchfuss and co-workers have demonstrated that $[(\mu\text{-PDT})Fe_2(CO)_4PMe_3(CN)]^-$ serves as a catalyst for electrochemical hydrogen evolution [196]. In parallel, Darensbourg and co-workers have reported that $[(\mu\text{-H})(\mu\text{-PDT})Fe_2(CO)_4(PMe_3)_2]^+$ is a catalyst for H_2 / D_2 scrambling [25] and Ott *et al.* have recently reported that $[(\mu\text{-ADT})_2Fe_2(CO)_6]$ serves as a catalyst for electrochemical hydrogen production [27]. For a comprehensive review on abiological iron-carbonyl cluster see ref. [197].

In this chapter, we have pursued to use the compounds synthesized in Chapter 3 and 5 as new classes of ligand for binuclear iron complexes. We thus open a new field of investigation, using supramolecular self-assembly as chelate for d-block metal to mimic the active site of hydrogenase.

6.1 Ferrocene-cysteine/iron-carbonyls derivatives

6.1.1 Deprotection of side chain protective groups

The experience gained in Chapters 2 and 3 about protection of thiol led us to use Trt group as protective group because it is the easiest to cleave. Unfortunately, as explained in chapter 3, attempts to couple trityl-protected dipeptide to ferrocene mono or dicarboxylic acid failed. Therefore, for dipeptide derivatives the *tert*-butyl protective group was chosen

as protective group. *Tert*-butyl is the better compromise between stability, availability, steric hindrance, and ease of synthesis. However, the cleavage, in two steps synthesis, is not as straight forward as the one-step deprotection of trityl group.

Free thiol derivatives **33a**, **33b**, **33c** and **33d** were prepared from the deprotection of **27a**, **27b**, **28c** and **28d** respectively (see Figure 6.1). Compounds **27a** and **27b**, are protected with the Trityl group. This group is easily removable, in one-step, in TFA, to yield **33a** and **33b**. An excess of triisopropylsilane (2 eq.) is also added to the mixture to quench the resulting carbocation. However, the first attempts to obtain the free thiol failed because of degradation of ferrocene. We assume that this degradation is due to the oxidation of iron(II) to iron(III) catalyzed by the acidic media. This challenge can be easily overcome by the addition of a large excess of Phenol (10 eq.) in the reaction mixture. Indeed, presence of phenol prevents ferrocene to be spoiled, acting as an anti-oxidant.

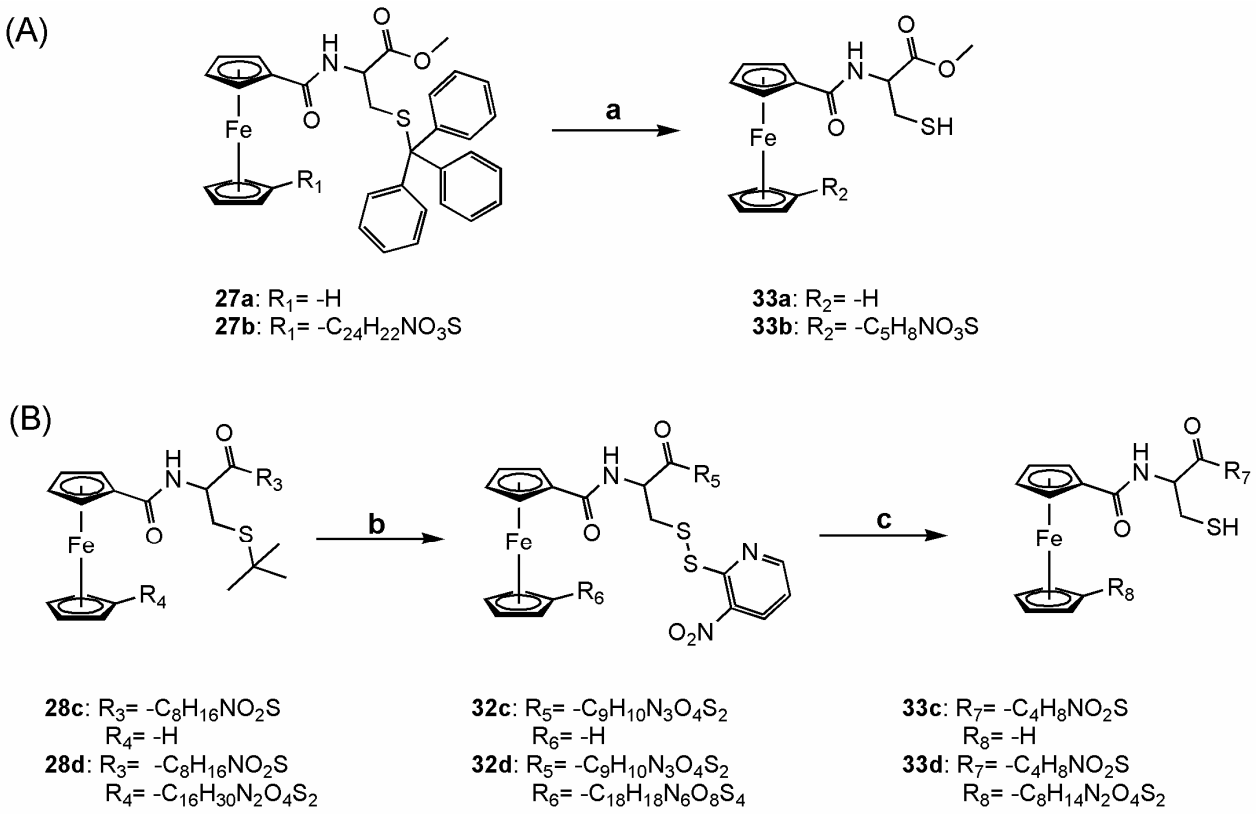

Figure 6.1 Deprotection of (**A**) trityl and (**B**) tertio-butyl protective groups on ferrocene-peptides derivatives. Reactions conditions are: (**a**) TFA, TIS (2 eq.), Phenol (10 eq.), 2 h, rt; (**b**) NpySCl, acetic acid, 6 h rt; (**c**) tri-n-butylphopshine, acetone/water, 12 h, rt.

Compounds **28c** and **28d** are protected with *tert*-butyl group; this protective group is cleavable in two steps involving: (i) the substitution reaction in presence of para-nitro-

pyridine sulfenyl chloride, in glacial acetic acid and, (ii) the subsequent reduction of the disulfide bridge with tri-n-butylphosphine in aqueous media. The free thiols thus obtained should be carefully handled (protection from oxidation sources such as water and oxygen) and preferably used within a couple of days. **33a**, **33b**, **33c** and **33d** were extensively characterized using all standard analytical methods along with electrochemical measurement. Results are discussed partly in this chapter and partly in chapter 3.

6.1.2 Complexation with Iron-carbonyls

The preparation of diiron dithiolate complexes by oxidative addition of thiol to iron(0) carbonyl compounds can be traced back more than half a century [198]. Many diiron complexes with the general formula $[(\mu\text{-SR})_2Fe_2(CO)_6]$ can be obtained by using the traditional protocol described in ref. [18, 199, 200]. Iron carbonyl dissolved in dried $CHCl_3$ is added to the sulfur containing ligand dissolved in MeOH. The resulting mixture is refluxed for 1 h at 90°C. A change in colour from deep green to deep red, consistent with a change in oxidation degree of iron, indicates that reaction occurs. The work-up varies with the type of the sulfur ligand used for complexation. If a column chromatography purification step is needed it was performed by flash chromatography on silica gel. Other groups [38] reported purification on Al_2O_3, but in our hand the separation was not accurate enough. The Fe-CO complexes thus obtained are air-stable and more generally relatively stable in the solid state but decompose slowly in solution and especially in chlorinated solvents such as chloroform. We assumed that one of the reactions that occurs in chlorinated solvents is the oxidation of iron(I) to iron(II) or (III) followed by the precipitation of iron chloride. Moreover, we have also noticed that compounds are not stable at vacuum for a long time. It is assumed that carbonyls are probably pumped out of the coordination sphere by reduced pressure.

$[Fc\text{-}Cys\text{-}OMe]_2(Fe_2(CO)_6)$ **35** was synthesized according to the protocol previously described. The purification step consists of precipitation from cold methanol. After filtration, the product was obtained in good yield, as a dark-red crystalline powder.

$Fe[C_5H_4\text{-}CO\text{-}Cys\text{-}OMe]_2(Fe_2(CO)_6)$ **36** was synthesized in a diluted system so as to avoid polymerization. Unfortunately, in diluted system the reaction is hindered. However, we were able to isolate product from a complex reaction mixture by column chromatography.

$[Fc\text{-}Cys(Fe(CO)_3)\text{-}Cys(Fe(CO)_3)\text{-}OMe]_2$ **37** was synthesized according to a similar procedure. Nevertheless, in this case, an additional purification step was also needed since

the precipitation from cold methanol yielded a mixture. Purification by column chromatography yielded a deep red solid. At this point of the work, it is not possible to determine the exacte composition of the product with standard analytical methods, since no mass peak were detected by ESI masse spectrometry (the different possibilities for the structures are presented in Figure 6.9.

One of the major side product obtained during the complexation step are the disulfide-bridged compounds. Indeed, either intermolecular or intramolecular S-S bond, easily form by oxidation. Two of these side products, **34a** and **34b**, have been isolated and characterized as depicted in Scheme 6.1.

Initial attempts to synthesize $Fe[C_5H_4\text{-CO-Cys-Cys-OMe}]_2(Fe_2(CO)_6)$ from reaction of the bis-dipeptide **33d** with stoichiometric amount of iron carbonyl precursor in refluxing methanol were not successful as the target product could not be separated from the complex reaction mixture. It is assumed that chain polymerization took place and multiple products are formed even when reaction takes place in large dilution. No further attempts were tried to get products from this reaction.

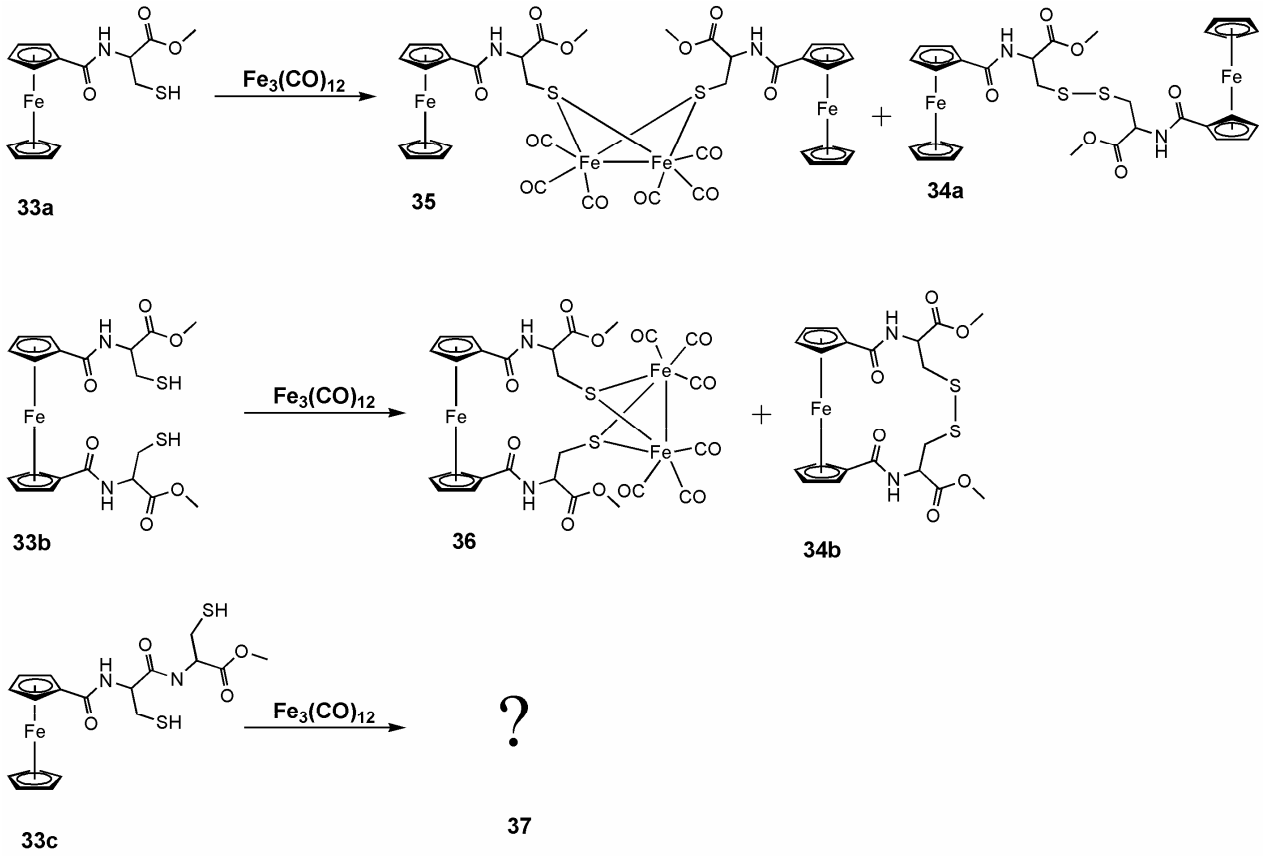

Scheme 6.1 Reaction of free thiol-containing compound with iron carbonyl with three different sulfur ligand. (**a**) $Fe_3(CO)_{12}$, MeOH, reflux, 1 h.

6.1.3 Characterization

Compounds were fully characterized using standard spectroscopic techniques. The signals of the carbon of the metal carbonyl are observed at 208 ppm in ^{13}C NMR in $CDCl_3$, and thus confirmed the complexation with the diiron core. The ^{1}H and the ^{13}C NMR spectra both show that the bis(ferrocenoylcysteinyl-*S*) diiron complex obtained is a mixture of three different conformation e,e (**35a**) e,a (**35b**) a,a (**35c**) isomers (e, equatorial; a, axial). The e,e : e,a : a,a ratio is about 1:6:1 as determined by integration on the ^{1}H NMR spectrum. We assumed that the major isomers is the e,a since the geometry seems to be less hindered. This kind of geometrical isomerization, derived from the orientation of the C_α atom on the bridging thiolates, has previously been reported for $[(\mu\text{-}RS)_2Fe_2(CO)_6]$ complexes ($R = CH_3$, CH_2CH_3, $CH_2C_6H_5$) by King [198] and Seyferth [201, 202]. No isomeric effects were observed for derivatives **36** and **37**.

EI mass spectrometry measurements also give clues about the composition of this compound. Indeed, the $[M]^+$ peak is one of the strongest signal and the base peak is a fragment of the composition $[M - 6CO]^+$ this kind of fragmentation has already been reported for iron carbonyl complex [203].

The UV / Vis spectra of **35**, **36** and **3**7 are dominated by a strong absorption in the visible region respectively at 334 nm, 333 nm, and 336 nm (as it is shown in Figure 6.2). The red colour is attributed to this absorption in the visible region with a maximal extinction coefficient of 9881 $L.mol^{-1}.cm^{-1}$ for **36** and 6111 $L.mol^{-1}.cm^{-1}$ for **37** which is characteristic from metal-to-ligand charge-transfer transitions in iron-carbonyl core [204]. Intense absorption in the 330 – 380 nm region is characteristic of both {2Fe2S}- and {2Fe3S}- systems possessing metal-metal bonds. A second intense absorption is visible around 450 nm, attributed to metal-to-ligand charge transfer in ferrocene moiety. Thereby suggesting that, these spectra can be regarded as a linear combination of the spectra of ferrocene-peptide derivatives and iron carbonyl complex.

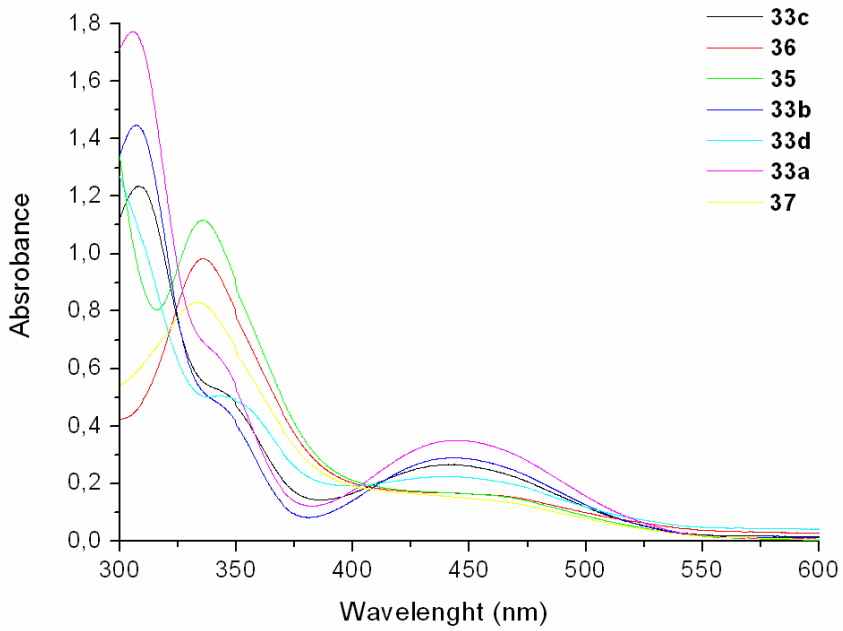

Figure 6.2 Comparison of UV Absorption spectra for ferrocene-peptide and ferrocene-iron-carbonyl complexes.

IR spectrum measured as KBr disks also confirms formation of sulfur-iron-carbonyl complexes with strong CO stretch bands observed around 2000 cm^{-1}, this vibration is characteristic from terminal carbonyls in iron-carbonyls derivatives, no bridging CO stretch vibration are observed in the IR spectra. For example, in the IR spectra of **35**, five C=O stretch vibration bands were observed at 2073, 2031, 2001, 1976 and 1957 cm^{-1} (as it is shown in Figure 6.3). Even though CO scrambling is known to be extremely fast in iron-carbonyls type complexes, the time scale of IR measurement is even faster and therefore, allow us to conclude that the multiple CO bands confirm the presence of different isomers.

Table 6.1 Summary of selected IR and NMR data for **33a**, **33b**, **33c**, **35**, **36** and **37**

Compound	ν (NH valence) [(a)]	ν ($C=O_{ester}$ valence) [(a)]	ν ($C=O_{amide}$ valence) [(a)]	δ_{NH} [(b)]
33a	3299	1745	1635	6.58
33b	3294	1752	1654 / 1628	7.55
33c	3284	1747	1654 / 1624	7.20 / 6.64
35	3401	1748	1636	6.63
36	3327	1753 / 1729	1649	7.04 / 6.46
37	3284	1745	1644	7.71 / 7.53

Measured as KBr disks for IR and in CDCl3 for NMR and given [(a)] in cm^{-1} [(b)] in ppm

A summary of IR data of peptide region for **35**, **36**, **37** are given in Table 6.1 along with the data collected for their precursors: **33a**, **33b** and **33c**. NH stretch bands are observed below 3400 cm^{-1} for **36** and **37**, this indicates that peptide strands seems to be H-bonded. Nevertheless, amide vibration band is significantly shifted to larger values in the case of **35** and **36**, which seems to indicate a change in the pattern. Signals for **37** are broader. It is therefore difficult to point out clear trends.

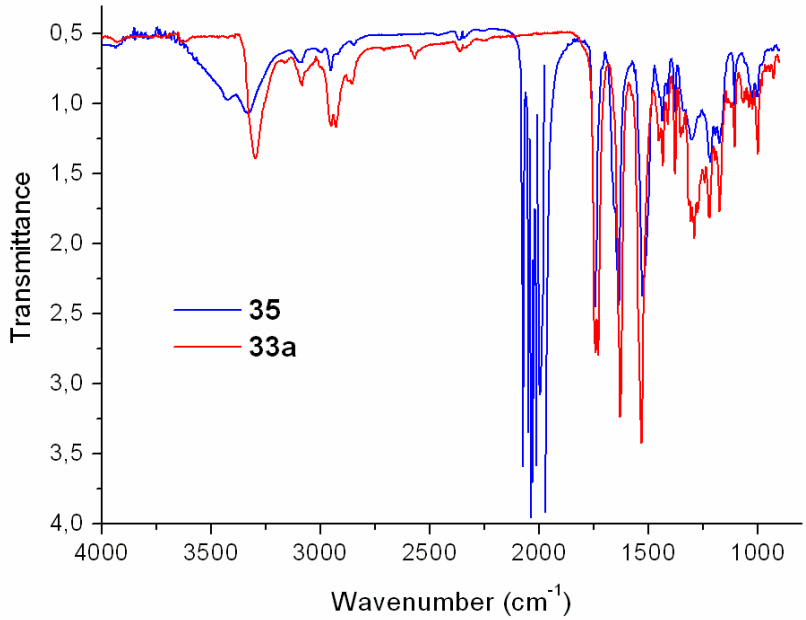

Figure 6.3 Comparison of IR spectra of **33a** and **35**; the presence of carbonyl band confirms formation of the target compound.

Questions arise about the intramolecular H-bond pattern discussed in chapter 3 and observed for **33b**. We attempt to answer these questions by using Circular Dichroism (see Figure 6.4). No Cotton effect, and therefore, no chiral activity are observed for compound **36**. The disubstituted ferrocene **33b**, which is a chiral compound according to the strong cotton effect observed around 450 nm, seems to lose its chirality during the complexion with the iron carbonyl core. We assume that the intramolecular H-bonds, which results in the helical chirality, are broken during the complexation step. This hypothesis is supported by the shift of vibrational NH bands observed in IR, meaning a change in H-bond pattern probably from intramolecular to intermolecular.

Nevertheless, a weak negative Cotton effect is observed at 366 nm in the CD spectra of **36**, this is attributed to iron carbonyl core.

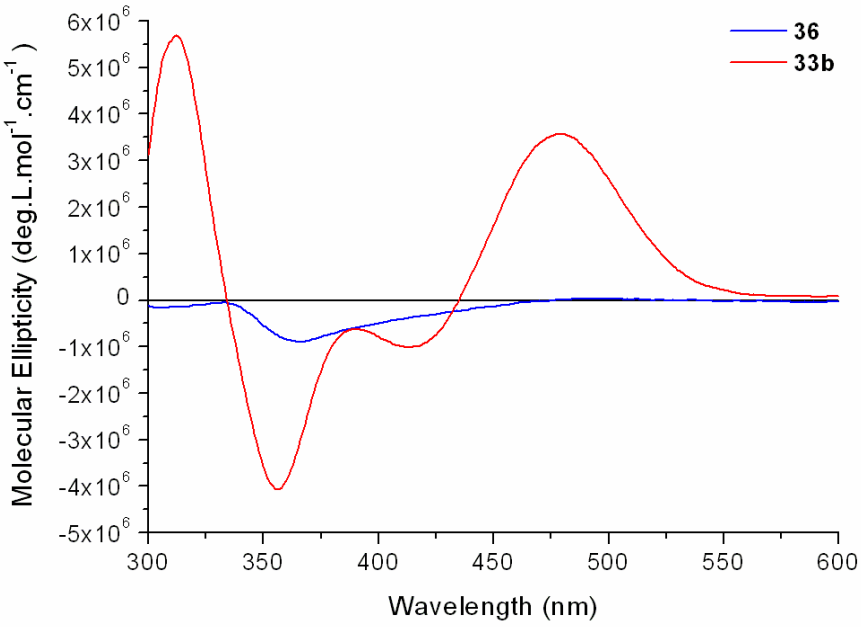

Figure 6.4 Comparison of CD spectra of **33b** and **36**. Disubstituted ferrocene lost its chirality after complexation with iron-carbonyls

6.2 Electrochemical properties

6.2.1 Electrochemistry

To assess a potential electron transfer from the Fe(II) core of the ferrocene to the Fe(I) core of the iron carbonyl, cyclic and square wave voltammograms were recorded for **35**, **36** and **37**. This is of particular interest since no electrochemical data concerning electron transfer between ferrocene and iron carbonyl core have been reported in the literature to date. Nevertheless, peak frequency shifts during redox processes in iron carbonyl-attached biferrocene and terferrocene have already been monitored by the IRAS technique, the authors suspect electron communication between the two metal cores [205].

The cyclic voltammogram of **36** in CH_3CN with *tert*-butyl ammonium as supporting electrolyte shows one anodic redox process at 0.468 V (vs. Fc / Fc^+) with an intensity of 34.8 µA and three cathodic redox processes at -1.73 V, -0.642 V and 0.358 mV with respective intensity of 50.1 µA, 10.1 µA and 0.9 µA. The cathodic process at 0.358 mV and the anodic process at 0.468 mV correspond to the results obtained for **33b**, which is the precursor of **36**. These signals are attributed to the one-electron oxydo-reduction of

disubstituted ferrocene. This process is assumed reversible when the current is reversed at 0 mV as it is shown as insert on Figure 6.6. Moreover, the process completes the rule of Randles-Sevcik (see Equation 6). As it is shown as insert on Figure 6.5 the intensity of the redox wave at 0.468 mV proportionally decreased with $\sqrt{\nu}$, with a $\Delta E_p = 45(5)$ mV.

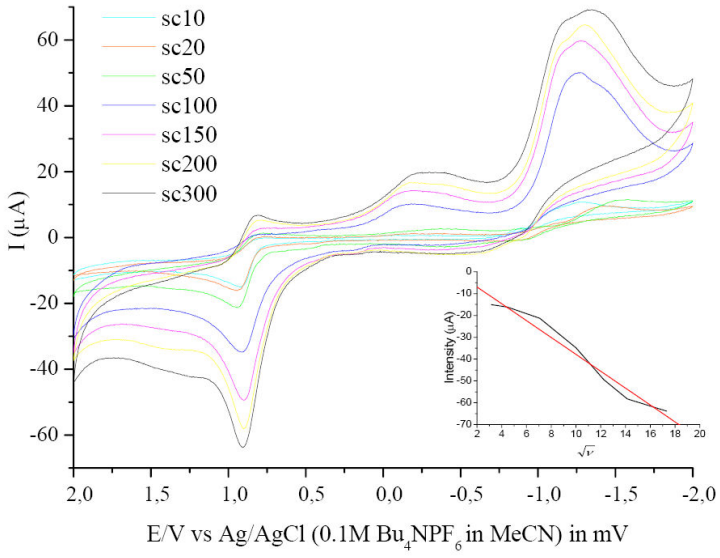

Figure 6.5 Shape of the CV of **36** with different scan rate. In insert, the Randles-Sevcik plot (black) of **36** and its linear fit (red)

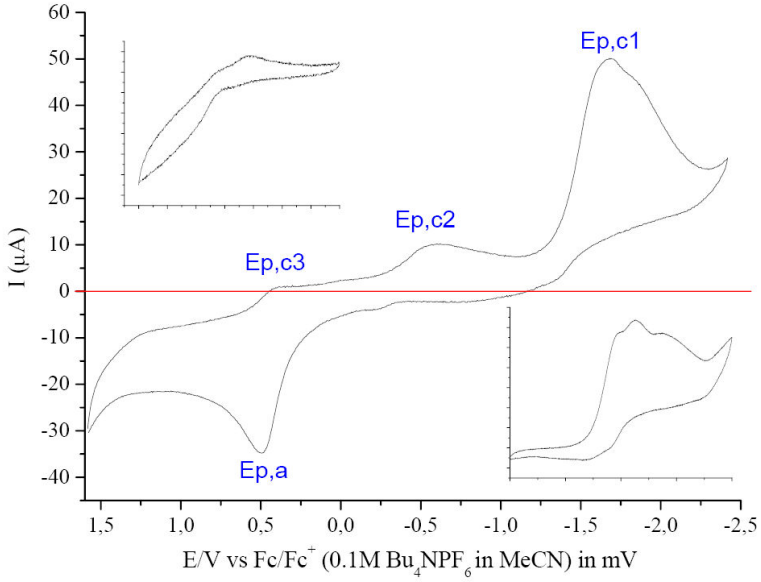

Figure 6.6 Cyclic voltammogram of **36** measured between -2.4 V – 1.6 V in CH_3CN with Bu_4NPF_6 as supporting electrolyte. The insert represent the cyclic voltammogram of **36** when the potential varied between -2.4 V – 0 V (bottom) and 0 V – 1.6 V (top)

$$\Delta E_p = 2.218\frac{RT}{nF} = \frac{57}{n}mV \qquad 6$$

$$I_p = -0.446 \times nFA \times [Ox^{n^+}] \times \sqrt{\frac{nF\nu D}{RT}} \propto \sqrt{\nu} \qquad 7$$

The cyclic voltammogram of **37** in CH_3CN shows one anodic redox process at 0.250 V (vs. Fc / Fc^+) with an intensity of 15.8 µA and three cathodic redox processes at -1.56 V, -0.89 V and 0.163 mV with respective intensity of 6.3 µA, 4.6 µA and 8.4 µA. The main redox process is attributed to the one electron oxydo-reduction of monosubstituted ferrocene. This signal is assumed to be reversible when the current is reversed between 0 and 1 V with a ΔE_p = 44(5) mV.

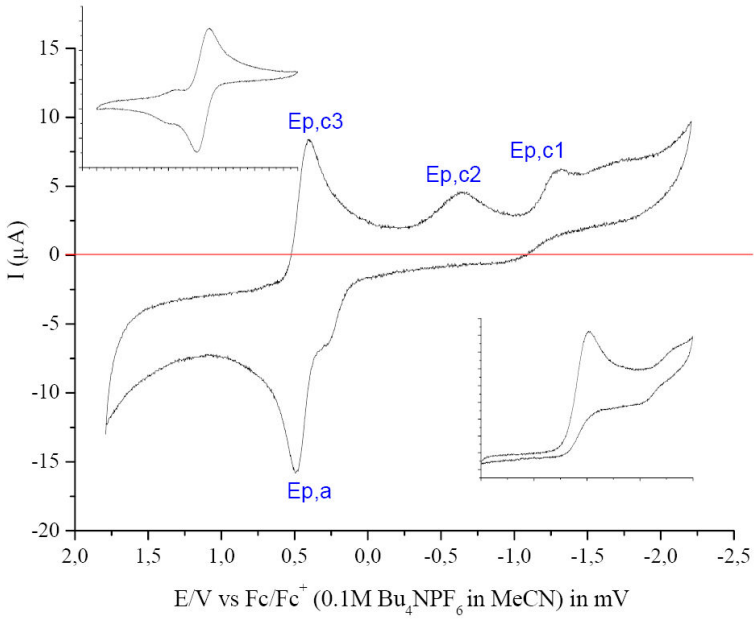

Figure 6.7 Cyclic voltammogram of **37** measured between -2.4 V – 1.6 V in CH_3CN with Bu_4NPF_6 as supporting electrolyte. The insert represent the cyclic voltammogram of **37** when the potential varied between -2.4 V – 0 V (bottom) and 0 V – 1.6 V (top)

In both cases, the reversible one-electron redox process of ferrocene is still present. However in both cases, the $E_{1/2}$ is slightly shifted to higher potential from 398 mV, observed for **33b**, to 420 mV, observed for **36**, and from 196 mV, observed for **33a**, to 210 mV, observed for **35** in the case of the monosubstituted derivative. This shift seems to indicate that an additional electron withdrawing effect occurs for the ferrocene moiety when the iron carbonyl core is present in the molecule. However, because of the small

variations observed, no clear trends could be isolated from this experiment. Further electrochemical measurement has to be done in order to elucidate whether or not electronic communication occurs between ferrocene and iron carbonyl core. One of the methods of choice often used for the evaluation of electronic properties of iron-containing compound is the Moessbauer spectroscopy.

6.2.2 Moessbauer Spectroscopy

Moessbauer parameters for the derivatives **35**, **36** and **37** are given in Table 6.2. A rigorous analysis shows a better fit of the spectrum by two, overlapping, subspectra with different I.S. and Q.S. (i) The first subspectrum (depicted in green colour in Figure 6.8, for other spectra see Appendix) as the typical value observed for Fe(I) carbonyl complexes and are consistent with those reported earlier [18, 23, 206]. However, the authors reported a better fit of the spectrum, by two, overlapping, quadrupole split doublet with similar I.S. but different Q.S. (see Table 6.2). They assumed that the origin of the differentiation of the iron sites in the solid state is due to the positioning of the ethanethiolate CH_2 above one of the iron atoms. (ii) The second subspectrum corresponds to the Cp-Iron complex. The isomer shifts are in the range of those measured for ferrocene in previous studies. The value of quadrupole split measured on these subspectra are also consistent with the one obtained for ferrocene. However, the values of the quadrupole splitting are lower than for ferrocene-peptides derivatives. It has been noted before that the quadrupole splitting of ferrocene decrease when ferrocene is substituted with electron-withdrawing substituents. These results are consistent with the shift observed for electrochemical measurement; the presence of iron carbonyl in the molecule has an influence in the electronic environment of the iron of the ferrocene moiety. However, here again, the shifts observed are not large enough to conclude.

Table 6.2 Moessbauer parameters ($mm.s^{-1}$) of {2Fe2S}-carbonyl assemblies

Compounds	Isomer shift (I.S.)	quadrupole split (Q.S.)
$[Fe_2(SC_3H_6S)(CO)_6]$ [(a), (b)]	0.041	0.871
$[Fe_2(SC_3H_6S)(CO)_6]$ [(a), (b)]	0.031	0.702
$[Fe_2(SCH_2C(CH_2OH)S)(CO)_6]$ [(a), (c)]	0.011	0.950
$[Fe_2(SCH_2C(CH_2OH)S)(CO)_6]$ [(a), (c)]	0.011	0.750
Subspectra 1 of **35** [(a)]	0.046	0.942
Subspectra 2 of **35** [(a)]	0.531	2.332
Subspectra 1 of **36** [(a)]	0.045	0.893
Subspectra 2 of **36** [(a)]	0.512	2.295
Subspectra 1 of **37** [(a)]	0.048	0.980
Subspectra 2 of **37** [(a)]	0.527	2.324

(a) Measured as solid samples at 80 K, [(b)] from ref. [18], [(c)] from ref. [23].

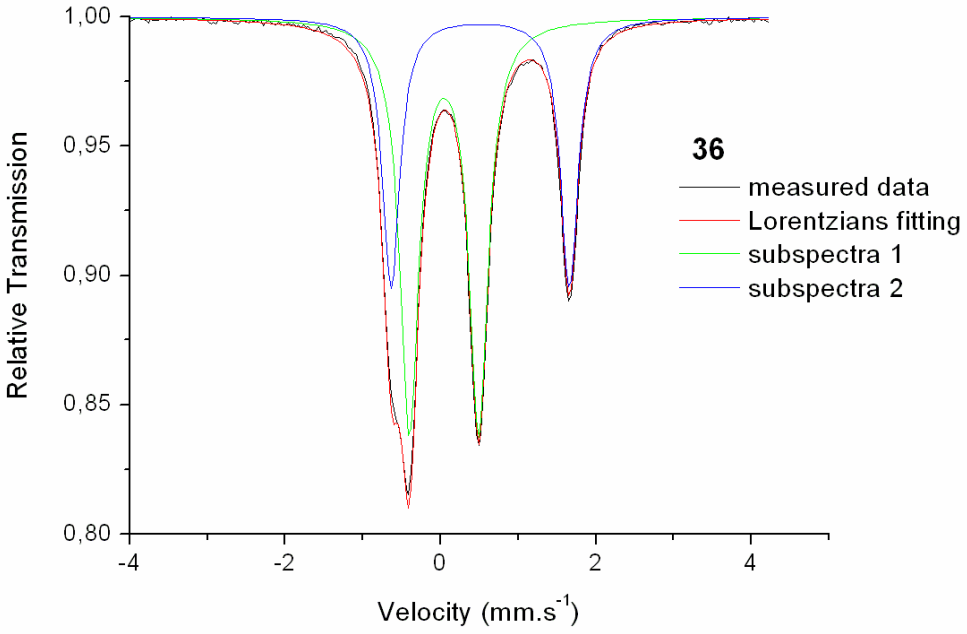

Figure 6.8 Selected Moessbauer spectrum of **36** recorded at 80 K as solid state samples

From the relative intensity of the signal, it is possible to deduct the relative proportion of the different iron sites in a same molecule. It is interesting to note that in the case of **37**, a 1:1 ratio was measured (see Table 6.3) as is the case for **35**. Even though we had to go through several approximations and uncertainties, such as the Debye-Waller factor for the position of iron, the statistical fit errors and the saturation effect we had to

correct our structural prediction. We assume that the compound **37** has a dimeric structure as it is depicted in Figure 6.9. Three equivalent possible structures are represented. The iron carbonyl core can be chelated either by the first cysteines attached to the ferrocene **37**$^{1,1'}$ or by the second cysteines of peptide strands **37**$^{2,2'}$ or by both, the first and the second **37**$^{1,2'}$ (see Figure 6.9). In the later conformation, both ferrocene-peptide residues are not equivalents and therefore this possibility can be eliminated too. Indeed, according to the NMR spectra, the molecule has a plane of symmetry. Unfortunately, the mass peak is not visible in mass spectra, and until now we were not able to grow single crystal of X-ray quality, the structure remains unsolved yet.

Table 6.3 Moessbauer relative peak intensities

Compounds	Area [%]	Relative intensity [%]
Fe-CO part of **35**	7.15	54.98
Fe-Cp part of **35**	6.69	45.02
Fe-CO part of **36**	15.84	62.49
Fe-Cp part of **36**	10.45	37.51
Fe-CO part of **37**	7.54	51.71
Fe-Cp part of **37**	8.08	48.29

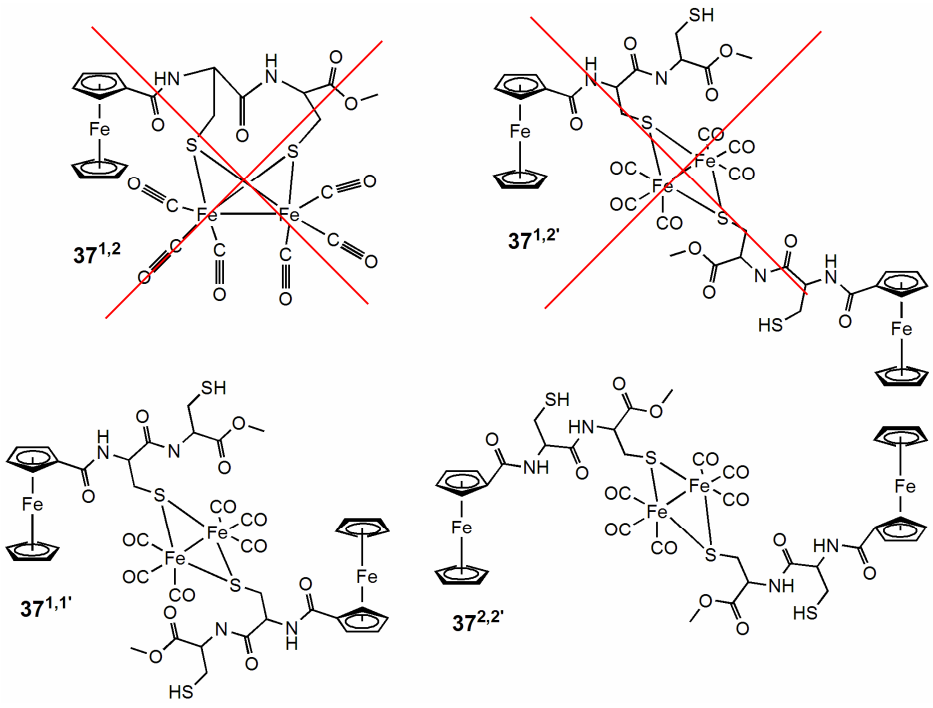

Figure 6.9 Structural prediction revised according to Moessbauer measurements correlated with elemental analysis collected on **37**

After this relative success obtained from the complexation of iron carbonyl core to the ferrocene-peptide ligand, we were intrigued by the possibility of transferring this technique for complexation of the iron-carbonyl core to the oligoquinoline ligand.

6.3 Complexation with Quinoline derived oligomer

Several synthetic problems not solved yet prevent us to finish this part of the work. However, some preliminary results can be presented. For derivatives **B13**, **B29** and **B30** (see chapter 5) complexation with iron carbonyl derivatives was tried as it is depicted in Figure 6.10. Unfortunately, these reactions were performed only one time and therefore optimization of the yield and the isolation remain necessary. However, some promising trends have been observed.

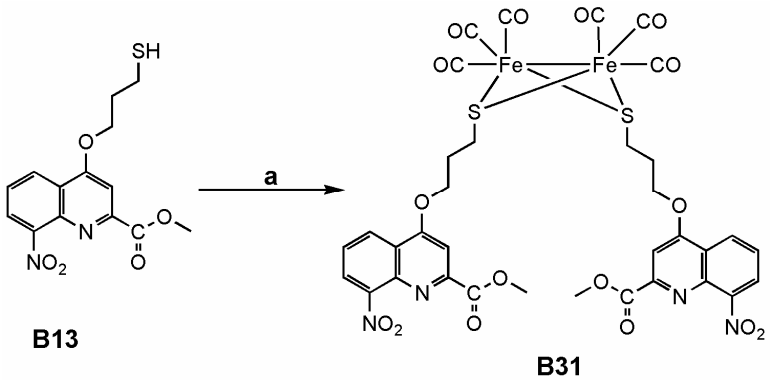

Figure 6.10 Synthesis of iron-carbonyl derivatives for the quinoline series. With standards reaction conditions (a) $Fe_3(CO)_{12}$, 2 h, MeOH reflux.

B31 was isolated without majors difficulties. The spectroscopic analysis, notably ^{13}C NMR, along with the ESI-TOF mass spectrometry validates the formation of the desired product. As for the ferrocene derivatives, characteristics signal of the carbon of the carbonyl group are observed around 200 ppm. ESI-TOF High resolution mass spectra confirm the composition of the proposed compounds. This reaction was considered as a test reaction; therefore, electrochemical properties of **B31** were not extensively studied as it was the case for **35**, **36** and **37**.

Reaction of the pentamers with $Fe_3(CO)_{12}$ yield a complex reaction mixture. Analysis by mass spectroscopy confirms that iron carbonyl derivatives are formed. From NMR data we also suspect that a major part of the starting materials is converted to disulfide-bridged derivatives; either intermolecular bridges or intramolecular disulfide bridges are formed. These very exciting preliminary results led us to push further the investigations. At the first place, synthesis of the pentamers has to be scaled up and then reactions conditions for the complexation and purification steps have to be optimized.

6.4 Concluding remarks

In this part, we have presented the synthesis and the characterization of a new class of sulfur rich iron carbonyl cluster with ferrocene as scaffold. The protective group strategy for derivatives **28a**, **28b**, **28c** prepared in Chapter 3 was optimized and it appears that for steric reasons, two different protections are needed, the Trityl group for amino acid derivatives **27a** and **27b** and the tertiobutyl for dipeptide derivatives **28c** and **28d**. The iron carbonyl complex were subsequently synthesized by a simple stoichiometric oxidative addition of $Fe_3(CO)_{12}$ on **33a**, **33b**, **33c** and **33d** to yield respectively **35**, **36**, **37**, and a complex reaction mixture in the case of **33d**. Cyclic and square wave experiment led on these compounds reveal that the one electron redox process of ferrocene might be slightly affected by the presence of the iron-carbonyl core. The same trends are observed in Moessbauer spectroscopy. It is suspected that iron-carbonyl core have an electron withdrawing effect on the ferrocene moiety. However, for infrared spectroscopy, the spectra of Ferrocene-iron-carbonyl conjugates can be regarded as a linear combination of Ferrocene-peptides derivatives and sulfur rich iron-carbonyl derivatives.

Besides, the same reaction of complexation was performed on oligoamides, and promising preliminary results were observed. A quinoline iron carbonyl derivatives has been isolated and fully characterized and traces of pentameric derivative of iron carbonyl has been seen. However, this part of the work has still to be continued.

7. Summary & Conclusion

7.1 Summary

Along this PhD, the challenging project of modelling hydrogenase active site was investigated using a multidisciplinary approach; three different techniques were used and the results obtained by these three approaches were interconnected and used in tight relationship. The first one deals with potential scaffolds based on ferrocene-peptide derivatives, therefore coined as *organometallic* approach. The second deals with folded aromatic oligoamides, which was also seen as potential scaffold for hydrogenase mimicry; this part of the work is purely *organic*. Finally, the theoretical predictions by molecular dynamics, performed on these both systems represent the third approach coined as *theoretical*. These three approaches were led in parallel, and a tight connection was kept so as experience gained in one field serves the progression of the other field.

After a brief introduction, the second Chapter of this work deals with the study about different sulfhydryl protecting groups. They were tested in terms of their suitability for the organometallic solution phase synthesis, their technical and commercial availability. This has resulted in the elimination of some of them such as S-tertiobutyl (StBu), and Acetamidomethyl (Acm) because of the stability in the first case and because of the price in the second case. Besides, the carboxylic acid protecting group -methyl esters- was optimized for the different amino acid derivatives. Subsequently, a variety of dipeptides was prepared using the mixed anhydride coupling strategy. They were characterized with either N-Boc protected group or Fmoc. Subsequent removals of the N-terminal protective group yield the free amine dipeptides as methyl esters.

Protected amino acids and dipeptides prepared and tested in chapter 2 were coupled either to ferrocene mono carboxylic acid or to ferrocene 1,1'dicarboxylic acid. For this coupling it is has been found that TBTU and HOBt coupling reagents provided better yield than the mixed-anhydride coupling strategy using DCC or EDCl. A wide range of ferrocenoyl amino acids or peptides with sulfur-containing side chains derivatives was synthesized and fully characterized. A comprehensive study was subsequently carried out. The most interesting observations relate to the question of intramolecular hydrogen bonding and chirality organization around the metallocene backbone, which acts as a template for the organization of the peptide strands, particularly in the disubstituted derivatives. In the solid state, intra- and intermolecular hydrogen bonds are of similar strength and hence other factors may dominate the molecular conformation. In solution, however, intramolecular hydrogen bonding is strongly promoted and the same pattern seems to emerge for most disubstituted compounds ("Herrick conformation"), namely a symmetrical 1,2' orientation of the amide substituents on the Cp ring with two strong intramolecular hydrogen bonds. NMR, IR and CD spectroscopic investigations all support this assumption. However, the spectroscopic and crystallographic properties of $Fe[C_5H_4$-CO-Met-Met-$OMe]_2$ clearly suggest that a racemisation has occurred during the synthesis, presumably in the deprotection step with KOH. The two H-bonded amide groups observed in the IR spectrum and the weak CD signal at about 480 nm support the presence of a diastereomeric mixture. While racemisation is a well known problem in peptide chemistry, this is the first report in the field of ferrocene peptides.

Besides, DFT calculations (B3LYP/LanlDZ) on model ferrocenoyl peptides $Fe[C_5H_4$-CO-Gly-$NH_2]_2$ and $Fe[C_5H_4$-CO-Ala-$OMe]_2$ were performed in order to elucidate the H-bond pattern in terms of energy. The calculations reveal that conformers with different hydrogen bonding patterns have significantly different stabilities, with a stabilization of the system by about 30 kJ mol^{-1} per hydrogen bond. The "Herrick conformation" with two hydrogen bonds is the most stable one, which is in agreement with solid state (X-ray) and solution (CD, NMR, IR) studies. On the other hand, conformers $Fe[C_5H_4$-CO-Ala-$OMe]_2$, which differ only in the amino acid chirality, have similar stabilities with $\Delta E < 10$ kJ mol^{-1}. Due to the small energy differences and the large number of different conformations possible, it is difficult to predict the most stable one by DFT calculations.

The ready preparation of ferrocene peptides with functional side chains opens the way to further derivatization. In particular, thiol derivatives provide easy access to further conjugation, for example with fluorescent dyes, by reaction with maleiimide or iodo acetic acid reagents or with metal from the d-block entail. In our group, these compounds are seen as potential chelate for nickel or iron. Therefore, some questions arise concerning sterical and mechanical interactions that occur in this family of compounds. We have pursued the answers to these questions using Molecular Dynamics (MD). In chapter 4, parameter set for ferrocene-bearing peptides has been developed for the all-atom CHARMM molecular mechanics force field. The development of this parameter was performed on the basis of chemical best guess corrected with quantum mechanic calculations using AFMM.

The new parameters were subsequently tested and validated on independent, experimental structures and the results obtained are overall in good agreement with experimental data. Impressive energy minimization and molecular dynamics of the Fc-(D-Ala-D-Pro)$_2$ crystal structure led to unit cell dimensions and volume being reproduced within less than 0.1 % of the experimental. Intrinsic geometrical properties of the molecules, such as the intramolecular H-bond pattern were also accurately reproduced.

The force field thus obtained was used in order to study the structures and dynamics of possible hydrogenase mimics. To this end, different model systems were created and simulated. The size of the peptide strands and the incorporation of a nickel core were specifically tested in terms of their geometry and possible steric hindrance. It has been found that ferrocene podand shorter peptides exhibit a larger potential as chelate for nickel. Other experiences demonstrated that from a steric point of view, the attachment of peptides to the ferrocene moiety should be performed to the C-terminus of the peptide strands instead of to the N-terminus as it is done in our labs. This has led to a reorientation of the synthetic route. An ethylene diamine linker was attached to the carboxylic group of ferrocene in order to change the C-termination to an N-termination, but also to provide more flexibility to the structure. We assume that preliminary synthetic results are very encouraging.

In chapter 5 of this thesis, another potential scaffold for hydrogenase active site is investigated. Oligoamides based on quinoline and phenantroline amide assembly are known to form well-defined helical arrangements in the solid state as well as in solution.

This ordered arrangement is highly predictable by using commercial MM force fields and this predictability has been used to design folded sulfur-rich ligands for iron carbonyl core. The synthesis, functionalization and structural study of a family of quinoline-derived oligomers was achieved. We emphasize the efficiency of computational prediction and the relative ease of the synthetic production. Solid state and solution phase structural studies, performed on several pentameric derivatives, validate the theoretical prediction performed with Macromodel. Deprotection of thiol moieties is also a success, even though we had to go through several synthetic dilemmas. Conformational study in solution phase and in the solid state reveals strong helical propensities of the pentameric structures, as predicted. NMR experiments demonstrate that helicity is conserved even if H-bonds are broken; helices are then held by π-π interactions.

Finally, folded oligomers with free thiols obtained and characterized in chapters 3 and 5 were used as chelates for an iron-carbonyl core. This part of the work is described in chapter 6. Three ferrocene-peptide-iron-carbonyls derivatives were successfully synthesized and fully characterized. The reaction conditions and the characterizations are presented along with spectro-electrochemical studies on the hydrogenase active site mimics thus obtained. Three different iron-carbonyl complexes were successfully synthesized and characterized. IR, NMR, Voltammetry, UV, and mass spectroscopic analysis all confirm the formation of sulfur iron complexes. Results obtained from Moessbauer spectroscopy gave hints to the structural determination of derivative **37**. Preliminary hints about potential intramolecular electron transfer between the ferrocene moiety and the iron-carbonyl core were observed during the electronic analysis by cyclic voltammetry and Moessbauer spectroscopy. However, the electronic communication between the iron carbonyl core and the ferrocene moiety is not as strong as expected. Set up of electrochemical experiments has to be improved.

The work about metal complexation with oligoquinolines remains in progress, only promising preliminary results are presented.

7.2 Concluding remarks and Outlook

In this thesis, besides synthetic and spectroscopic achievements, we have demonstrated the efficiency of the multidisciplinary approach towards a unique goal; the synthesis of hydrogenase active site mimics. Techniques of one field are being used with great success in another field of research; as theoretical prediction was useful for the design of the supramolecular scaffold, or dynamic studies was useful to understand steric hindrance and gave clues to optimize or to change experimental synthetic pathways. However, the set up of different techniques is surely more time consuming than focusing on one strategy. This work has to be continued. Therefore, we planned to push further theoretical investigation by performing simulation in explicit solvent. X-ray diffraction analysis of derivatives **35**, **36** and **37** could also be helpful for an eventual reorientation of the synthesis in order to synthesize a second generation of mimics. Finally, the reaction conditions for complexation of iron carbonyl cores with oligoamides foldamer will be improved. To perform these achievements, a tight relationship between these three different approaches will be kept.

8 Experimental Section

8.1 Materials and Methods

8.1.1 Materials

Elemental Analysis

Elemental analyses were performed on a Foss Heraeus Vario EL Elementar Analysator in C, H, N mode.

Infrared spectroscopy

Infrared spectra were recorded at 20°C either on Bruker Equinox55 FT-IR spectrometer, or on a Perkin Elmer 1600 series FTIR, in dried $CHCl_3$ or CH_2Cl_2, or between NaCl windows and / or as KBr discs, with a spectral resolution of 2.0 cm^{-1}. The concentration was about 10^{-2} M to 10^{-4} M, unless otherwise noted. Wavenumbers, ν, are given in cm^{-1}.

NMR spectroscopy

NMR spectra of the compounds in Chapters 1, 2, 3 and 6 were determined either on Bruker AM 360 spectrometer, ^1H operating at 360.14 MHz and ^{13}C operating at 95.56 MHz, or on a Varian Mercury plus ^1H operating at 300.07 MHz and ^{13}C operating at 75.46 MHz. 2D spectra were recorded on a Varian Unity 400 spectrometer with an inverse probe and z-gradients. 2D-NOESY spectra were recorded with 0.5 s and 1 s mixing time and compared. NMR spectra of the compounds in Chapter 5 were determined either on a Bruker 400 Ultrashield spectrometer ^1H operating at 400.13 MHz, ^{13}C operating at 100.62 MHz, or on a Bruker 300 Ultrashield Advance II Spectrometer ^1H operating at 300.13 MHz, ^{13}C operating at 75.46 MHz.

Spectra of peptides only are referenced to the residual MeOH signal (3.31 ppm for ^1H, 49.0 ppm for ^{13}C). All others compounds are referenced to the TMS signal for ^1H or of the

residual $CHCl_3$ signal (7.26 ppm for ^1H, 77.2 ppm for ^{13}C). Coupling constants, J, are given in Hz. Concentration of samples are about 10^{-2} M. Spectra are measured at room temperature (293 K) unless otherwise noted.

Mass spectrometry

Mass spectra were measured on a Mat 8200 instrument, EI (70 eV) and FAB (glycerol or NBA were used as a matrix), or on a Finnigan TSQ 700 for ESI-MS. Only the mass peak, the base peak and the characteristic fragments with possible composition are given in brackets. For fragments containing metals, only the isotopomer with highest intensity was described. High Resolution ESI-TOF mass spectra, were recorded on Waters LCT Premier spectrometer in positive modus. Calibration was performed with Leucine Enkephaline.

UV-Visible spectroscopy

UV / VIS spectra were measured in dried CH_2Cl_2 on a Varian CARY 100 instrument in 1 cm quartz Suprasil cells thermostated at 20°C. Absorption maxima, λ_{max}, and molar absorption coefficients, ε, are given in nm and $L.mol^{-1}.cm^{-1}$, respectively.

Circular Dichroism spectroscopy

Circular Dichroism spectra were recorded in dried CH_2Cl_2 on a JASCO J-810 Spectropolarimeter in 1 cm quarz Suprasil cells thermostated at 20°C under inert atmosphere.

Electrochemistry

Cyclic voltammograms and square wave voltammograms in CH_3CN solutions with NBu_4PF_6 as supporting electrolytes were recorded on a Perkin Elmer BES Potentiostat / Galvanostat. A three-electrode cell was employed with a glassy carbon of 1.5 mm diameter as the working electrode, a platinum-wire as the auxiliary electrode and an Ag / Ag^+ as the reference electrode. For determination of the redox potentials, ferrocene was added as internal standard. Measurements were performed in a copper Faraday cage. The oxidation potentials are given as anodic peak potential E_{pa}, and the reduction potentials are given as cathodic peak potentials E_{pc}. Cyclic voltammograms were obtained for 0.5 mM solutions of the analyte in dry acetonitrile, containing 0.1 M tetrabutylammonium hexafluorophosphate at a scan rate of 100 $mV.s^{-1}$, unless otherwise noted. $E_{1/2}$ were calculated from the cyclic voltammograms and are given in mV.

Mössbauer spectroscopy

^{57}Fe Mössbauer spectra were recorded on an Oxford Instruments Mössbauer spectrometer in the constant acceleration mode, by using ^{57}Co / Rh as the radiation source. The measurements were performed on solid samples at 80 K containing a natural abundance of ^{57}Fe. The minimum experimental line width was 0.24 mm.s^{-1}. Isomers shifts were determined relative to α-iron at 300 K.

Mössbauer spectroscopy

^{57}Fe Mössbauer spectra were recorded on an Oxford Instruments Mössbauer spectrometer in the constant acceleration mode, by using ^{57}Co / Rh as the radiation source. The measurements were performed on solid samples at 80 K containing a natural abundance of ^{57}Fe. The minimum experimental line width was 0.24 mm.s^{-1}. Isomers shifts were determined relative to α-iron at 300 K.

X-Ray crystallographic data collection and refinement of the structures

For compounds of then Chapter 3, the crystals were coated with perfluoropolyether, picked up with a glass fibber and mounted in the nitrogen cold stream of a Bruker-Nonius Kappa-CCD diffractometer. Intensity data were collected at 100 K using graphite monochromated Mo-K_α radiation ($\lambda = 0.71073$ Å) of rotating anode setup. Final cell constants were obtained from least squares fit of a subset of several thousand strong reflections. Data collection was performed by hemisphere runs taking frames at 1.5° and 1.0° in ω. Crystal faces were indexed and the Gaussian type absorption correction routine embedded in XPREP was used to correct for absorption. The ShelXTL software package [207] was used for solution and artwork of the structures. Refinement was performed with ShelX97 [208]. The structures were readily solved by direct methods and difference Fourier techniques. Absolute structure parameters were checked by refining the inverse structure and are reliable. All non-hydrogen atoms were refined anisotropically. Hydrogen atoms bound to carbon were placed at calculated positions and refined as riding atoms with isotropic displacement parameters. Hydrogen atoms bound to amide nitrogens were located from the difference map and were isotropically refined with a displacement parameter being 1.2 times the value of U_{eq} of the amide nitrogen atom.

For compound of the Chapter 5, data were collected using a Rigaku Rapid diffractometer equipped with an MM007 micofocus rotating anode generator with monochromatized Cu-

K_α radiation (1.54178 Å) and varimax optics. The data collection, unit cell refinement and data reduction were performed using the CrystalClear software package. The positions of non-H atoms were determined by the program SHELXS 87 and the position of the H atoms were deduced from coordinates of the non-H atoms and confirmed by Fourier Synthesis. H atoms were included for structure factor calculations but not refined. Selected single crystal were mounted on a cryloop under oil and frozen into a N_2 stream at 140 K.
Crystallographic data can be obtained free of charge at http://www.ccdc.cam.ac.uk/cgi-bin/catreq.cgi or from the Cambridge Crystallographic Data Centre, 12 Union Road, Cambridge CB2 1EZ, UK; Fax: (internat.) ++44-1223-336-033; E-mail: deposit@ccdc.cam.ac.uk.

Computational details

A comprehensive description of computational details is given in Chapter 4.

8.1.2 Standard procedures

CH_2Cl_2, Et_3N, DIEA were dried over CaH_2 and distilled under argon prior to use, THF was dried over Na / benzophenone and distilled under argon prior to use. All chemicals as well as other solvents were obtained from commercial sources and used without further purification, unless otherwise noted. All reactions were carried out under inert gas atmosphere in thoroughly dried glassware. The synthesis of the iron-carbonyl complexes were performed under an atmosphere of argon using standard Schlenk techniques. For gravity column chromatography, columns were packed with 0.040 - 0.063 mm silica gel 60 (VWR). For flash chromatography, columns were packed with 0.063 - 0.200 mm silica gel 60 (VWR). For TLC, either plates coated with silica gel F_{254} or plates coated with aluminium oxide were used.

8.2 Syntheses and Characterization of ferrocenoyl compounds

8.2.1 Synthesis of literature compounds

The two steps synthesis of ferrocene 1,1'-dicarboxylic acid

Ferrocene dicarboxylic acid was obtained according to a modified protocol described in ref. [209] for the synthesis of ferrocene monocarboxylic acid.

Fe-(η-C_5H_4-COPhCl) **(1)**: A thoroughly dried 1 L three-necked round bottom flask was equipped with an inert gas inlet and an over pressure outlet. Throughout the ensuing reaction a positive pressure of dry argon was applied to the system through the gas inlet. The flask was charged with 18.6 g (100 mmol) of ferrocene, 73.75 g (250 mmol) of 2-chlorobenzoyl chloride and 300 mL of dichloromethane. Flask was then placed in a water bad equipped with a thermometer. Besides, 35.0 g (250 mmol) of anhydrous aluminium chloride were weighted in a glove box and stocked in a dried Schlenk. When the solution has been chilled thoroughly, the aluminium chloride was added in small portions at such a rate that the reaction remains at room temperature. Appearance of a deep blue colour indicates that the reaction is occurring. This addition required approximately 20 min, and after this completion stirring was continued for 4 h at room temperature. 400 mL of water were added cautiously to quench the reaction, and the resultant 2 phases mixture was stirred vigorously for 30 min. The layers were separated, and the aqueous layer was extracted two times with 100 mL CH_2Cl_2. The combined organic layers were washed with 100 mL of distilled water and 100 mL NaOH 1 M. The organic layer was then dried over $MgSO_4$ and rotary evaporated to yield viscous red oil, which gradually solidified to a dark red solid. Yield: 61 %. $C_{24}H_{16}Cl_2FeO_2$ = 463.13 g.mol^{-1}. Elemental analysis calc. for $C_{24}H_{16}Cl_2FeO_2$: C, 62.24; H, 3.48; found: C, 61.70; H, 3.66. MS (EI): *m/z* = 462 $[M]^+$. ^{1}H NMR ($CDCl_3$): δ 7.45 - 7.30 (8H, m, CH_{cb-ar}), 4.81 (4H, s, $CH_{Cp-ortho}$), 4.69 (4H, s, $CH_{Cp-meta}$).

Fe(η-C_5H_4-COOH)$_2$ **(2)**: A dry, 250 mL, three necked, round bottomed flask was equipped with a magnetic stirrer and a reflux condenser topped with an Argon inlet tube and then charged with 25 mL of 1,2-dimethoxyethane and 8.4 g (74 mmol) of potassium tert-butoxide [2-Propanol,2-methyl-potassium salt]. An argon atmosphere was established in

the system, and approximately 2 mL of Millipore water were added under a continuous stirring, resulting in slurry. Beside, the crude (2-chlorobenzoyl)-ferrocene **(1)** was dissolved in 1,2-dimethoxyethane (50 mL) and subsequently added to the slurry, giving a dark red solution. Reaction mixture was stirred at reflux under inert atmosphere for 3 h (84°C), and then cooled and poured into 200 mL of water. The resulting aqueous layer was washed 3 times with 50 mL diethyl ether; organics layers were combined and back-extracted two times with 20 mL of NaOH (1 M). The aqueous layers were then combined and acidified to pH 1 with fuming hydrochloric acid, resulting in the formation of a precipitate. The precipitate was collected by filtration dried to yield ferrocene dicarboxylic acid as a dark orange solid. Yield: 93 %. $C_{12}H_{10}FeO_4$ = 274.05 g.mol^{-1}. MS (EI): *m/z* = 274 $[M]^+$. ^{1}H NMR (MeOD): δ 12.4 - 12.3 (bs, COOH), 4.70 (4H, m, $CH_{Cp\text{-}ortho}$), 4.46 (4H, m, $CH_{Cp\text{-}meta}$).

Activation of ferrocene carboxylic acid with Isobutylchloroformate

To a stirred suspension of either ferrocene carboxylic acid or ferrocene 1,1'-dicarboxylic acid in freshly distilled THF an equimolar amount of N-methylmorpholine was added. Isobutyl chloroformate was then added dropwise, at room temperature, to this suspension. The resulting mixture was stirred at ambient temperature until the disappearance of starting material was observed by TLC (2 h). Solvents were then removed by rotary evaporation and the residue was triturated in cold pentane and subsequently filtered to yield red oil, which can be stored for months in the fridge.

Fe[η-C_5H_4-$COCOCH_2CH(CH_3)_2$]$_2$ **(3)***:* Yield: 86 %. $C_{22}H_{26}FeO_8$ = 474.28 g.mol^{-1}. Elemental analysis calc. for $C_{22}H_{26}FeO_8$: C, 55.71; H, 5.53, found: C, 56.45; H, 5.29. MS (EI): *m/z* = 474 $[M]^+$, 274 $[Fe(COO)_2]^+$. ^{1}H NMR ($CDCl_3$): δ 4.79 (4H, m, $CH_{Cp\text{-}ortho}$), 4.67 (4H, m, $CH_{Cp\text{-}meta}$), 4.10 (1H, d, J_{HH} = 6.7 Hz, $CH_{2\text{-}IBF}$), 2.06 (2H, sep, J_{HH} = 6.7 Hz, CH_{IBCF}), 1.00 (12H, d, J_{HH} = 6.7 Hz, $CH_{3\text{-}IBCF}$). ^{13}C NMR ($CDCl_3$): δ 165.2 and 149.4 ($C{=}O_{anhydride}$), 75.6 ($CH_{2\text{-}IBCF}$), 69.8 ($C_{q\text{-}Cp}$), 74.8, 72.6 (CH_{Cp}), 27.7 (CH_{IBCF}), 18.8 $CH_{3\text{-}IBCF}$).

Activation of ferrocene carboxylic acid with TBTU

A stirred suspension of ferrocene carboxylic acid (1 mmol; 230 mg) or ferrocene-1-1'-dicarboxylic acid **(2)** (1 mmol; 274 mg) in freshly distilled CH_2Cl_2 (30 mL) was degassed over a period of 15 min. To this suspension, stoichiometric amounts of O-(Benzotriazol-1-

yl)-N,N,N',N'-tetramethyluronium tetrafluoroborate (TBTU) (either 1 mmol; 321.1 mg, or 2 mmol; 622.2 mg) and DIPEA (either 1 mmol; 386 μL or 2 mmol; 772 μL) were added. The resulting suspension was stirred at ambient temperature for 30 min. The reaction mixture was subsequently filtered to remove unreacted materials and solvents were rotary evaporated to yield red solids.

Fc-($C_6H_4N_3$) **(4a)***:* Yield: Quant. $C_{17}H_{13}FeN_3O_2$ = 347.15 g.mol^{-1}. Elemental analysis calc. for $C_{17}H_{13}FeN_3O_2$: C, 58.82; H, 3.77; N, 12.10, found: C, 59.08; H, 3.94; N, 11.91. MS (EI): *m/z* = 347 $[M]^+$, 213 $[FcCOO]^+$. ^{1}H NMR ($CDCl_3$): δ 8.09 (1H, d, J_{HH} = 8.4 Hz, $CH_{ar\text{-}bt}$), 7.55 – 7.26 (3H, m, $CH_{ar\text{-}bt}$), 5.09 (2H, m, $CH_{Cp\text{-}ortho}$), 4.69 (2H, m, $CH_{Cp\text{-}meta}$), 4.44 (5H, m, $CH_{Cp\text{-}unsub}$). ^{13}C NMR ($CDCl_3$): δ $C_{q\text{-}amide}$ signal is missing, 128.6, 124.7, 120.5, 108.4 ($CH_{ar\text{-}bt}$), 73.4, 70.9 ($CH_{Cp\text{-}sub}$), 70.8 ($CH_{Cp\text{-}unsub}$), 33.6 ($C_{q\text{-}bt}$).

Fe[η-C_5H_4-$C_6H_4N_3$]$_2$ **(4b)***:* Yield: Quant. $C_{24}H_{16}FeN_6O_4$ = 508.27 g.mol^{-1}. Elemental analysis calc. for $C_{24}H_{16}FeN_6O_4$: C, 56.71; H, 3.17; N, 16.53, found: C, 58.10; H, 5.49; N, 14.78. MS (FAB): *m/z* = 508 $[M]^+$. ^{1}H NMR ($CDCl_3$): δ 8.08 (2H, s, $^3J_{HH}$ = 8.3 Hz, CH_{bt}), 7.57 – 7.38 (6H, m, CH_{bt}), 5.35 (4H, m, $CH_{Cp\text{-}ortho}$), 5.00 (4H, m, $CH_{Cp\text{-}meta}$). ^{13}C NMR ($CDCl_3$): δ 144.5 ($C_{q\text{-}amide}$), 129.7, 128.3, 126.6 ($CH_{ar\text{-}bt}$), 70.1 (CH_{Cp}), 34.1 ($C_{q\text{-}bt}$).

Protection of the thiol

H-Cys(tBu)-OH **(5)** was obtained according to the protocol described in ref. [85] and Fmoc-Cys(Fmoc)-OH **(6)** was obtained according to the protocol described in ref. [92].

H-Cys(tBu)-OH **(5)***:* Yield: 20 %. $C_7H_{13}NO_2S$, HCl= 211.75 g.mol^{-1}. MS (EI): *m/z* = 175 $[M]^+$. ^{1}H NMR (MeOD): δ NH_2 signal is missing, 4.04 (1H, t, J_{HH} = 4.05 Hz, CH_α), 2.99 (2H, d, J_{HH} = 5.59 Hz, $CH_{2\text{-}\beta}$), 1.27 (9H, s, $CH_{3\text{-}tBu}$).

Fmoc-Cys(Fmoc)-OH **(6)***:* Yield: 82 %. $C_{33}H_{27}NO_6S$ = 565.64 g.mol^{-1}. MS (EI): *m/z* = 566.2 $[M + H]^+$. ^{1}H NMR ($CDCl_3$): δ 7.80 – 7.25 (16H, m, $CH_{Fmoc\text{-}ar}$), 4.50 – 4.00 (7H, m, CH_{Fmoc}, $CH_{2\text{-}Fmoc}$ and CH_α), 3.50 – 3.20 (2H, m, $CH_{2\text{-}\beta}$).

Formation of the methyl ester

H-Cys(Bzl)-OMe and H-Met-OMe were purchased from Novabiochem. Other methyl ester protected amino-acids were prepared following the protocole described in ref. [85]:

amino-acids of the general formula H-Cys(PG)-OH were refluxed overnight in MeOH in presence of $SOCl_2$ (10 eq.). After evaporation of all volatiles, the product was purified by precipitation from cold diethyl ether and dried under reduced pressure. The obtained products were used without further purification.

H-Cys(pOMeBzl)-OMe **(7)***:* Yield: 98 %. $C_{12}H_{17}NO_3S$, HCl = 291.07 g.mol^{-1}. MS (EI): *m/z* = 255 $[M]^+$. IR (KBr): 3477 (br, ν_{NH}), 3000 – 2840 (br, ν_{OH} and $\nu_{CH\text{-}Bzl}$), 1744 (s, $\nu_{C=O}$), 1511 (s, $\nu_{NH\text{-}deformation}$). ^{1}H NMR (MeOD): δ 7.25 (2H, m, $CH_{ar\text{-}pOMeBzl}$), 6.90 (2H, m, $CH_{ar\text{-}pOMeBz}$), 3.76 – 3.74 (3H, s, $CH_{3\text{-}pOMe}$ and 3H, s, $CH_{3\text{-}ester}$), 4.65 (1H, m, CH_α), 3.40 (2H, s, $CH_{2\text{-}Bzl}$), 3.0 – 2.90 (2H, m, $CH_{2\text{-}\beta}$).

H-Cys(S-tBu)-OMe **(8)***:* Yield: 81 %. $C_8H_{17}NO_2S_2$, HCl = 259.82 g.mol^{-1}. MS (EI): *m/z* = 167 $[M - tBu]^+$, 223 $[M]^+$. ^{1}H NMR ($CDCl_3$): δ 8.80 (2H, bs, NH_2), 4.56 (1H, t, J_{HH} = 5.6 Hz, CH_α), 3.85 (3H, s, $CH_{3\text{-}ester}$), 3.44 (2H, d, J_{HH} = 5.84 Hz, $CH_{2\text{-}\beta}$), 1.33 (9H, s, $CH_{3\text{-}tBu}$).

H-Cys(Trt)-OMe **(9)***:* Yield: 98 %. $C_{23}H_{22}NO_2S$, HCl = 412.5 g.mol^{-1}. MS (FAB): *m/z* = 247 $[Trt]^+$, 378 $[M + H]^+$. ^{1}H NMR ($CDCl_3$): δ 8.58 (2H, bs, NH_2), 7.45 – 7.10 (15H, m, $CH_{ar\text{-}Trt}$), 3.54 (3H, s, $CH_{3\text{-}ester}$), 3.37 (1H, m, CH_α), 2.92 (2H, m, $CH_{2\text{-}\beta}$).

H-Cys(tBu)-OMe **(10)***:* Yield: 99 %. $C_8H_{17}NO_2S$, HCl = 226.29 g.mol^{-1}. MS (EI): *m/z* = 191 $[M]^+$. ^{1}H NMR (MeOD): δ NH_2 are missing, 4.28 (1H, dd, J_{HH} = 2.05, 4.78 Hz, CH_α), 3.84 (3H, s, $CH_{3\text{-}ester}$), 3.11 (2H, m, $CH_{2\text{-}Bzl}$), 3.0 – 2.90 (2H, m, $CH_{2\text{-}\beta}$), 1.35 (9H, s, $CH_{3\text{-}tBu}$).

H-Cys(Acm)-OMe **(11)***:* Yield: 90 %. $C_7H_{14}N_2O_3S$, HCl = 238.72 g.mol^{-1}. MS (EI): *m/z* = 147.6 $[M - NHCOCH_3]^+$. ^{1}H NMR (MeOD): δ NH_2 signal is missing, CH_α and $CH_{3\text{-}Acm}$ signal are obscured by residual H_2O signal, 4.48 (2H, d, J_{HH} = 9.21 Hz, $CH_{\alpha\text{-}Acm}$), 3.88 (3H, s, $CH_{3\text{-}ester}$), 3.58 – 3.40 (2H, m, $CH_{2\text{-}\beta}$).

[H-Cys-OMe]$_2$ **(12)***:* Yield: 88 %. $C_8H_{16}N_2O_4S_2$, 2×HCl = 341.28 g.mol^{-1}. MS (EI): *m/z* = 268 $[M]^+$. ^{1}H NMR (MeOD): δ NH_2 are missing, 4.70 (2H, m, CH_α), 3.98 (6H, s $CH_{3\text{-}ester}$), 3.57 – 3.44 (4H, m, $CH_{2\text{-}\beta}$).

8.2.2 Solution phase peptide synthesis

Boc-Cys(Bzl)-Cys(Bzl)-OMe **(13)**: To a stirred solution of Boc-Cys(Bzl)-OH (3.12 g; 10 mmol) in THF (75 mL), N-methylmorpholine (1.02 g; 1.10 mL; 10 mmol) and isobutyl chloroformate (1.39 g; 1.32 mL; 10 mmol) were added, resulting in the formation of a precipitate. Beside, in another flask, H-Cys(Bzl)-OMe, HCl (2.62 mg; 10 mmol) was suspended in THF (50 mL) followed by addition of NEt_3 (1.11 g; 1.39 mL; 10 mmol). The suspensions were mixed and the resulting slurry was stirred overnight at ambient temperature. Reaction mixture was subsequently filtered to remove unreacted materials. Solvents were evaporated at reduced pressure. The residue was dissolved in CH_2Cl_2 (150 mL) and the organic layer was washed with distilled water (100 mL). After the phases were separated, the aqueous layer was back-extracted with CH_2Cl_2 (3×70 mL). The combined organic layers were dried over $MgSO_4$. Evaporation of the solvent yield the dipeptide as a white solid which can be purified by flash column chromatography, using EtOAc / Hexane (1:2); (R_f = 0.25) as eluant. Yield: 93 %. $C_{26}H_{34}N_2O_5S_2$ = 518.19 g.mol^{-1}. MS (EI): *m/z* = 518 $[M]^+$. MS (FAB): *m/z* = 519 $[M + H]^+$, 419 $[M – Boc + H]^+$. IR (KBr): 3331 (s, ν_{NH}), 3100 – 2900 (m, br, ν_{OH} and $\nu_{CH\text{-}Bzl}$), 1743 (s, $\nu_{C=O\text{-}ester}$), 1688 (s, $\nu_{C=O\text{-}amide}$), 1643 (s, $\nu_{C=O\text{-}amide}$ and s, $\nu_{C=O\text{-}Boc}$), 1511 (s, $\nu_{NH\text{-}deformation}$). ^{1}H NMR ($CDCl_3$): δ 7.3 – 7.2 (10H, m, CH_{ar}), 7.23 (1H, d, J_{HH} = 7.0 Hz, NH), 7.03 (1H, d, J_{HH} = 7.5 Hz, NH), 4.75 (1H, m, CH_α), 3.92 (1H, m, CH_α), 3.76 (4H, s, $CH_{2\text{-}Bzl}$), 3.73 (3H, s, $CH_{3\text{-}ester}$), 2.95 – 2.70 (4H, m, $CH_{2\text{-}\beta}$), 1.46 (9H, s, CH_{Boc}). ^{13}C NMR ($CDCl_3$): δ 170.5 ($C{=}O_{ester}$ and $C{=}O_{Boc}$), 137.6 ($C{=}O_{Cys}$), 129.0, 128.9, 128.6, 128.5, 127.3, 127.2 ($CH_{Cp\text{-}ar}$ and $CH_{ar\text{-}Bzl}$), $C_{q\text{-}Boc}$ and $C_{q\text{-}Bzl}$ signals are missing, 52.7 (CH_α), 51.8 ($CH_{3\text{-}ester}$), 36.6 ($CH_{2\text{-}Bzl}$), 33.3 ($CH_{2\text{-}\beta}$), 28.3 ($CH_{3\text{-}Boc}$).

Boc-Cys(pOMeBzl)-Cys(pOMeBzl)-OMe **(14)**: was prepared via a similar procedure as described for Boc-Cys(Bzl)-Cys(Bzl)-OMe **(13)** using Boc-Cys(pOMeBzl)-OH (1.4 g; 4.1 mmol) and H-Cys(pOMeBzl)-OMe, HCl **(7)** (1.05 g; 4.1 mmol). The product was chromatographed on silica gel using EtOAc / Hexane (1:2); (R_f = 0.20) as eluant. Yield: 90 %. $C_{28}H_{38}N_2O_7S_2$ = 578.21 g.mol^{-1}. MS (EI): *m/z* = 578 $[M]^+$. MS (FAB): *m/z* = 579 $[M + H]^+$, 479 $[M – Boc + H]^+$. FT-IR (KBr): 3329 (s, $\nu_{NH\text{-}amide}$), 3100 – 2900 (br, ν_{OH} and $\nu_{CH\text{-}Bzl}$), 1744 (s, $\nu_{C=O\text{-}ester}$), 1688 (s, $\nu_{C=O\text{-}amide}$), 1642 (s, $\nu_{C=O\text{-}amide}$ and $\nu_{C=O\text{-}Boc}$), 1511 (s, $\nu_{NH\text{-}deformation}$). ^{1}H NMR ($CDCl_3$): δ 7.30 – 7.21 (4H, m, $CH_{ar\text{-}pOMeBzl}$),

7.05 (1H, d, J_{HH} = 7.0 Hz, NH), 6.80 – 6.70 (4H, m, $CH_{ar\text{-}pOMeBzl}$), 5.28 (1H, bs, NH), 4.75 (1H, m, CH_{α}), 3.78 – 3.64 (10H, m, $CH_{3\text{-}ester}$, $CH_{3\text{-}ether}$, $CH_{2\text{-}Bzl}$ and CH_{α}), 2.88 – 2.82 (4H, m, $CH_{2\text{-}\beta}$), 1.45 (9H, s, $CH_{3\text{-}Boc}$).

Boc-Met-Met-OMe **(15)**: was prepared as described for Boc-Cys(Bzl)-Cys(Bzl)-OMe **(13)** using Boc-Met-OH (2.5 g; 10 mmol) and H-Met-OMe, HCl (2.0 g; 10 mmol). The product was purified by column chromatography, EtOAc / Hexane (1:1); R_f = 0.30. Yield: 92 %. $C_{16}H_{30}N_2O_5S_2$ = 394.54 g.mol^{-1}. Elemental analysis calc. for $C_{16}H_{30}N_2O_5S_2$: C, 48.71; H, 7.66; N, 7.10, found: C, 48.90; H, 5.74; N, 6.93. MS (EI): *m/z* = 394.1 $[M]^+$, 320.2 $[M - OtBu]^+$, 264.1 $[M - NHBoc - CH_3]^+$. ^{1}H NMR ($CDCl_3$): δ 6.87 (1H, d, J_{HH} = 6.5 Hz, NH_{Boc}), 5.23 (1H, d, J_{HH} = 6.8 Hz, NH), 4.70 (1H, m, CH_{α}), 4.27 (1H, m, CH_{α}), 3.72 (3H, s, $CH_{3\text{-}ester}$), 2.55 (4H, m, $CH_{2\text{-}\beta}$), 2.20 – 1.60 (10H, m, overlapping of SCH_3, $CH_{2\text{-}\gamma}$), 1.42 (9H, s, $CH_{3\text{-}Boc}$). ^{13}C NMR ($CDCl_3$): δ 171.8, 171.2 ($C{=}O_{ester}$ and $C{=}O_{Boc}$), 155.3 ($C{=}O_{Met}$), 80.0 ($C_{q\text{-}Boc}$), 52.7, 51.8 (CH_{α}), 51.2 ($CH_{3\text{-}ester}$), 31.7, 31.2, 31.1, 29.8 ($CH_{2\text{-}\beta}$ and $CH_{2\text{-}\gamma}$), 28.8 ($CH_{3\text{-}Boc}$), 15.2, 15.9 (SCH_3).

Fmoc-Cys(Trt)-Cys(Trt)-OMe **(16)**: was prepared from Fmoc-Cys(Trt)-OH (8.0 g; 13.7 mmol) and H-Cys(Trt)-OMe, HCl (5.6 g; 13.7 mmol) **(9)**. The product was purified by column chromatography, with EtOAc / Hexane (1:3) as eluant (R_f = 0.30). Yield: 72 %. $C_{60}H_{52}N_2O_5S_2$ = 945.20 g.mol^{-1}. Elemental analysis calc. for $C_{60}H_{52}N_2O_5S_2$: C, 76.24; H, 5.55; N, 2.96, found: C, 75.68; H, 6.00; N, 2.77. MS (FAB): *m/z* = 945.0 $[M]^+$, 701 $[M - Trt]^+$. ^{1}H NMR ($CDCl_3$): δ 7.78 – 7.11 (38H, m, overlapping of $CH_{ar\text{-}Trt}$ and CH_{Fmoc}), 6.33 (1H, d, J_{HH} = 7.7 Hz, NH), 5.00 (1H, d, J_{HH} = 7.9 Hz, NH), 4.47 – 4.26 (3H, m, overlapping $CH_{2\text{-}Fmoc}$ and CH_{α}), 4.17 (1H, t, J_{HH} = 7.0 Hz, CH_{Fmoc}), 3.78 (1H, dt, J_{HH} = 1.9, 5.7 Hz, CH_{α}), 3.71 (3H, s, $CH_{3\text{-}ester}$), 2.69 – 2.51 (4H, m, overlapping of $CH_{2\text{-}\beta}$). ^{13}C NMR ($CDCl_3$): δ 170.1, 169.6 ($C{=}O_{ester}$), 144.3, 143.8 ($C{=}O_{Fmoc}$ and $C_{q\text{-}Fmoc}$), 141.2 ($C{=}O_{Met}$), 127.7, 127.1, 125.1, 120.0 (CH_{Fmoc} and CH_{Trt}), 52.5, 51.2 (CH_{α}), 47.0 ($CH_{3\text{-}ester}$), 33.9, 33.5 ($CH_{2\text{-}\beta}$).

Boc-Cys(tBu)-Cys(tBu)-OMe **(17)**: was prepared identically as for Boc-Cys(Bzl)-Cys(Bzl)-OMe using Boc-Cys(tBu)-OH (6.38 g; 23.0 mmol) and H-Cys(tBu)-OMe, HCl **(10)** (5.24 g; 23.0 mmol). The product was purified by column chromatography, with EtOAc / Hexane (1:2) as eluant (R_f = 0.25). Yield: 87 %.

$C_{20}H_{38}N_2O_5S_2$ = 450.65 g.mol^{-1}. Elemental analysis calc. for $C_{20}H_{38}N_2O_5S_2$: C, 53.36; H, 8.51; N, 6.22; found: C, 53.35; H, 8.51; N, 6.15. MS (FAB): *m/z* = 451 $[M + H]^+$. ^{1}H NMR ($CDCl_3$): δ 7.11 (1H, d, J_{HH} = 5.9 Hz, NH), 5.35 (1H, bs, NH), 4.80 (1H, m, CH_α), 4.27 (1H, m, CH_α), 3.76 (3H, s, $CH_{3\text{-ester}}$), 3.01 – 2.95 (3H, m, $CH_{2\text{-}\beta}$), 2.83 (1H, dd, J_{HH} = 6.6, 13.0 $CH_{2\text{-}\beta}$), 1.46 (9H, s, $CH_{3\text{-Boc}}$), 1.34 (9H, s, $CH_{3\text{-tBu}}$), 1.30 (9H, s, $CH_{3\text{-tBu}}$). ^{13}C NMR ($CDCl_3$): δ 170.6 ($C{=}O_{ester}$), 170.4 ($C{=}O_{amide}$), $C_{q\text{-Boc}}$ is missing, 52.6, 52.2 (CH_α), 42.9, 42.6 ($C_{q\text{-tBu}}$), 30.9 ($CH_{3\text{-ester}}$), 31.1, 31.0 ($CH_{3\text{-tBu}}$), 30.3, 30.2 ($CH_{2\text{-}\beta}$), 28.3 ($CH_{3\text{-Boc}}$).

Fmoc-Cys(tBu)-Cys(tBu)-OMe **(18)**: was prepared using Fmoc-Cys(Trt)-OH (4.0 g; 10 mmol) and H-Cys(Trt)-OMe, HCl (2.27 g; 10 mmol) **(10)**. The product was purified by flash column chromatography on silica, with EtOAc / Hexane (1:3) as eluant (R_f = 0.30). Yield: 95 %. $C_{30}H_{40}N_2O_5S_2$ = 572.78 g.mol^{-1}. Elemental analysis calc. for $C_{30}H_{40}N_2O_5S_2$: C, 62.91; H, 7.04; N, 4.89, found: C, 62.58; H, 7.07; N, 4.77. MS (FAB): *m/z* = 573.1 $[M]^+$. ^{1}H NMR ($CDCl_3$): δ 7.80 – 7.28 (8H, m, CH_{Fmoc}), 7.2 (1H, bs, NH_{Fmoc}), 5.78 (1H, d, J_{HH} = 6.2 Hz, NH), 4.81 (1H, dt, J_{HH} = 5.1, 7.8 Hz, CH_α), 4.45 – 4.32 (3H, m, $CH_{2\text{-Fmoc}}$ and CH_α), 4.23 (1H, t, J_{HH} = 7.1 Hz, CH_{Fmoc}) 3.75 (3H, s, $CH_{3\text{-ester}}$), 3.1 – 2.76 (4H, m, $CH_{2\text{-}\beta}$), 1.36 (9H, s, $CH_{3\text{-tBu}}$), 1.28 (9H, s, $CH_{3\text{-tBu}}$). ^{13}C NMR ($CDCl_3$): δ 170.5, 169.9 ($C{=}O_{ester}$ and $C{=}O_{Fmoc}$), 141.3 ($C{=}O_{Met}$), 141.3 ($C_{q\text{-Fmoc}}$), 127.7, 127.1, 125.1, 120.0 (CH_{Fmoc}), 67.3 ($C_{q\text{-tBu}}$), 52.6, 52.3 (CH_α), 47.0 ($CH_{3\text{-ester}}$), 30.8 ($CH_{3\text{-Boc}}$), 30.9, 30.8 ($CH_{2\text{-}\beta}$).

8.2.3 Removal of Boc and Fmoc

General procedure for Boc deprotection

Boc protected derivative were dissolved in a 1:1 (v:v) solution of TFA in CH_2Cl_2 at a concentration of approximately 0.1 M. The resulting mixture was stirred at room temperature for 30 min (reaction completion checked by TLC). The solvents were subsequently removed by rotary evaporation and the product was thoroughly dried. The residue was precipitated from cold diethyl ether and filtered to yield a white solid. Products were used without further purification unless otherwise noted.

H-Cys(Bzl)-Cys(Bzl)-OMe **(19)**: Yield: Quant. $C_{21}H_{26}N_2O_3S_2$ = 418.57 g.mol^{-1}. MS (EI): *m/z* = 418 $[M]^+$, 294 $[M - SBzl + H]^+$. ^{1}H NMR ($CDCl_3$): δ 7.69 (1H, d, J_{HH} = 7.5 Hz,

NH), 7.40 – 7.18 (10H, m, $CH_{ar\text{-}Bzl}$), 4.65 (1H, q, J_{HH} = 7.3 Hz, CH_{α}), 3.92 (1H, t, J_{HH} = 6.1 Hz, CH_{α}), 3.76 (3H, s, $CH_{3\text{-}ester}$), 3.65 (4H, s, $CH_{2\text{-}Bzl}$), 2.96 – 2.80 (4H, m, $CH_{2\text{-}\beta}$).

H-Cys(pOMeBzl)-Cys(pOMeBzl)-OMe **(20)**: Yield: 89 %. $C_{23}H_{30}N_2O_2S_2$ = 478.62 g.mol^{-1}. MS (EI): *m/z* = 479 $[M + H]^+$, 294 $[M – pOMeBzl]^+$. ^{1}H NMR ($CDCl_3$): δ 7.45 – 6.91 (10H, m, NH and $CH_{ar\text{-}Bzl}$), 7.03 (1H, d, J_{HH} = 7.5 Hz, NH), 4.56 (1H, q, J_{HH} = 7.6 Hz, CH_{α}), 3.98 (1H, t, J_{HH} = 6.2 Hz, CH_{α}), 3.81 – 3.67 (13H, m, $CH_{3\text{-}ester}$, $CH_{3\text{-}ether}$ and $CH_{2\text{-}Bzl}$), 2.98 – 2.78 (4H, m, $CH_{2\text{-}\beta}$).

H-Cys(tBu)-Cys(tBu)-OMe **(21)**: Yield: Quant. $C_{15}H_{30}N_2O_3S_2$ = 350.54 g.mol^{-1}. Elemental analysis calc. for $C_{15}H_{30}N_2O_3S_2$, 2.5×CF_3COOH: C, 37.78, H, 5.15, N, 4.41, found: C, 36.47, H, 5.56, N, 4.74. MS (FAB): *m/z* = 351.4 $[M + H]^+$. ^{1}H NMR ($CDCl_3$): δ 7.94 (1H, d, J_{HH} = 7.7 Hz, NH), 4.80 (1H, m, CH_{α}), 4.07 (1H, m, CH_{α}), 3.76 (3H, s, $CH_{3\text{-}ester}$), 3.14 – 2.90 (4H, m, $CH_{2\text{-}\beta}$), 1.36 (9H, s, $CH_{3\text{-}tBu}$), 1.30 (9H, s, $CH_{3\text{-}tBu}$). ^{13}C NMR ($CDCl_3$): δ 170.2 ($C{=}O_{ester}$), 167.7 ($C{=}O_{amide}$), 54.5, 52.8 (CH_{α}), 44.3, 42.9 ($C_{q\text{-}tBu}$), 31.0, 30.6 ($CH_{3\text{-}ester}$ and $CH_{3\text{-}tBu}$), 29.7, 28.8 ($CH_{2\text{-}\beta}$).

General procedure for Fmoc deprotection

H-Cys(Trt)-Cys(Trt)-OMe **(22)***:* Fmoc-Cys(Trt)-Cys(Trt)-OMe **(16)** (5 mmol, 5.0 g) was dissolved in 150 mL of a solution of piperidine / CH_2Cl_2 1:2 (v:v). The resulting mixture was stirred at room temperature for 1 h. The solvents were subsequently removed by rotary evaporation. The residue was purified by column chromatography (EtOAc / n-Hexane 2:1, R_f = 0.15) to yield a white solid (m = 2.2 g). Yield: 61 %. $C_{45}H_{42}N_2O_3S_2$ = 722.96 g.mol^{-1}. MS (FAB): *m/z* = 722.6 $[M]^+$, 243 $[Trt]^+$. ^{1}H NMR ($CDCl_3$): δ 7.39 – 7.24 (30H, m, $CH_{ar\text{-}Trt}$), 5.98 (2H, bs , NH_2), 3.11 (2H, m, CH_{α}), 2.85 (2H, m, $CH_{2\text{-}\beta}$), 2.85 (2H, m, $CH_{2\text{-}\beta}$), 2.45 (3H, s, $CH_{3\text{-}ester}$). ^{13}C NMR ($CDCl_3$): δ 165.6 ($C{=}O_{ester}$), 144.0 ($C{=}O_{amide}$), 129.4, 128.1, 127.2, 127.0 ($CH_{ar\text{-}Trt}$), 67.4, 64.3 ($C_{q\text{-}Trt}$), 53.1, 52.9 (CH_{α} and $CH_{3\text{-}ester}$), 36.0 ($CH_{2\text{-}\beta}$).

8.2.4 Peptide coupling with ferrocene

A stirred suspension of ferrocene carboxylic acid (1 mmol; 230 mg) or ferrocene 1,1'-dicarboxylic acid **(2)** (1 mmol; 274 mg) in freshly distilled CH_2Cl_2 (30 mL) was degassed

over a period of 15 min. To this suspension stoichiometric amounts of HOBt monohydrate (1 mmol; 153.5 mg of the mono acid, or 2 mmol; 307 mg of (**2**)), EDC (1 mmol; 191.7 mg, or 2 mmol; 383.4 mg) and DIPEA (1 mmol; 386 µL, or 2 mmol; 772 µL) were added. The resulting suspension was stirred at ambient temperature for 30 min, followed by filtration to remove unreacted materials. A stoichiometric amount of corresponding amino acid or dipeptide methyl ester (either 1 mmol for reaction with monoacid or 2 mmol for reaction with diacid) was added to this solution and stirring was resumed for an additional 12 h. The disappearance of starting material was observed by TLC using EtOAc / n-Hexane (1:1). The reaction mixture was then diluted to 100 mL with CH_2Cl_2 and the organic layer was consecutively washed with 50 mL distilled water, 50 mL HCl (0.1 M), 50 mL distilled water, 50 mL saturated $NaHCO_3$ and 50 mL distilled water. The organic phase was dried over $MgSO_4$, filtered and the solvent removed by rotary evaporation to yield the crude product, usually yellowish in the case of monosubstituted derivatives and orange in the case of disubstituted derivatives.

Fe[C_5H_4-CO-Cys(Bzl)-OMe]$_2$ **(23b)**: Chromatographed on silica, EtOAc / n-Hexane (1:1) R_f = 0.4 as eluant. Yield: 75 %. $C_{34}H_{36}FeN_2O_6S_2$ = 688.14 g.mol^{-1}. Elemental analysis calc. for $C_{34}H_{36}FeN_2O_6S_2$: C, 59.30; H, 5.27; N, 4.07, found: C, 59.12; H, 5.36; N, 3.96. MS (EI): *m/z* = 688 $[M]^+$, 564 $[M - Bzl - OMe]^+$. UV/Vis ($CHCl_3$): 442.4 (254). $E_{1/2}$ = 448 mV (vs. Fc/Fc$^+$). FT-IR (KBr): 3273 (br, ν_{NH}), 3084 – 2840 (m, ν_{OH} and $\nu_{CH\text{-}Bzl}$), 1745 (s, $\nu_{C=O\text{-}ester}$), 1627 (s, $\nu_{C=O\text{-}amide}$), 1540 (s, $\nu_{NH\text{-}deformation}$). FT-IR ($CHCl_3$): 3378 (s, ν_{NH}), 3076 – 2856 (br, ν_{OH} and $\nu_{CH\text{-}Bzl}$), 1731 (s, $\nu_{C=O\text{-}ester}$), 1648 (s, $\nu_{C=O\text{-}amide}$), 1533 (s, $\nu_{NH\text{-}deformation}$). ^{1}H NMR ($CDCl_3$): δ 7.54 (2H, d, J_{HH} = 8.3 Hz, NH), 7.31 - 7.20 (10H, m, $CH_{ar\text{-}Bzl}$), 4.99 (2H, m, CH_α), 4.88 (2H, ddd, J_{HH} = 1.1, 2.5, 2.5 Hz, $CH_{Cp\text{-}ortho}$), 4.72 (2H, ddd, J_{HH} = 1.1, 2.5, 2.5 Hz, $CH_{Cp\text{-}ortho}$), 4.54 (2H, ddd, J_{HH} = 1.3, 2.6, 2.6 Hz, $CH_{Cp\text{-}meta}$), 4.39 (2H, ddd, J_{HH} = 1.3, 2.6, 2.6 Hz, $CH_{Cp\text{-}meta}$), 3.73 (10H, m, $CH_{3\text{-}ester}$ and $CH_{2\text{-}Bzl}$), 2.85 (4H, m, $CH_{2\text{-}\beta}$). ^{13}C NMR ($CDCl_3$): δ 172.7 ($C{=}O_{ester}$), 169.3 ($C{=}O_{amide}$), 137.6 ($C_{q\text{-}ar}$), 128.0, 127.5, 126.2 (CH_{ar}), 74.8 ($C_{q\text{-}Cp}$), 71.0, 70.6, 69.7, 69.2 (CH_{Cp}), 51.9, 50.6 (CH_α and $CH_{3\text{-}ester}$), 35.7, 31.2 ($CH_{2\text{-}Bzl}$ and $CH_{2\text{-}\beta}$).

Fc-Cys(Bzl)-Cys(Bzl)-OMe **(23c)**: Chromatographed on silica with EtOAc / Hexane (1:2) as eluant (R_f = 0.3). Yield: 83 %. $C_{32}H_{34}FeN_2O_4S_2$ = 630.13 g.mol^{-1}. Elemental analysis calc. for $C_{32}H_{34}FeN_2O_4S_2$: C, 60.95; H, 5.44; N, 4.44, found: C, 60.68; H, 5.58; N, 4.35. MS (EI): *m/z* = 630.2 $[M]^+$. UV/Vis ($CHCl_3$): 443.2 (229). $E_{1/2}$ = 182 mV (vs. Fc/Fc$^+$). FT-

IR (KBr): 3272 (s, ν_{NH}), 3070 - 2900 (br, ν_{OH} and $\nu_{CH\text{-}Bzl}$), 1747 (s, $\nu_{C=O\text{-}ester}$), 1629 (s, $\nu_{C=O\text{-}amide}$), 1550 (s, $\nu_{NH\text{-}deformation}$). FT-IR ($CHCl_3$): 3409 (s, ν_{NH}), 3069 – 2925 (m, ν_{OH} and $\nu_{CH\text{-}Bzl}$), 1746 (s, $\nu_{C=O\ ester}$), 1678 (s, $\nu_{C=O\text{-}amide\text{-}Fc}$), 1645 (s, $\nu_{C=O\text{-}amide}$), 1495 (s, $\nu_{NH\text{-}deformation}$). ^{1}H NMR ($CDCl_3$): δ 7.43 – 7.25 (10H, m, $CH_{ar\text{-}Bzl}$), 7.12 (1H, d, J_{HH} = 7.4 Hz, NH), 6.55 (1H, d, J_{HH} = 7.0 Hz, NH), 4.78 – 4.65 (4H, m, $CH_{Cp\text{-}ortho}$ and CH_α), 4.38 (2H, m, $CH_{Cp\text{-}meta}$), 4.22 (5H, s, $CH_{Cp\text{-}unsub}$), 3.86 (2H, m, $CH_{2\text{-}Bzl}$), 3.74 (3H, s, $CH_{3\text{-}ester}$), 3.70 (2H, s, $CH_{2\text{-}Bzl}$), 3.0 – 2.77 (4H, m, $CH_{2\text{-}\beta}$). ^{13}C NMR ($CDCl_3$): δ 177.5 ($C{=}O_{ester}$), 177.6 ($C{=}O_{amide}$), 137.5 ($C_{q\text{-}ar\text{-}Bzl}$), 129.1, 128.9, 128.7, 128.6 ($CH_{ar\text{-}Bzl}$), 74.9 ($C_{q\text{-}Cp}$), 70.8, 69.9, 68.5, 68.1 (CH_{Cp}), 52.7, 52.0 (CH_α and CH_3), 36.5, 33.7, 33.1 ($CH_{2\text{-}Bzl}$ and $CH_{2\text{-}\beta}$).

Fe[C_5H_4-CO-Cys(Bzl)-Cys(Bzl)-OMe]$_2$ **(23d)**: Chromatographed on silica gel with EtOAc / Hexane (1:1) as eluant (R_f = 0.25). Yield: 70 %. $C_{54}H_{58}FeN_4O_8S_4$ = 1074.25 g.mol^{-1}. Elemental analysis calc. for $C_{54}H_{58}FeN_4O_8S_4$: C, 60.32; H, 5.44; N, 5.21, found: C, 60.02; H, 5.61; N, 5.19. MS (EI): *m/z* = 1074 $[M]^+$, 630 $[M - COCys(Bzl)Cys(Bzl)OMe]^+$. UV/Vis ($CHCl_3$): 445.2 (402). $E_{1/2}$ = 387 mV (vs. Fc/Fc^+). FT-IR (KBr): 3275 (s, ν_{NH}), 3084 – 2840 (br, ν_{OH} and $\nu_{CH\text{-}Bzl}$), 1745 (s, $\nu_{C=O\text{-}ester}$), 1627 (s, $\nu_{C=O\text{-}amide}$), 1541 (s, $\nu_{NH\text{-}deformation}$). FT-IR ($CHCl_3$): 3378 (s, ν_{NH}), 3086 – 2847 (br, ν_{OH} and $\nu_{CH\text{-}Bzl}$), 1731 (s, $\nu_{C=O\text{-}ester}$), 1648 (s, $\nu_{C=O\text{-}amide}$), 1533 (s, $\nu_{NH\text{-}deformation}$). ^{1}H NMR ($CDCl_3$): δ 8.21 (2H, d, J_{HH} = 8.0 Hz, NH), 7.41 – 7.19 (20H, m, $CH_{ar\text{-}Bzl}$), 7.23 (2H, d, J_{HH} = 7.7 Hz, NH), 4.84 (2H, m, $CH_{Cp\text{-}ortho}$), 4.65 (6H, m, CH_α and $CH_{Cp\text{-}ortho}$), 4.45 (2H, m, $CH_{Cp\text{-}meta}$), 4.30 (2H, m, $CH_{Cp\text{-}meta}$), 3.80 – 3.60 (14H, m, $CH_{2\text{-}Bzl}$ and CH_3), 2.88 – 2.69 (8H, m, $CH_{2\text{-}\beta}$). ^{13}C NMR ($CDCl_3$): δ 172.7 ($C{=}O_{ester}$), 170.7 ($C{=}O_{amide}$), 137.7, 137.5 ($C_{q\text{-}ar}$), 129.0, 128.7, 127.3 ($CH_{ar\text{-}Bzl}$), 75.9 ($C_{q\text{-}Cp}$), 71.8, 71.3, 70.7, 70.1 (CH_{Cp}), 52.5, 52.1 (CH_α and $CH_{3\text{-}ester}$), 36.0, 32.5 ($CH_{2\text{-}Bzl}$ and $CH_{2-\beta}$).

Fc-Cys(pOMeBzl)-OMe **(24a)**: Chromatographed on silica EtOAc / Hexane (1:2); R_f = 0.3. Yield: 82 %. $C_{23}H_{35}FeNO_4S$ = 477.16 g.mol^{-1}. Elemental analysis calc. for $C_{23}H_{35}FeNO_4S$: C, 57.86; H, 7.39; N, 2.93, found: C, 57.82; H, 7.20; N, 2.89. MS (EI): *m/z* = 467 $[M]^+$, 213 $[FcCO]^+$. $E_{1/2}$ = 240 mV (vs. Fc/Fc^+). FT-IR (KBr): 3278 (s, ν_{NH}), 3082 – 2834 (br, ν_{OH} and $\nu_{CH\text{-}Bzl}$), 1737 (s, $\nu_{C=O\text{-}ester}$), 1628 (s, $\nu_{C=O\text{-}amide}$), 1538 (s, $\nu_{NH\text{-}deformation}$). ^{1}H NMR ($CDCl_3$): 7.20 (2H, m, $CH_{ar\text{-}ortho\text{-}pOMeBzl}$), 6.80 (2H, m, $CH_{ar\text{-}meta\text{-}pOMeBzl}$), 6.45 (1H, d, J_{HH} = 7.34 , NH), 4.95 (1H, m, CH_α), 4.73 (2H, m, $CH_{Cp\text{-}ortho}$) 4.67 (2H, m, $CH_{Cp\text{-}meta}$),

4.25 (5H, s, $CH_{Cp\text{-}unsub}$), 3.78 (5H, m, $CH_{3\text{-}pOMeBzl}$ and $CH_{2\text{-}pOMeBzl}$), 3.71 (3H, s, $CH_{3\text{-}ester}$), 2.91 – 2.76 (2H, m, $CH_{2\text{-}\beta}$).

Fe[C_5H_4-CO-Cys(pOMeBzl)-OMe]$_2$ **(24b)**: Chromatographed on silica gel EtOAc / Hexane (1:1): $R_f = 0.22$. Yield: 76 %. $C_{36}H_{40}FeN_2O_8S_2 = 748.16$ g.mol^{-1}. Elemental analysis calc. for $C_{36}H_{40}FeN_2O_8S_2$: C, 57.91; H, 5.13; N, 3.75, found: C, 57.67; H, 5.42; N, 3.63. MS (EI): *m/z* = 748 $[M]^+$. UV/Vis ($CHCl_3$): 443.5 (219). $E_{1/2} = 402$ mV (vs. Fc/Fc^+). FT-IR (KBr): 3287 (s, ν_{NH}), 3085 – 2835 (m, ν_{OH} and $\nu_{CH\text{-}Bzl}$), 1740 (s, $\nu_{C=O\text{-}ester}$), 1631 (s, $\nu_{C=O\text{-}amide}$), 1511 (s, $\nu_{NH\text{-}deformation}$). FT-IR ($CHCl_3$): 3378 (s, ν_{NH}), 3002 – 2838 (m, ν_{OH} and $\nu_{CH\text{-}Bzl}$), 1731 (s, $\nu_{C=O\text{-}ester}$), 1648 (br, $\nu_{C=O\text{-}amide\text{-}Fc}$ and $\nu_{C=O\text{-}amide}$), 1536 (s, $\nu_{NH\text{-}deformation}$). ^{1}H NMR ($CDCl_3$): 7.55 (2H, d, $J_{HH} = 8.0$ Hz, NH), 7.20 (4H, m, $CH_{ar\text{-}ortho\text{-}pOMeBzl}$), 6.80 (4H, m, $CH_{ar\text{-}meta\text{-}pOMeBzl}$), 4.99 (2H, m, CH_α), 4.88 (2H, m, $CH_{Cp\text{-}ortho}$), 4.72 (2H, m, $CH_{Cp\text{-}ortho}$), 4.54 (2H, m, $CH_{Cp\text{-}meta}$), 4.39 (2H, m, $CH_{Cp\text{-}meta}$), 3.78 – 3.68 (9H, m, $CH_{3\text{-}pOMeBzl}$ and $CH_{3\text{-}ester}$), 3.01 – 2.80 (8H, m, $CH_{2\text{-}Bzl}$ and $CH_{2\text{-}\beta}$). ^{13}C NMR ($CDCl_3$): 173.7 ($C{=}O_{ester}$), 170.3 ($C{=}O_{amide}$), 158.8 ($C_{q\text{-}ar\text{-}\text{-}pOMeBzl}$), 130.0 ($CH_{ar\text{-}meta\text{-}pOMeBzl}$), 129.3 ($C_{q\text{-}ar\text{-}pOMeBzl}$), 113.6 ($CH_{ar\text{-}ortho\text{-}pOMeBzl}$), 76.0 ($C_{q\text{-}Cp}$), 72.0, 71.6, 70.7, 70.2 (CH_{Cp}), 55.2 ($CH_{3\text{-}pOMeBzl}$), 52.9, 51.6 (CH_α and $CH_{3\text{-}ester}$), 35.5, 32.2 ($CH_{2\text{-}Bzl}$ and $CH_{2\text{-}\beta}$).

Fc-Cys(pOMeBzl)-Cys(pOMeBzl)-OMe **(24c)**: Chromatographed on silica EtOAc / Hexane (1:2); $R_f = 0.2$. Yield: 72 %. $C_{34}H_{38}FeN_2O_6S_2 = 690.15$ g.mol^{-1}. Elemental analysis calc. for $C_{34}H_{38}FeN_2O_6S_2$: C, 59.13; H, 5.55; N, 4.06, found: C, 58.94; H, 5.62; N, 3.86. MS (EI): *m/z* = 690 $[M]^+$, 626 $[M - OMe]^+$. UV/Vis ($CHCl_3$): 441.2 (562). $E_{1/2} = 192$ mV (vs. Fc/Fc^+). FT-IR (KBr): 3278 (s, ν_{NH}), 3083 – 2900 (m, ν_{OH} and $\nu_{CH\text{-}Bzl}$), 1738 (s, $\nu_{C=O\text{-}ester}$), 1628 (s, $\nu_{C=O\text{-}amide}$), 1535 (s, $\nu_{NH\text{-}deformation}$). FT-IR ($CHCl_3$): 3434 (s, ν_{NH}), 3015 – 2976 (m, ν_{OH} and $\nu_{CH\text{-}Bzl}$), 1740 (s, $\nu_{C=O\text{-}ester}$), 1653 (s, $\nu_{C=O\text{-}amide\text{-}Fc}$), 1609 (s, $\nu_{C=O\text{-}amide}$), 1511 (s, $\nu_{NH\text{-}deformation}$). ^{1}H NMR ($CDCl_3$): δ 7.19 (4H, m, $CH_{ar\text{-}pOMeBzl\text{-}ortho}$), 6.78 (4H, m, $CH_{ar\text{-}pOMeBzl\text{-}meta}$), 6.55 (2H, d, $J_{HH} = 7.3$ Hz, NH), 4.79 – 4.68 (4H, m, $CH_{Cp\text{-}ortho}$ and CH_α), 4.38 (2H, m, $CH_{Cp\text{-}meta}$), 4.22 (5H, s, $CH_{Cp\text{-}unsub}$), 3.78 – 3.65 (9H, m, $CH_{3\text{-}pOMe}$ and $CH_{3\text{-}ester}$), 3.0 – 2.75 (8H, m, $CH_{2\text{-}Bzl}$ and $CH_{2\text{-}\beta}$). ^{13}C NMR ($CDCl_3$): 174.8 ($C{=}O_{ester}$), 170.3 ($C{=}O_{amide}$), 158.8 ($C_{ar\text{-}pOMeBzl}$), 130.0 ($CH_{ar\text{-}Bzl\text{-}meta}$), 129.3 ($CH_{ar\text{-}pOMeBzl}$), 113.6 ($CH_{ar\text{-}ortho}$), 76.3 ($C_{Cp\text{-}q}$), 70.8, 69.9, 68.5, 68.1 (), 55.2 ($CH_{3\text{-}pOMe}$), 52.9, 51.6 (CH_α and $CH_{3\text{-}ester}$), 35.5, 32.2 ($CH_{2\text{-}pOMeBzl}$ and $CH_{2\text{-}\beta}$).

Fc-Met-OMe **(25a)**: Chromatographed on silica EtOAc / Hexane (7:1); $R_f = 0.25$. Yield: 87 %. $C_{17}H_{21}FeNO_3S = 375.06$ g.mol^{-1}. Elemental analysis calc. for $C_{17}H_{21}FeNO_3S$: C, 54.41; H, 5.64; N, 3.73, found: C, 54.14; H, 5.67; N, 3.71. MS (EI): *m/z* = 375 $[M]^+$, 213 $[Fc - CO]^+$. UV/Vis ($CHCl_3$): 442.7 (211). $E_{1/2} = 190$ mV (vs. Fc/Fc^+). FT-IR (KBr): 3269 (s, ν_{NH}), 3100 – 2916 (m, br, ν_{OH} and $\nu_{CH\text{-}ar}$), 1747 (s, $\nu_{C=O\text{-}ester}$), 1625 (s, $\nu_{C=O\text{-}amide}$), 1530 (s, $\nu_{NH\text{-}deformation}$). FT-IR ($CHCl_3$): 3432 (s, ν_{NH}), 3100 – 2849 (m, br, ν_{OH} and $\nu_{CH\text{-}ar}$), 1738 (s, $\nu_{C=O\text{-}ester}$), 1655 (s, $\nu_{C=O\text{-}amide}$), 1509 (s, $\nu_{NH\text{-}deformation}$). ^{1}H NMR ($CDCl_3$): δ 6.57 (1H, d, $J_{HH} = 7.8$ Hz, NH), 4.86 (1H, m, CH_α), 4.75 (2H, m, $CH_{Cp\text{-}meta}$), 4.36 (2H, s, CH_{Cp}), 4.24 (5H, s, $CH_{Cp\text{-}unsub}$), 3.81 (3H, s, $CH_{3\text{-}ester}$), 2.6 (2H, t, $J_{HH} = 7.2$ Hz, SCH_2), 2.2 – 2.0 (2H, m, $CH_{2\text{-}\beta}$), 2.13 (3H, s, SCH_3). ^{13}C NMR ($CDCl_3$): 172.6 ($C{=}O_{ester}$), 170.3 ($C{=}O_{amide}$), 75.0 ($C_{Cp\text{-}q}$), 70.5, 69.7, 68.4, 68.0 (CH_{Cp}), 52.1, 51.2 (CH_α and $CH_{3\text{-}ester}$), 31.3, 30.1 (SCH_2 and $CH_{2\text{-}\beta}$), 15.4 (SCH_3).

Fe[C_5H_4-CO-Met-OMe]$_2$ **(25b)**: Chromatographed on silica gel with EtOAc / Hexane (8:1) as eluant ($R_f = 0.3$). Yield: 85 %. $C_{24}H_{32}FeN_2O_6S_2 = 564.11$ g.mol^{-1}. Elemental analysis calc. for $C_{24}H_{32}FeN_2O_6S_2$: C, 51.06; H, 5.71; N, 4.96, found: C, 50.96; H, 5.76; N, 5.08. MS (EI): *m/z* = 564 $[M]^+$. UV/Vis ($CHCl_3$): 443.6 (413). $E_{1/2} = 390$ mV (vs. Fc/Fc^+). FT-IR (KBr): 3306 (s, ν_{NH}), 3085 – 2844 (br, ν_{OH} and $\nu_{CH\text{-}ar}$), 1739 (s, $\nu_{C=O\text{-}ester}$), 1634 (s, $\nu_{C=O\text{-}amide}$), 1539 (s, $\nu_{NH\text{-}deformation}$). FT-IR ($CHCl_3$): 3369 (s, ν_{NH}), 3003 – 2850 (br, ν_{OH} and $\nu_{CH\text{-}ar}$), 1727 (s, $\nu_{C=O\text{-}ester}$), 1644 (s, $\nu_{C=O\text{-}amide}$), 1537 (s, $\nu_{NH\text{-}deformation}$). ^{1}H NMR ($CDCl_3$): δ 7.80 (2H, d, $J_{HH} = 8.75$ Hz, NH), 4.95 (4H, m, CH_α and $CH_{Cp\text{-}ortho}$), 4.75 (2H, ddd, $J_{HH} = 1.2$, 2.4, 2.4 Hz, $CH_{Cp\text{-}ortho}$), 4.55 (2H, ddd, $J_{HH} = 1.6$, 1.6, 2.7 Hz, $CH_{Cp\text{-}meta}$), 4.35 (2H, ddd, $J_{HH} = 1.6$, 1.6, 2.7 Hz, $CH_{Cp\text{-}meta}$), 3.83 (6H, s, $CH_{3\text{-}ester}$), 2.70 (2H, m, $CH_{2\text{-}\gamma}$), 2.55 (2H, m, $SCH_{2\text{-}\gamma}$), 2.15 (2H, m, $CH_{2\text{-}\beta}$), 2.11 (6H, s, SCH_3), 1.85 (2H, m, $CH_{2\text{-}\beta}$). ^{13}C NMR ($CDCl_3$): 175.9 ($C{=}O_{ester}$), 170.7 ($C{=}O_{amide}$), 75.8 ($C_{Cp\text{-}q}$), 72.3, 71.7, 70.5, 70.4 (CH_{Cp}), 53.2, 51.6 (CH_α and $CH_{3\ ester}$), 31.0, 30.9 (SCH_2 and $CH_{2\text{-}\beta}$), 15.8 (SCH_3).

Fc-Cys(StBu)-OMe **(26a)***:* Chromatographed on silica gel EtOAc / Hexane (1:2); $R_f = 0.25$. Yield: Quant. $C_{19}H_{25}FeNO_3S_2 = 435.38$ g.mol^{-1}. Elemental analysis calc. for $C_{19}H_{25}NO_3S_2$: C, 52.41; H, 5.79; N, 3.22, found: C, 52.18; H, 5.87; N, 3.12. MS (EI): *m/z* = 435 $[M + H]^+$, 213 $[FcCO]^+$. $E_{1/2} = 190$ mV (vs. Fc/Fc^+). FT-IR (KBr): 3284 (s, ν_{NH}),

3084, 2965 (br, ν_{OH} and $\nu_{CH\text{-}ar}$), 1747 (s, $\nu_{C=O\text{-}ester}$), 1629 (s, $\nu_{C=O\text{-}amide}$), 1534 (s, $\nu_{NH\text{-}deformation}$). ^{1}H NMR ($CDCl_3$): δ 6.60 (1H, d, J_{HH} = 7.6 Hz, NH), 5.01 (1H, dt, J_{HH} = 2.5, 7.6 Hz, CH_α), 4.73 (2H, m, $CH_{Cp\text{-}ortho}$), 4.37 (2H, m, $CH_{Cp\text{-}meta}$), 4.27 (5H, s, $CH_{Cp\text{-}unsub}$), 3.81 (3H, s, $CH_{3\text{-}ester}$), 3.27 (2H, d, J_{HH} = 4.7 Hz, $CH_{2\text{-}\beta}$), 1.35 (9H, s, $CH_{3\text{-}tBu}$). ^{13}C NMR ($CDCl_3$): δ 171.1 ($C{=}O_{ester}$), 170.2 ($C{=}O_{amide}$), 75.0 ($C_{Cp\text{-}q}$), 70.6, 69.9, 68.4, 68.2 (CH_{Cp}), 52.5, 52.0 (CH_α and $CH_{3\text{-}ester}$), 48.4 ($CH_{2\text{-}\beta}$), 42.5 ($C_{q\text{-}tBu}$), 15.4 ($CH_{3\text{-}tBu}$).

Fe[C_5H_4-CO-Cys(StBu)-OMe]$_2$ **(26b)***:* Chromatographed on silica gel EtOAc / Hexane (1:2); R_f = 0.15. Yield: Quant. $C_{28}H_{40}FeN_2O_6S_4$ = 684.73 g.mol^{-1}. Elemental analysis calc. for $C_{28}H_{40}FeN_2O_6S_4$: C, 49.11; H, 5.89; N, 4.09, found: C, 49.74; H, 6.04; N, 4.32. MS (EI): *m/z* = 684 $[M + H]^+$, 213 $[FcCO]^+$. $E_{1/2}$ = 404 mV (vs. Fc/Fc^+). FT-IR (KBr): 3311 (bs, ν_{NH}), 2960 – 2890 (br, ν_{OH} and $\nu_{CH\text{-}ar}$), 1747 (s, $\nu_{C=O\text{-}ester}$), 1635 (s, $\nu_{C=O\text{-}amide}$), 1534 (s, $\nu_{NH\text{-}deformation}$). ^{1}H NMR ($CDCl_3$): δ 7.59 (2H, d, J_{HH} = 6.5 Hz, NH), 5.12 (2H, m, CH_α), 4.89 (2H, m, $CH_{Cp\text{-}ortho}$), 4.78 (2H, m, $CH_{Cp\text{-}ortho}$), 4.55 (2H, m, $CH_{Cp\text{-}meta}$), 4.40 (2H, m, $CH_{Cp\text{-}meta}$), 3.86 (6H, s, $CH_{3\text{-}ester}$), 3.22 – 3.05 (2H, m, $CH_{2\text{-}\beta}$), 1.36 (18H, s, $CH_{3\text{-}tBu}$). ^{13}C NMR ($CDCl_3$): δ 173.2 ($C{=}O_{ester}$), 170.3 ($C{=}O_{amide}$), 76.0 ($C_{Cp\text{-}q}$), 72.8, 72.5, 71.6, 71.2 (CH_{Cp}), 52.9, 52.2 (CH_α and $CH_{3\text{-}ester}$), 48.14 ($C_{q\text{-}tBu}$), 42.2 ($CH_{2\text{-}\beta}$), 29.8 ($CH_{3\text{-}tBu}$).

Fc-C_5H_4-CO-Cys(Trt)-OMe **(27a)**: Was prepared the same way as described above, the reaction mixture was stirred at ambient temperature for 48 h. Purification by flash-chromatography on silica gel with EtOAc / Hexane (1:4) (R_f = 0.3) as eluant. Yield: 70 %. $C_{34}H_{31}FeNO_3S$ = 589.52 g.mol^{-1}. Elemental analysis calc. for $C_{34}H_{31}FeNO_3S$: C, 69.27; H, 5.30; N, 2.38, found: C, 69.14; H, 5.60; N, 2.95. MS (EI): *m/z* = 589 $[M]^+$. ^{1}H NMR ($CDCl_3$): δ 7.43 – 7.17 (15H, m, $CH_{ar\text{-}Trt}$), 6.25 (1H, d, J_{HH} = 8.0 Hz, NH), 4.77 (1H. m, $CH_{Cp\text{-}ortho}$), 4.76 (1H, m CH_α), 4.70 (1H. m, $CH_{Cp\text{-}ortho}$), 4.36 (2H. m, $CH_{Cp\text{-}meta}$), 4.23 (5H, s, $CH_{Cp\text{-}unsub}$), 3.75 (3H, s, $CH_{3\text{-}ester}$), 2.71 (2H, m, $CH_{2\text{-}\beta}$). ^{13}C NMR ($CDCl_3$): δ 171.6 ($C{=}O_{ester}$), 169.3 ($C{=}O_{amide}$), 144.3 ($C_{q\text{-}ar}$), 129.5, 127.9, 126.9, 126.6 (CH_{ar}), $C_{q\text{-}Cp}$ signal is missing, 70.9, 70.6, 69.9, 68.3 (CH_{Cp}), $C_{q\text{-}Trt}$ signal is missing, 52.6, 50.8 (CH_α and $CH_{3\text{-}ester}$), 34.1 ($CH_{2\text{-}\beta}$).

Fe[C_5H_4-CO-Cys(Trt)-OMe]$_2$ **(27b)**: Was prepared as described above, the reaction mixture was stirred at rt for 48 h. Chromatographed on silica gel, EtOAc / Hexane (1:4) R_f = 0.4. Yield: 65 %. $C_{58}H_{52}FeN_2O_6S_2$ = 993.02 g.mol^{-1}. Elemental analysis calc. for

$C_{58}H_{52}FeN_2O_6S_2$: C, 70.15; H, 5.28; N, 2.82, found: C, 69.82; H, 5.21; N, 2.71. MS (EI): *m/z* = 993 $[M]^+$, 750 $[M - Trt]^+$. $E_{1/2}$ = 396 mV (vs. Fc/Fc^+). FT-IR (KBr): 3326 (br, ν_{NH}), 3056 – 2925 (ν_{OH} and $\nu_{CH\text{-}Bzl}$), 1781 (s, $\nu_{C=O\text{-}ester}$), 1740 (s, $\nu_{C=O\text{-}amide}$), 1653 (s, $\nu_{NH\text{-}deformation}$). ^1H NMR ($CDCl_3$): δ 7.47 (2H, d, J_{HH} = 8.3 Hz, NH), 7.37 - 7.20 (30H, m, $CH_{ar\text{-}Trt}$), 4.83 (2H, m, $CH_{Cp\text{-}ortho}$), 4.73 (4H, m, CH_α and $CH_{Cp\text{-}ortho}$), 4.50 (2H, m, $CH_{Cp\text{-}meta}$), 4.34 (2H, m, $CH_{Cp\text{-}meta}$), 3.55 (6H, s, $CH_{3\text{-}ester}$), 2.73 (2H, m, $CH_{2\text{-}\beta}$), 2.52 (2H, m, $CH_{2\text{-}\beta}$). ^{13}C NMR ($CDCl_3$): δ 173.4 ($C{=}O_{ester}$), 170.3 ($C{=}O_{amide}$), 144.6 ($C_{q\text{-}ar}$), 129.7, 128.2, 127.0 ($CH_{ar\text{-}Trt}$), 76.0 ($C_{q\text{-}Cp}$), 72.2, 71.8, 70.8, 70.4 (CH_{Cp}), 67.3 ($C_{q\text{-}Trt}$), 53.1, 51.9 (CH_α and $CH_{3\text{-}ester}$), 33.5 ($CH_{2\text{-}\beta}$).

Fc-Cys(tBu)-OMe **(28a)***:* Chromatographed on silica gel with EtOAc / Hexane (1:2); R_f = 0.35 as eluant. Yield: 72 %. $C_{19}H_{25}FeNO_3S$ = 403.32 g.mol^{-1}. Elemental analysis calc. for $C_{19}H_{25}FeNO_3S$: C, 56.58; H, 6.25; N, 3.47, found: C, 55.82; H, 6.07; N, 3.95. MS (FAB): *m/z* = 403.2 $[M]^+$, 213 $[FcCO]^+$. UV/Vis (CH_2Cl_2): 441.6 (285). $E_{1/2}$ = 193 mV (vs. Fc/Fc^+). FT-IR (KBr): 3274 (s, ν_{NH}), 3086 – 2965 (br, ν_{OH} and $\nu_{CH\text{-}ar}$), 1754, 1735 (s, $\nu_{C=O\text{-}ester}$), 1631 (s, $\nu_{C=O\text{-}amide}$), 1542 (s, $\nu_{NH\text{-}deformation}$). ^1H NMR ($CDCl_3$): δ 6.48 (1H, d, J_{HH} = 7.6 Hz, NH), 4.97 (1H, m, CH_α), 4.72 - 4.68 (2H, m, $CH_{Cp\text{-}ortho}$), 4.34 (2H, m, $CH_{Cp\text{-}meta}$), 4.25 (5H, s, $CH_{cp\text{-}unsub}$), 3.78 (3H, s, $CH_{3\text{-}ester}$), 3.11 – 3.01 (2H, m, $CH_{2\text{-}\beta}$), 1.31 (9H, s, $CH_{3\text{-}tBu}$). ^{13}C NMR ($CDCl_3$): δ 173.6 ($C{=}O_{ester}$), 170.4 ($C{=}O_{amide}$), 76.2 ($C_{Cp\text{-}q}$), 72.2, 71.8, 70.9, 70.4 (CH_{Cp}), 53.1 and 52.9 (CH_α and $CH_{3\text{-}ester}$), 42.5 ($C_{q\text{-}tBu}$), 31.1 ($CH_{3\text{-}tBu}$), 30.1 ($CH_{2\text{-}\beta}$).

$Fe[C_5H_4$-CO-Cys(tBu)-OMe$]_2$ **(28b)***:* Chromatographed on silica gel EtOAc / Hexane (1:2); R_f = 0.25. Yield: 55 %. $C_{28}H_{40}FeN_2O_6S_2$ = 620.60 g.mol^{-1}. Elemental analysis calc. for $C_{28}H_{40}FeN_2O_6S_2$: C, 54.19; H, 6.50; N, 4.51, found: C, 54.55; H, 6.99; N, 5.02. MS (FAB): *m/z* = 620.5 $[M]^+$, 374.1 $[Fe(C_5H_4\text{-}CO)(Cys(SH)\text{-}OMe]^+$. UV/Vis ($CH_2Cl_2$): 442.5 (304). $E_{1/2}$ = 395 mV (vs. Fc/Fc^+). FT-IR (KBr): 3304 (br, ν_{NH}), 2959 – 2900 (br, ν_{OH} and $\nu_{CH\text{-}ar}$), 1744 (s, $\nu_{C=O\text{-}ester}$), 1635 (s, $\nu_{C=O\text{-}amide}$), 1535 (s, $\nu_{NH\text{-}deformation}$). ^1H NMR ($CDCl_3$): δ 7.48 (2H, d, J_{HH} = 8.4 Hz, NH), 5.00 (2H, m, CH_α), 4.86 (2H, m, $CH_{Cp\text{-}ortho}$), 4.78 (2H, m, $CH_{Cp\text{-}ortho}$), 4.52 (2H, m, $CH_{Cp\text{-}meta}$), 4.37 (2H, m, $CH_{Cp\text{-}meta}$), 3.83 (6H, s, $CH_{3\text{-}ester}$), 3.08 – 2.90 (2H, m, $CH_{2\text{-}\beta}$), 1.33 (18H, s, $CH_{3\text{-}tBu}$). ^{13}C NMR ($CDCl_3$): δ 171.6 ($C{=}O_{ester}$), 170.4 ($C{=}O_{amide}$), 75.3 ($C_{Cp\text{-}q}$), 70.8, 70.1, 68.5 (CH_{Cp}), 52.9, 51.9 (CH_α and $CH_{3\text{-}ester}$), 42.9 ($C_{q\text{-}tBu}$), 31.1 ($CH_{3\text{-}tBu}$), 30.9 ($CH_{2\text{-}\beta}$).

Fc-Cys(tBu)-Cys(tBu)-OMe) **(28c)***:* To a stirred suspension of ferrocene carboxylic acid (1.14 g, 4.96 mmol) in freshly distilled and degassed CH_2Cl_2 (50.0 mL) stoichiometric amounts of TBTU (1.59 g, 4.96 mmol) and DIPEA (0.95 mL, 2.49 mmol) were added. In another flask, H-Cys(tBu)-Cys(tBu)-OMe **(21)** (1.96 g, 4.96 mmol) was suspended in distilled and degassed CH_2Cl_2 (50.0 mL), followed by addition of DIPEA (0.95 mL, 2.49 mmol). The suspensions were mixed, and resulting slurry was stirred overnight at ambient temperature. The reaction mixture was subsequently filtered to remove unreacted materials and diluted with 30.0 mL CH_2Cl_2. The organic layer was consecutively washed with 100 mL distilled water, 100 mL saturated $NaHCO_3$, 100 mL distilled water, 100 mL HCl (0.1 M), and 100 mL distilled water. The organic phase was dried over $MgSO_4$, filtered and the solvent was removed at reduced pressure to yield the crude product. The product was purified by column chromatography with EtOAc / Hexane (1:1) as eluant (R_f = 0.3). Yield: 46 %. $C_{26}H_{38}FeN_2O_4S_2$ = 562.16 g.mol^{-1}. Elemental analysis calc. for $C_{26}H_{38}FeN_2O_4S_2$: C, 55.51; H, 6.81; N, 4.98; found: C, 55.42; H, 6.71; N, 5.01. MS (FAB): *m/z* = 562 $[M]^+$. UV/Vis (CH_2Cl_2): 442.1 (249). $E_{1/2}$ = 202 mV (vs. Fc/Fc^+). FT-IR (KBr): 3294 (bs, ν_{NH}), 3080, 2962, 2863 (s, ν_{OH} and $\nu_{CH\text{-}ar}$), 1752 (s, $\nu_{C=O\text{-}ester}$), 1654, 1628 (s, $\nu_{C=O\text{-}amide}$), 1542 (s, $\nu_{NH\text{-}deformation}$). ^{1}H NMR ($CDCl_3$): δ 7.35 (1H, d, J_{HH} = 9.9 Hz, NH), 6.67 (1H, d, J_{HH} = 6.0 Hz, NH), 4.83 – 4.78 (1H, m, CH_α), 4.72 – 4.66 (3H, m, overlapping CH_α and $CH_{Cp\text{-}ortho}$), 4.37 (2H, m, $CH_{Cp\text{-}meta}$), 4.25 (5H, m, $CH_{Cp\text{-}unsub}$), 3.77 (3H, s, $CH_{3\text{-}ester}$), 3.13 (1H, m, $CH_{2\text{-}\beta}$), 3.02 (2H, m, $CH_{2\text{-}\beta}$), 2.86 (1H, m, $CH_{2\text{-}\beta}$), 1.40 (9H, s, $CH_{3\text{-}tBu}$), 1.29 (9H, s, $_{tBu}$). ^{13}C NMR ($CDCl_3$): δ 170.5 ($C{=}O_{ester}$), 170.4 ($C{=}O_{amide}$), 75.6 ($C_{q\text{-}Cp}$), 70.6, 69.8, 68.3, 68.2 (CH_{Cp}), 53.0, 52.6 52.4 (CH_α), 43.3, 42.7 ($C_{q\text{-}tBu}$), 31.0, 30.8 ($CH_{3\text{-}tBu}$), 30.6, 30.2 ($CH_{2\text{-}\beta}$).

Fe[Cys(tBu)-Cys(tBu)-OMe]$_2$ **(28d)**: To a stirred suspension of ferrocene 1,1'-dicarboxylic acid (290 mg, 1.05 mmol) in freshly distilled and degassed CH_2Cl_2 (20.0 mL) stoichiometric amounts of TBTU (675 mg, 2.1 mmol) and an excess of DIPEA (347 µL, 2.1 mmol) were added. In another flask, H-Cys(tBu)-Cys(tBu)-OMe **(21)** (2.0 g; 2.1 mmol) was suspended in distilled and degassed CH_2Cl_2 (20.0 mL), followed by addition of DIPEA (347 µL, 2.1 mmol). The suspensions were mixed, and resulting slurry was stirred overnight at ambient temperature. The reaction mixture was filtered to remove unreacted materials and diluted with 60.0 mL CH_2Cl_2. The organic layer was washed with 500 mL distilled water, 50 mL saturated $NaHCO_3$, 50 mL distilled water, 50 mL HCl (0.1 M), and

50 mL distilled water. The organic phase was dried over $MgSO_4$, filtered and the solvent rotary evaporated to yield the crude orange product. The product was additionally purified by column chromatography (EtOAc / Hexane (1:1); $R_f = 0.2$). Yield: 95 %. $C_{42}H_{66}FeN_4O_8S_4$ = 939.10 g.mol^{-1}. Elemental analysis calc. for $C_{42}H_{66}FeN_4O_8S_4$: C, 53.72; H, 7.08; N, 5.97; found: C, 53.19; H, 6.93; N, 6.21. MS (FAB): *m/z* = 938.3 $[M]^+$, 748.2 $[M - Cys(tBu)OMe]^+$. UV/Vis (CH_2Cl_2): 448.5 (347). $E_{1/2}$ = 420 mV (vs. Fc/Fc^+). FT-IR (KBr): 3288 (bs, ν_{NH}), 2960, 2863 (s, ν_{OH} and $\nu_{CH\text{-}ar}$), 1750 (s, $\nu_{C=O\text{-}ester}$), 1664, 1635 (s, $\nu_{C=O\text{-}amide}$), 1539 (s, $\nu_{NH\text{-}deformation}$). ^{1}H NMR ($CDCl_3$): δ 8.19 (2H, d, J_{HH} = 8.5 Hz, NH), 7.45 (2H, d, J_{HH} = 7.9 Hz, NH), 4.90 – 4.74 (6H, m, CH_α and $CH_{Cp\text{-}ortho}$), 4.50 (2H, m, $CH_{Cp\text{-}meta}$), 4.35 (2H, m, $CH_{Cp\text{-}meta}$), 3.78 (3H, s, $CH_{3\text{-}ester}$), 3.13 (4H, m, $CH_{2\text{-}\beta}$), 3.13 – 2.98 (4H, m, $CH_{2\text{-}\beta}$), 2.88 (4H, m, $CH_{2\text{-}\beta}$), 1.35 (9H, s, $CH_{3\text{-}tBu}$), 1.34 (9H, s, $CH_{3\text{-}tBu}$). ^{13}C NMR ($CDCl_3$): δ 170.3 ($C{=}O_{ester}$), 170.6, 169.9 ($C{=}O_{amide}$), 76.2 ($C_{q\text{-}Cp}$), 71.8, 71.3, 70.9, 70.1 (CH_{Cp}), 53.5, 52.8, 52.5 (CH_α), 43.3, 42.8 ($C_{q\text{-}tBu}$), 31.0, 30.8 ($CH_{3\text{-}tBu}$), 30.4, 30.3 ($CH_{2\text{-}\beta}$).

8.2.5 Preparation of methionine derivatives

Either Fc-Met-OMe **(25a)** (2.4 mmol; 895 mg) or $Fe[C_5H_4\text{-}CO\text{-}Met\text{-}OMe]_2$ **(25b)** (1.2 mmol; 676 mg) were dissolved in 40 mL dioxane/water (1:1) and a stoichiometric amount of NaOH (100 mg; 2.4 mmol) was added at 0°C (ice bath). The mixture stirred at 0°C for 10 min and then for an additional 60 min at room temperature. Disappearance of the starting material was observed by TLC using EtOAc / Hexane (9:1) as eluant. The pH was adjusted to 1 by addition of 1 M HCl. The reaction mixture was extracted with EtOAc (3 × 70 mL). The combined organic layers were dried over $MgS0_4$, filtered, and the solvent was subsequently removed by rotary evaporation to yield the orange crude product.

Fc-Met-OH **(25a')**: was purified by crystallisation from cold diethyl ether. Yield: 98 %. $C_{16}H_{19}FeNO_3S$ = 361.04 g.mol^{-1}. Elemental analysis calc. for $C_{16}H_{19}FeNO_3S$: C, 53.20; H, 5.30; N, 3.88, found: C, 53.09; H, 5.34; N, 3.55. MS (EI): *m/z* = 361 $[M]^+$, 213 $[FcCO]^+$. UV/Vis ($CHCl_3$): 445.3 (275). FT-IR (KBr): 3260 (s, ν_{NH}), 3110 – 2923 (br, ν_{OH} and $\nu_{CH\text{-}ar}$), 1718 (s, $\nu_{C=O\text{-}acid}$), 1609 (s, $\nu_{C=O\text{-}amide}$), 1545 (s, $\nu_{NH\text{-}deformation}$). FT-IR ($CHCl_3$): 3432 (s, ν_{NH}), 3089 – 2836 (br, ν_{OH} and $\nu_{CH\text{-}ar}$), 1731 (s, $\nu_{C=O\text{-}acid}$), 1652, 1601 (s, $\nu_{C=O\text{-}amide}$), 1511 (s, $\nu_{NH\text{-}deformation}$). ^{1}H NMR ($CDCl_3$): δ 4.84 (1H, m, CH_α), 4.54 (2H, s, $CH_{Cp\text{-}ortho}$), 4.40 (2H, s, $CH_{Cp\text{-}meta}$), 4.36 (5H, s, $CH_{Cp\text{-}unsub}$), 3.42 (2H, m, SCH_2), 2.74 (2H, m, $CH_{2\text{-}\beta}$),

2.26 (3H, s, SCH_3). ^{13}C NMR (Acetone d^6): δ 172.3 ($C{=}O_{ester}$), 170.2 ($C{=}O_{amide}$), 76.4 ($C_{Cp\text{-}q}$), 69.9, 69.2, 67.8, 67.6 (), 50.8 (CH_α), $CH_{2\text{-}\gamma}$, SCH_2 and $CH_{2\text{-}\beta}$ signals are obscured by solvent signal, 14.6 (SCH_3).

Fe[C_5H_4-CO-Met-OH]$_2$ **(25b')**: was purified by crystallisation from cold diethyl ether. Yield: 97 %. $C_{22}H_{28}FeN_2O_6S_2$ = 536.1 g.mol^{-1}. Elemental analysis calc. for $C_{22}H_{28}FeN_2O_6S_2$: C, 49.26; H, 5.26; N, 5.22, found: C, 49.24; H, 5.56; N, 4.91. MS (EI): *m/z* = 536 $[M]^+$. FT-IR (KBr): 3338 (s, ν_{NH}), 3096 – 2017 (br, ν_{OH} and $\nu_{CH\text{-}ar}$), 1718 (s, $\nu_{C=O\text{-}ester}$), 1616 (s, $\nu_{C=O\text{-}amide}$), 1545 (s, $\nu_{NH\text{-}deformation}$). FT-IR ($CHCl_3$): 3366 (s, ν_{NH}), 3003 – 2850 (br, ν_{OH} and $\nu_{CH\text{-}ar}$), 1721 (s, $\nu_{C=O\text{-}ester}$), 1601 (s, $\nu_{C=O\text{-}amide}$), 1538 (s, $\nu_{NH\text{-}deformation}$). ^1H NMR ($CDCl_3$): δ 4.95 – 4.80 (6H, m, CH_α and $CH_{Cp\text{-}ortho}$), 4.58 (2H, m, $CH_{Cp\text{-}meta}$), 4.47 (2H, m, $CH_{Cp\text{-}meta}$), 2.70 (2H, m, SCH_2), 2.55 (2H, m, SCH_2), 2.15 (2H, m, $CH_{2\text{-}\beta}$), 2.09 (6H, s, SCH_3), 1.91 (2H, m, $CH_{2\text{-}\beta}$). ^{13}C NMR (Acetone d^6): δ 174.6 ($C{=}O_{ester}$), 169.1 ($C{=}O_{amide}$), 76.2 ($C_{Cp\text{-}q}$), 70.9, 70.6, 70.0, 69.2 (), 50.6 (CH_α), $CH_{2\text{-}\gamma}$, SCH_2 and $CH_{2\text{-}\beta}$ signals are obscured by solvent signal, 13.8 (SCH_3).

To a stirred solution of either Fc-Met-OH **(25a')** (722 mg; 2 mmol) or Fc-(Met-OH)$_2$ **(25b')** (536 mg; 1 mmol), in THF (20 mL) N-methylmorpholine (203 mg; 221 µL; 2.0 mmol) and isobutyl chloroformate (277 mg; 264 µL; 2.0 mmol) were added, resulting in formation of a precipitate. In another flask, H-Met-OMe, HCl (400 mg; 2.0 mmol) was suspended in THF (20 mL), followed by addition of NEt_3 (222 mg; 277 µL; 2.0 mmol). The suspensions were mixed, and resulting mixture was stirred overnight at ambient temperature. The reactor was then filtered to remove unreacted materials. The solvent was removed under reduced pressure, the residue was then dissolved in CH_2Cl_2 (100 mL) and the organic layer was washed with distilled water (70 mL). After the phases were separated, the aqueous layer was extracted with CH_2Cl_2 (3×30 mL), and the combined organic solutions were dried over $MgSO_4$. Evaporation of the solvent under reduced pressure yield either Fc-Met-Met-OMe **(25c)** or Fc-(Met-Met-OMe)$_2$ **(25d)** as orange solids.

Fc-Met-Met-OMe **(25c)**: Chromatographed on silica gel (EtOAc / Hexane (2:1); R_f = 0.4) Yield: 86 %. $C_{22}H_{30}FeN_2O_4S_4$ = 506.45 g.mol^{-1}. MS (EI): *m/z* = 596 $[M + 80]^+$. UV/Vis ($CHCl_3$): 445. FT-IR (KBr): 3267 (s, ν_{NH}), 3075 – 2954 (br, ν_{OH} and $\nu_{CH\text{-}ar}$), 1744 (s,

$\nu_{C=O\text{-}ester}$), 1628 (s, $\nu_{C=O\text{-}amide}$), 1545 (s, $\nu_{NH\text{-}deformation}$). FT-IR ($CHCl_3$): 3416 – 3316 (two s, ν_{NH}), 3033 – 2879 (br, ν_{OH} and $\nu_{CH\text{-}ar}$), 1741 (s, $\nu_{C=O\text{-}ester}$), 1647 (s, $\nu_{C=O\text{-}amide}$), 1534 (s, $\nu_{NH\text{-}deformation}$). ^{1}H NMR ($CDCl_3$): δ 7.20 (2H, m, NH), 4.80 – 4.75 (2H, m, CH_α), 4.52 – 4.20 (9H, m, CH_{Cp}), 4.00 (3H, s, $CH_{3\text{-}ester}$), 2.10 – 1.95 (8H, m, SCH_2 and $CH_{2\text{-}\beta}$), 1.51 (6H, m, SCH_3). ^{13}C NMR ($CDCl_3$): δ 172.5 ($C{=}O_{ester}$), 170.8 ($C{=}O_{amide}$), 170.1 ($C{=}O_{amide}$), 76.4 ($C_{Cp\text{-}q}$), 72.04, 71.2, 70.1, 70.0 (), 53.7, 52.9, 52.7 (CH_α and $CH_{3\text{-}ester}$), 43.6, 43.1 ($CH_{2\text{-}\gamma}$), 31.2, 31.1 ($CH_{3\text{-}ester}$), 30.6, 30.3 (SCH_2 and $CH_{2\text{-}\beta}$), SCH_3 signal is missing.

Fe[C_5H_4-CO-Met-Met-OMe]$_2$ **(25d)**: Chromatographed on silica gel (EtOAc / Hexane (2:1); R_f = 0.3) Yield: 67 %. $C_{34}H_{50}FeN_4O_8S_4$ = 826.89 g.mol^{-1}. MS (EI): *m/z* = 826 $[M]^+$. UV/Vis ($CHCl_3$): 448. FT-IR (KBr): 3279 (s, ν_{NH}), 3082 – 2918 (br, ν_{OH} and $\nu_{CH\text{-}ar}$), 1744 (s, $\nu_{C=O\text{-}ester}$), 1628 (s, $\nu_{C=O\text{-}amide}$), 1545 (s, $\nu_{NH\text{-}deformation}$). FT-IR ($CHCl_3$): 3416 (s, ν_{NH}), 3316 (s, ν_{NH}), 3034 – 2878 (br, ν_{OH} and $\nu_{CH\text{-}ar}$), 1741 (s, $\nu_{C=O\text{-}ester}$), 1640 (s, $\nu_{C=O\text{-}amide}$), 1529 (s, $\nu_{NH\text{-}deformation}$). ^{1}H NMR ($CDCl_3$): δ 8.55 (2H, d, J_{HH} = 8.8 Hz, NH), 7.81 (2H, d, J_{HH} = 6.0 Hz, NH), 4.80 (8H, m, CH_α and $CH_{Cp\text{-}ortho}$), 4.52 (2H, s, $CH_{Cp\text{-}meta}$), 4.29 (2H, s, $CH_{Cp\text{-}meta}$), 3.74 (6H, s, $CH_{3\text{-}ester}$), 2.60 (8H, m, SCH_2), 2.28 – 1.92 (20H, m, SCH_3 and $CH_{2\text{-}\beta}$). ^{13}C NMR ($CDCl_3$): δ 174.3 ($C{=}O_{ester}$), 172.1 ($C{=}O_{amide}$), 170.7 ($C{=}O_{amide}$), 75.5 ($C_{Cp\text{-}q}$), 71.8, 71.2, 70.1, 70.0 (), 52.8, 52.4, 51.8 (CH_α and $CH_{3\text{-}ester}$), 31.3, 30.6 (SCH_2, $CH_{2\text{-}\gamma}$ and $CH_{2\text{-}\beta}$), 15.4 and 15.3 (SCH_3).

8.2.6 Preparation of ethylendiamine derivatives

Fe[C_5H_4-CO-EDA-Fmoc]$_2$ **(29)**: To a stirred suspension of ferrocene 1,1'-dicarboxylic acid (2.6 mmol; 719 mg) in freshly distilled and degassed CH_2Cl_2 (50 mL) stoichiometric amount of TBTU (5.2 mmol; 1.67 g), and DIEA (2.5 mmol; 1.0 mL) were added. The resulting mixture was stirred at ambient temperature for 15 min (until everything dissolved). Reaction mixture was filtered to remove unreacted materials. The filtrate was cooled to 0°C. In parallel, another flask was charged with (9H-fluoren-9-yl)methyl-2-aminoethylcarbamate (2.0 eq., 5.2 mmol, 1.12 g) and 20 mL CH_2Cl_2 and DIEA (2.5 eq., 1.0 mL) were added. After 5 min at room temperature, this mixture was transfered to the other flask via a stainless steel canula. Reaction mixture was subsequently stirred for 4 h at ambient temperature. Reaction mixture was then diluted with 100 mL CH_2Cl_2 and the organic layer was washed subsequently with 50 mL distilled

water, 50 mL saturated $NaHCO_3$, 50 mL water, 50 mL 0.1 M HCl and 50 mL distilled water. The organic layer was then dried over $MgSO_4$, filtered and rotary evaporated to yield an orange solid (m = 1.98 g). Yield: 95 %. $C_{46}H_{42}FeN_4O_6$ = 802.69 g.mol^{-1}. Elemental analysis calc. for $C_{46}H_{42}FeN_4O_6$: C, 68.83; H, 5.27; N, 6.98; found: C, 68.68; H, 5.44; N, 6.73. MS (FAB): *m/z* = 803.3 $[M + H]^+$. FT-IR (KBr): 3300 (br, ν_{NH}), 3050 – 2850 (br, ν_{OH} and $\nu_{CH\text{-}ar}$), 1699 (s, $\nu_{C=O\text{-}ester}$), 1634 (s, $\nu_{C=O\text{-}amide}$), 1540 (s, $\nu_{NH\text{-}deformation}$). ^{1}H NMR ($CDCl_3$); δ 7.73 (4H, d, J_{HH} = 7.5 Hz, CH_{Fmoc}), 7.57 (4H, d, J_{HH} = 7.7 Hz, CH_{Fmoc}); 7.37 (4H, t, J_{HH} = 7.4 Hz, CH_{Fmoc}), 7.24 (4H, t, J_{HH} = 7.2 Hz, CH_{Fmoc}), 7.07 (1H, bs, NH), 6.06 (1H, bs, NH), 4.52 (4H, bs, $CH_{Cp\text{-}ortho}$). 4.35 – 4.45 (8H, m, $CH_{Cp\text{-}meta}$ and $CH_{2\text{-}Fmoc}$), 4.18 (2H, t, J_{HH} = 4.2 Hz, $CH_{ar\text{-}Fmoc}$), 3.48 (8H, m, $CH_{2\text{-}EDA}$). ^{13}C NMR ($CDCl_3$): δ 143.8, 141.2 ($C{=}O_{amide}$ and $C{=}O_{Fmoc}$), $C_{q\text{-}Fmoc}$ signal is missing, 127.7, 127.0, 127.8, 125.1 ($CH_{ar\text{-}Fmoc}$), 71.1, 70.7 (CH_{Cp}), 66.7 ($C_{q\text{-}Cp}$), 47.2 (CH_{Fmoc}), 40.9, 40.6 ($CH_{2\text{-}EDA}$).

Fe[C_5H_4-CO-EDA-Boc]$_2$ **(30)**: the Boc derivative was obtained via a similar procedure, using the commercial Boc-EDA-NH_2 (1.0 g; 5.2 mmol) as starting material. Yield: Quant. $C_{26}H_{38}FeN_4O_6$ = 558.45 g.mol^{-1}. MS (FAB): *m/z* = 557 $[M]^+$. ^{1}H NMR ($CDCl_3$); δ 7.32 (2H, bs, NH), 5.90 (2H, bs, NH), 4.52 (4H, m, $CH_{Cp\text{-}ortho}$), 4.34 (4H, m, $CH_{Cp\text{-}meta}$), 3.65 – 3.47 (8H, m, $CH_{2\text{-}EDA}$), 1.41 (18H, s, $CH_{3\text{-}tBu}$). ^{13}C NMR ($CDCl_3$): δ 170.8 ($C{=}O_{amide}$), 156.8 ($C{=}O_{Boc}$), 79.4 ($C_{q\text{-}tBu}$), 71.0, 70.7 (CH_{Cp}), 40.7 ($CH_{q\text{-}Boc}$), 34.0, 34.9 ($CH_{2\text{-}EDA}$), 28.4 ($CH_{3\text{-}tBu}$).

Fe[C_5H_4-CO-EDA-H]$_2$ **(31)**: The protecting groups were removed using standard procedure for Fmoc or Boc cleavage to yield an air sensitive red solid. Yield: 74 %. $C_{16}H_{22}FeN_4O_2$ = 358.11 g.mol^{-1}. MS (EI): *m/z* = 358.2 $[M]^+$. ^{1}H NMR (CD_3OD): δ 4.79 (4H, t, J_{HH} = 1.71 Hz, $CH_{Cp\text{-}ortho}$), 4.47 (4H, t, J_{HH} = 1.74 Hz, $CH_{Cp\text{-}meta}$), 3.54 (4H, t, J_{HH} = 5.8 Hz, $CH_{2\text{-}EDA}$), 3.08 (4H, dt, J_{HH} = 0.5, 5.88 Hz, $CH_{2\text{-}EDA}$), NH_2 signals are obscured by H-D exchange with water. ^{13}C NMR (CD_3OD): δ 172.9 ($C{=}O_{amide}$), 78.8 ($C_{q\text{-}Cp}$), 73.2, 71.5 (CH_{Cp}), 41.5, 40.0 ($CH_{2\text{-}EDA}$).

8.2.7 Deprotection of sulfur protective groups

Deprotection of the Trityl group

In a 100 mL round-bottomed flask, either Fc-Cys(Trt)-OMe **(27a)** or Fe[C_5H_4-CO-Cys(Trt)-OMe]$_2$ **(27c)** (1.0 mmol) were dissolved in TFA (20 mL), an excess

of phenol (2.2 g) and TIS (1.0 mL) were added. The reaction mixture was subsequently stirred at ambient temperature, under an inert atmosphere, for 30 min. Reaction mixture was then by rotary evaporation and the residue chromatographed on silica gel using CH_2Cl_2 / MeOH (99:1) as eluant. In both cases an orange solid was obtained.

Fc-Cys(SH)-OMe **(33a)**: Yield: 68 %. $C_{15}H_{17}FeNO_3S$ = 347.21 g.mol^{-1}. Elemental analysis calc. for $C_{15}H_{17}FeNO_3S$: C, 51.89; H, 4.94; N, 4.03, found: C, 51.55; H, 4.95; N, 3.94. MS (EI): *m/z* = 347 $[M]^+$. UV/Vis (CH_2Cl_2): 443.5 (226). $E_{1/2}$ = 199 mV (vs. Fc/Fc^+). FT-IR (KBr): 3299 (bs, ν_{NH}), 3092, 2950 (bs, ν_{OH} and $\nu_{CH\text{-}ar}$), 1745 (s, $\nu_{C=O\text{-}ester}$), 1635 (s, $\nu_{C=O\text{-}amide}$), 1531 (s, $\nu_{NH\text{-}deformation}$). ^{1}H NMR ($CDCl_3$): δ SH signal are missing, 6.58 (1H, d, J_{HH} = 7.2 Hz, NH), 4.76 (1H, dt, J_{HH} = 4.1, 7.42 Hz, CH_α), 4.77 – 4.70 (2H, m, $CH_{Cp\text{-}ortho}$), 4.39 (2H, m, $CH_{Cp\text{-}meta}$), 4.26 (5H, s, $CH_{Cp\text{-}unsub}$), 3.82 (3H, s, $CH_{3\text{-}ester}$), 3.19 – 3.02 (2H, m, $CH_{2\text{-}\beta}$). ^{13}C NMR ($CDCl_3$): δ 171.4 ($C{=}O_{ester}$), $C{=}O_{amide}$ and $C_{q\text{-}Cp}$ signals are missing, 71.0, 70.1, 68.7, 68.5 (CH_{Cp}), 53.0, 51.9 (CH_α and $CH_{3\text{-}ester}$), 41.3 ($CH_{2\text{-}\beta}$).

Fe[Cys(SH)-OMe]$_2$ **(33b)**: Yield: 56 %. $C_{20}H_{24}FeN_2O_6S_2$ = 508.39 g.mol^{-1}. Elemental analysis calc. for $C_{20}H_{24}FeN_2O_6S_2$: C, 47.25; H, 4.76; N, 5.51, found: C, 46.25; H, 4.86; N, 5.97. MS (EI): *m/z* = 509 $[M + H]^+$. UV/Vis (CH_2Cl_2): 442.1 (249). $E_{1/2}$ = 398 mV (vs. Fc/Fc^+). FT-IR (KBr): 3294 (bs, ν_{NH}), 3080, 2962, 2863 (bs, ν_{OH} and $\nu_{CH\text{-}ar}$), 1752 (s, $\nu_{C=O\text{-}ester}$), 1654, 1628 (s, $\nu_{C=O\text{-}amide}$), 1542 (s, $\nu_{NH\text{-}deformation}$). ^{1}H NMR ($CDCl_3$): δ SH signals are obscured by solvent exchange, 7.55 (2H, d, J_{HH} = 8.5 Hz, NH), 5.14 – 5.06 (2H, m, CH_α), 4.88 (2H, m, $CH_{Cp\text{-}ortho}$), 4.79 (2H, m, $CH_{Cp\text{-}ortho}$), 4.55 (2H, m, $CH_{Cp\text{-}meta}$), 4.42 (2H, m, $CH_{Cp\text{-}meta}$), 3.84 (6H, s, $CH_{3\text{-}ester}$), 3.05 – 2.92 (4H, m, $CH_{2\text{-}\beta}$). ^{13}C NMR ($CDCl_3$): δ 171.4 ($C{=}O_{ester}$), $C{=}O_{amide}$ is missing, $C_{q\text{-}Cp}$ is missing, 71.0, 70.1, 68.7, 68.5 (CH_{Cp}), 53.0 and 51.9 (CH_α and $CH_{3\text{-}ester}$), 41.3 ($CH_{2\text{-}\beta}$).

Substitution of the tertiobutyl with NbSCl or NpySCl

Boc-Cys(NbS)-Cys(NbS)-OMe **(17a)**: Boc-Cys(tBu)-Cys(tBu)-OMe **(17)** (1.00 g, 2.22 mmol) was dissolved in acetic acid (40.0 mL) and a stoichiometric amount of 2-nitrophenylsulfenyl chloride (0.84 g 4.44 mmol) was added. The mixture was stirred for 2 h at ambient temperature, followed by filtration to remove a yellow solid. The solvent were removed at vacuum and the residue was subsequently dissolved in CH_2Cl_2 (70 mL). The organic layer was washed 2 times with distilled water (30.0 mL) and dried over $MgSO_4$. Evaporation of the solvent by rotary evaporation yield the crude Boc-Cys(NbS)-

Cys(NbS)-OMe as a yellow oilish residue. The product was purified by column chromatography with EtOAc / Hexane (1:1) (R_f = 0.3) as eluant. Yield: 34 %. $C_{24}H_{28}N_4O_9S_4$ = 644.07 g.mol^{-1}. Elemental analysis calc. for $C_{24}H_{28}N_4O_9S_4$: C, 44.71, H, 4.38, N, 8.69, found: C, 45.26, H, 4.60, N, 8.30. MS (FAB): *m/z* = 645 $[M + H]^+$. ^{1}H NMR ($CDCl_3$): δ 8.22 – 8.30 (4H, m, $CH_{ar\text{-}NbS}$), 7.72 (2H, tdd, J_{HH} = 1.3, 3.1, 7.7 Hz, $CH_{ar\text{-}NbS}$), 7.38 (2H, tt, J_{HH} = 1.3, 7.7 Hz, $CH_{ar\text{-}NbS}$), 4.82 (1H, m, CH_α), 4.43 (1H, m, CH_α), 3.76 (3H, s, $CH_{3\text{-}ester}$), 3.38 – 3.16 (4H, m, $CH_{2\text{-}\beta}$), 1.48 (9H, s, $CH_{3\text{-}tBu}$). ^{13}C NMR ($CDCl_3$): δ 169.8 ($C{=}O_{ester}$), 169.8 ($C{=}O_{amide}$), 145.6 ($C{=}O_{amide}$), 136.7, 136.7, 134.3, 134.3 ($C_{q\text{-}ar\text{-}NbS}$), 127.19, 127.16, 126.54, 126.47, 126.26 ($CH_{ar\text{-}NbS}$), $C_{q\text{-}Boc}$ signal is missing, 52.9, 52.2 (CH_α), 39.7($CH_{2\text{-}\beta}$), $C_{q\text{-}tBu}$ is missing, 28.3 ($CH_{3\text{-}tBu}$).

Boc-Cys(Npys)-Cys(Npys)-OMe **(17b)***:* Boc-Cys(tBu)-Cys(tBu)-OMe **(17)** (457 mg, 1.0 mmol) was dissolved in glacial acetic acid (30.0 mL) and a stoichiometric amount of 3-nitro-2-pyridylsulfenyl chloride (382 mg, 2.0 mmol) was added. The mixture was stirred for 2 h at ambient temperature. The disappearance of starting material was observed by TLC using EtOAc / Hexane (1:2) as eluant. The solvent was removed under reduced pressure and the residue was subsequently dissolved in CH_2Cl_2 (100 mL). The organic layer was washed 2 times with distilled water (50.0 mL), dried over $MgSO_4$. After filtration, the solvent was evaporated to yield the crude Boc-Cys(Npys)-Cys(Npys)-OMe as a yellow oil. The product was purified by column chromatography using EtOAc / Hexane (1:1) (R_f = 0.2) as eluant. Yield: 16 %. $C_{22}H_{26}N_6O_9S_4$ = 646.06 g.mol^{-1}. Elemental analysis calc. for $C_{22}H_{26}N_6O_9S_4$: C, 40.90; H, 4.06; N, 13.01; found: C, 42.34; H, 4.61; N, 12.21. MS (FAB): *m/z* = 647 $[M + H]^+$. ^{1}H NMR ($CDCl_3$): δ 9.07 – 8.92 (2H, m, $CH_{ar\text{-}NpyS}$), 8.51 (2H, m, $CH_{ar\text{-}NpyS}$), 8.14 (1H, d, J_{HH} = 6.1 Hz, NH), 7.43 – 7.36 (2H, m, $CH_{ar\text{-}NpyS}$), 7.17 (1H, d, J_{HH} = 4.3 Hz, NH), 4.91 (1H, m, CH_α), 3.71 (1H, bs, CH_α), 3.71 (3H, s, $CH_{3\text{-}ester}$), 3.65-2.97 (4H, m, $CH_{2\text{-}\beta}$), 1.47 (9H, s, $CH_{3\text{-}tBu}$). ^{13}C NMR ($CDCl_3$): δ 170.3 ($C{=}O_{ester}$), 170.2 ($C{=}O_{amide}$), 157.0 ($C{=}O_{amide}$), 143.1, 142.8 ($C_{q\text{-}ar}$), 134.4, 134.0, 121.9 (CH_{ar}), 80.9 ($C_{q\text{-}Boc}$), 52.9, 52.4 (CH_α and $CH_{3\text{-}Boc}$), 43.0, 40.2 ($CH_{2\text{-}\beta}$), 28.6 ($CH_{3\text{-}Boc}$).

Fc-Cys(Npys)-Cys(Npys)-OMe **(32c)***:* Fc-Cys(tBu)-Cys(tBu)-OMe **(28c)** (844 mg, 1.50 mmol) was dissolved in glacial acetic acid (40.0 mL) and 3-nitro-2-pyridylsulfenyl chloride (572 mg, 3.0 mmol) was added. The mixture was stirred for 2 h, until the disappearance of starting material spot was observed on TLC, using EtOAc / Hexane (1:1)

as eluant. Evaporation of the solvent under reduced pressure yield the crude product as an orange solid. The product was purified by column chromatography with EtOAc / Hexane (1:3); R_f = 0.3. Yield: 47 %. $C_{28}H_{26}FeN_6O_8S_4$ =758.64 g.mol^{-1}. Elemental analysis calc. for $C_{28}H_{26}FeN_6O_8S_4$: C, 44.33; H, 3.45; N, 11.09; found: C, 44.75; H, 3.90; N, 10.50. MS (FAB): *m/z* = 758 $[M]^+$. MS (MALDI): *m/z* = 758 $[M]^+$. FT-IR (KBr): 3408 (s, ν_{NH}), 3078 – 2944 (br, ν_{OH} and $\nu_{CH\text{-}ar}$), 1744 (s, $\nu_{C=O\text{-}ester}$), 1640 (s, $\nu_{C=O\text{-}amide}$), 1582 (s, $\nu_{NH\text{-}deformation}$), 1514 (s, $\nu_{N=O}$), 1340 (s, $\nu_{N=O}$). ^{1}H NMR ($CDCl_3$): δ 8.40 – 7.40 (4H, m, $CH_{ar\text{-}NpyS}$), 7.43 - 7.16 (4H, m, NH and $CH_{ar\text{-}NpyS}$), 4.93 (2H, m, CH_α), 4.74 (1H, bs, $CH_{Cp\text{-}ortho}$), 4.68 (1H, bs, $CH_{cp\text{-}ortho}$), 4.36 (2H, bs, $CH_{Cp\text{-}meta}$), 4.26 (5H, s, $CH_{Cp\text{-}unsub}$), 3.74 (3H, s, $CH_{3\text{-}ester}$), 3.47 – 3.20 (4H, m, $CH_{2\text{-}\beta}$). ^{13}C NMR ($CDCl_3$): δ 170.1 ($C{=}O_{ester}$), 170.0 ($C{=}O_{amide}$), 145.9 ($C{=}O_{amide}$), 136.9 ($C_{q\text{-}ar}$), one $C_{q\text{-}ar}$ signal is missing, 127.4, 126.6, 126.4 ($CH_{ar\text{-}NpyS}$), 71.9, 71.1, 70.7, 69.5 (CH_{Cp}), 53.2, 52.4 (CH_α), 39.9 ($CH_{2\text{-}\beta}$).

Fe[Cys(NbS)-Cys(NbS)OMe]$_2$ **(32d)***:* Yield: 34 %. $C_{50}H_{46}FeN_8O_{16}S_8$ = 1327.31 g.mol^{-1}. Elemental analysis calc. for $C_{50}H_{46}FeN_8O_{16}S_8$: C, 45.24; H, 3.49; N, 8.44; found: C, 44.97; H, 3.11; N, 8.76. MS (FAB): *m/z* = 1327 $[M]^+$, 1173 $[M - NbS]^+$. 1018 $[M - 2NbS]^+$. 775 $[M - 3NbS]^+$. ^{1}H NMR ($CDCl_3$): δ 8.30 (2H, d, J_{HH} = 8.2 Hz, NH), 8.20 (4H, d, J_{HH} = 8.9 Hz, $CH_{ar\text{-}NbS}$), 8.05 (2H, d, J_{HH} = 7.6 Hz, NH), 7.98 (4H, d, J_{HH} = 10.6 Hz, $CH_{ar\text{-}NbS}$), 7.68 (4H, d, J_{HH} = 8.7 Hz, $CH_{ar\text{-}NbS}$), 8.56 (4H, d, J_{HH} = 8.7 Hz, $CH_{ar\text{-}NbS}$), 5.05 – 4.93 (2H, m, CH_α), 4.84 – 4.76 (2H, m, CH_α), 4.74 (2H, m, $CH_{Cp\text{-}ortho}$), 4.55 (2H, m, $CH_{Cp\text{-}ortho}$), 4.41 (2H, m, $CH_{Cp\text{-}meta}$), 4.32 (2H, m, $CH_{Cp\text{-}meta}$), 3.82 (6H, s, $CH_{3\text{-}ester}$), 3.36 – 3.04 (8H, m, $CH_{2\text{-}\beta}$). ^{13}C NMR ($CDCl_3$): δ 172.9 ($C{=}O_{ester}$), 170.8 ($C{=}O_{amide}$), 170.0 ($C{=}O_{amide}$), 146.7, 146.3, 145.4, 145.0 ($C_{q\text{-}ar\text{-}NbS}$), 126.4, 126.2, 124.4, 124.1 ($CH_{ar\text{-}NbS}$), 74.8 ($C_{q\text{-}Cp}$), 72.2, 71.9, 70.5, 69.9 (CH_{Cp}), 53.2, 52.9, 52.5 (CH_α), 39.5, 38.9 ($CH_{2\text{-}\beta}$), 28.6 ($CH_{3\text{-}tBu}$).

Removal of NbS or Npys

Boc-Cys(H)-Cys(H)-OMe **(17c)***:* To a stirred solution of Boc-Cys(NbS)-Cys(NbS)-OMe **(17a)** (0.40 g, 0.62 mmol) in acetone (40.0 mL) and distilled water (10 mL), *n*-tributylphosphine (0.25 g, 308 µL, 1.24 mmol) was added. The suspension was stirred for 4 h at ambient temperature, followed by TLC (EtOAc / Hexane (1:2)). Solvent was rotary evaporated to yield a yellowish solid. The product was purified by column chromatography with EtOAc / Hexane (1:2); R_f = 0.2. Yield: 48 %. $C_{12}H_{22}N_2O_5S_2$ = 338.44 g.mol^{-1}. Elemental analysis calc. for $C_{12}H_{22}N_2O_5S_2$: C, 42.59; H, 6.55; N, 8.28; found: C, 42.56; H,

5.94; N, 7.74. ^{1}H NMR ($CDCl_3$): δ 7.71 (1H, m, NH), 7.28 (1H, m, NH), 4.99 – 4.53 (2H, m, CH_{α}), 3.78 (3H, s, $CH_{3\text{-ester}}$), 3.83 – 3.75 (1H, m, $CH_{2\text{-}\beta}$), 3.26 – 2.97 (3H, m, $CH_{2\text{-}\beta}$), 1.45 (9H, s, $CH_{3\text{-tBu}}$). ^{13}C NMR ($CDCl_3$): δ 171.5 ($C{=}O_{ester}$), 170.9 ($C{=}O_{amide}$), 80.5 ($C_{q\text{-Boc}}$), 53.0, 52.3, 51.9 (CH_{α} and $CH_{3\text{-ester}}$), 40.5 ($CH_{2\text{-}\beta}$), 28.6 ($CH_{3\text{-tBu}}$).

Fc-Cys(H)-Cys(H)-OMe **(33c)***:* To a stirred solution of Fc-Cys(Npys)-Cys(Npys)-OMe (250 mg, 0.33 mmol) in acetone (40.0 mL) and distilled water (10 mL), *n*-tributylphosphine (167 µL, 0.66 mmol) was added. The suspension was stirred for 3 h at ambient temperature. The disappearance of starting material was observed by TLC using EtOAc / Hexane (1:1) as eluant. After evaporation of the solvent the product was purified by flash chromatography, using EtOAc / Hexane (1:1) (R_f = 0.1) as eluting system. Yield: 81 %. $C_{18}H_{22}FeN_2O_4S_2$ = 450.35 g.mol^{-1}. Elemental analysis calc. for $C_{18}H_{22}FeN_2O_4S_2$: C, 48.00, H, 4.93, N, 6.22, found: C, 47.34, H, 5.01, N, 6.17. MS (FAB): *m/z* = 451 $[M + H]^+$. UV/Vis (CH_2Cl_2): 443.1 (266). $E_{1/2}$ = 196 mV (vs. Fc/Fc^+). FT-IR (KBr): 3284 (bs, ν_{NH}), 3082, 2946 (s, ν_{OH} and $\nu_{CH\text{-ar}}$), 1747 (s, $\nu_{C=O\text{-ester}}$), 1654, 1624 (s, $\nu_{C=O\text{-amide}}$), 1539 (s, $\nu_{NH\text{-deformation}}$). ^{1}H NMR ($CDCl_3$): δ 7.20 (1H, s, NH), 6.64 (1H, d, J_{HH} = 7.3 Hz, NH), 4.91 – 4.78 (2H, m, CH_{α}), 4.74 (2H, m, $CH_{Cp\text{-ortho}}$), 4.41 (2H, t, J_{HH} = 2.0 Hz, $CH_{Cp\text{-meta}}$), 4.25 (5H, s, $CH_{Cp\text{-unsub}}$), 3.81 (3H, s, $CH_{3\text{-ester}}$), 3.24 (1H, m, $CH_{2\text{-}\beta}$), 3.06 (2H, m, $CH_{2\text{-}\beta}$), 2.83 (1H, m, $CH_{2\text{-}\beta}$). ^{13}C NMR ($CDCl_3$): δ 171.2 ($C{=}O_{ester}$), 170.3 ($C{=}O_{amide}$), 170.2 ($C{=}O_{amide}$), 75.0 ($C_{q\text{-Cp}}$), 71.2, 70.1, 68.8 (CH_{Cp}), 54.1, 53.2 (CH_{α} and $CH_{3\text{-ester}}$), 27.0, 26.8 ($CH_{2\text{-}\beta}$).

Fe[C_5H_4-CO-Cys(H)-Cys(H)-OMe]$_2$ **(33d)***:* To a stirred solution of $Fe[C_5H_4\text{-}CO\text{-}Cys(NbS)\text{-}Cys(NbS)\text{-}OMe]_2$ **(1)** (320 mg, 0.24 mmol) in 40.0 mL acetone and 10 mL distilled water *n*-tributylphosphin (250 µL, 1.00 mmol) was added. The resulting suspension was stirred for 4 h at ambient temperature. The reaction was followed by TLC using EtOAc / Hexane (1:1). After rotary evaporation of the solvent, the residue was flash-chromatographed with EtOAc / Hexane (1:1) (R_f = 0.1). Yield: 30 %. $C_{26}H_{34}FeN_4O_8S_4$ = 714.68 g.mol^{-1}. MS (FAB): *m/z* = 714 $[M]^+$. UV/Vis (CH_2Cl_2): 440.8 (282). $E_{1/2}$ = 398 mV (vs. Fc/Fc^+). FT-IR (KBr): 3293 (bs, ν_{NH}), 2955, 2945, 2870 (s, ν_{OH} and $\nu_{CH\text{-ar}}$), 1745 (s, $\nu_{C=O\text{-ester}}$), 1671, 1626 (s, $\nu_{C=O\text{-amide}}$), 1542 (s, $\nu_{NH\text{-deformation}}$). ^{1}H NMR ($CDCl_3$): δ 8.10 (2H, d, J_{HH} = 8.0 Hz, NH), 7.28 (2H, m, NH), 4.98 – 4.78 (4H, m, $CH_{Cp\text{-ortho}}$ and CH_{α}), 4.78 – 4.58 (4H, m, $CH_{Cp\text{-ortho}}$ and CH_{α}), 4.53 (2H, m, $CH_{Cp\text{-meta}}$),

4.38 (2H, m, $CH_{Cp\text{-}meta}$), 3.84 (6H, s, $CH_{3\text{-}ester}$), 3.11 (2H, dd, J_{HH} = 4.4, 8.8 Hz, $CH_{2\text{-}\beta}$), 2.89 (2H, m, $CH_{2\text{-}\beta}$). ^{13}C NMR ($CDCl_3$): δ 170.5 ($C{=}O_{ester}$), 167.9, 166.5 ($C{=}O_{amide}$), 71.2, 70.7, 70.5, 68.9 (CH_{Cp}), 54.7, 53.1, 52.9 (CH_{α}), 44.5, 42.9 ($CH_{2\text{-}\beta}$), 31.3, 30.9 ($CH_{3\text{-}ether}$).

8.2.8 Preparation of disulfide bridged derivatives

To a stirred suspension of ferrocene di-carboxylic acid **(1)** (2.0 mmol; 548 mg) in freshly dried and degassed benzene (100 mL) PCl_5 was added and the reaction mixture was stirred at ambient temperature for 90 min. The reaction mixture was then filtered and the solvent was rotary evaporated. The residue was subsequently dissolved in a large volume of dichloromethane (800 mL) and *[H-Cys-OMe]$_2$* **(12)** was added in small portion. The resulting mixture was stirred overnight at ambient temperature. The volume of solvent was subsequently reduced to 100 mL and the organic layer was washed consecutively with 50 mL distilled water, 50 mL HCl (0.1 M), 50 mL distilled water, 50 mL saturated $NaHCO_3$ and 50 mL distilled water. The organic phase was dried over $MgSO_4$, filtered and the solvent removed at vacuum to yield orange solids.

Fc-Cys(OMe)-S-S-Cys(OMe)-Fc **(34a)**: Yield: 49 %. $C_{30}H_{32}Fe_2N_2O_6S_2$ = 692.4 g.mol^{-1}. Elemental analysis calc. for $C_{30}H_{32}Fe_2N_2O_6S_2$: C, 52.04; H, 4.66; N, 4.05, found: C, 51.49; H, 4.74; N, 3.96. MS (FAB): *m/z* = 691.9 $[M]^+$, 347.1 $[M]^{2+}$. UV/Vis (CH_2Cl_2): 444 (211). $E_{1/2}$ = 238 mV (vs. Fc/Fc^+). FT-IR (KBr): 3298 (s, ν_{NH}), 2951 (s, $\nu_{CH\text{-}ar}$), 1744, 1730 (s, $\nu_{C=O\text{-}ester}$), 1629 (s, $\nu_{C=O\text{-}amide}$), 1532 (s, $\nu_{NH\text{-}deformation}$). ^1H NMR ($CDCl_3$): δ 6.63 (2H, d, J_{HH} = 6.7 Hz, NH), 5.02 (2H, m, CH_{α}), 4.76 (1H, m, $CH_{Cp\text{-}ortho}$), 4.72 (1H, s, $CH_{Cp\text{-}ortho}$), 4.37 (2H, s, $CH_{Cp\text{-}meta}$), 4.26 (5H, s, $CH_{Cp\text{-}unsub}$), 3.80 (6H, s, $CH_{3\text{-}ester}$), 3.32 (4H, m, $CH_{2\text{-}\beta}$). ^{13}C NMR ($CDCl_3$): δ 171.4 ($C{=}O_{ester}$), $C{=}O_{amide}$ and $C_{q\text{-}Cp}$ are missing, 71.0, 69.7, 68.5 (CH_{Cp}), 70.1 ($CH_{Cp\text{-}unsub}$), 53.1, 51.9 (CH_{α} and $CH_{3\text{-}ester}$), 41.3 ($CH_{2\text{-}\beta}$).

Fe[Cys(OMe)-S-S-Cys(OMe)] **(34b)**: Yield: 72 %. $C_{20}H_{22}FeN_2O_6S_2$ = 506.37 g.mol^{-1}. Elemental analysis calc. for $C_{20}H_{22}FeN_2O_6S_2$: C, 47.44; H, 4.38; N, 5.53, found: C, 47.54; H, 5.06; N, 5.08. MS (FAB): *m/z* = 506 $[M]^+$. UV/Vis (CH_2Cl_2): 446 (259). $E_{1/2}$ = 378 mV (vs. Fc/Fc^+). FT-IR (KBr): 3390, 3265 (s, ν_{NH}), 2951 (s, $\nu_{CH\text{-}ar}$), 1749 (s, $\nu_{C=O\text{-}ester}$), 1663, 1644 (s, $\nu_{C=O\text{-}amide}$), 1543 (s, $\nu_{NH\text{-}deformation}$). ^1H NMR ($CDCl_3$): δ 7.34 (2H, d, J_{HH} = 7.0 Hz, NH), 5.12 (2H, dt, J_{HH} = 4.7, 7.1 Hz, CH_{α}), 4.84 (2H, m, $CH_{Cp\text{-}ortho}$), 4.60 – 4.54 (4H, m, $CH_{Cp\text{-}ortho}$ and $CH_{Cp\text{-}meta}$), 4.44 (2H, m, $CH_{Cp\text{-}meta}$), 3.80 (6H, s, $CH_{3\text{-}ester}$), 3.49 – 3.34 (4H,

dd, J_{HH} = 4.0, 10.1 Hz, $CH_{2\text{-}\beta}$). ^{13}C NMR (CD_3OD): 175.8 ($C{=}O_{ester}$), 174.9 ($C{=}O_{amide}$), 80.9 ($C_{q\text{-}Cp}$), 78.5, 74.7, 73.9, 70.8 (CH_{Cp}), 55.0, 54.2 (CH_α and $CH_{3\text{-}ester}$), 48.3 ($CH_{2\text{-}\beta}$).

8.2.9 Complexation with Iron carbonyl

[Fc-Cys-OMe]$_2$(Fe$_2$(CO)$_6$) **(35)***:* To a stirred suspension of Fc-Cys(H)-OMe **(33a)** (208 mg, 0.6 mmol) in distilled MeOH (2.0 mL), a solution of $Fe_3(CO)_{12}$ (100.7 mg, 0.2 mmol) in distilled $CHCl_3$ (2.0 mL) was added dropwise. The mixture was refluxed for 90 min at 90°C, which resulted in formation of a dark-red solution. The solvents were removed at reduced pressure and the residue was triturated in cold MeOH and subsequently filtered to yield a dark red solid. Yield: 90 %. $C_{36}H_{32}Fe_4N_2O_{12}S_2$ = 972.17 g.mol^{-1}. Elemental analysis calc. for $C_{36}H_{34}Fe_4N_2O_{12}S_2$: C, 44.48; H, 3.32; N, 2.88, found: C, 43.39; H, 3.62; N, 2.88. MS (FAB): *m/z* = 973 $[M + H]^+$, 804 $[M - 6{*}CO]^+$. FT-IR (KBr): 3401 (bs, ν_{NH}), 3124 – 2933 (br, ν_{OH} and $\nu_{CH\text{-}ar}$), 2073, 2031, 1992 (s, $\nu_{Fe\text{-}C=O}$), 1748 (s, $\nu_{C=O\text{-}ester}$), 1636 (s, $\nu_{C=O\text{-}amide}$), 1526 (s, $\nu_{NH\text{-}deformation}$). ^1H NMR ($CDCl_3$): δ 6.63 (2H, d, J_{HH} = 7.9 Hz, NH), 5.03 (2H, m, CH_α), 4.78 (1H, m, $CH_{Cp\text{-}ortho}$), 4.77 (1H, m, $CH_{Cp\text{-}ortho}$), 4.38 (2H, m, $CH_{Cp\text{-}meta}$), 4.25 (10H, s, $CH_{Cp\text{-}unsub}$), 3.81 (6H, s, $CH_{3\text{-}ester}$), 3.45 – 3.28 (4H, m, $CH_{2\text{-}\beta}$). ^{13}C NMR ($CDCl_3$): δ 208.8, 208.7, 208.0, 207.9 ($C{=}O_{Fe\text{-}CO}$), 170.8, 170.7 ($C{=}O_{ester}$), 170.5, 170.3 ($C{=}O_{amide}$), 75.0, 74.8 ($C_{q\text{-}Cp}$), 71.5, 71.4, 71.2, 71.1, 71.0, 70.8, 70.7, 70.5, 70.4, 68.9, 68.7, 68.5 (CH_{Cp}), 53.7, 53.6, 53.5, 53.3, 53.1 ($CH_{3\text{-}ester}$ and CH_α), 41.3, 40.9 ($CH_{2\text{-}\beta}$).

Fe[C$_5$H$_4$-CO-Cys-OMe]$_2$(Fe$_2$(CO)$_6$) **(36)***:* Was prepared as described above starting from Fe[Cys(SH)-OMe]$_2$ **(33b)**. Chromatographed on silica gel with EtOAc / Hexane (2:1), R_f = 0.2. Yield: 50 %. $C_{26}H_{22}Fe_3N_2O_{12}S_2$ = 786.12 g.mol^{-1}. Elemental analysis calc. for $C_{26}H_{22}Fe_3N_2O_{12}S_2$: C, 40.39; H, 3.00; N, 3.62, found: C, 40.98; H, 3.53; N, 3.58. MS (FAB): *m/z* = 786.9 $[M + H]^+$, 617.9 $[M - 6{\times}CO]^+$. UV/Vis (CH_2Cl_2): 336 (9881), 450 (1638). $E_{1/2}$ = 418 mV (vs. Fc/Fc^+). FT-IR (KBr): 3327 (s, ν_{NH}), 2930 (bs, $\nu_{CH\text{-}ar}$), 2074, 2034, 1993, 1976, 1961 (s, $\nu_{Fe\text{-}C=O}$), 1753, 1729 (s, $\nu_{C=O\text{-}ester}$), 1649 (bs, $\nu_{C=O\text{-}amide}$), 1543, 1512, 1493 (s, $\nu_{NH\text{-}deformation}$).$^1H$ NMR ($CDCl_3$): δ 7.04 (1H, d, J_{HH} = 6.9 Hz, NH), 6.46 (1H, d, J_{HH} = 7.2 Hz, NH), 5.07 (1H, m, CH_α), 4.85 – 4.77 (3H, m, CH_α and $CH_{Cp\text{-}ortho}$), 4.59 – 4.34 (6H, m, $CH_{Cp\text{-}ortho}$ and $CH_{Cp\text{-}meta}$), 3.94 (3H, s, $CH_{3\text{-}ester}$), 3.78 (3H, s, $CH_{3\text{-}ester}$), 3.21 (1H, dd, J_{HH} = 4.7, 13.7 Hz, $CH_{2\text{-}\beta}$), 2.98 (1H, dd, J_{HH} = 3.0, 13.7 Hz, $CH_{2\text{-}\beta}$), 2.80 (1H, dd, J_{HH} = 5.1, 13.3 Hz, $CH_{2\text{-}\beta}$), 2.54 (1H, dd, J_{HH} = 3.2 Hz,

J_{HH} = 13.3 Hz, $CH_{2\text{-}\beta}$). ^{13}C NMR ($CDCl_3$): δ 207.7 ($C{=}O_{Fe\text{-}CO}$), 170.0, 169.8, 169.6 ($C{=}O_{ester}$ and $C{=}O_{amide}$), 79.5 ($C_{q\text{-}Cp}$), 72.0, 71.9, 71.8, 71.5, 71.4, 69.7, 68.8 (CH_{Cp}), 53.3, 53.0, 52.8 ($CH_{3\text{-}ester}$ and CH_{α}), 41.3, 25.0 ($CH_{2\text{-}\beta}$).

Fc-Cys(FeCO$_3$)-Cys(FeCO$_3$)-OMe **(37)***:* To a stirred suspension of Fc-Cys(H)-Cys(H)-OMe **(33c)** (250 mg, 0.56 mmol) in degassed MeOH (12.0 mL), $Fe_3(CO)_{12}$ (186 mg, 0.37 mmol) in of $CHCl_3$ (2.0 mL) was added dropwise via stainless steel canula. The mixture was refluxed for 90 min at 90°C, which resulted in formation of a deep-red solution. The solvent were removed under reduced pressure giving the crude product as a dark red solid. The complex was isolated by column chromatography using EtOAc / Hexane (9:1) R_f = 0.3 as eluant. Yield: 40 %. $C_{42}H_{46}Fe_4N_4O_{14}S_4$ = 1181.93 g.mol^{-1}. Elemental analysis calc. for $C_{42}H_{46}Fe_4N_4O_{14}S_4$: C, 42.66; H, 3.92; N, 4.75, found: C, 42.90; H, 3.82; N, 4.37. MS (MALDI): *m/z* = 727 $[M - H]^+$. UV/Vis (CH_2Cl_2): 333 (6111), 450 (1068). $E_{1/2}$ = 210 mV (vs. Fc/Fc^+). FT-IR (KBr): 3284 (bs, ν_{NH}), 2926 (bs, $\nu_{CH\text{-}ar}$), 2074, 2037, 1994 (s, $\nu_{Fe\text{-}C=O}$), 1745 (s, $\nu_{C=O\text{-}ester}$), 1644 (bs, $\nu_{C=O\text{-}amide}$), 1512 (s, $\nu_{NH\text{-}deformation}$). ^1H NMR ($CDCl_3$): δ 7.71 (1H, dd, J_{HH} = 3.3, 5.7 Hz, NH), 7.53 (1H, dd, J_{HH} = 3.3, 5.8 Hz, NH), 4.80 – 4.69 (2H, m, CH_{α}), 4.45 – 4.10 (12H, m, CH_{Cp}, $CH_{3\text{-}ester}$), 3.85 – 3.74 (4H, m, $CH_{2\text{-}\beta}$). ^{13}C NMR ($CDCl_3$): δ 208.1, 208.0, 207.9 ($C{=}O_{Fe\text{-}CO}$), 171.4 ($C{=}O_{ester}$), 170.0 ($C{=}O_{amide}$), second $C{=}O_{amide}$ signal is missing, 74.7 ($C_{q\text{-}Cp}$), 70.2, 70.1, 70.0 (CH_{Cp}), 53.2 ($CH_{3\text{-}ester}$), 32.0 (CH_{α}), 29.9 ($CH_{2\text{-}\beta}$).

8.3 Syntheses and Characterization of Oligoamides

NMR signals were attributed on the basis of literature review and chemical best guess and are given only for the monomers. The acid chloride are air sensitive and they were produced in situ and used without further purification they are considered as reactionnal intermediate and therefore their fully characterization is not presented here.

8.3.1 Synthesis of the monomers

The monomer quinoline with isobutoxy side chain was synthesized as it is described in ref [183] However some modifications in work up were performed in order to ease the purification and therefore to upscale the synthesis

3-(tert-butylthio)propan-1-ol **(B1)** is not commercially available and was therefore prepared according to the modified literature protocol described in ref. [190] 2-methyl-2-propanthiol (5.61 g; 50 mmol) was dissolved in methanol (50 mL), 3-chloro-propanol (4.18 mL; 50 mmol) was added, and the solution was left at room temperature for 1 h. The reaction mixture was then refluxed for 1 h. Precipitated sodium chloride was filtered off and washed with methanol. The solvent was removed from the filtrate at vacuum. Diethyl ether (50 mL) was added to the residue, and a small amount of sodium chloride was filtered off. The product was isolated by distillation under vacuum; bp 48 – 50°C / 0.1 mmHg. Yield: 73 %. $C_7H_{16}OS$ = 148.09 g.mol^{-1}. MS (EI): *m/z* = 149 $[M + H]^+$, 57 $[tBu]^+$. ^{1}H NMR ($CDCl_3$): δ 3.73 (2H, m, $CH_{2\text{-}\alpha}$), 2.61 (2H, t, J_{HH} = 7.1 Hz, $CH_{2\text{-}\gamma}$), 2.05 (1H, t, J_{HH} = 5.2 Hz, OH), 1.85 (2H, m, $CH_{2\text{-}\beta}$), 1.28 (9H, s, $CH_{3\text{-}tBu}$).

Formation of the maleate

dimethyl 2-(2-nitrophenylamino)maleate **(B2)***:* 2-nitroaniline (13.8 g; 100 mmol) was dissolved in methanol (150 mL), an equimolar amount of dimethylbut-2-ynedioate (100 mmol; 14.2 g; 12.25 mL) was added and the resulting mixture was heated at reflux for 24 h. The solution was then cooled and the volume of solvent was reduced to approximately 70 mL by rotary evaporation. The flask was then placed at -18°C for precipitation. The resulting yellow prisms were collected by filtration, and washed several times with cold methanol and dried at reduced pressure. Yield: 85 %. $C_{12}H_{12}N_2O_6$ = 280.23 g.mol^{-1}. Elemental analysis calc. for $C_{12}H_{12}N_2O_6$: C, 51.43; H, 4.32; N, 10.00, found: C, 51.20; H, 4.39; N, 9.99. MS (FAB): *m/z* = 281 $[M + H]^+$, 249 $[M – OMe]^+$. ^{1}H NMR ($CDCl_3$): δ 11.11 (1H, bs, NH), 8.14 (1H, dd, J_{HH} = 1.4, 8.3 Hz, $CH_{ar\text{-}ortho}$), 7.46 (1H, t, J_{HH} = 8.8Hz, CH_{ar}), 7.08 (1H, t, J_{HH} = 8.4 Hz, CH_{ar}), 6.78 (1H, dd, J_{HH} = 1.3, 8.4 Hz, CH_{ar}), 5.04 (1H, s, $CH_{maleate}$), 3.81 (3H, s, $CH_{3\text{-}ester}$), 3.76 (3H, s, $CH_{3\text{-}ester}$). ^{13}C NMR ($CDCl_3$): δ 167.9, 164.3 (C=O), 143.4 (C_{ar}), 136.8 ($C_{maleate}$), 134.1, 126.1, 121.4, 120.3 (CH_{ar}), 102.9 ($CH_{maleate}$), 52.9, 51.7 ($CH_{3\text{-}ester}$).

Intramolecular cyclisation

Methyl 1,4-dihydro-8-nitro-4-oxoquinoline-2-carboxylate **(B3)***:* A mixture of 2-(2-nitrophenylamino)maleate **(B2)** (17.8 g; 63 mmol) and polyphosphoric acid (PPA) (90 g) was placed in a 1 L round bottom flask equipped with a condenser and a mechanic stirrer. Reaction mixture was heated at 130°C for 4 hours. The solution was then cooled and quenched slowly by addition of an oversaturated solution of $NaHCO_3$ at 0°C. The resulting precipitate was filtered through a fine sintered glass funnel and washed several times with distilled water. The brown solid was precipitated from cold MeOH and subsequently filtered to yield a yellow solid after evaporation of residual solvents. Yield: 65 %. $C_{11}H_8N_2O_5$ = 248.19 g.mol^{-1}. Elemental analysis calc. for $C_{11}H_8N_2O_5$: C, 53.23; H, 3.25; N, 11.29; found: C, 52.71; H, 3.40; N, 11.21. MS (EI): *m/z* = 248 $[M]^+$, 188 $[M - NO_2]^+$, 154 $[C_{10}H_4NO]^+$. ^{1}H NMR ($CDCl_3$): δ 11.80 (1H, bs, NH), 8.74 (2H, m, $CH_{ar\text{-}ortho}$), 7.47 (1H, t, J_{HH} = 8.8 Hz, $CH_{ar\text{-}para}$), 7.08 (1H, s, $CH_{quinone}$), 4.09 (3H, s, $CH_{3\text{-}ester}$). ^{13}C NMR ($CDCl_3$): δ 170.2 (C=O), one carbonyl signal is missing, 146.9, 145.4 ($C_{q\text{-}ar}$), 143.2, 139.1, 136.2, 130.8, (CH_{ar}), 121.4 ($CH_{quinone}$), 62.1 ($CH_{3\text{-}ester}$).

Mitsunobu's reaction [210]

Methyl 4-isobutoxy-8-nitroquinoline-2-carboxylate **(B4)***:* In a flame-dried 250 mL round-bottom-flask placed in an inert atmosphere, methyl 1,4-dihydro-8-nitro-4-oxoquinoline-2-carboxylate **(B3)** (20.5 mmol; 5.08 g), freshly distilled 2-methyl propanol (1.1 eq.; 22.5 mmol; 2.09 mL) and triphenylphosphine (1.05 eq.; 21.5 mmol; 5.64 g) were dissolved in 45 mL anhydrous THF. Flask was then hermetically closed and remains under protecting gas during the reaction time. Reaction mixture was then cooled to 0°C and diisopropyl azodicarboxylate was added. Resulting slurry was stirred at 0°C for 30 min and then at rt for an additional 4 h. Solvent was removed by rotary evaporation and residue was subsequently precipitated from cold Methanol. The yellow crystalline powder was collected by filtration. Yield: 83 %. $C_{15}H_{16}N_2O_5$ = 304.3 g.mol^{-1}. Elemental analysis calc. for $C_{15}H_{16}N_2O_5$: C, 59.21; H, 5.30; N, 9.21; found: C, 58.79; H, 5.34; N, 9.14. MS (FAB): *m/z* = 305 $[M]^+$, 249 $[M - CH_2CH(CH_3)_2]^+$, 154 $[C_{10}H_4NO]^+$. ^{1}H NMR ($CDCl_3$): δ 8.48 (1H, dd, J_{HH} = 1.3, 6.7 Hz, $CH_{ar\text{-}ortho}$), 8.11 (1H, dd, J_{HH} = 1.3, 6.0 Hz, $CH_{ar\text{-}para}$), 7.67 (2H, m, $CH_{ar\text{-}quinone}$ and $CH_{ar\text{-}meta}$), 4.09 (2H, d, J_{HH} = 6.2 Hz, $CH_{2\text{-}\alpha}$), 4.02 (3H, s, $CH_{3\text{-}ester}$), 2.25 (1H, m, CH_β), 1.14 (6H, d, J_{HH} = 6.7 Hz, $CH_{3\text{-}\gamma}$). ^{13}C NMR ($CDCl_3$): δ 165.7 (C=O), 162.7, 151.3, 140.0, 106.7 ($C_{q\text{-}ar}$), 126.2, 125.9, 125.0 (CH_{ar}), 102.2 ($CH_{quinone}$), 75.6 ($CH_{2\text{-}\alpha}$), 53.2 ($CH_{3\text{-}ester}$), 28.1 (CH_β), 19.1 ($CH_{3\text{-}\gamma}$).

Methyl 4-(3-(tert-butylthio)propoxy)-8-nitroquinoline-2-carboxylate **(B5)***:* was prepared via a similar protocol involving freshly distilled 3-(tert-butylthio)propan-1-ol **(B1)** instead of the 2-methylpropanol. Yield: 87 %. $C_{18}H_{22}N_2O_5S$ = 378.44 g.mol^{-1}. Elemental analysis calc. for $C_{18}H_{22}N_2O_5S$: C, 57.13; H, 5.86; N, 7.40; found: C, 57.11; H, 5.86; N, 7.36. MS (FAB): *m/z* = 379 $[M]^+$, 249 $[M –CH_2CH_2CH_2SC(CH_3)_3]^+$, 154 $[C_{10}H_4NO]^+$. ^{1}H NMR ($CDCl_3$): δ 8.48 (1H, d, J_{HH} = 8.4 Hz, $CH_{ar\text{-}ortho}$), 8.11 (1H, d, J_{HH} = 7.4 Hz, $CH_{ar\text{-}para}$), 7.66 (2H, m, $CH_{ar\text{-}quinone}$ and $CH_{ar\text{-}meta}$), 4.44 (2H, d, J_{HH} = 6.1 Hz, $CH_{2\text{-}\alpha}$), 4.04 (3H, s, $CH_{3\text{-}ester}$), 2.80 (1H, t, J_{HH} = 7.0 Hz, $CH_{2\text{-}\gamma}$), 2.26 (1H, q, J_{HH} = 6.5 Hz, $CH_{2\text{-}\beta}$), 1.34 (9H, s, $CH_{3\text{-}tBu}$). ^{13}C NMR ($CDCl_3$): δ 162.7 (C=O), 151.5, 123.4 ($C_{q\text{-}ar}$), 126.5, 126.2, 125.3 (CH_{ar}), 102.5 ($CH_{quinone}$), 68.4 ($CH_{2\text{-}\alpha}$), 53.2 ($CH_{3\text{-}ester}$), 42.6 ($C_{q\text{-}tBu}$), 31.1 ($CH_{3\text{-}tBu}$), 29.3 ($CH_{2\text{-}\gamma}$), 24.8 ($CH_{2\text{-}\beta}$). ^{13}C NMR ($CDCl_3$): δ 164.0 (C=O), 163.5, 162.7, 151.3, 106.7 ($C_{q\text{-}ar}$), 127.0, 126.6, 126.2 (CH_{ar}), 100.3 ($CH_{quinone}$), 77.2 ($CH_{2\text{-}\alpha}$), 68.8 ($CH_{3\text{-}ester}$), 30.9 ($CH_{2\text{-}\beta}$), 28.9 ($CH_{2\text{-}\gamma}$), 24.5 ($CH_{3\text{-}tBu}$).

Saponification of the Monomers

4-isobutoxy-8-nitroquinoline-2-carboxylic acid **(B6)***:* In a 500 mL round bottomed flask equipped with a large magnetic stirrer, Methyl 4-isobutoxy-8-nitroquinoline-2-carboxylate **(B4)** (16.0 mmol; 4.85 g) and THF / MeOH (2/1) (200 mL) were mixed. KOH (2.5 eq., 40 mmol; 2.24 g) was then added and resulting mixture was stirred overnight. Apparition of slurry indicates that the reaction was occurring. Reaction was then quenched by addition of acetic acid, and solvents were rotary evaporated. Residue was dissolved in 150 mL dichloromethane and organic layer was washed 3 times with 75 mL distilled water ans saturated NaCl. Combined aqueous layers were back extracted with dichloromethane (50 mL). Combined organic layers were then dried over $MgSO_4$ and filtered. After evaporation, isobutoxy-8-nitroquinoline-2-carboxylic acid was obtained as an off-white solid. Yield: 99 %. $C_{14}H_{14}N_2O_5$ = 290.27 g.mol^{-1}. MS (FAB): *m/z* = 291 $[M]^+$, 235 $[M – CH_2CH(CH_3)_2]^+$, 154 $[C_{10}H_4NO]^+$. ^{1}H NMR ($CDCl_3$): δ 8.54 (1H, dd, J_{HH} = 1.4, 8.5 Hz, $CH_{ar\text{-}ortho}$), 8.22 (1H, dd, J_{HH} = 1.4, 7.5 Hz, $CH_{ar\text{-}para}$), 7.74 (2H, m, $CH_{ar\text{-}quinone}$ and $CH_{ar\text{-}meta}$), 4.13 (2H, d, J_{HH} = 6.5 Hz, $CH_{2\text{-}\alpha}$), 2.33 (1H, m, CH_β), 1.15 (6H, d, J_{HH} = 6.7 Hz, $CH_{3\text{-}\gamma}$).

4-(3-(tert-butylthio)propoxy)-8-nitroquinoline-2-carboxylic acid **(B7)***:* was prepared via a similar protocol starting from Methyl 4-(3-(tert-butylthio)propoxy)-8-nitroquinoline-2-

carboxylate **(B5)**. Yield: 99 %. $C_{17}H_{20}N_2O_5S$ = 364.42 g.mol^{-1}. MS (FAB): *m/z* = 365 $[M + H]^+$, 307 $[M – tBu]^+$, 154 $[C_{10}H_4NO]^+$. ^{1}H NMR ($CDCl_3$): δ 8.58 (1H, dd, J_{HH} = 1.4, 8.5 Hz, $CH_{ar\text{-}ortho}$), 8.24 (1H, dd, J_{HH} = 1.4, 7.5 Hz, $CH_{ar\text{-}para}$), 7.82 (1H, s, $CH_{ar\text{-}quinone}$), 7.77 (1H, t, J_{HH} = 8.5 Hz, $CH_{ar\text{-}meta}$), 4.49 (2H, t, J_{HH} = 6.2 Hz, $CH_{2\text{-}\alpha}$), 2.80 (1H, t, J_{HH} = 6.9 Hz, $CH_{2\text{-}\gamma}$), 2.28 (1H, q, J_{HH} = 6.3 Hz, $CH_{2\text{-}\beta}$), 1.34 (9H, s, $CH_{3\text{-}tBu}$).

Carboxylic acid activation

4-isobutoxy-8-nitroquinoline-2-carbonyl chloride **(B8)***:* 4-isobutoxy-8-nitroquinoline-2-carboxylic acid **(B6)** (4.6 g, 16.0 mmol) and $SOCl_2$ 80 mL were introduced in a 250 mL round bottomed flask equipped with a magnetic stirring bar and a reflux condenser. The round bottomed flask was placed in an oil bath previously heated to 90°C. Reaction mixture was then stirred at 90°C for 20 min and subsequently cooled by addition of Toluene (80 mL). Solvents were azeotroped by rotary evaporation and residue was dried at reduced pressure to yield a yellowish solid. Yield: Quant. $C_{14}H_{13}N_2O_4Cl$= 308.72 g.mol^{-1}. ^{1}H NMR ($CDCl_3$): δ 8.53 (1H, d, J_{HH} = 8.4 Hz, $CH_{ar\text{-}ortho}$), 8.17 (1H, d, J_{HH} = 7.4 Hz, $CH_{ar\text{-}para}$), 7.79 (1H, t, J_{HH} = 7.8 Hz, $CH_{ar\text{-}meta}$), 7.57 (1H, s, $CH_{ar\text{-}quinone}$), 4.14 (2H, d, J_{HH} = 6.4 Hz, $CH_{2\text{-}\alpha}$), 2.37 (1H, m, CH_β), 1.20 (6H, d, J_{HH} = 6.6 Hz, $CH_{3\text{-}\gamma}$).

4-(3-(tert-butylthio)propoxy)-8-nitroquinoline-2-carbonyl chloride **(B9)***:* was prepared from 4-(3-(tert-butylthio)propoxy)-8-nitroquinoline-2-carboxylic acid **(B7)** as described previously. Yield: Quant. $C_{17}H_{19}N_2O_4SCl$ = 382.86 g.mol^{-1}. ^{1}H NMR ($CDCl_3$): δ 8.51 (1H, d, J_{HH} = 8.5 Hz, $CH_{ar\text{-}ortho}$), 8.17 (1H, d, J_{HH} = 7.4 Hz, $CH_{ar\text{-}para}$), 7.78 (1H, t, J_{HH} = 8.0 Hz, $CH_{ar\text{-}meta}$), 7.60 (1H, s, $CH_{ar\text{-}quinone}$), 4.49 (2H, t, J = 6.1 Hz, $CH_{2\text{-}\alpha}$), 2.84 (1H, t, J_{HH} = 6.9 Hz, $CH_{2\text{-}\gamma}$), 2.32 (1H, q, J_{HH} = 6.5 Hz, $CH_{2\text{-}\beta}$), 1.38 (9H, s, $CH_{3\text{-}tBu}$).

Reduction of the monomers

Methyl 8-amino-4-isobutoxyquinoline-2-carboxylate **(B10)***:* In a 250 mL round bottomed flask, Methyl 4-isobutoxy-8-nitroquinoline-2-carboxylate **(B4)** (4.48 g; 14.7 mmol) was dissolved in ethyl acetate (150 mL). A catalytic amount of Pd / C (10 %) catalyst (450 mg) was then added and the mixture was placed at a 4 bar atmosphere of hydrogen and stirred at ambient temperature for 4 h. Reaction mixture was then filtered through Celite and solvent was rotary evaporated to yield a flashy green solid. Yield: 98%. $C_{15}H_{18}N_2O_3$ = 274.32 g.mol^{-1}. MS (FAB): *m/z* = 275 $[M + H]^+$, 154 $[C_{10}H_4NO]^+$. ^{1}H NMR ($CDCl_3$): δ 7.5 (1H, dd, J_{HH} = 1.3, 8.3 Hz, $CH_{ar\text{-}ortho}$), 7.48 (1H, s, $CH_{ar\text{-}quinone}$), 7.35 (1H, t,

J_{HH} = 7.5 Hz, $CH_{ar\text{-}meta}$), 6.93 (1H, dd, J_{HH} = 1.3, 7.5 Hz, $CH_{ar\text{-}para}$), 4.02 (3H, s, $CH_{3\text{-}ester}$), 4.00 (2H, d, J_{HH} = 6.5 Hz, $CH_{2\text{-}\alpha}$), 2.32 – 2.20 (1H, sep, J_{HH} = 6.7 Hz, CH_{β}), 1.12 (6H, d, J_{HH} = 6.7 Hz, $CH_{3\text{-}\gamma}$). ^{13}C NMR ($CDCl_3$): δ 166.4 (C=O), 162.6, 145.8, 144.8, 122.9, 107.0 ($C_{q\text{-}ar}$), 128.5, 110.7, 109.5 (CH_{ar}), 100.7 ($CH_{quinone}$), 74.8 ($CH_{2\text{-}\alpha}$), 52.7 ($CH_{3\text{-}ester}$), 28.2 (CH_{β}), 19.2 ($CH_{3\text{-}\gamma}$).

Methyl 4-(3-(tert-butylthio)propoxy)-8-aminoquinoline-2-carboxylate **(B11)***:* was prepared with 4-(3-(tert-butylthio)propoxy)-8-nitroquinoline-2-carboxylic acid **(B5)** as starting material, the resulting dark green solid is not air stable and should be used within a day and manipulated under inert atmosphere. Yield: Quant. $C_{18}H_{24}N_2O_3S$ = 348.46 g.mol^{-1}. MS (FAB): *m/z* = 349 $[M + H]^+$, 154 $[C_{10}H_4NO]^+$. ^1H NMR ($CDCl_3$): δ 7.60 – 7.50 (1H, m, $CH_{ar\text{-}ortho}$ and $CH_{ar\text{-}quinone}$), 7.41 (1H, t, J_{HH} = 8.2 Hz, $CH_{ar\text{-}meta}$), 6.99 (1H, dd, J_{HH} = 1.0, 6.5 Hz, $CH_{ar\text{-}para}$), 4.40 (2H, t, J_{HH} = 6.0 Hz, $CH_{2\text{-}\alpha}$), 4.07 (3H, s, $CH_{3\text{-}ester}$), 2.86 (1H, t, J_{HH} = 7.1 Hz, $CH_{2\text{-}\gamma}$), 2.26 (1H, q, J_{HH} = 6.4 Hz, $CH_{2\text{-}\beta}$), 1.38 (9H, s, $CH_{3\text{-}tBu}$).

8.3.2 Dimers

Coupling to dimers, general procedure for coupling

Methyl 8-(4-isobutoxy-8-nitroquinoline-2-carboxamido)-4-isobutoxyquinoline-2-carboxylate **(B12)**: In a 250 mL round bottomed flask methyl 8-amino-4-isobutoxyquinoline-2-carboxylate **(B10)** (2.36 g; 8.6 mmol) and N,N-Diisopropylethylamine (5.5 eq.; 47.3 mmol; 8.23 mL) were dissolved in 60 mL of freshly distilled dichloromethane. The flask was then cooled to 0°C and placed in an inert atmosphere. In a separate flask, 4-isobutoxy-8-nitroquinoline-2-carbonyl chloride **(B8)** (1.05 eq.; 9.03 mmol, 2.78 g) was dissolved in 40 mL of freshly distilled dichloromethane and placed in an argon atmosphere. Solution of 4-isobutoxy-8-nitroquinoline-2-carbonyl chloride was then added via a stainless steel canula to the solution of methyl 8-amino-4-isobutoxyquinoline-2-carboxylate over a period of 30 min at 0°C. Resulting mixture was taken away from the ice bath and stirred at ambient temperature overnight. Reaction mixture was subsequently diluted with 40 mL dichloromethane and organic layer was washed successively with 50 mL distilled water, 50 mL saturated $NaHCO_3$, 50 mL distilled water, 50 mL 0.1 M HCl, 50 mL distilled water. Organic layer was then dried over $MgS0_4$, filtered and rotary evaporated. Crude product was recrystallized from cold MeOH / $CHCl_3$ mixture to yield yellow needles. Yield: 76 %. $C_{29}H_{30}N_4O_7$ = 546.57 g.mol^{-1}. Elemental

analysis calc. for $C_{29}H_{30}N_4O_7$: C, 63.73; H, 5.53; N, 10.25; found: C, 63.25; H, 5.65; N, 10.11. MS (FAB): *m/z* = 546 $[M]^+$, 301 $[C_{16}H_{17}N_2O_4]^+$, 154 $[C_{10}H_4NO]^+$. ^{1}H NMR ($CDCl_3$): δ 11.86 (1H, bs), 9.09 (1H, d, J_{HH} = 6.8 Hz), 8.51 (1H, d, J_{HH} = 8.3 Hz), 8.18 (1H, d, J_{HH} = 7.3 Hz), 8.00 (1H, d, J_{HH} = 8.3 Hz), 7.94 (3H, m), 4.23 (3H, s), 4.15 (2H, d, J_{HH} = 6.2 Hz), 4.07 (2H, d, J_{HH} = 6.3 Hz), 2.30 (2H, qu, J_{HH} = 6.9 Hz), 1.16 (12H, m). ^{13}C NMR ($CDCl_3$): δ 166.9, 163.2, 162.7, 162.5, 154.0, 148.3, 147.8, 139.7, 139.3, 134.9, 127.8, 126.6, 125.3, 123.4, 122.3, 118.7, 116.7, 101.5, 100.2, 75.7, 75.1, 53.6, 28.3, 28.2, 28.1, 19.2, 19.1.

Methyl 4-(3-(tert-butylthio)propoxy)-8-(4-isobutoxy-8-nitroquinoline-2-carboxamido)-quinoline-2-carboxylate **(B13)**: was prepared the same way as described above using methyl 4-(3-(tert-butylthio)propoxy)-8-aminoquinoline-2-carboxylate **(B11)** and 4-isobutoxy-8-nitroquinoline-2-carbonyl chloride **(B8)**. Yield: 85 %. $C_{32}H_{36}N_4O_7S$ = 620.72 g.mol^{-1}. Elemental analysis calc. for $C_{32}H_{36}N_4O_7S$: C, 61.92; H, 5.95; N, 9.03; found: C, 61.59; H, 6.06; N, 8.96. MS (FAB): *m/z* = 621 $[M + H]^+$, 375 $[C_{19}H_{23}N_2O_4S]^+$. ^{1}H NMR ($CDCl_3$): δ 11.88 (1H, bs), 9.11 (1H, dd, J_{HH} = 1.2, 7.8 Hz), 8.54 (1H, dd, J_{HH} = 1.3, 8.4 Hz), 8.20 (1H, dd, J_{HH} = 1.4, 7.4 Hz), 8.01 (1H, dd, J_{HH} = 1.2, 8.4 Hz), 7.99 (1H, s), 7.67 (3H, m), 4.41 (2H, t, J_{HH} = 6.0 Hz), 4.23 (3H, s), 4.17 (2H, d, J_{HH} = 6.5 Hz), 2.82 (2H, t, J_{HH} = 7.1 Hz), 2.40 – 2.20 (3H, m), 1.35 (9H, s), 1.16 (6H, d, J_{HH} = 6.8 Hz). ^{13}C NMR ($CDCl_3$): δ 166.8, 166.7, 163.2, 162.4, 153.9, 148.3, 147.8, 139.7, 139.3, 134.9, 127.9, 126.6, 126.5, 125.3, 123.4, 123.3, 122.1, 118.7, 116.5, 101.5, 100.2, 75.7, 67.6, 53.6, 42.2, 31.0, 30.9, 29.3, 28.1, 24.8, 24.7, 19.2.

Methyl 8-(4-(3-(tert-butylthio)propoxy)-8-nitroquinoline-2-carboxamido)-4-isobutoxy-quinoline-2-carboxylate **(B14)**: was prepared starting from Methyl 8-amino-4-isobutoxyquinoline-2-carboxylate **(B10)** and 4-(3-(tert-butylthio)propoxy)-8-nitroquinoline-2-carbonyl chloride **(B9)**. Yield: 54 %. $C_{32}H_{36}N_4O_7S$ = 620.72 g.mol^{-1}. Elemental analysis calc. for $C_{32}H_{36}N_4O_7S$: C, 61.92; H, 5.95; N, 9.03; found: C, 62.03; H, 5.89; N, 9.18. MS (FAB): *m/z* = 621 $[M + H]^+$. ^{1}H NMR ($CDCl_3$): δ 11.86 (1H, bs), 9.08 (1H, d, J_{HH} = 7.6 Hz), 8.51 (1H, d, J_{HH} = 8.2 Hz), 8.18 (1H, d, J_{HH} = 7.1 Hz), 7.98 (2H, m), 7.60 (3H, m), 4.50 (2H, t, J_{HH} = 6.0 Hz), 4.21 (3H, s), 4.06 (2H, d, J_{HH} = 6.4 Hz), 2.81 (2H, t, J_{HH} = 7.0 Hz), 2.27 (3H, m), 1.34 (9H, s), 1.16 (6H, d, J_{HH} = 6.6 Hz). ^{13}C NMR ($CDCl_3$): δ 171.1, 166.9, 163.0, 162.8, 162.4, 154.0, 148.3, 147.9,

139.7, 139.4, 134.8, 127.8, 126.6, 125.4, 123.3, 122.3, 118.8, 116.7, 101.5, 100.3, 75.2, 68.3, 53.6, 30.9, 29.1, 28.2, 24.7, 19.2.

Saponification of a dimer nitro-ester

8-(4-isobutoxy-8-nitroquinoline-2-carboxamido)-4-isobutoxyquinoline-2-carboxylic acid **(B15)**: Methyl-8-(4-isobutoxy-8-nitroquinoline-2-carboxamido)-4-isobutoxyquinoline-2-carboxylate **(B12)** (1.0 mmol; 546 mg) and of THF / MeOH (3 / 1) (30 mL) were introduced in a 100 mL round bottomed flask equipped with a large magnetic stirrer. KOH (2.5 eq., 2.5 mmol, 140 mg) was subsequently added to this mixture. Resulting slurry was stirred 3 h at 40°C. Reaction was quenched by addition of acetic acid, and solvents were rotary evaporated. Residue was then dissolved in 20 mL dichloromethane and the organic layer was washed with 15 mL distilled water and 15 mL of saturated NaCl. Combined aqueous layers were then back extracted with 10 mL dichloromethane. Combined organic layers were dried over $MgSO_4$ and filtered. Solvents were removed by rotary evaporation to yield a yellowish solid. Yield: Quant. $C_{28}H_{28}N_4O_7$ = 532.54 g.mol^{-1}. Elemental analysis calc. for $C_{28}H_{28}N_4O_7$: C, 63.15; H, 5.30; N, 10.52; found: C, 62.94; H, 5.43; N, 10.47. MS (FAB): *m/z* = 533.2 $[M + H]^+$, 154 $[C_{10}H_4NO]^+$. ^{1}H NMR ($CDCl_3$): δ 11.67 (1H, bs), 9.13 (1H, d, J_{HH} = 7.6 Hz), 8.51 (1H, d, J_{HH} = 8.1 Hz), 8.25 (1H, d, J_{HH} = 7.4 Hz), 8.05 (1H, d, J_{HH} = 8.2 Hz), 7.91 (1H, s), 7.77 (1H, s), 7.67 (2H, t, J_{HH} = 8.0 Hz), 4.16 (2H, d, J_{HH} = 6.5 Hz), 4.11 (2H, d, J_{HH} = 6.4 Hz), 2.35 – 2.25 (2H, m), 1.25 – 1.12 (12H, m). ^{13}C NMR ($CDCl_3$): δ 164.9, 164.0, 163.7, 162.3, 153.5, 147.5, 146.9, 139.4, 138.7, 134.3, 128.5, 127.3, 126.1, 125.8, 123.6, 123.1, 119.6, 117.3, 100.4, 100.2, 76.1, 75.8, 28.3, 19.4.

Activation of a dimer carboxylic acid

8-(4-isobutoxy-8-nitroquinoline-2-carboxamido)-4-isobutoxyquinoline-2-carbonyl chloride **(B16)**: The 8-(4-isobutoxy-8-nitroquinoline-2-carboxamido)-4-isobutoxyquinoline-2-carboxylic acid **(B15)** (532 mg; 1.0 mmol) was dissolved in $SOCl_2$ (10 mL). The resulting solution was introduced in a 50 mL round bottomed flask equipped with a magnetic stirring bar and a reflux condenser. The round bottomed flask was placed in an oil bath previously heated to 90°C. Reaction mixture was stirred at 90°C under protecting gas for 20 min and subsequently cooled by addition of 20 mL of dry Toluol. Solvents were azeotroped by rotary evaporation and residue was thoroughly dried under reduced pressure to yield the air-sensitive carbonyl chloride as a brownish oily residue. Yield: Quant. $C_{28}H_{27}ClN_4O_6$ = 550.16 g.mol^{-1}. ^{1}H NMR ($CDCl_3$): δ 11.82 (1H, bs), 9.11 (1H, d,

J_{HH} = 7.4 Hz), 8.53 (1H, d, J_{HH} = 7.9 Hz), 8.16 (1H, d, J_{HH} = 7.9 Hz), 8.02 (1H, d, J_{HH} = 7.9 Hz), 7.96 (1H, s), 7.73 (1H, t, J_{HH} = 8.1 Hz), 7.66 (1H, t, J_{HH} = 7.9 Hz), 7.51 (1H, s), 4.18 (2H, d, J_{HH} = 6.4 Hz), 4.07 (2H, d, J_{HH} = 6.5 Hz), 2.30 – 2.40 (2H, m), 1.13 – 1.20 (12H, m).

Reduction of dimers

Methyl 8-(4-isobutoxy-8-aminoquinoline-2-carboxamido)-4-isobutoxyquinoline-2-carboxylate **(B17)***:* In a 500 mL round bottomed flask, Methyl 8-(4-isobutoxy-8-nitroquinoline-2-carboxamido)-4-isobutoxyquinoline-2-carboxylate **(B12)** (2.47 g; 4.52 mmol) was dissolved in ethyl acetate (300 mL). A catalytic amount of Pd / C (10 %) catalyst (180 mg) was added to this mixture. Mixture was subsequently placed at a 4 bar atmosphere of hydrogen and resulting mixture was stirred at ambient temperature for 4 h. Reaction mixture was then filtered through Celite and solvent was rotary evaporated to yield a green solid. Yield: 99 %. $C_{29}H_{32}N_4O_5$ = 516.59 g.mol^{-1}. Elemental analysis calc. for $C_{29}H_{32}N_4O_5$: C, 67.43; H, 6.24; N, 10.85; found: C, 67.25; H, 6.48; N, 10.11. MS (FAB): *m/z* = 517 $[M]^+$. ^{1}H NMR ($CDCl_3$): δ 12.67 (1H, bs), 9.04 (1H, dd, J_{HH} = 1.2, 7.7 Hz), 7.94 (1H, dd, J_{HH} = 1.3, 8.4 Hz), 7.75 (1H, s), 7.67 (1H, t, J_{HH} = 8.2 Hz), 7.56 – 7.52 (2H, m), 7.37 (1H, t, J_{HH} = 7.5 Hz), 6.99 (1H, dd, J_{HH} = 1.2, 7.5 Hz), 5.51 (2H, bs), 4.15 – 4.11 (8H, m), 2.35 – 2.21 (2H, m), 1.17 – 1.13 (12H, m). ^{13}C NMR ($CDCl_3$): δ 165.6, 163.4, 163.3, 163.1, 148.5, 147.0, 144.9, 144.0, 139.8, 137.6, 135.4, 128.7, 128.3, 123.2, 122.4, 117.4, 115.8, 111.1, 109.7, 104.9, 101.5, 98.4, 75.3, 75.2, 53.1, 28.4, 28.3, 19.5.

Methyl 4-(3-(tert-butylthio)propoxy)-8-(4-isobutoxy-8-aminoquinoline-2-carboxamido) quinoline-2-carboxylate **(B18)**: Was prepared the same way as described before using Methyl 4-(3-(tert-butylthio)propoxy)-8-(4-isobutoxy-8-nitroquinoline-2-carboxamido)-quinoline-2-carboxylate **(B13)** as starting materials. However, 12 h stirring at ambient temperature were required to reach reaction completion. Yield: 99 %. $C_{32}H_{38}N_4O_5S$ = 590.73 g.mol^{-1}. Elemental analysis calc. for $C_{32}H_{38}N_4O_5S$: C, 65.06; H, 6.48; N, 9.48; found: C, 64.26; H, 6.49; N, 10.22. MS (FAB): *m/z* = 591 $[M]^+$. ^{1}H NMR ($CDCl_3$): δ 12.66 (1H, bs), 9.04 (1H, dd, J_{HH} = 1.0, 7.6 Hz), 7.91 (1H, dd, J_{HH} = 0.9, 7.5 Hz), 7.74 (1H, s), 7.67 (1H, t, J_{HH} = 8.1 Hz), 7.58 – 7.50 (2H, m), 7.36 (1H, t, J_{HH} = 7.8 Hz), 6.99 (1H, dd, J_{HH} = 0.8, 7.5 Hz), 4.39 (2H, t, J_{HH} = 6.0 Hz), 4.11 – 4.06 (5H, m), 2.82 (2H, t, J_{HH} = 7.0 Hz), 2.35 – 2.20 (3H, m), 1.35 (9H, s), 1.15 (6H, d, J_{HH} = 6.7 Hz).

Methyl 8-(4-(3-(tert-butylthio)propoxy)-8-aminoquinoline-2-carboxamido)-4-isobutoxyquinoline-2-carboxylate **(B19)**: Was prepared the same way as described above using methyl 8-(4-(3-(tert-butylthio)propoxy)-8-nitroquinoline-2-carboxamido)-4-isobutoxy quinoline-2-carboxylate **(B14)**. Yield: 99 %. $C_{32}H_{38}N_4O_5S$ = 590.73 g.mol^{-1}. Elemental analysis calc. for $C_{32}H_{38}N_4O_5S$: C, 65.06; H, 6.48; N, 9.48; found: C, 64.47; H, 6.39; N, 9.99. MS (FAB): *m/z* = 591 $[M]^+$. ^{1}H NMR ($CDCl_3$): δ 12.67 (1H, s), 9.03 (1H, d, J_{HH} = 7.7 Hz), 7.95 (1H, d, J_{HH} = 7.5 Hz), 7.77 (1H, s), 7.67 (1H, t, J_{HH} = 8.1 Hz), 7.55 – 7.47 (2H, m), 7.38 (1H, t, J_{HH} = 8.0 Hz), 7.01 (1H, d, J_{HH} = 7.4 Hz), 4.42 (2H, t, J_{HH} = 6.1 Hz), 4.09 (3H, s), 4.06 (2H, d, J_{HH} = 6.4 Hz), 2.82 (2H, t, J_{HH} = 7.2 Hz), 2.31 – 2.19 (3H, m), 1.34 (9H, s), 1.16 (6H, d, J_{HH} = 6.7 Hz).

8.3.3 Trimers

Coupling to trimers

Trimer nitro-isobutoxy-isobutoxy-tertbutylthiopropoxy-methylester **(B20)**: was prepared according to the general procedure for coupling, using methyl 4-(3-(tert-butylthio)propoxy)-8-aminoquinoline-2-carboxylate **(B11)** and 8-(4-isobutoxy-8-nitroquinoline-2-carboxamido)-4-isobutoxyquinoline-2-carbonyl chloride **(B16)**. Product was purified by flash-chromatography on silica gel with 0.1 % MeOH in DCM as eluant. Yield: 86 %. $C_{46}H_{50}N_6O_9S$ = 862.99 g.mol^{-1}. Elemental analysis calc. for $C_{46}H_{50}N_6O_9S$: C, 64.02; H, 5.84; N, 9.74; found: C, 63.81; H, 5.81; N, 9.65. MS (FAB): *m/z* = 862.9 $[M]^+$. ^{1}H NMR ($CDCl_3$): δ 12.36 (1H, s), 12.20 (1H, s), 9.03 (1H, dt, J_{HH} = 0.6, 8.2 Hz), 8.47 (1H, dd, J_{HH} = 1.3, 8.2 Hz), 8.05 (1H, dd, J_{HH} = 1.2, 8.4 Hz), 7.91 – 7.87 (3H, m), 7.83 (1H, s), 7.72 (1H, t, J_{HH} = 8.2 Hz), 7.67 (1H, t, J_{HH} = 8.2 Hz), 7.55 (2H, dd, J_{HH} = 1.3, 7.5 Hz), 7.46 (1H, t, J_{HH} = 7.8 Hz), 6.77 (1H, s), 4.23 – 4.13 (6H, m), 3.45 (3H, s), 2.84 (2H, t, J_{HH} = 6.8 Hz), 2.45 – 2.15 (4H, m), 1.38 (9H, s), 1.21 (6H, d, J_{HH} = 6.7 Hz), 1.17 (6H, d, J_{HH} = 6.7 Hz). ^{13}C NMR ($CDCl_3$): δ 164.7, 163.8, 163.5, 163.0, 162.8, 162.2, 154.4, 151.1, 145.8, 145.6, 140.2, 139.3, 139.3, 135.8, 134.7, 129.1, 129.0, 128.9, 127.7, 127.5, 126.0, 125.0, 123.6, 122.6, 122.0, 118.3, 118.2, 117.0, 115.7, 104.9, 100.4, 99.7, 99.4, 76.0, 75.6, 67.3, 52.6, 49.8, 42.6, 31.2, 29.3, 28.4, 24.8, 23.2, 19.5, 19.4.

Reduction of a trimer

Trimer amino-isobutoxy-isobutoxy-tertbutylthiopropoxy-methylester **(B21)**: In a 50 mL round bottomed flask, the trimer nitro-isobutoxy-isobutoxy-tertbutylthiopropoxy-methylester **(B20)** (420 mg, 0.49 mmol) was dissolved in ethyl acetate (200 mL). A catalytic amount of Pd / C (20 %) catalyst (84 mg) was added. Solution was subsequently placed at a 4 bar atmosphere of hydrogen and resulting mixture was stirred at ambient temperature for 24 h. Reaction mixture was then filtered through Celite and solvent was rotary evaporated to yield a yellow solid. Yield: Quant. $C_{46}H_{52}N_6O_7S$ = 833.01 g.mol^{-1}. Elemental analysis calc. for $C_{46}H_{52}N_6O_7S$: C, 66.33; H, 6.29; N, 10.09; found: C, 66.32; H, 5.82; N, 9.74. MS (FAB): *m/z* = 833.3 $[M]^+$. ^{1}H NMR ($CDCl_3$): δ 12.37 (1H, s), 12.35 (1H, s), 9.02 (1H, dd, J_{HH} = 1.3, 7.7 Hz), 8.90 (1H, dd, J_{HH} = 1.2, 7.7 Hz), 8.00 (1H, dd, J_{HH} = 1.3, 8.4 Hz), 7.91 (1H, dd, J_{HH} = 1.3, 8.4 Hz), 7.74 (1H, s), 7.72 (1H, t, J_{HH} = 8.2 Hz), 7.67 (1H, t, J_{HH} = 8.2 Hz), 7.55 (1H, dd, J_{HH} = 1.3, 7.5 Hz), 7.72 – 7.63 (2H, m), 7.53 – 7.48 (1H, m), 7.42 (1H, dd, J_{HH} = 0.9, 8.4 Hz), 7.04 (1H, t, J_{HH} = 8.2 Hz), 6.79 (1H, s), 5.93 (1H, dd, J_{HH} = 0.8, 7.5 Hz), 4.22 – 4.07 (9H, m), 3.45 (3H, s), 2.82 (2H, t, J_{HH} = 7.0 Hz), 2.40 – 2.14 (4H, m), 1.37 (9H, s), 1.21 (12H, d, J_{HH} = 6.7 Hz). ^{13}C NMR ($CDCl_3$): δ 164.7, 163.9, 163.8, 163.5, 163.0, 162.8, 162.2, 154.4, 151.1, 145.7, 145.6, 140.2, 139.3, 135.7, 134.8, 134.7, 131.1, 129.0, 128.9, 127.8, 127.6, 127.5, 126.0, 125.0, 123.6, 122.6, 122.0, 118.5, 118.4, 118.2, 117.0, 115.7, 100.4, 99.7, 99.4, 76.0, 75.6, 67.3, 52.6, 42.6, 31.2, 29.3, 28.4, 24.8, 19.6, 19.4.

8.3.4 Pentamers

1,10-phenanthroline-2,9-dicarboyl dichloride **(B22)***:* 1,10-phenanthroline 2,9-dicarboxylic acid (135 mg; 0.5 mmol) and $SOCl_2$ (10 mL) were introduced in a 50 mL round bottomed flask equipped with a magnetic stirring bar and a reflux condenser. The round bottomed flask was placed in an oil bath previously heated to 90°C. Reaction mixture was stirred at 90°C for 1 h and subsequently cooled by addition of dry Toluol (20 mL). Solvents were then azeotroped by rotary evaporation and residue was dried under reduced pressure to yield 1,10-phenanthroline 2,9-dicarboyl dichloride as a brownish solid. Yield: Quant. $C_{14}H_6O_2Cl_2$= 305.11 g.mol^{-1}. ^{1}H NMR (DMSO d6): δ 9.07 (2H, d, J_{HH} = 8.2 Hz), 8.76 (2H, d, J_{HH} = 8.3 Hz), 8.56 (2H, s).

Coupling to pentamers

Methylester-tertbutylthiopropoxy-isobutoxy-phenantroline-isobutoxy-tertbutylthio propoxy-methylester **(B23)**: was prepared following the general procedure for coupling, using 1,10-phenanthroline 2,9-dicarboyl dichloride **(B22)** and two equivalents of Methyl 4-(3-(tert-butylthio)propoxy)-8-(4-isobutoxy-8-aminoquinoline-2-carboxamido)quinoline 2-carboxylate **(B18)**. Product was purified by flash-chromatography on silica with EtOAc / Hexane (1:1). Yield: 73 %. $C_{78}H_{80}N_{10}O_{12}S_2$ = 1413.66 g.mol^{-1}. Elemental analysis calc. for $C_{78}H_{80}N_{10}O_{12}S_2$: C, 66.27; H, 5.70; N, 9.91; found: C, 65.91; H, 5.57; N, 10.00. MS (FAB): *m/z* = 1413.8 $[M]^+$. TOF MS ES$^+$ (HR-MS): calc. for $[M + H]^+$: 1413.5477 g.mol^{-1}; found for $[M + H]^+$: 1413.5470 g.mol^{-1}. ^{1}H NMR ($CDCl_3$): δ 12.78 (2H, s), 11.80 (2H, s), 8.93 (2H, dd, J_{HH} = 1.4, 7.3 Hz), 8.81 (2H, dd, J_{HH} = 1.3, 7.3 Hz), 7.88 – 7.71 (8H, m), 7.64 – 7.52 (4H, m), 6.87 (2H, s), 6.40 (2H, s), 4.12 – 3.79 (8H, m), 3.21 (6H, s), 3.00 – 2.74 (4H, m), 2.36 – 2.14 (4H, m), 1.45 (18H, s), 1.20 (6H, d, J_{HH} = 6.7 Hz), 1.17 (6H, d, J_{HH} = 6.6 Hz). ^{13}C NMR ($CDCl_3$): δ 164.2, 162.6, 161.8, 161.6, 161.1, 149.0, 148.9, 144.8, 142.4, 138.7, 138.4, 136.0, 134.6, 134.2, 127.9, 126.8, 121.4, 120.5, 119.7, 118.9, 118.8, 115.8, 115.4, 100.2, 97.9, 75.3, 67.2, 67.1, 52.6, 49.5, 42.7, 31.3, 31.2, 29.6, 29.5, 28.4, 24.9, 24.8, 19.6, 19.5.

Methylester-isobutoxy-tertbutylthiopropoxy-phenantroline-tertbutylthiopropoxy-isobutoxy-methylester **(B24)**: was prepared following the general procedure for coupling, using 1,10-phenanthroline 2,9-dicarboyl dichloride **(B22)** and two equivalents of methyl 8-(4-isobutoxy-8-aminoquinoline-2-carboxamido)-4-isobutoxyquinoline-2-carboxylate **(B17)**. Product was purified by flash-chromatography on silica with EtOAc / Hexane (1:1). Yield: 58 %. $C_{78}H_{80}N_{10}O_{12}S_2$ = 1413.66 g.mol^{-1}. Elemental analysis calc. for $C_{78}H_{80}N_{10}O_{12}S_2$: C, 66.27; H, 5.70; N, 9.91; found: C, 65.97; H, 5.68; N, 10.05. MS (FAB): *m/z* = 1413.8 $[M]^+$. TOF MS ES$^+$ (HR-MS): calc. for $[M + H]^+$: 1413.5477 g.mol^{-1}; found for $[M + H]^+$: 1413.5442 g.mol^{-1}. ^{1}H NMR ($CDCl_3$): δ 12.76 (2H, s), 11.78 (2H, s), 8.92 (2H, dd, J_{HH} = 1.6, 7.1 Hz), 8.81 (2H, dd, J_{HH} = 2.0, 6.8 Hz), 7.84 – 7.71 (8H, m), 7.61 – 7.52 (4H, m), 7.42 (2H, s), 6,87 (2H, s), 6.34 (2H, s), 4.32 – 4.20 (4H, m), 3.74 – 3.62 (4H, m), 3.21 (6H, s), 2.95 – 2.72 (4H, m), 2.36 – 2.14 (4H, m), 1.39 (18H, s), 1.22 (6H, d, J_{HH} = 6.7 Hz), 1.16 (6H, d, J_{HH} = 6.7 Hz). ^{13}C NMR ($CDCl_3$): δ 164.1, 162.1, 161.4, 161.4, 161.1, 148.7, 144.5, 142.2, 138.5, 138.2,

135.8, 134.4, 134.0, 128.3, 128.2, 127.9, 126.4, 121.0, 120.4, 119.6, 118.7, 115.6, 115.3, 100.0, 97.7, 74.8, 71.1, 67.7, 52.4, 42.4, 31.0, 29.5, 28.1, 24.8, 21.8, 19.5, 19.2.

8.3.5 Deprotection of tertio butyl group

Deprotection steps on the monomer

Methyl 4-(3-(2-(3-nitropyridin-2-yl)disulfanyl)propoxy)-8-nitroquinoline-2-carboxylate **(B25a)***:* Methyl 4-(3-(tert-butylthio)propoxy)-8-nitroquinoline-2-carboxylate **(B5)** and Nitropyridine sulfenyl chloride were dissolved in acetic acid (20 mL). Resulting mixture was stirred at ambient temperature overnight (apparition of a precipitate). The solvent was subsequently removed by rotary evaporation and the residue was chromatographed on silica using 100 % dichloromethane as eluant, to yield a yellow solid. Yield: 69 %. $C_{19}H_{16}N_4O_7S_2$ = 476.48 g.mol^{-1}. Elemental analysis calc. for $C_{19}H_{16}N_4O_7S_2$: C, 47.89; H, 3.38; N, 11.76; found: C, 47.11; H, 3.86; N, 11.36. MS (FAB): *m/z* = 477 $[M + H]^+$, 307 $[C_{14}H_{13}NO_3S_2]^+$, 154 $[C_{10}H_4NO]^+$. ^{1}H NMR ($CDCl_3$): δ 8.81 – 8.79 (1H, m, $CH_{ar\text{-}Npys}$), 8.48 (1H, d, J_{HH} = 8.2 Hz, $CH_{ar\text{-}ortho}$), 8.11 (1H, d, J_{HH} = 7.4 Hz, $CH_{ar\text{-}para}$), 8.40 (1H, d, J_{HH} = 8.5 Hz, $CH_{ar\text{-}Npys}$), 7.70 (1H, s, $CH_{ar\text{-}quinone}$), 7.62 (1H, t, J_{HH} = 8.4 Hz, $CH_{ar\text{-}meta}$), 7.35 – 7.31 (1H, m, $CH_{ar\text{-}Npys}$), 4.52 (2H, m, $CH_{2\text{-}\alpha}$), 4.04 (3H, s, $CH_{3\text{-}ester}$), 3.16 (1H, t, J_{HH} = 6.6 Hz, $CH_{2\text{-}\gamma}$), 2.41 (1H, q, J_{HH} = 6.4 Hz, $CH_{2\text{-}\beta}$).

Methyl 4-(3-(2-(2-nitrophenyl)disulfanyl)propoxy)-8-nitroquinoline-2-carboxylate **(B25b)**: was prepared via a similar protocol using Nitrophenyl sulfenyl chloride. Yield: 60 %. $C_{20}H_{17}N_3O_7S_2$ = 475.49 g.mol^{-1}. Elemental analysis calc. for $C_{20}H_{17}N_3O_7S_2$: C, 50.52; H, 3.60; N, 8.84; found: C, 49.30; H, 3.70; N, 8.51. MS (FAB): *m/z* = 476 $[M + H]^+$, 307 $[C_{14}H_{13}NO_3S_2]^+$, 154 $[C_{10}H_4NO]^+$. ^{1}H NMR ($CDCl_3$): δ 8.42 (1H, d, J_{HH} = 8.4 Hz, $CH_{ar\text{-}ortho}$), 8.32 (1H, t, J_{HH} = 8.9 Hz, $CH_{ar\text{-}Nbs}$), 8.16 (1H, d, J_{HH} = 7.4 Hz, $CH_{ar\text{-}para}$), 7.71 – 7.65 (4H, m, $CH_{ar\text{-}quinone}$, $CH_{ar\text{-}Nbs}$ and $CH_{ar\text{-}meta}$), 7.40 (1H, t, J_{HH} = 7.8 Hz, $CH_{ar\text{-}Nbs}$), 4.48 (2H, d, J_{HH} = 5.5 Hz, $CH_{2\text{-}\alpha}$), 4.09 (3H, s, $CH_{3\text{-}ester}$), 3.06 (1H, t, J_{HH} = 6.7 Hz, $CH_{2\text{-}\gamma}$), 2.45 (1H, q, J_{HH} = 6.6 Hz, $CH_{2\text{-}\beta}$).

methyl 4-(3-mercaptopropoxy)-8-nitroquinoline-2-carboxylate **(B26)***:* To a solution of either methyl 4-(3-(2-(3-nitropyridin-2-yl)disulfanyl)propoxy)-8-nitroquinoline-2-carboxylate **(B25a)** or ethyl 4-(3-(2-(2-nitrophenyl)disulfanyl)propoxy)-8-nitroquinoline-2-carboxylate **(B25b)** (10 mmol; 4.7 g) in acetone (80 mL) and water (20 mL), a

stoichiometric amount of tri-*n*-butylphosphine (2.02 g; 10 mmol) was added at room temperature with continuous stirring. The resulting mixture was stirred for 4 h at ambient temperature. The acetone was removed at vacuum and the residue was dissolved in dichloromethane (300 mL), followed by successive washing with 5 % citric acid and water. The organic layers were dried over $MgSO_4$ and filtered. After removal of the solvent at vacuum, the residue was chromatographed on silica gel using 0.5 % MeOH in dichloromethane, to yield a yellowish solid. Yield: 66 %. $C_{14}H_{14}N_2O_5S$ = 322.34 g.mol^{-1}. Elemental analysis calc. for $C_{14}H_{14}N_2O_5S$: C, 57.12; H, 4.38; N, 8.69; found: C, 57.11; H, 3.86; N, 8.36. MS (FAB): *m/z* = 322 $[M]^+$. ^{1}H NMR ($CDCl_3$): δ 8.44 (1H, d, J_{HH} = 8.4 Hz, $CH_{ar\text{-}ortho}$), 8.11 (1H, d, J_{HH} = 7.1 Hz, $CH_{ar\text{-}para}$), 7.70 – 7.63 (2H, m, $CH_{ar\text{-}quinone}$ and $CH_{ar\text{-}meta}$), 4.46 (2H, m, $CH_{2\text{-}\alpha}$), 4.04 (3H, s, $CH_{3\text{-}ester}$), 2.83 (2H, m, $CH_{2\text{-}\gamma}$), 2.29 (1H, m, $CH_{2\text{-}\beta}$). ^{13}C NMR ($CDCl_3$): δ 163.0 (C=O), 151.6, 122.9 ($C_{q\text{-}ar}$), 127.4, 126.7, 122.3 (CH_{ar}), 102.3 ($CH_{quinone}$), 60.9 ($CH_{2\text{-}\alpha}$), 53.4 ($CH_{3\text{-}ester}$), 30.7 ($CH_{2\text{–}\gamma}$), 27.9 ($CH_{2\text{-}\beta}$).

Deprotection steps on the pentamer

Methylester-(NpyS)thiopropoxy-isobutoxy-phenantroline-isobutoxy-(NpyS)thiopropoxy-methylester **(B27)**: To a solution of methylester-tertbutylthiopropoxy-isobutoxy-phenantroline-isobutoxy-tertbutylthio propoxy-methylester **(B23)** (100 mg; 62.5 nmol) in acetic acid (3 mL) a slight excess of sodium para-nitro-pyridine sulfenyl chloride was added (0.15 mmol, 26 mg) and the reaction was stirred 24 h at ambient temperature, resulting in the apparition of a precipitate. Acetic acid was subsequently removed at vacuum and the residue was purified by flash-chromatography on silica with dichloromethane as eluant. Yield: 67 %. $C_{80}H_{68}N_{14}O_{16}S_4$ = 1609.74 g.mol^{-1}. MS (ESI+): *m/z* = 1609.38 $[M + H]^+$, 1631.37 $[M + Na]^+$. TOF MS ES$^+$ (HR-MS): calc. for $[M + H]^+$: 1609.3899 g.mol^{-1}; found for $[M + H]^+$: 1609.3881 g.mol^{-1}. ^{1}H NMR ($CDCl_3$): δ 12.86 (2H, s), 11.81 (2H, s), 8.96 – 8.83 (6H, m), 8.57 (2H, dd, J_{HH} = 1.5, 8.0 Hz), 7.91 (2H, d, J_{HH} = 8.1 Hz), 7.88 – 7.71 (6H, dqu, J_{HH} = 1.5, 7.4 Hz), 7.64 (2H, s), 7.60 (2H, t, J_{HH} = 7.6 Hz), 7.51 (2H, d, J_{HH} = 8.0 Hz), 7.44 (2H, dd, J_{HH} = 3.4, 8.2 Hz), 6.90 (2H, s), 6.46 (2H, s), 4.31 – 4.22 (2H, m), 4.14 – 4.05 (2H, m), 4.02 – 3.94 (2H, m), 3.90 – 3.82 (2H, m), 3.37 – 3.17 (10H, m), 2.43 – 2.25 (8H, m), 1.23 (6H, d, J_{HH} = 6.5 Hz), 1.20 (6H, d, J_{HH} = 6.4 Hz). ^{13}C NMR ($CDCl_3$): δ 163.9, 162.5, 161.6, 161.4, 160.8, 153.7, 153.5, 148.8, 148.7, 144.5, 142.9, 142.2, 138.4, 138.2, 135.9, 134.4, 134.0, 133.6, 128.5, 128.3, 127.7, 121.2, 120.8, 120.2, 119.5, 118.8, 118.6, 115.7, 115.1, 100.1, 97.7, 75.1, 66.2, 52.5, 34.5, 28.2, 27.6, 20.4, 19.4, 19.3.

Methylester-isobutoxy-(NpyS)thiopropoxy-phenantroline-(NpyS)thiopropoxy-isobutoxy-methylester **(B28)**: was prepared as described for the **(B27)** starting from Methylester-isobutoxy-tertbutylthiopropoxy-phenantroline-tertbutylthiopropoxy-isobutox-methylester **(B24)**. Yield: 74 %. $C_{80}H_{68}N_{14}O_{16}S_4$ = 1609.74 g.mol^{-1}. MS (ESI+): *m/z* = 1299.41 $[M + H - 2\times Npys]^+$, 1609.38 $[M + H]^+$, 1631.37 $[M + Na]^+$. TOF MS ES$^+$ (HR-MS): calc. for $[M + H]^+$: 1609.3899 g.mol^{-1}; found for $[M + H]^+$: 1609.3973 g.mol^{-1}. ^{1}H NMR ($CDCl_3$): δ 12.83 (2H, s), 11.76 (2H, s), 8.91 (2H, dd, J_{HH} = 1.2, 7.4 Hz), 8.81 (2H, dt, J_{HH} = 2.5, 6.6 Hz), 7.85 – 7.51 (18H, m), 7.42 (2H, s), 7.36 (4H, d, J_{HH} = 4.4 Hz), 6.91 (2H, s), 6.36 (2H, s), 4.70 (2H, s), 4.34 – 4.25 (4H, m), 4.23 – 4.15 (3H, m), 4.02 – 3.94 (2H, m), 3.75 – 6.61 (2H, m), 3.25 – 3.08 (7H, m), 2.55 – 2.18 (8H, m), 1.22 (6H, dd, J_{HH} = 2.0, 8.7 Hz), 1.16 (6H, dd, J_{HH} = 2.8, 6.7 Hz). ^{13}C NMR ($CDCl_3$): δ 164.0, 162.4, 161.6, 161.4, 160.8, 148.8, 148.8, 144.6, 138.5, 138.2, 135.7, 134.5, 134.0, 128.5, 128.3, 127.6, 126.5, 121.2, 120.3, 119.5, 118.8, 118.6, 115.6, 115.1, 100.0, 97.7, 77.2, 75.1, 65.9, 52.4, 32.5, 31.9, 29.7, 29.3, 28.2, 22.7, 21.2, 19.4, 19.3, 14.1, 13.6.

Methylester-thiopropoxy-isobutoxy-phenantroline-isobutoxy-thiopropoxy-methylester **(B29)**: To a solution of methylester-(NpyS)thiopropoxy-isobutoxy-phenantroline-isobutoxy-(NpyS)thiopropoxy-methylester **(B27)** (200 mg; 0.15 mmol) in acetone (10 mL) and water (2 mL), two equivalents of tri-*n*-butylphosphine (60 mg; 0.15 mmol) was added at rt with continuous stirring and the resulting mixture was stirred overnight. After removal of the solvent at vacuum, the residue was chromatographed on silica gel using 2 % MeOH in dichloromethane as eluant to yield a yellowish solid. Yield: 80 %. $C_{70}H_{64}N_{10}O_{12}S_2$ = 1301.45 g.mol^{-1}. MS (ESI+): *m/z* = 1301.42 $[M + H]^+$, 1324.41 $[M + Na]^+$. TOF MS ES$^+$ (HR-MS): calc. for $[M + H]^+$: 1301.4225 g.mol^{-1}; found for $[M + H]^+$: 1301.4244 g.mol^{-1}. ^{1}H NMR ($CDCl_3$): δ 12.81 (2H, s), 11.78 (2H, s), 8.90 (2H, dd, J_{HH} = 1.4, 7.3 Hz), 8.82 (2H, dd, J_{HH} = 1.0, 7.2 Hz), 7.91 – 7.46 (16H, m), 6.86 (2H, s), 6.41 (2H, s), 4.78 – 3.76 (12H, m), 3.20 (6H, m), 2.92 (3H, q, J_{HH} = 7.0 Hz), 2.28 (5H, qu, J_{HH} = 6.0 Hz), 1.18 (6H, d, J_{HH} = 6.6 Hz), 1.16 (6H, d, J_{HH} = 6.4 Hz).

Methylester-isobutoxy-thiopropoxy-phenantroline-thiopropoxy-isobutoxy-methylester **(B30)**: was prepared as described for the **(B29)** starting from Methylester-isobutoxy-(NpyS)thiopropoxy-phenantroline-(NpyS)thiopropoxy-isobutoxy-methylester **(B28)**.

Yield: 69 %. $C_{70}H_{64}N_{10}O_{12}S_2$ = 1301.45 g.mol^{-1}. MS (ESI+): *m/z* = 1301.42 $[M + H]^+$, 1324.41 $[M + Na]^+$. TOF MS ES$^+$ (HR-MS): calc. for $[M + H]^+$: 1301.4225 g.mol^{-1}; found for $[M + H]^+$: 1301.4226 g.mol^{-1}. ^{1}H NMR ($CDCl_3$): δ 12.82 (2H, s), 11.76 (2H, s), 8.91 (2H, dd, J_{HH} = 2.6, 6.2 Hz), 8.81 (2H, dt, J_{HH} = 2.4, 6.4 Hz), 7.83 – 7.70 (8H, m), 7.59 – 7.56 (2H, m), 7.41 (2H, s), 6.90 (2H, s), 6.36 (2H, s), 4.37 – 4.19 (6H, m), 3.69 (4H, q, J_{HH} = 6.9 Hz), 3.21 (6H, m), 2.90 (4H, sep, J_{HH} = 8.0 Hz), 2.37 – 2.19 (8H, m), 1.22 (6H, d, J_{HH} = 6.7 Hz), 1.16 (6H, d, J_{HH} = 6.7 Hz).

8.3.6 Iron carbonyls complexation

Complexation of the monomer

Methyl 4-(3-mercaptodiironhexacarbonyl)-8-nitroquinoline-2-carboxylate **(B31)***:* To a solution of methyl 4-(3-mercaptopropoxy)-8-nitroquinoline-2-carboxylate **(B26)** (0.54 mmol, 170 mg) in 5 mL of dried methanol, a stoichiometric amount of triiron dodecarbonyl (181 mg, 0.26 mmol) in dried chloroform was added at room temperature via a stainless steel canula. The chloroform is subsequently distilled off and the resulting mixture was refluxed at 90°C for 1 h. The methanol was removed in vacuum and the residue was purified on silica gel with MeOH / CH_2Cl_2 as the eluant to yield the desired product as a dark red crystalline powder. Yield: 27 %. $C_{34}H_{28}Fe_2N_4O_{16}S_2$ = 924.42 g.mol^{-1}. MS (ESI): *m/z* = 925 $[M + H]^+$, 944 $[M + Na]^+$, 643 $[M – 6CO – 2×Fe]^+$. TOF MS ES$^+$ (HR-MS): calc. for $[M + H]^+$: 925.62 g.mol^{-1}; found for $[M + H]^+$: 925.9597 g.mol^{-1}. ^{1}H NMR ($CDCl_3$): δ 8.38 (2H, t, J_{HH} = 8.5 Hz, $CH_{ar\text{-}ortho}$), 8.11 (2H, d, J_{HH} = 7.5 Hz, $CH_{ar\text{-}para}$), 7.71 – 7.64 (4H, m, $CH_{ar\text{-}quinone}$ and $CH_{ar\text{-}meta}$), 4.45 (3H, m, $CH_{2\text{-}\alpha}$), 4.35 (1H, t, J_{HH} = 5.1 Hz, $CH_{2\text{-}\alpha}$), 4.04 (6H, s, $CH_{3\text{-}ester}$), 2.72 (2H, q, J_{HH} = 7.0 Hz, $CH_{2\text{-}\gamma}$), 2.45 – 2.25 (6H, m, $CH_{2\text{-}\gamma}$ and $CH_{2\text{-}\beta}$). ^{13}C NMR ($CDCl_3$): δ 209.1, 208.2, 198.3 ($C{=}O_{Fe\text{-}CO}$), 161.1 ($C{=}O_{ester}$), 148.5, 122.9 ($C_{q\text{-}ar}$), 1126.1, 125.1, 122.9 (CH_{ar}), 102.2, 100.0 ($CH_{quinone}$), 67.6, 67.3, 67.1 ($CH_{2\text{-}\alpha}$), 53.4 ($CH_{3\text{-}ester}$), 35.3, 34.1, 31.9, 31.9, 31.8, 31.2 ($CH_{2\text{–}\gamma}$ and $CH_{2\text{-}\beta}$).

8.4 Crystallographic Tables

Table 8.1

	23b	**23c**	**25a**	**25d . H_2O**
chemical formula	$C_{34}H_{36}FeN_2O_6S_2$	$C_{32}H_{34}FeN_2O_4S_2$	$C_{17}H_{21}FeNO_3S\cdot$	$C_{34}H_{52}FeN_4O_9S_4$
Fw	688.62	630.58	375.26	844.89
Crystal size, mm	0.10 × 0.06 × 0.02	0.24 × 0.12 × 0.04	0.163 × 0.050 × 0.045	0.26 × 0.26 × 0.23
crystal system	Monoclinic	Tetragonal	Orthorhombic	Orthorhombic
Space group	$P2_1$ (No.4)	$P4_3$ (No.78)	$P2_12_12_1$ (No.19)	$P2_12_12_1$ (No.19)
a, Å	9.7500(6)	13.5835(3)	10.5221(3)	19.8819(3)
b, Å	12.4980(9)	13.5835(3)	16.5013(4)	11.3307(2)
c, Å	13.9735(9)	16.6873(4)	19.6449(6)(12)	17.6048(3)
β, deg	105.74(1)	90	90	90
V, $Å^3$	1638.90(19)	3079.00(12)	3410.91(16)	3965.94(11)
Z	2	4	8	4
D (calcd.), g/cm^3	1.395	1.360	1.462	1.415
temp. (K)	100(2)	100(2)	100(2)	100(2)
$2\theta_{max}$, ° / total no. of refl. coll.	62.14 / 42167	62 / 81349	62.08 / 82966	62 / 99604
abs. coeff. (mm^{-1})	0.635	0.664	1.020	0.647
*R*1 ($I > 2\sigma(I)$) [a]	0.0352	0.0304	0.0385	0.0426
w*R*2 (all data) [b]	0.0757	0.0720	0.0744	0.1015
data/restraints/ parameters	10397 /1 / 406	9800 / 2 / 377	10885 / 1 / 425	12634 / 35 / 508
GooF on F^2 [c]	1.035	1.071	1.040	1.140
Min. / Max. res. density, $eÅ^{-3}$	0.519 / -0.291	0.293 / -0.202	0.471 / -0.382	1.193 / -0.568
Flack parameter	-0.003(8)	0.001(7)	0.000(9)	0.029(10)

[a] $R1 = \Sigma||F_0|-|F_c||/\Sigma|F_0|$

[b] $wR2 = [\Sigma[w(F_0^2-F_c^2)^2]/\Sigma[w(F_0^2)_2]^{1/2}$, where $w = 1/\sigma^2(F_0^2)+(aP)^2+bP$, $P = (F_0^2+2F_c^2)/3$

[c] $GooF = [\Sigma[w(F_0^2-F_c^2)^2]/(n-p)]^{1/2}$ where n = no. of reflections and p = no. of refined parameters.

Table 8.2

	B23*	**B24***	**B29***
chemical formula	$C_{94}H_{98}N_{10}O_{12.5}S_2$	$C_{93.5}H_{85}N_{11}O_{14}S_2$	$C_{90}H_{59}N_{10}O_{12}S_2$
Fw	1631.94	1650.85	1536.59
Crystal size, mm	0.15 × 0.10 × 0.10	0.30 × 0.30 × 0.30	0.20 × 0.40 × 0.40
crystal system	Monoclinic	Triclinic	Orthorombic
Space group	$P2_1/c$ (No.4)	P-1	Pbcn (No.60)
a, Å	11.2360(10)	10.7380(10)	41.6850
b, Å	20.1960(10)	19.218(2)	20.2560
c, Å	39.8870(2)	20.879(2)	20.1800
β, deg	92.001(3)	103.717(6)	90
V, Å^3	9045.7(10)	4185.7(7)	17039.4
Z	4	2	8
D (calcd.), g/cm^3	1.198	1.310	1.198
temp. (K)	296(2)	193(2)	293(2)
$2\theta_{max}$, ° / total no. of refl. coll.	17376 / 96205	14476 / 58658	16452 / 16452
abs. coeff. (mm^{-1})	1.061	1.174	1.101
$R1$ ($I > 2\sigma(I)$) [a]	0.1339	0.1189	0.1525
w$R2$ (all data) [b]	0.4415	0.4014	0.4129
data/restraints/ parameters	17376 / 52 / 999	14476 / 0 / 1045	16452 / 1 / 1033
GooF on F2 [c]	1.028	1.064	1.703
Min. / Max. res. density, eÅ^{-3}	0.613 / -0.643	0.726 / -0.469	1.436 / -3.090
Flack parameter	-0.00001(7)	0.0005(2)	0.00000(5)

[a] $R1 = \Sigma||F_0|-|F_c||/\Sigma|F_0|$

[b] $wR2 = [\Sigma[w(F_0^2-F_c^2)^2]/\Sigma[w(F_0^2)_2]^{1/2}$, where $w = 1/\sigma^2(F_0^2)+(aP)^2+bP$, $P = (F_0^2+2F_c^2)/3$

[c] $GooF = [\Sigma[w(F_0^2-F_c^2)^2]/(n-p)]^{1/2}$ where n = no. of reflections and p = no. of refined parameters.

[*] including solvents molecules

9. Literature

1. M. Frey; Hydrogenases: Hydrogen-activating enzymes, *Chem. Biochem.,* **2002**, 3, 153-60.

2. R. Cammack; Bioinorganic chemistry: Hydrogenase sophistication, *Nature,* **1999**, 397, 214-15.

3. P. F. Weaver, S. Lien and M. Seibert; Photobiological production of hydrogen, *Sol. Energy,* **1980**, 24, 3-45.

4. D. J. Evans and C. J. Pickett; Chemistry and the hydrogenases, *Chem. Soc. Rev.,* **2003**, 32, 268-75.

5. M. Y. Darensbourg, E. J. Lyon and J. J. Smee; The bio-organometallic chemistry of active site iron in hydrogenases, *Coordin. Chem. Rev.,* **2000**, 206-207, 533-61.

6. T. B. Rauchfuss; Research on Soluble Metal Sulfides: From Polysulfido Complexes to Functional Models for the Hydrogenases, *Inorg. Chem.,* **2004**, 43, 14-26.

7. M. Stephenson and L. H. Stickland; Hydrogenase: a bacterial enzyme activating molecular oxygen. I. The properties of the enzyme, *Biochem. J.,* **1931**, 25, 205-14.

8. M. W. W. Adams and E. I. Stiefel; Biological hydrogen production: not so elementary, *Science,* **1998**, 282, 1842-43.

9. M. Frey; Nickel-iron hydrogenases: structural and functional properties, *Struct. Bond.,* **1998**, 90, 98-126.

10. Y. Montet, E. Garcin, A. Volbeda, C. Hatchikian, M. Frey and J. C. Fontecilla-Camps; Structural bases for the catalytic mechanism of NiFe hydrogenase, *Pure Appl. Chem.,* **1998**, 70, 25-31.

11. A. Berkessel and R. K. Thauer; On the mechanism of catalysis by a metal-free hydrogenase from methanogenic archaea: enzymic transformation of H2 without a metal and its analogy to the chemistry of alkanes in superacidic solution, *Angew. Chem. Int. Edit.,* **1995**, 34, 2247-50.

12. A. Volbeda, M.-H. Charon, C. Piras, E. C. Hatchikian, M. Frey and J. C. Fontecilla-Camps; Crystal structure of the nickel-iron hydrogenase from Desulfovibrio gigas, *Nature,* **1995**, 373, 580-7.

13. R. M. Mege and C. Bourdillon; Nickel controls the reversible anaerobic activation/inactivation of the Desulfovibrio gigas hydrogenase by the redox potential, *J. Biol. Chem.,* **1985**, 260, 14701-6.

14. Y. Nicolet, C. Piras, P. Legrand, C. E. Hatchikian and J. C. Fontecilla-Camps; Desulfovibrio desulfuricans iron hydrogenase: the structure shows unusual coordination to an active site Fe binuclear center, *Structure,* **1999**, 7, 13-23.

15. J. W. Peters, W. N. Lanzilotta, B. J. Lemon and L. C. Seefeldt; X-ray crystal structure of the Fe-only hydrogenase (CpI) from Clostridium pasteurianum to 1.8 angstrom resolution, *Science,* **1998**, 282, 1853-58.

16. J. W. Peters, W. N. Lanzilotta, B. J. Lemon and L. C. Seefeldt; X-ray crystal structure of the Fe-only hydrogenase (CpI) from Clostridium pasteurianum to 1.8 angstrom resolution. [Erratum to document cited in CA130:135847], *Science,* **1999**, 283, 35.

17. Y. Nicolet, B. J. Lemon, J. C. Fontecilla-Camps and J. W. Peters; A novel FeS cluster in Fe-only hydrogenases, *Trends Biochem. Sci.,* **2000**, 25, 138-43.

18. A. Winter, L. Zsolnai and G. Huttner; Dinuclear and trinuclear carbonyliron complexes containing 1,2- and 1,3-dithiolato bridging ligands, *Z. Naturforsch.,* **1982**, 37B, 1430-6.

19. T. Yamamura, H. Miyamae, Y. Katayama and Y. Sasaki; Nickel thiolates. Simple synthesis, the behavior upon protolysis and oxidation potentials, *Chem. Lett.,* **1985**, 269-72.

20. A. C. Marr, D. J. E. Spencer and M. Schroder; Structural mimics for the active site of [NiFe] hydrogenase, *Coordin. Chem. Rev.,* **2001**, 219-221, 1055-74.

21. F. Gloaguen, J. D. Lawrence, M. Schmidt, S. R. Wilson and T. B. Rauchfuss; Synthetic and Structural Studies on $[Fe_2(SR)_2(CN)_x(CO)_{6-x}]^{x-}$ as Active Site Models for Fe-Only Hydrogenases, *J. Am. Chem. Soc.,* **2001**, 123, 12518-27.

22. E. J. Lyon, I. P. Georgakaki, J. H. Reibenspies and M. Y. Darensbourg; Coordination sphere flexibility of active-site models for Fe-only hydrogenase: studies in intra- and intermolecular diatomic ligand exchange, *J. Am. Chem. Soc.,* **2001**, 123, 3268-78.

23. M. Razavet, S. C. Davies, D. L. Hughes and C. J. Pickett; {2Fe3S} clusters related to the di-iron sub-site of the H-centre of all-iron hydrogenases, *Chem. Commun.,* **2001**, 847-48.

24. X. Zhao, Y.-M. Hsiao, C.-H. Lai, J. H. Reibenspies and M. Y. Darensbourg; Oxidative Addition of Phosphine-Tethered Thiols to Iron Carbonyl: Binuclear Phosphinothiolate Complexes, $(m\text{-}SCH_2CH_2PPh_2)_2Fe_2(CO)_4$, and Hydride Derivatives, *Inorg. Chem.,* **2002**, 41, 699-708.

25. X. Zhao, I. P. Georgakaki, M. L. Miller, R. Mejia-Rodriguez, C.-Y. Chiang and M. Y. Darensbourg; Catalysis of H_2/D_2 Scrambling and Other H/D Exchange Processes by [Fe]-Hydrogenase Model Complexes, *Inorg. Chem.,* **2002**, 41, 3917-28.

26. F. Gloaguen, J. D. Lawrence, T. B. Rauchfuss, M. Benard and M.-M. Rohmer; Bimetallic Carbonyl Thiolates as Functional Models for Fe-Only Hydrogenases, *Inorg. Chem.,* **2002**, 41, 6573-82.

27. S. Ott, M. Kritikos, B. Akermark, L. Sun and R. Lomoth; A biomimetic pathway for hydrogen evolution from a model of the iron hydrogenase active site, *Angew. Chem. Int. Edit.,* **2004**, 43, 1006-09.

28. L. Schwartz, G. Eilers, L. Eriksson, A. Gogoll, R. Lomoth and S. Ott; Iron hydrogenase active site mimic holding a proton and a hydride, *Chem. Commun.,* **2006**, 520-22.

29. C. Tard, X. Liu, S. K. Ibrahim, M. Bruschi, L. De Gioia, S. C. Davies, X. Yang, L.-S. Wang, G. Sawers and C. J. Pickett; Synthesis of the H-cluster framework of iron-only hydrogenase, *Nature,* **2005**, 433, 610-13.

30. C. He, M. Wang, X. Zhang, Z. Wang, C. Chen, J. Liu, B. Akermark and L. Sun; An unusual cyclization in a bis(cysteinyl-S) diiron complex related to the active site of Fe-only hydrogenases, *Angew. Chem. Int. Edit.,* **2004**, 43, 3571-4.

31. T. Yamamura; Oxidation potentials of nickel thiolates, and nickel(III) sites of hydrogenases in hydrogen uptake bacteria, *Chem. Lett.,* **1986**, 801-4.

32. S. G. Rosenfield, W. H. Armstrong and P. K. Mascharak; Convenient synthesis and properties of $(R_4N)_2[Ni(SAr)_4]$ (Ar = C_6H_5, p-C_6H_4Cl, p-$C_6H_4CH_3$, and m-C_6H_4Cl) and the structure of tetraethylammonium tetrakis(p-chlorobenzenethiolato)nickelate(II), *Inorg. Chem.,* **1986**, 25, 3014-18.

33. N. Baidya, P. K. Mascharak, D. W. Stephan and C. F. Campagna; Mononuclear nickel(II) thiolates of square-planar geometry: syntheses, spectral and redox properties of $[Ni(SCH_2CH_2S)_2]^{2-}$ and $[Ni(SCH(CH_3)CH(CH_3)S)_2]^{2-}$ and the structure of $(Ph_4P)_2[Ni(SCH_2CH_2S)_2].4H_2O$, *Inorg. Chem. Acta,* **1990**, 177, 233-8.

34. D. Sellmann, S. Funfgelder, G. Pohlmann, F. Knoch and M. Moll; Transition-metal complexes with sulfur ligands. 55. Nickel complexes with thiolato-thioether ligands including nitrogen and oxygen donors in S6, S5, OS4, NS4, and S4 donor sets. Syntheses, properties, and x-ray structure determinations of [Ni('S6')], [Ni('S5')], [Ni('OS4')]2, [Ni('S4-C5')]2, and [Ni('S4-C3')], *Inorg. Chem.,* **1990**, 29, 4772-8.

35. D. Sellmann, M. Geck and M. Moll; Transition-metal complexes with sulfur ligands. 62. Hydrogen evolution upon reaction of protons with sulfur-coordinated iron(II) complexes. Investigation of the proton, hydrogen and hydride interactions with iron 1,2-benzenedithiolate complexes, *J. Am. Chem. Soc.,* **1991**, 113, 5259-64.

36. C. J. Curtis, A. Miedaner, R. Ciancanelli, W. W. Ellis, B. C. Noll, M. R. DuBois and D. L. DuBois; $[Ni(Et_2PCH_2NMeCH_2PEt_2)_2]^{2+}$ as a Functional Model for Hydrogenases, *Inorg. Chem.,* **2003**, 42, 216-27.

37. S. Ott, M. Borgstroem, M. Kritikos, R. Lomoth, J. Bergquist, B. Aakermark, L. Hammarstroem and L. Sun; Model of the Iron Hydrogenase Active Site

Covalently Linked to a Ruthenium Photosensitizer: Synthesis and Photophysical Properties, *Inorg. Chem.,* **2004**, 43, 4683-92.

38. S. Ott, M. Kritikos, B. Akermark and L. Sun; Synthesis and structure of a biomimetic model of the iron hydrogenase active site covalently linked to a ruthenium photosensitizer, *Angew. Chem. Int. Edit.,* **2003**, 42, 3285-88.

39. T. J. Kealy and P. L. Paulson; A new type of organo-iron compound, *Nature,* **1951**, 168, 1039-40.

40. G. Wilkinson, M. Rosenblum, M. C. Whiting and R. B. Woodward; The structure of iron biscyclopentadienyl, *J. Am. Chem. Soc.,* **1952**, 74, 2125-6.

41. R. B. Woodward, M. Rosenblum and M. C. Whiting; A new aromatic system, *J. Am. Chem. Soc.,* **1952**, 74, 3458-9.

42. N. Metzler-Nolte; Labeling of biomolecules for medicinal applications-bioorganometallic chemistry at its best, *Angew. Chem. Int. Edit.,* **2001**, 40, 1040-43.

43. G. Jaouen, A. Vessières and I. S. Butler; Bioorganometallic Chemistry: A Future Direction for Transition Metal Organometallic Chemistry, *Accounts Chem. Res.,* **1993**, 26, 361-69.

44. P. Köpf-Maier and H. Köpf; Non-Platinum-Group Metal Antitumor Agents: History, Current Status, and Perspectives, *Chem. Rev.,* **1987**, 89, 1137-52.

45. P. Köpf-Maier and H. Köpf; Metallocene und Krebs - Review, *Struct. Bond.,* **1988**, 70, 105-85.

46. U. Hoffmanns; Selective Labelling of Peptides with Organometallic Compounds - Chemical and Biological Characterization, Dissertation, **2004**, 183 pp.

47. F. Noor, A. Wuestholz, R. Kinscherf and N. Metzler-Nolte; A cobaltocenium-peptide bioconjugate shows enhanced cellular uptake and directed nuclear delivery, *Angew. Chem. Int. Edit.,* **2005**, 44, 2429-32.

48. E. I. Edwards, R. Epton and G. Marr; A new class of semi-synthetic antibiotics: ferrocenyl-penicillins and -cephalosporins, *J. Organomet. Chem.,* **1976**, 107, 351-57.

49. E. I. Edwards, R. Epton and G. Marr; Organometallic derivatives of penicillin, *Chem. Abstracts,* **1977**, 87, 728.

50. E. I. Edwards, R. Epton, G. Marr, G. K. Rogers and K. J. Thompson; Ferrocene Derivatives of 6-aminopenicillanic acid and 7-aminocephalosporanic acid, *Spec. Publ. Chem. Soc.,* **1977**, 128, 92-100.

51. R. Epton, G. Marr and G. K. Rogers; The ferrocene analogues of salicyclic acid and aspirin, *J. Organomet. Chem.,* **1976**, 110, C42-C44.

52. L. Delhaes, H. Abessolo, C. Biot, L. Berry, P. Delcourt, L. A. Maciejewski, J. S. Brocard, D. Camus and D. Dive; In vitro and in vivo antimalarial activity of

ferrocenechloroquine, a ferrocenyl analogue of chloroquine against chloroquine-resistant malaria parasites, *Parasitol. Res.,* **2001**, 87, 239-44.

53. C. Biot, L. Delhaes, L. A. Maciejewski, M. Mortuaire, D. Camus, D. Dive and J. S. Brocard; Synthetic ferrocenic mefloquine and quinine analogues as potential antimalarial agents, *European Journal of Medicinal Chemistry,* **2000**, 35, 707-14.

54. S. Top, A. Vessieres, C. Cabestaing, I. Laios, G. Leclercq, C. Provot and G. Jaouen; Studies on organometallic selective estrogen receptor modulators. (SERMs) Dual activity in the hydroxy-ferrocifen series, *J. Organomet. Chem.,* **2001**, 637-639, 500-06.

55. C.-H. Chen, Y.-S. Chang, C.-Y. Yang, T.-N. Chen, C.-M. Lee and W.-F. Liaw; Preparative and structural studies on iron(II)-thiolate cyanocarbonyls: Relevance to the [NiFe]/[Fe]-hydrogenases, *J. Chem. Soc. Dalton,* **2004**, 137-43.

56. K. Schlogel; Ferrocene amino acids, *Monatsh. Chem.,* **1957**, 88, 601-21.

57. D. R. van Staveren and N. Metzler-Nolte; Bioorganometallic Chemistry of Ferrocene, *Chem. Rev.,* **2004**, 104, 5931-85.

58. A. Nomoto, T. Moriuchi, S. Yamazaki, A. Ogawa and T. Hirao; A highly ordered ferrocene system regulated by podand peptide chains, *Chem. Commun.,* **1998**, 1963-64.

59. T. Moriuchi, A. Nomoto, K. Yoshida and T. Hirao; Characterization of ferrocene derivatives bearing podand dipeptide chains (-L-Ala-L-Pro-OR), *J. Organomet. Chem.,* **1999**, 589, 50-58.

60. P. Saweczko and H. B. Kraatz; The interaction of ferrocenoyl peptides with 3-aminopyrazole, *Coordin. Chem. Rev.,* **1999**, 190-192, 185-98.

61. R. S. Herrick, R. M. Jarret, T. P. Curran, D. R. Dragoli, M. B. Flaherty, S. E. Lindyberg, R. A. Slate and L. C. Thornton; Ordered conformations in bis(amino acid) derivatives of 1,1'-ferrocenedicarboxylic acid, *Tetrahedron Lett.,* **1996**, 37, 5289-92.

62. D. R. van Staveren, T. Weyhermueller and N. Metzler-Nolte; Organometallic b-turn mimetics. A structural and spectroscopic study of inter-strand hydrogen bonding in ferrocene and cobaltocenium conjugates of amino acids and dipeptides, *J. Chem. Soc. Dalton,* **2003**, 210-20.

63. Y. Xu and H. B. Kraatz; Efficient synthesis of unsymmetrically disubstituted ferrocenes: towards electrochemical dipeptide-Fc-biosensors, *Tetrahedron Lett.,* **2001**, 42, 2601-03.

64. X. de Hatten, T. Weyhermueller and N. Metzler-Nolte; Ferrocenoyl peptides with sulfur-containing side chains: synthesis, solid state and solution structures, *J. Organomet. Chem.,* **2004**, 689, 4856-67.

65. S. I. Kirin, H.-B. Kraatz and N. Metzler-Nolte; Systematizing structural motifs and nomenclature in 1,N'-disubstituted ferrocene peptides, *Chem. Soc. Rev.,* **2006**, 35, 348-54.

66. I. Huc; Aromatic oligoamide foldamers, *Eur. J. Org. Chem.,* **2004**, 17-29.

67. S. H. Gellman; Foldamers: A Manifesto, *Accounts Chem. Res.,* **1998**, 31, 173-80.

68. R. P. Cheng, S. H. Gellman and W. F. DeGrado; beta-Peptides: from structure to function, *Chem. Rev.,* **2001**, 101, 3219-32.

69. Y. Hamuro, J. P. Schneider and W. F. DeGrado; De Novo design of antibacterial b-peptides, *J. Am. Chem. Soc.,* **1999**, 121, 12200-01.

70. D. J. Hill, M. J. Mio, R. B. Prince, T. S. Hughes and J. S. Moore; A Field Guide to Foldamers, *Chem. Rev.,* **2001**, 101, 3893-4011.

71. H. Jiang, V. Maurizot and I. Huc; Double versus single helical structures of oligopyridine-dicarboxamide strands. Part 1: Effect of oligomer length, *Tetrahedron,* **2004**, 60, 10029-38.

72. J. Garric, J.-M. Leger and I. Huc; Molecular apple peels, *Angew. Chem. Int. Edit.,* **2005**, 44, 1954-58.

73. B. H. Huynh, D. S. Patil, I. Moura, M. Teixeira, J. J. Moura, D. V. DerVartanian, M. H. Czechowski, B. C. Prickril, H. D. Peck, Jr. and J. LeGall; On the active sites of the [NiFe] hydrogenase from Desulfovibrio gigas. Mossbauer and redox-titration studies, *J. Biol. Chem.,* **1987**, 262, 795-800.

74. C. Sanchez, H. Arribart, M. Madeleine and G. Guille; Biomimetism and bioinspiration as tools for the design of innovative materials and systems, *Nature Materials,* **2005**, 4, 277-88.

75. H. Wild; Protective groups in b-lactam chemistry, *Org. Chem. ,* **1993**, 1-48.

76. J. G. Moffatt and H. G. Khorana; Nucleoside polyphosphates. X. The synthesis and some reactions of nucleoside 5'-phosphoromorpholidates and related compounds. Improved methods for the preparation of nucleoside 5'-polyphosphates, *J. Am. Chem. Soc.,* **1961**, 83, 649-58.

77. F. Cavelier, J. Daunis and R. Jacquier; Bibliographic and critical study of thiol protection in peptide synthesis (review), *B. Soc. Chim. Fr.,* **1990**, 210-25.

78. T. W. Greene and P. G. M. Wuts; Protective Groups in Organic Synthesis., **1991**, 473 pp.

79. T. W. Greene and P. G. M. Wuts; Protective Groups in Organic Synthesis, **1999**, 779 pp.

80. R. G. Hiskey; Sulfhydryl group protection in peptide synthesis, *Peptides,* **1981**, 3, 137-67.

81. V. du Vigneaud, L. F. Audrieth and H. S. Loring; Reduction of cystine in liquid ammonia by metallic sodium, *J. Am. Chem. Soc.,* **1930**, 52, 4500-4.

82. L. S. Richter, J. C. Marsters, Jr. and T. R. Gadek; Two new procedures for the introduction of benzyl-type protecting groups for thiols, *Tetrahedron Lett.,* **1994**, 35, 1631-4.

83. J. Chiba, K. Tanaka, Y. Ohshiro, R. Miyake, S. Hiraoka, M. Shiro and M. Shionoya; Artificial Nucleosides Possessing Metal Binding Sites at the 3'- and 5'-Positions of the Deoxyribose Moieties, *J. Org. Chem.,* **2003**, 68, 331-38.

84. D. F. Veber, J. D. Milkowski, S. L. Varga, R. G. Denkewalter and R. Hirschmann; Acetamidomethyl. A novel thiol protecting group for cysteine, *J. Am. Chem. Soc.,* **1972**, 94, 5456-61.

85. J. J. Pastuszak and A. Chimiak; tert-Butyl group as thiol protection in peptide synthesis, *J. Org. Chem.,* **1981**, 46, 1868-73.

86. U. Weber, P. Hartter and L. Flohe; S-alkylmercapto groups for the SH-function protection of cysteine. II. Thiol-disulfide exchange reaction of asymmetric cysteine disulfides, *H-S Z. Physiol. Chem. ,* **1970**, 351, 1389-94.

87. L. Zervas, I. Photaki and I. Phocas; S-Trityl-L-cysteine, *Chem. Ber.,* **1968**, 101, 3332-3.

88. R. Matsueda, T. Kimura, E. T. Kaiser and G. R. Matsueda; 3-Nitro-2-pyrinedinesulfenyl group for protection and activation of the thiol function of cysteine, *Chem. Lett.,* **1981**, 737-40.

89. R. Matsueda, S. Higashida, R. J. Ridge and G. R. Matsueda; 3-Nitro-2-pyridinesulfenyl (Npys) protecting group: protection and activation of the thiol function, *Peptide Chem.,* **1982**, 19th, 31-6.

90. R. Matsueda, S. Higashida, R. J. Ridge and G. R. Matsueda; Activation of conventional S-protecting groups of cysteine by conversion into the 3-nitro-2-pyridinesulfenyl (Npys) group, *Chem. Lett.,* **1982**, 921-4.

91. I. Phocas, C. Yovanidis, I. Photaki and L. Zervas; New methods in peptide synthesis. IV. N-> S transfer of N-o-nitrophenylsulfenyl groups in cysteine pepties, *J. Chem. Soc. C,* **1967**, 15/6-9.

92. C. W. West, M. A. Estiarte and D. H. Rich; New methods for side-chain protection of cysteine, *Org. Lett.,* **2001**, 3, 1205-8.

93. E. Atherton, M. Pinori and R. C. Sheppard; Peptide synthesis. Part 6. Protection of the sulfhydryl group of cysteine in solid-phase synthesis using Na-fluorenylmethoxycarbonyl amino acids. Linear oxytocin derivatives, *J. Chem. Soc. Perk. T 1,* **1985**, 2057-64.

94. M. A. Bednarek and M. Bodanszky; 9-Fluorenylmethyl esters, *Int. J. Pept. Prot. Res.,* **1983**, 21, 196-201.

95. M. Bodanszky and M. A. Bednarek; Derivatives of S-9-fluorenylmethyl-L-cysteine, *Int. J. Pept. Prot. Res.,* **1982**, 20, 434-7.

96. S. Wawzonek and E. Dufek; Acid-catalyzed reaction of 9-fluorenol with 9-alkylidenefluorenes, *J. Am. Chem. Soc.,* **1956**, 78, 3530-3.

97. F. M. Callahan, G. W. Anderson, R. Paul and J. E. Zimmerman; Tertiary butyl group as a blocking agent for hydroxyl, sulfhy-dryl, and amido functions in peptide synthesis, *J. Am. Chem. Soc.,* **1963**, 85, 201-7.

98. J. Meienhofer; The mixed carbonic anhydride method of peptide synthesis, *Peptides,* **1979**, 1, 263-314.

99. L. A. Carpino, P. H. Terry and P. J. Crowley; Examination of synthetic routes to monosubstituted diimides. II. Synthesis of tert-butyl aryl- and acylazoformates. Acid-induced cleavage of the thionocarbo-tert-butoxy group, *J. Org. Chem.,* **1961**, 26, 4336-40.

100. L. A. Carpino and G. Y. Han; 9-Fluorenylmethoxycarbonyl amino-protecting group, *J. Org. Chem.,* **1972**, 37, 3404-9.

101. M. D. Threadgill and A. P. Gledhill; Synthesis of peptides containing S-(N-alkylcarbamoyl)cysteine residues, metabolites of N-alkylformamides in rodents and in humans, *J. Org. Chem.,* **1989**, 54, 2940-9.

102. K. Severin, R. Bergs and W. Beck; Biometallorganische Chemie - Übergangsmetallkomplexe mit a-Aminosäuren und Peptiden, *Angew. Chem. Ger. Edit.,* **1998**, 110, 1722-43.

103. Y. Xu, P. Saweczko and H.-B. Kraatz; 1,1'-Ferrocenoyl-oligoprolines. A synthetic, structural and electrochemical study, *J. Organomet. Chem.,* **2001**, 637-639, 335-42.

104. P. D. Beer and P. A. Gale; Anion recognition and sensing: the state of the art and future perspectives, *Angew. Chem. Int. Edit.,* **2001**, 40, 486-516.

105. T. Moriuchi and T. Hirao; Highly ordered structures of peptides by using molecular scaffolds, *Chem. Soc. Rev.,* **2004**, 33, 294-301.

106. I. R. Butler and S. C. Quayle; The synthesis and characterization of heterosubstituted aminoferrocenes, *J. Organomet. Chem.,* **1998**, 552, 63-68.

107. T.-a. Okamura, K. Sakauye, N. Ueyama and A. Nakamura; An Amide-Linked Ferrocene Dimer, $[(CH_3CONHC_5H_4)Fe(C_5H_4CONHC_5H_4)Fe(C_5H_4CONHCH_3)]$. Formation of Inter- and Intramolecular NH...O:C Hydrogen Bonds, *Inorg. Chem.,* **1998**, 37, 6731-36.

108. K. Heinze and M. Schlenker; Main chain ferrocenyl amides from 1-aminoferrocene-1'-carboxylic acid, *Eur. J. Inorg. Chem.,* **2004**, 2974-88.

109. L. Barisic, M. Dropucic, V. Rapic, H. Pritzkow, S. I. Kirin and N. Metzler-Nolte; The first oligopeptide derivative of 1'-aminoferrocene-1-carboxylic acid shows helical chirality with antiparallel strands, *Chem. Commun.,* **2004**, 2004-05.

110. T. Moriuchi, A. Nomoto, K. Yoshida and T. Hirao; Intramolecular Conformational Control in Ferrocenes Bearing Podand Dipeptide Chains, *Organometallics,* **2001**, 20, 1008-13.

111. T. Moriuchi, A. Nomoto, K. Yoshida, A. Ogawa and T. Hirao; Chirality Organization of Ferrocenes Bearing Podand Dipeptide Chains: Synthesis and Structural Characterization, *J. Am. Chem. Soc.,* **2001**, 123, 68-75.

112. T. Moriuchi, K. Yoshida and T. Hirao; Structural characterization and complexation behavior of ferrocene bearing dipeptide chain (-L-Ala-L-Pro-NHPy), *J. Organomet. Chem.,* **2001**, 637-639, 75-79.

113. T. Moriuchi, K. Yoshida and T. Hirao; Complexation Stabilized Conformational Regulation of Ferrocene Bearing Podand Dipeptide Chains (-L-Ala-L-Pro-NHPy), *Organometallics,* **2001**, 20, 3101-05.

114. S. H. Gellman, G. P. Dado, G. B. Liang and B. R. Adams; Conformation-directing effects of a single intramolecular amide-amide hydrogen bond: variable-temperature NMR and IR studies on a homologous diamide series, *J. Am. Chem. Soc.,* **1991**, 113, 1164-73.

115. G. B. Liang, G. P. Dado and S. H. Gellman; Anatomy of a stable intramolecularly hydrogen bonded folding pattern, *J. Am. Chem. Soc.,* **1991**, 113, 3994-5.

116. H.-B. Kraatz, J. Lusztyk and G. D. Enright; Ferrocenoyl Amino Acids: A Synthetic and Structural Study, *Inorg. Chem.,* **1997**, 36, 2400-05.

117. L. Lin, A. Berces and H.-B. Kraatz; Ferrocenic acid derivatives: towards rationalizing changes in the electronic and geometric structures, *J. Organomet. Chem.,* **1998**, 556, 11-20.

118. C. N. Kirsten and T. H. Schrader; Intermolecular b-Sheet Stabilization with Aminopyrazoles, *J. Am. Chem. Soc.,* **1997**, 119, 12061-68.

119. S. I. Kirin, D. Wissenbach and N. Metzler-Nolte; Unsymmetrical 1,n'-disubstituted ferrocenoyl peptides: convenient one pot synthesis and solution structures by CD and NMR spectroscopy, *New J. Chem.,* **2005**, 29, 1168-73.

120. S. M. Kelly, T. J. Jess and N. C. Price; How to study proteins by circular dichroism, *Biochim. Biophys. Acta,* **2005**, 1751, 119-39.

121. A. Rodger and B. Norden; Circular Dichroism and Linear Dichroism, **1997**, 449 pp.

122. A. Hess, J. Sehnert, T. Weyhermueller and N. Metzler-Nolte; Chiral Ferrocene Amines Derived from Amino Acids and Peptides: Synthesis, Solution and X-ray Crystal Structures and Electrochemical Investigations, *Inorg. Chem.,* **2000**, 39, 5437-43.

123. D. R. van Staveren and N. Metzler-Nolte; Bioorganometallic Chemistry of Ferrocene, *Chemical Reviews,* **2004**, 104, 5931-85.

124. T. Moriuchi and T. Hirao; Highly ordered structures of peptides by using molecular scaffolds, *Chemical Society Reviews,* **2004**, 33, 294-301.

125. S. I. Kirin, H.-B. Kraatz and N. Metzler-Nolte; Systematizing structural motifs and nomenclature in 1,n-disubstituted ferrocene peptides, *Chemical Society Reviews,* **2006**, 35, DOI: 10.1039/b511332f.

126. W. Koch and M. C. Holthausen; A Chemist's Guide to Density Functional Theory, **2001**, 528 pp.

127. K. Heinze and M. Schlenker; Anion-induced motion in a ferrocene diamide, *Eur. J. Inorg. Chem.,* **2005**, 66-71.

128. M. J. Frisch, G. W. Trucks, H. B. Schlegel, G. E. Scuseria, M. A. Robb, J. R. Cheeseman, V. G. Zakrzewski, J. J. A. Montgomery, R. E. Stratmann, J. C. Burant, S. Dapprich, J. M. Millam, A. D. Daniels, K. N. Kudin, M. C. Strain, O. Farkas, J. Tomasi, V. Barone, M. Cossi, R. Cammi, B. Mennucci, C. Pomelli, C. Adamo, S. Clifford, J. Ochterski, G. A. Petersson, P. Y. Ayala, Q. Cui, K. Morokuma, D. K. Malick, A. D. Rabuck, K. Raghavachari, J. B. Foresman, J. Cioslowski, J. V. Ortiz, A. G. Baboul, B. B. Stefanov, G. Liu, A. Liashenko, P. Piskorz, I. Komaromi, R. Gomperts, R. L. Martin, D. J. Fox, T. Keith, M. A. Al-Laham, C. Y. Peng, A. Nanayakkara, C. Gonzalez, M. Challacombe, P. M. W. Gill, B. Johnson, W. Chen, M. W. Wong, J. L. Andres, C. Gonzalez, M. Head-Gordon, E. S. Replogle and J. A. Pople; Gaussian98*,* **1998**.

129. G. Schaftenaar and J. H. Noordik; Molden: a pre- and post-processing program for molecular and electronic structures, *J. Comput. Aid. Mol. Des.,* **2000**, 14, 123-34.

130. A. D. Becke; Density-functional thermochemistry. III. The role of exact exchange, *J. Chem. Phys.,* **1993**, 98, 5648-52.

131. C. Lee, W. Yang and R. G. Parr; Development of the Colle-Salvetti correlation-energy formula into a functional of the electron density, *Phys. Rev. B,* **1988**, 37, 785-9.

132. W. R. Wadt and P. J. Hay; Ab initio effective core potentials for molecular calculations. Potentials for main group elements sodium to bismuth, *J. Chem. Phys.,* **1985**, 82, 284-98.

133. P. J. Hay and W. R. Wadt; Ab initio effective core potentials for molecular calculations. Potentials for the transition metal atoms scandium to mercury, *J. Chem. Phys.,* **1985**, 82, 270-83.

134. A. V. Yatsenko, I. K. Kudryavtsev, M. A. Zakharov and L. A. Aslanov; Static Influence of Ligands: Comparison of DFT Calculations with Experimental Data, *Russ. J. Coord. Chem.,* **2004**, 30, 1-7.

135. I. Bediako-Amoa, R. Silerova and H.-B. Kraatz; Ferrocenoyl glycylcystamine: organization into a supramolecular helicate structure, *Chem. Commun.,* **2002**, 2430-31.

136. H. Huang, L. Mu, J. He and J.-P. Cheng; Ferrocenyl-bearing cyclopseudopeptides as redox-switchable cation receptors, *J. Org. Chem.,* **2003**, 68, 7605-11.

137. H. B. Kraatz; personal communication, **2004**,

138. P. V. Bernhardt and P. Comba; Molecular mechanics calculations of transition metal complexes, *Inorg. Chem.,* **1992**, 31, 2638-44.

139. B. R. Brooks, R. E. Bruccoleri, B. D. Olafson, D. J. States, S. Swaminathan and M. Karplus; CHARMM: a program for macromolecular energy, minimization, and dynamics calculations, *J. Comput. Chem.,* **1983**, 4, 187-217.

140. B. Bosnich; Molecular mechanics force fields for cyclopentadienyl complexes, *Chem. Soc. Rev.,* **1994**, 23, 387-95.

141. M. J. Sherrod; Exploration of cyclomalto-oligosaccharide (cyclodextrin) chemistry with molecular mechanics: docking calculations on the complexation of ferrocenes with cyclodextrins, *Carbohyd. Res.,* **1989**, 192, 17-32.

142. Y.-D. Gao, K. B. Lipkowitz and F. A. Schultz; Molecular Mechanics Calculation of Inner-Shell Activation Barriers to Heterogeneous Electron Transfer in $M(tacn)_2^{3+/2+}$ Redox Couples (M = Fe, Co, Ni; tacn = 1,4,7-Triazacyclononane), *J. Am. Chem. Soc.,* **1995**, 117, 11932-8.

143. Insight II, **1998**.

144. A. D. MacKerell, Jr., D. Bashford, M. Bellott, R. L. Dunbrack, J. D. Evanseck, M. J. Field, S. Fischer, J. Gao, H. Guo, S. Ha, D. Joseph-McCarthy, L. Kuchnir, K. Kuczera, F. T. K. Lau, C. Mattos, S. Michnick, T. Ngo, D. T. Nguyen, B. Prodhom, W. E. Reiher, III, B. Roux, M. Schlenkrich, J. C. Smith, R. Stote, J. Straub, M. Watanabe, J. Wiorkiewicz-Kuczera, D. Yin and M. Karplus; All-Atom Empirical Potential for Molecular Modeling and Dynamics Studies of Proteins, *J. Phys. Chem. B,* **1998**, 102, 3586-616.

145. A Computational Chemistry Package for Parallel Computers, **2001**.

146. E. Bencze, J. Mink, C. Nemeth, W. A. Herrmann, B. V. Lokshin and F. E. Kuhn; Vibrational spectroscopic and force field studies of $(h_5\text{-Cp})ML_3$-type complexes (M = Mn, Re; L = CO, O), *J. Organomet. Chem.,* **2002**, 642, 246-58.

147. M. Swart and J. G. Snijders; Accuracy of geometries: influence of basis set, exchange-correlation potential, inclusion of core electrons, and relativistic corrections., *Theor. Chem. Acc.,* **2004**, 111, 56.

148. S. Huzinaga and C. Arnau; Simple basis set for molecular wavefunctions containing first- and second-row atoms, *J. Chem. Phys.,* **1970**, 53, 451-2.

149. A. P. Scott and L. Radom; Harmonic Vibrational Frequencies: An Evaluation of Hartree-Fock, Moeller-Plesset, Quadratic Configuration Interaction, Density Functional Theory, and Semi-empirical Scale Factors, *J. Phys. Chem.,* **1996**, 100, 16502-13.

150. C. M. Breneman and K. B. Wiberg; Determining atom-centered monopoles from molecular electrostatic potentials. The need for high sampling density in formamide conformational analysis, *J. Comput. Chem.,* **1990**, 11, 361-73.

151. J. L. Lebowitz, J. K. Percus and L. Verlet; Ensemble dependence of fluctuations with application to machine computations, *Phys. Rev.,* **1967**, 153, 250-4.

152. R. Blom, A. Hammel, A. Haaland, J. Weidlein, T. V. Timofeeva and Y. T. Struchkov; Molecular structures of tris(methylcyclopentadienyl)scandium and -ytterbium as studied by gas phase electron diffraction and molecular mechanics calculations: the scandium atom is too small to accommodate three pentahapto cyclopentadienyl rings, *J. Organomet. Chem.,* **1993**, 462, 131-9.

153. T. N. Doman, C. R. Landis and B. Bosnich; Molecular mechanics force fields for linear metallocenes, *J. Am. Chem. Soc.,* **1992**, 114, 7264-72.

154. P. Comba and T. W. Hambley; Molecular Modeling of Inorganic Compounds, **2000**, 317 pp.

155. A. C. Vaiana, Z. Cournia, I. B. Costescu and J. C. Smith; AFMM: A molecular mechanics force field vibrational parametrization program, *Comput. Phys. Commun.,* **2005**, 167, 34-42.

156. A. C. Vaiana, H. Neuweiler, A. Schulz, J. Wolfrum, M. Sauer and J. C. Smith; Fluorescence Quenching of Dyes by Tryptophan: Interactions at Atomic Detail from Combination of Experiment and Computer Simulation, *J. Am. Chem. Soc.,* **2003**, 125, 14564-72.

157. A. C. Vaiana, A. Schulz, J. Wolfrum, M. Sauer and J. C. Smith; Molecular mechanics force field parameterization of the fluorescent probe rhodamine 6G using automated frequency matching, *J. Comput. Chem.,* **2003**, 24, 632-39.

158. Z. Cournia, A. C. Vaiana, G. M. Ullmann and J. C. Smith; Derivation of a molecular mechanics force field for cholesterol, *Pure Appl. Chem.,* **2004**, 76, 189-96.

159. Z. Cournia, J. C. Smith and G. M. Ullmann; A molecular mechanics force field for biologically important sterols, *J. Comput. Chem.,* **2005**, 26, 1383-99.

160. S. Kim and M. Lim; Picosecond Dynamics of Ligand Interconversion in the Primary Docking Site of Heme Proteins, *J. Am. Chem. Soc.,* **2005**, 127, 5786-87.

161. S.-Y. Sheu; Molecular dynamics simulation of entropy driven ligand escape process in heme pocket, *J. Chem. Phys.,* **2005**, 122, 104905/1-05/7.

162. J. Bredenberg; *personal communication,* **2004**, www.charmm.org,

163. A. Volbeda, E. Garcin, C. Piras, A. L. de Lacey, V. M. Fernandez, E. C. Hatchikian, M. Frey and J. C. Fontecilla-Camps; Structure of the [NiFe] hydrogenase active site: Evidence for biologically uncommon Fe ligands, *J. Am. Chem. Soc.,* **1996**, 118, 12989-96.

164. A. Mueller and G. Henkel; $[Ni_5S(SBut)_5]$- and $[Ni_3S(SBut)_3(CN)_3]^{2-}$, novel complexes with sulfur-capped, thiolate-bridged polygonal metal frames, *Chem. Commun.,* **1996**, 1005-06.

165. A. Mueller and G. Henkel; $[Ni_2(SC_4H_9)_6]^{2-}$, a novel binuclear nickel-thiolate complex with NiS4 tetrahedra sharing edges and $[Ni(SC_6H_4SiMe_3)_4]^{2-}$, a structurally related mononuclear complex ion, *Z. Naturforsch. B,* **1995**, 50, 1464-8.

166. M. Koeckerling and G. Henkel; Nickel complexes with chelating thioether ligands. Electrochemical properties and crystal structures of $[Ni(MeSCH_2CH_2SMe)_2(NCS)_2]$, $[Ni(EtSCH_2CH_2SEt)_2(NCS)_2]$, and $[Ni(MeSCH_2CH_2SMe)_2Br_2]$, *Z. Naturforsch. B,* **1996**, 51, 178-86.

167. G. Henkel, M. Kockerling and A. Muller; Modeling the nickel site of Ni-Fe hydrogenases, *Bioinorg. Chem.,* **1997**, 456-67.

168. K. Schulbert and R. Mattes; Structures of two polynuclear nickel thiolato complexes $[(m\text{-}SMe)_2/Ni(MeNHCS_2))_2]$ and cyclo-$[(m\text{-}SMe)_2Ni]_6$, *Z. Naturforsch. B,* **1994**, 49, 770-2.

169. T. A. Wark and D. W. Stephan; Early metal thiolato species as metalloligands in the formation of early/late heterobimetallic complexes: syntheses and molecular structures of $Cp_2Ti(SMe)_2$, $Cp_2V(SMe)_2$, $(Cp_2Ti(m\text{-}SMe)_2)_2Ni$ and $(Ni(m\text{-}SMe)_2)_6$, *Organometallics,* **1989**, 8, 2836-43.

170. F.-F. Jian, K. Jiao, Y. Li, P.-S. Zhao and L.-D. Lu; $[Ni_6(SCH_2CH_2OH)_{12}]$: A double crown [12]metallacrown-6 nickel(II) cluster, *Angew. Chem. Int. Edit.,* **2003**, 42, 5722-24.

171. E. Feller Scott, K. Gawrisch and D. MacKerell Alexander, Jr.; Polyunsaturated fatty acids in lipid bilayers: intrinsic and environmental contributions to their unique physical properties, *J. Am. Chem. Soc.,* **2002**, 124, 318-26.

172. S. E. Feller and A. D. MacKerell, Jr.; An Improved Empirical Potential Energy Function for Molecular Simulations of Phospholipids, *J. Phys. Chem. B,* **2000**, 104, 7510-15.

173. S. I. Kirin, U. Schatzschneider, X. de Hatten, T. Weyhermüller and N. Metzler-Nolte; Helical chirality in 1,n'-disubstituted ferrocenoyl peptides: Conformational analysis by CD spectroscopy, X-ray crystallography and DFT calculations, **2006**, submitted,

174. P. Seiler and J. D. Dunitz; Low-temperature crystallization of orthorhombic ferrocene: structure analysis at 98 K, *Acta Crystallogr. B,* **1982**, B38, 1741-5.

175. P. Seiler and J. D. Dunitz; The structure of triclinic ferrocene at 101, 123 and 148 K, *Acta Crystallogr. B,* **1979**, B35, 2020-32.

176. N. J. Long; Metallocenes: An Introduction to Sandwich Complexes, **1998**, 453 pp.

177. A. Volbeda and J. C. Fontecilla-Camps; The active site and catalytic mechanism of NiFe hydrogenases, *J. Chem. Soc. Dalton,* **2003**, 4030-38.

178. S. Niu, L. M. Thomson and M. B. Hall; Theoretical Characterization of the Reaction Intermediates in a Model of the Nickel-Iron Hydrogenase of Desulfovibrio gigas, *J. Am. Chem. Soc.,* **1999**, 121, 4000-07.

179. L. Barisic, V. Rapic and V. Kovac; Ferrocene compounds. XXIX. Efficient syntheses of 1'-aminoferrocene-1-carboxylic acid derivatives, *Croat. Chem. Acta,* **2002**, 75, 199-210.

180. A. Shafir, M. P. Power, G. D. Whitener and J. Arnold; Synthesis, Structure, and Properties of 1,1'-Diamino- and 1,1'-Diazidoferrocene, *Organometallics,* **2000**, 19, 3978-82.

181. V. Berl, I. Huc, R. G. Khoury and J.-M. Lehn; Helical molecular programming: folding of oligopyridine-dicarboxamides into molecular single helices, *Chem. Eur. J.,* **2001**, 7, 2798-809.

182. I. Huc, V. Maurizot, H. Gornitzka and J.-M. Leger; Hydroxy-substituted oligopyridine dicarboxamide helical foldamers, *Chem. Commun.,* **2002**, 578-79.

183. H. Jiang, J.-M. Leger, C. Dolain, P. Guionneau and I. Huc; Aromatic d-peptides: design, synthesis and structural studies of helical, quinoline-derived oligoamide foldamers, *Tetrahedron,* **2003**, 59, 8365-74.

184. R. M. J. Liskamp; MacroModel: a versatile program, *Chemisch Magazine,* **1987**, 18-19, 21-4.

185. C. Tard, X. Liu, S. K. Ibrahim, M. Bruschi, L. De Gioia, S. C. Davies, X. Yang, L.-S. Wang, G. Sawers and C. J. Pickett; Synthesis of the H-cluster framework of iron-only hydrogenase, *Nature (London, United Kingdom),* **2005**, 433, 610-13.

186. Z.-Q. Hu, H.-Y. Hu and C.-F. Chen; Phenanthroline Dicarboxamide-Based Helical Foldamers: Stable Helical Structures in Methanol, *J. Org. Chem.,* **2006**, 71, 1131-38.

187. N. P. Peet, L. E. Baugh, S. Sunder and J. E. Lewis; Synthesis and antiallergic activity of some quinolinones and imidazoquinolinones, *J. Med. Chem.,* **1985**, 28, 298-302.

188. N. D. Heindel, I. S. Bechara, P. D. Kennewell, J. Molnar, C. J. Ohnmacht, S. M. Lemke and T. F. Lemke; Cyclization of aniline-acetylenedicarboxylate adducts. A modified Conrad-Limpach method for the synthesis of potential antimalarials, *J. Med. Chem.,* **1968**, 11, 1218-21.

189. N. D. Heindel, T. A. Brodof and J. E. Kogelschatz; Cyclization of amine-acetylene diester adducts. Modification of the Conrad-Limpach method. I, *J. Heterocyclic Chem.,* **1966**, 3, 222-3.

190. H. C. Brown, M. Zaidlewicz, P. V. Dalvi and G. K. Biswas; Molecular Addition Compounds. 18. Borane Adducts with Hydroxydialkyl Sulfide Borates for

Hydroboration. New, Essentially Odorless, Water-Soluble Sulfide Borane Acceptors for Hydroboration, *J. Org. Chem.,* **2001**, 66, 4795-98.

191. B. Zeysing, C. Gosch and A. Terfort; Protecting Groups for Thiols Suitable for Suzuki Conditions, *Org. Lett.,* **2000**, 2, 1843-45.

192. T. L. Kurth and F. D. Lewis; Ground-State Conformational Equilibrium and Photochemical Behavior of Syn and Anti N,N'-Dimethyl-N,N'-di-1-naphthylurea Protophanes, *J. Am. Chem. Soc.,* **2003**, 125, 13760-67.

193. C. Dolain, A. Grelard, M. Laguerre, H. Jiang, V. Maurizot and I. Huc; Solution structure of quinoline- and pyridine-derived oligoamide foldamers, *Chem. Eur. J.,* **2005**, 11, 6135-44.

194. V. Berl, I. Huc, R. G. Khoury, M. J. Krische and J.-M. Lehn; Interconversion of single and double helices formed from synthetic molecular strands, *Nature,* **2000**, 407, 720-23.

195. H. Reihlen, A. v. Friedolsheim and W. Oswald; Nitric oxide and carbon monoxide compounds of apparently univalent iron and nickel, *Liebigs Ann. Chem.,* **1928**, 465, 72-96.

196. F. Gloaguen, J. D. Lawrence and T. B. Rauchfuss; Biomimetic hydrogen evolution catalyzed by an iron carbonyl thiolate, *J. Am. Chem. Soc.,* **2001**, 123, 9476-77.

197. H. Ogino, S. Inomata and H. Tobita; Abiological Iron-Sulfur Clusters, *Chem. Rev.,* **1998**, 98, 2093-121.

198. R. B. King; Organosulfur derivatives of metal carbonyls. I. The isolation of two isomeric products in the reaction of triiron dodecacarbonyl with dimethyl disulfide, *J. Am. Chem. Soc.,* **1962**, 84, 2460.

199. J. A. De Beer and R. J. Haines; Reactions of metal carbonyl derivatives. IV. Bridged sulfido derivatives of iron carbonyl, *J. Organomet. Chem.,* **1970**, 24, 757-67.

200. N. S. Nametkin, V. D. Tyurin and M. A. Kukina; Synthesis and some properties of sulfur-containing iron tricarbonyl complexes, *J. Organomet. Chem.,* **1978**, 149, 355-70.

201. D. Seyferth, R. S. Henderson and L. C. Song; Chemistry of m-dithio-bis(tricarbonyliron), a mimic of organic disulfides. 1. Formation of di-m-thiolate-bis(tricarbonyliron) dianion, *Organometallics,* **1982**, 1, 125-33.

202. D. Seyferth and R. S. Henderson; Di-m-thiolbis(tricarbonyliron), $(m\text{-}HS)_2Fe_2(CO)_6$: an inorganic mimic of organic thiols, *J. Organomet. Chem.,* **1981**, 218, C34-C36.

203. E. M. Markin and K.-i. Sugawara; Energy-Resolved Collision-Induced Dissociation of $Fe_2(CO)^{y+}$ (y = 1-9), *J. Phys. Chem. A,* **2000**, 104, 1416-22.

204. M. Kotzian, N. Roesch, H. Schroeder and M. C. Zerner; Optical spectra of transition-metal carbonyls: chromium hexacarbonyl, iron pentacarbonyl, and nickel tetracarbonyl, *J. Am. Chem. Soc.,* **1989**, 111, 7687-96.

205. T. Hirao, K. Aramaki and H. Nishihara; IR sensing of the electronic structure in the mixed-valence states of iron carbonyl-attached biferrocene and terferrocene, *B. Chem. Soc. Jpn.,* **1998**, 71, 1817-23.

206. M. Razavet, S. C. Davies, D. L. Hughes, J. E. Barclay, D. J. Evans, S. A. Fairhurst, X. Liu and C. J. Pickett; All-iron hydrogenase: synthesis, structure and properties of {2Fe3S}-assemblies related to the di-iron sub-site of the H-cluster, *J. Chem. Soc. Dalton,* **2003**, 586-95.

207. ShelXTL; Siemens Analytical X-ray Instruments. Inc., **1994**.

208. G. M. Sheldrick; ShelX97, **1997**.

209. P. C. Reeves; Carboxylation of aromatic compounds: ferrocenecarboxylic acid, *Org. Synth.,* **1977**, 56, 28-31.

210. M. Wada and O. Mitsunobu; Intermolecular dehydration between alcohols and active hydrogen compounds by means of diethyl azodicarboxylate and triphenylphosphine, *Tetrahedron Lett.,* **1972**, 1279-82.

10. Appendix

10.1 Appendix of Chapter 4

Dihedral Angles	k_χ [kcal.mol^{-1}]	n	χ_o [deg]
HP–CA2-CA2-HP	1.222	2	180.0
CA2–CA2-CA2-HP	4.281	2	180.0
CA2–CA2-CA2-CA2	19.575	2	180.0
CA2–CA2-CA2-C	3.230	2	180.0
HP–CA2-CA2-C	5.793	2	180.0
CA2–CA2-C-O	4.290	2	180.0
CA2–CA2-C-O	1.501	1	0.0
CA2–CA2-C-NH1	24.562	2	180.0
CA2–CA2-C-NH1	85.976	1	0.0
H-NH1-C-CA2	2.470	2	180.0
H-NH1-C-CA2	5.086	1	0.0
CA2–C-NH1-CT1	40.904	2	180.0
CA2–C-NH1-CT1	70.212	1	0.0
CA2–CA2-C-N	2.550	2	180.0
CA2–CA2-C-N	1.860	1	0.0
CA2–C-N-CP1	74.529	2	180.0
CA2–C-N-CP1	50.494	1	0.0
CA2–C-N-CP3	13.222	2	180.0
CA2–C-N-CP3	41.515	1	0.0
CP3–N-CP1-CD	3.664	3	0.0

Table 1 CHARMM dihedral angle parameters for the ferrocene, the ferrocene-peptide connection, and the nickel-sulfur ligand pocket.

Bonds	k_b [kcal.mol^{-1}.Å^{-2}]	b_o [Å]
HP–CA2	390.47	1.080
CA2–CA2	322.31	1.420
CA2-C	265.85	1.464

Table 2 CHARMM bond parameters for ferrocene and the ferrocene-peptide connection.

Angles	k_θ [kcal.mol^{-1}.rad^{-2}]	θ_o [deg]
CA2–CA2–CA2	50.575	108.0
HP-CA2–CA2	24.032	126.0
CA2–CA2-C	148.990	125.0
CA2–C-O	75.251	120.0
CA2–C–NH1	2.149	120.0
CA2–C-N	118.073	120.0
CT3–CT1-CD	96.177	108.0

Table 3 CHARMM angle parameters for ferrocene, the ferrocene-peptide connection, and the nickel-sulfur ligand pocket.

Improper torsions	k_ψ [kcal.mol^{-1}.rad^{-2}]	ψ_o [deg]
CA2–C-NH1-O	13.316	180.0
CA2–C-NH1-CT1	31.050	180.0
CA2–C-N-O	74.845	180.0
CA2–C-N-CP1	71.034	180.0

Table 4 CHARMM improper torsion parameters for the ferrocene, the ferrocene-peptide connection and the nickel-sulfur ligand pocket.

Atom type	ε [kcal.mol^{-1}]	$R_{min}/2$ [Å]	Charge [eV] [b]
CA2	-0.070	1.9924	-0.10
HP	-0.030	1.3582	-0.10
Fe	-0.020	1.4443	+2.0
Ni	-0.010	1.4125	+2.0

Table 5 CHARMM non-bonded parameters (LJ parameters and partial atomic charges). For the atoms constituting the ferrocene moiety (*i.e.* atom types CA2 and HP) the standard LJ parameters included in CHARMM were used. For the iron and nickel atoms, LJ parameters were taken from Ref. [33] (personal communication).

10.2 Appendix of Chapter 5

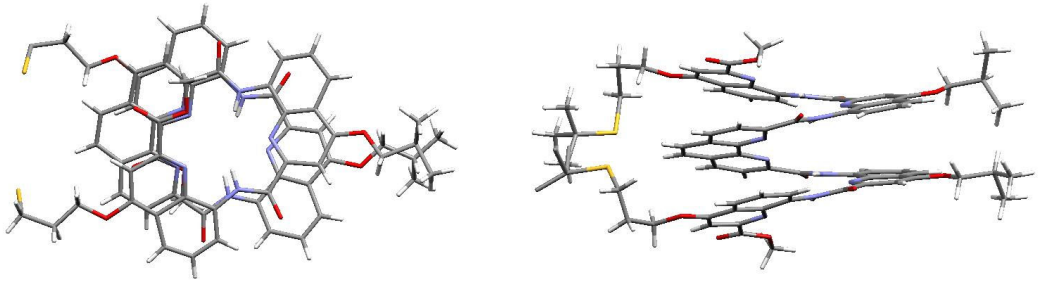

Figure 10.1 Crystal structure of **B29**, side view and top view of the entire structure. Included solvent molecules have been omitted for clarity.

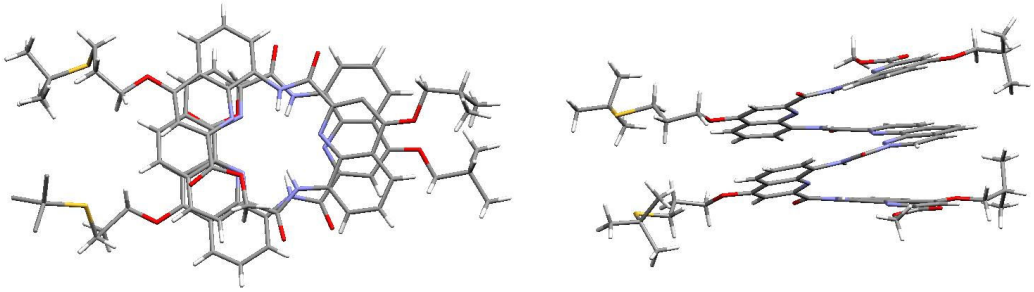

Figure 10.2 Crystal structure of **B24**, side view and top view of the entire structure. Included solvent molecules have been omitted for clarity.

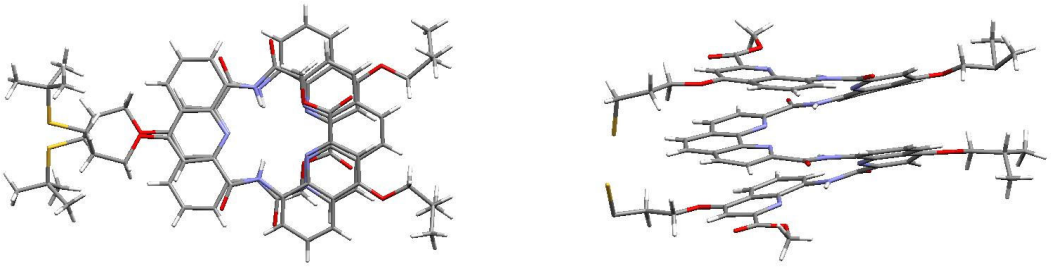

Figure 10.3 Crystal structure of **B23**, side view and top view of the entire structure. Included solvent molecules have been omitted for clarity.

10.3 Appendix of Chapter 6

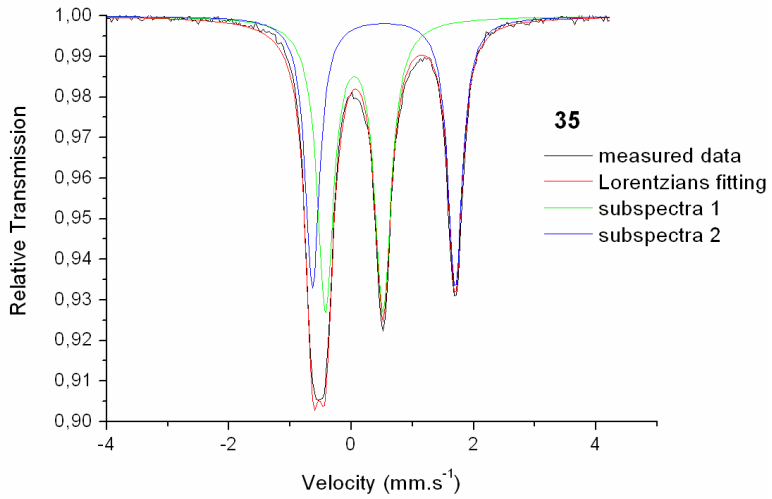

Figure 10.4 Moessbauer spectra of **35** measured as solid-state samples

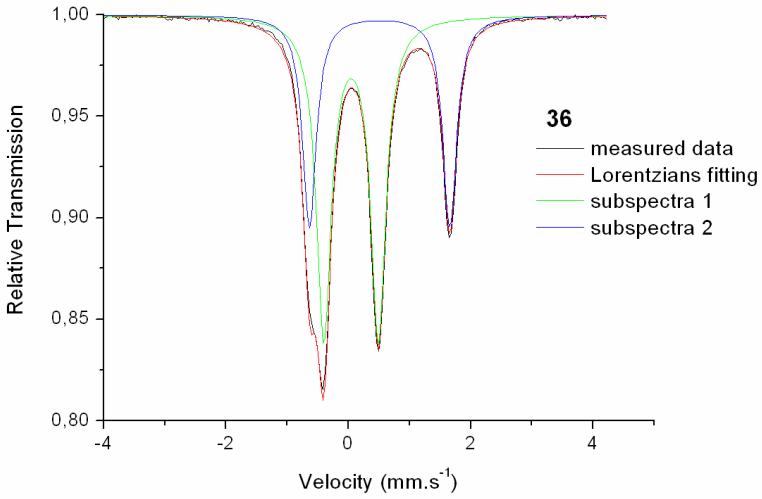

Figure 10.5 Moessbauer spectra of **36** measured as solid-state samples

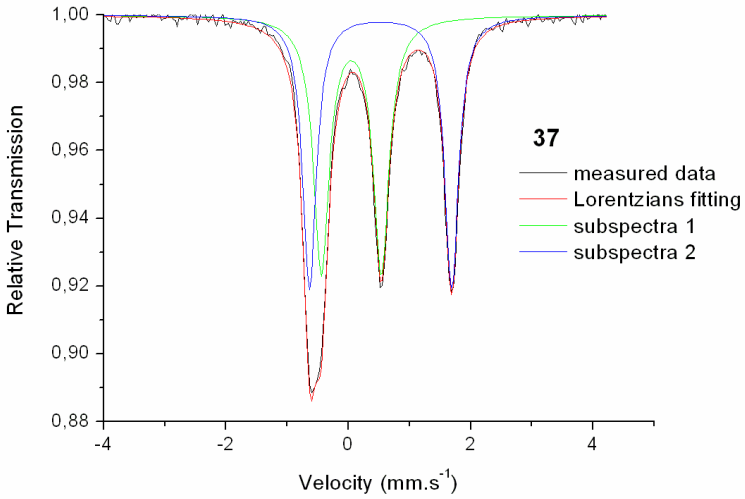

Figure 10.6 Moessbauer spectra of **37** measured as solid-state samples